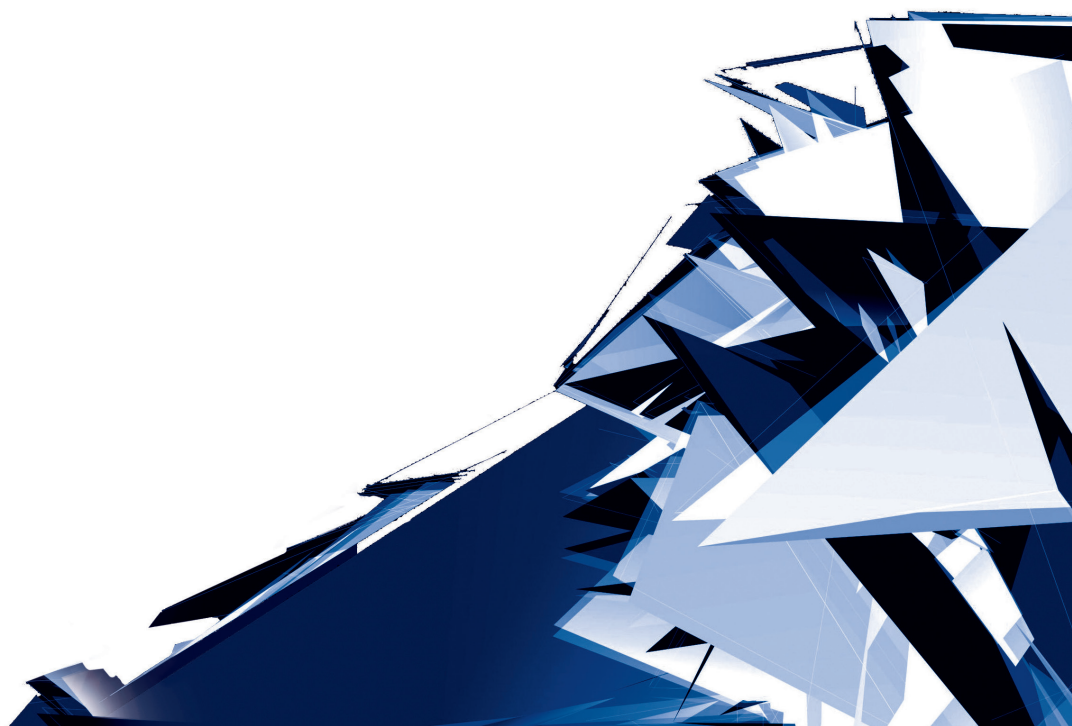


Technical Transactions

Czasopismo Techniczne

Volume 7

Year 2017 (114)



Chairman of the Cracow University of Technology Press Editorial Board
Przewodniczący Kolegium Redakcyjnego Wydawnictwa Politechniki Krakowskiej

Tadeusz Tatar

Editor-in-chief
Redaktor naczelny

Józef Gawlik
(jgawlik@mech.pk.edu.pl)

Scientific Council
Rada Naukowa

Jan Blachut – University of Liverpool (UK)
Wojciech Bonenberg – Poznan University of Technology (Poland)
Tadeusz Burczyński – Silesian University of Technology (Poland)
Massimo Corcione – Sapienza University of Rome (Italy)
Leszek Demkowicz – The University of Texas at Austin (USA)
Joseph El Hayek – University of Applied Sciences (Switzerland)
Ameen Farooq – Technical University of Atlanta (USA)
Zbigniew Florjańczyk – Warsaw University of Technology (Poland)
Marian Giżejowski – Warsaw University of Technology (Poland)
Sławomir Gzell – Warsaw University of Technology (Poland)
Allan N. Hayhurst – University of Cambridge (UK)
Maria Kušnierova – Slovak Academy of Sciences (Slovakia)
Krzysztof Magnucki – Poznan University of Technology (Poland)
Herbert Mang – Vienna University of Technology (Austria)
Arthur E. McGarity – Swarthmore College (USA)
Antonio Monestiroli – Polytechnic of Milan (Italy)
Marek Pabich – Lodz University of Technology (Poland)
Ivor Samuels – University of Birmingham (UK)
Mirosław J. Skibniewski – University of Maryland (USA)
Günter Wozny – Technical University in Berlin (Germany)
Roman Zarzycki – Lodz University of Technology (Poland)

Native Speakers

Weryfikacja językowa

Tim Churcher
Justin Nnorom

Section Editor
Sekretarz Sekcji

Dorota Sapek
(dsapek@wydawnictwo.pk.edu.pl)

Editorial Compilation
Opracowanie redakcyjne

Aleksandra Urzędowska
(aurzedowska@pk.edu.pl)

Typesetting
Skład i łamanie

Małgorzata
Murat-Drożyńska

Design
Projekt graficzny

Michał Graffstein

Series Editors
Redaktorzy Serii

ARCHITECTURE AND URBAN PLANNING

Mateusz Gyurkovich
(mgyurkovich@pk.edu.pl)

CHEMISTRY

Radomir Jasiński
(radomir@chemia.pk.edu.pl)

CIVIL ENGINEERING

Marek Piekarczyk
(mpiekar@pk.edu.pl)

ELECTRICAL ENGINEERING

Piotr Drozdowski
(pdrozdow@usk.pk.edu.pl)

ENVIRONMENTAL ENGINEERING

Michał Zielina
(mziel@vistula.wis.pk.edu.pl)

**PHYSICS, MATHEMATICS
AND COMPUTER SCIENCES**

Włodzimierz Wójcik
(puwojcik@cyf-kr.edu.pl)

MECHANICS

Andrzej Sobczyk
(andrzej.sobczyk@mech.pk.edu.pl)

www.ejournals.eu/Czasopismo-Techniczne
www.technicaltransactions.com
www.czasopismotechniczne.pl

Contents

ARCHITECTURE AND URBAN PLANNING

Karolina Dudzic-Gyurkovich

Subject of urban tissue continuity in different urbanisation periods in Europe.

Selected aspects 5

Eliza Szczerek

International student workshops as an important element in architectural education 21

CIVIL ENGINEERING

Bożena Hoła, Tomasz Nowobilski, Jarosław Rudy, Ewa Borowa Błazik

Dangerous events related to the use of scaffolding 31

Krzysztof Ostrowski

The influence of CFRP sheets on the strength of specimens produced using normal concrete and high-performance concrete assessed using uniaxial compression tests 41

Elżbieta Pilecka, Krystyna Stec, Renata Szermer-Zaucha

The influence of the Kłodnica fault tectonic zone on the degree of damage to buildings resulting from high magnitude tremors 53

Anna Śpiewak, Małgorzata Ulewicz

Analysis of the impact of corrosion on loss of load capacity and time between failures of a bridge in the town of Wisła 65

ELECTRICAL ENGINEERING

Yaroslav Kovivchak

An analysis of electromagnetic processes in a turbogenerator with a real rotor and a stator tooth structure in the no-load mode 73

ENVIRONMENTAL ENGINEERING

Andrzej Bielski

Different optimisation tasks used in water quality management 95

Monika Szłapa, Paweł S. Hachaj

The impact of processes of sediment transport on storage reservoir functions 113

MECHANICS

Marcin Hojny

Hybrid model of liquid metal flow and solidification 127

Małgorzata Kowalczyk

Cutting forces during precise turning of NiTi shape memory alloy 137

Artur Krowiak, Jordan Podgórski

The adaptation of the cross validation approach for RBF-based collocation methods 147

Edward Lisowski, Janusz Rajda	
<i>Evaluation of pressure losses reduction possibility for WEH22 directional control valve by internal geometry correction</i>	157
Marcin Migus, Andrzej Kęsy, Zbigniew Kęsy	
<i>Flow simulation in hydrodynamic torque converter</i>	165
Andrzej Opaliński, Mirosław Głowacki	
<i>Mobile remote monitoring system of water reservoirs.....</i>	175
Paweł Piątek	
<i>Evaluation of particle size distribution of aggregates in asphalt concrete by means of image analysis software</i>	183
Karol Osowski, Zbigniew Kęsy, Andrzej Kęsy, Artur Olszak	
<i>Application of numerical calculations in the design process of hydrodynamic torque converter</i>	191
Robert Płatek, Łukasz Malinowski, Piotr Zwoliński	
<i>Numerical analysis of damage in silica filled epoxy products using XFEM and its verifications</i>	199
Piotr Woś, Ryszard Dindorf	
<i>Virtual prototyping of electro-hydraulic parallel manipulator control systems</i>	209
Bożena Zwolińska	
<i>Modelling of production processes with the use of witness simulator.....</i>	219

Karolina Dudzic-Gyurkovich (kdudzic-gyurkovich@pk.edu.pl)

Institute of Urban Design, Faculty of Architecture, Cracow University of Technology

SUBJECT OF URBAN TISSUE CONTINUITY IN DIFFERENT URBANISATION PERIODS IN EUROPE. SELECTED ASPECTS

ZAGADNIENIE CIĄGŁOŚCI TKANKI MIEJSKIEJ W RÓŻNYCH OKRESACH URBANIZACJI W EUROPIE. WYBRANE ASPEKTY

Abstract

21st century cities, owing to their size, concentration of capital, advanced services and production, are the main centres of the global economy. It is not, however, the domain of exclusively postmodern times. For centuries, cities have played a key role in the development of civilisation, and the processes taking place within them have had an effect on the functioning of entire societies. The urban form we deal with today is a resultant of many determining factors and transformations. This paper presents selected aspects of the urbanisation processes that took place in the past, which even today have their effect on the physical form of towns and cities in Europe. Special attention shall be paid to phenomena, which may influence the coherence of form and the creation of barriers within the urban tissue in a different way.

Keywords: Urban form, coherence, urban barrier

Streszczenie

Miasta w XXI wieku, ze względu na ich wielkość, koncentrację kapitału, nowoczesnych usług i produkcji, są głównymi ośrodkami światowej gospodarki. Nie jest to jednak domena wyłącznie czasów ponowoczesnych. Od wieków miasta pełniły kluczową rolę w rozwoju cywilizacji, a procesy nich zachodzące miały i nadal mają wpływ na funkcjonowanie całych społeczeństw. Forma urbanistyczna, z którą mamy obecnie do czynienia, jest wypadkową wielu determinujących czynników i przemian. W artykule zostaną przedstawione wybrane aspekty zachodzących w przeszłości procesów urbanizacyjnych, które również obecnie oddziałują na fizyczną postać ośrodków miejskich Europy. Szczególna uwaga zostanie poświęcona zjawiskom w różny sposób mogącym wpływać na spójność formy i tworzenie barier w obrębie tkanki miasta.

Słowa kluczowe: Forma urbanistyczna, spójność, bariera urbanistyczna

1. Introduction. Special role of the European city

The problem of continuity of urban form is being discussed not only in the field of architectural and urban design, but it seems to touch and influence the processes of everyday life of the citizens. In most of the cases, when the quality of urban environment is perceived as poor, we have to face the lack of harmony and presence of barriers within the urban tissue. The contemporary form of numerous contemporary towns and cities is, however, a result of the operation of staggered forces and phenomena. In case of European cities, amongst which a considerable part have historically shaped quarters, these are processes that were happening over the span of many centuries, which saw planned or spontaneous development and transformations of urbanised areas. A special set of properties that used to be characteristic for cities on the European continent was noticed by e.g. M. Weber, who, based on research into medieval towns, formulated a theoretical model, comprising physical as well as social and political attributes¹, which were to make them distinct from towns and cities on other continents. The meaning of cities in the historical urban development was also emphasised by L. Benevolo, who classified them as important and characteristic aspects of the cultural heritage [4]. Contemporary deliberations devoted to the phenomenon of ‘the European city’ go way beyond the framework of the academic discourse². Certain formal and organisational properties³ become guidelines for new urbanisation models, such as e.g. the concept of ‘a compact city’, which is deeply justified by the historical development of cities in Europe [26, 51] and is currently implemented as the development policy in compliance with recommendations issued by global organisations⁴. Maintaining the values of ‘the European city’, which are still significant for its uniqueness, with its simultaneous adaptation to contemporary requirements, is a remedy for the progressing processes of spatial, social, and cultural disintegration, which frequently constitute a consequence of expansive development.

Also today, when the globalisation processes and constant information flow change the distribution of forces, and the area of social contacts translates into a virtual dimension, the real space is still a subject of research carried out in numerous fields of science. The article attempts to present characteristic, selected stages of urbanisation of European cities, Polish cities included, from the morphological perspective, with special emphasis put on the effect of individual phenomena on the physical continuity of the structure observed these days.

¹ He emphasised the need of co-existence of fortifications, a market square (place of trade), a courthouse and independent laws, some form of assembly, and at least partial autonomy [49, p. 38].

² Although studies of the theoretical model are still in progress in different parts of the world; cf. e.g. [15, 23, 27, 20].

³ Like e.g. compactness of development, hierarchical organisation, presence of historical traces, defined centre and city limits, multi-functionality [5, p. 40].

⁴ Cf. e.g. [16, 47, 38].

2. The problems of development of contemporary cities

2.1. Continuity vs. Fragmentation

Amongst the problems that contemporary city struggles with, one of the most often discussed issues is the phenomenon of fragmentation, or even capsularisation of this space, which consequently lead to the disappearance of urban qualities. [15, 46, 40, 42, 12].

It is not, however, a new phenomenon, as the first to write about the disturbing condition of American cities in the 1960s was Jane Jacobs, who stigmatised the modernist planning concept implemented at the time. Earlier voices seeking the source of frustration of contemporary man in the city and its social and spatial organisation were coming from e.g. representatives of the Chicago School, who regarded the emerging trend in the sociology of the city as a diagnostic tool of social issues. Space segregation and polarisation observed in cities examined at the time, in theoretical models, assumed the forms of concentric zones [9], sectors [22], or numerous separate centres with specialised functions [19]. It was closely connected with social segregation capable of leading to the domination of one, strongest and most influential group [9, 36, 52]. Today, many researchers find a relation between growing social inequalities and spatial divisions of the city, which constitutes an area of activity of the communities inhabiting it. Such phrases as 'divided cities' [17, 35], 'dual cities' [37], 'polarised', 'fragmented cities' [8, 55] regularly appear in the literature of numerous fields of science tackling subjects relating to the city and its functioning.

In the approach of urban planning, the issue of spatial fragmentation as a problem that dominates many others is touched upon in the important publication 'Collage City', where in place of the manner of grasping the contemporary city, the authors propose a mosaic, a collection of different elements⁵ within the scheme of an urban collage, where individual components are not linked to any subordinate compositional concept. The lack of relations, also the spatial ones, between fragments of the city comprehended this way seems to be an inseparable part of this concept. Consequences of fragmentation or division are relatively easy to observe, which was pointed out already by K. Lynch, who stated that residents of the majority of American cities 'are quite aware of the abomination of the world they live in and they often complain about its (...) incoherence and monotony at the same time' [34, p. 3]. Well-developed transportation systems, intended most of all for car traffic, large-scale shopping and industrial facilities, as well as closed private housing estates, contribute to the creation of a landscape where 'no-places' neighbour each other and share places of traditional importance [1].

⁵ 'objets trouvés', such as e.g. exceptional streets, magnificent public terraces, mysterious and complex buildings [42].



Fig. 1. Urban structure of the vicinity of Milan, exhibiting the features of fragmentation: residential areas neighbour on large service and industrial facilities and farmlands (photo by K. Dudzic-Gyurkovich)

In the opposition, as it were, to the phenomena referred to above, continuity could be simply defined as compactness, cohesion of form, continuation of the built tissue as well as of systems of public spaces, priority of pedestrian accessibility over accessibility of individual means of transport. Continuity can constitute a value of the urban space of the historical origin, as well as the urban space that comes into being in contemporary times.

Structure fragmentation, observable in cities of today, can appear as a factor of numerous different processes, e.g. extensive urbanisation, consuming new areas located further and further from the main urban settlement, or transformations, demolitions, and replacement of the existing tissue⁶. The lack of the sensed coherence of urban spaces can be influenced by processes that occurred sometimes even in the distant past and still determine the development direction and opportunities of the urban organism, which will be discussed hereafter. For decades now, the mathematical approach to the issue of complexity and simultaneous fragmentation of urban structures has been gaining in importance⁷. Analyses of existing systems and theoretical models created by such researchers as m. Batty, B. Hillier, or N. Salingaros, point to the importance of accessibility and continuity most of all of public spaces in the process of forming a well-functioning urban system.

⁶ The current shape of many European cities was strongly influenced by the period of the World War II and the period of reconstruction that followed it, during which totally opposite concepts were implemented. The W-Z Route in Warsaw, the Nadodrzańska Artery in Szczecin, planned as new axes of the cities, are only two examples of new urban projects implemented in the post-war reality [31].

⁷ Such theories as 'complexity theory of cities', 'fractal cities', or advanced spatial analysis, such as 'space syntax', cf. e.g. [2, 3, 21].

2.2. Limits, edges, and barriers

The phenomenon of creating barriers and divisions is inscribed in the nature of creation and transformations of the urban tissue, which is subjected to diversified limitations of physical as well as economic, social and other character. The issue of boundaries and edges of the urban structure has been presented in a very interesting way by e.g. S. Kostof, who differentiated two types of borderlands according to their location towards the urban structure. The first one encompasses cases of shaping the edges in the form of a literary boundary – a wall, as well as – much more frequently encountered today – ‘blurred’ delimitation of peripheral areas. The second type are all sorts of divisions of the concerning the interior of urbanized area itself, which have been decisive for the special distinctness of specialised functional zones, starting from religion and authorities through commerce, trade, and business. The phenomena of social segregation caused by national, cultural or economic distinctness discussed above fall into the division category understood this very way [28]. In this approach, a certain dichotomy is discernible; an external edge of the urban system is examined predominantly in the categories of physical properties, whereas internal barriers seem to result rather from the social structure, morals, or economic conditions. Nevertheless, there are and still emerge limitations in the contemporary world, which could be defined as urban barriers, influencing the lack of the sensed coherence of space. They constitute barriers most of all at the level of the local traffic and pedestrian traffic, often utilised in a manner that testifies to a certain exterritoriality of the area towards the structure that surrounds it. Such structures as highways, railway areas, large industrial facilities and shopping malls create realistic divisions of the urban tissue frequently contributing to its fragmentation.



Fig. 2. Barcelona, area located at the edge of the revitalised district of El Poblenou. Continuity of the orthogonal layout is disturbed with transport routes running at several levels (photo by K. Dudzic-Gyurkovich)

3. Development of European cities throughout the history.

3.1. Before the industrial era

Amongst the factors, which, in the past, had their effect on the physical form of an urban organism, most of them also functioned as a barrier, which simultaneously enabled the city to develop and constituted its maximum range at the time. The history of urban planning classifies these determinants in many ways, and one of the many theories that deserves to be referred to here is an important theory formulated by T. Tolwiński, who defined a set of influences that have their effect on cities in the process of them coming into being. Explaining the process of building and organising cities basing on the 'urban factors' defined nearly a hundred years ago still seems to be valid to a certain extent. Prior to the modern period, physical barriers for the spatial development of cities included e.g. natural conditions, which in the most fundamental way influenced the form of an urban settlement [45]. Land relief, the presence of rivers, lakes, location at the seashore – all this can still have its effect on the direction of the spatial development of the city, constituting natural barriers that stop the development expansion until the next developmental leap⁸. Processes of shaping development edges at subsequent stages of the development of the city seem to have a crucial effect on its current appearance. Probably the most important factors that influences further development were military conditions, which determined e.g. the compactness of the system and its fitness for fortification. The external edge of compact development marked with the fortification system constituted a measurable limit of the city at the same time. Preserved parts of city walls and defensive systems, which today can be found usually in the very centres of cities, constitute their important historic heritage; traces visible in the names of streets⁹, their routes, or land allotment are of equal importance¹⁰.

3.2. Transformations of the industrial era

The 19th century brought about many changes in the priorities of the process of conscious city design, as well as in the directions assumed by its spontaneous development. Processes of dynamic urbanisation and urban sprawl in Europe were stimulated by the economic development relating to the industrial revolution. A significant increase in the number of city residents entailed the need of relevant transformations of urban spaces, so as to make them

⁸ Such a leap, in the literature devoted to urban morphology referred to as 'leapfrog', occurs at the time of intensified development of the city, when architecture, usually residential buildings, grow beyond the existing limits, which get absorbed and developed inside the still developing organism, <http://www.urbanform.org/glossary.html> (access: 27.01.17).

⁹ Such names as 'Wall Street' in New York, or 'Rampart Street' in New Orleans, are visible remains of the short period of fortifying American cities. Wooden fortifications fell into decay, or were disassembled in order to obtain materials and fuel [45, p. 38].

¹⁰ It is an element which is classified by researchers from the circles of urban morphology as belonging to the so-called 'morphological frame', that is a certain collection of properties and factors which appear in subsequent plans and stages of development of the city. Cf. e.g. [50].



Fig. 3. Location by the river, which constitutes a spatial barrier, determines the development of the central part of Poznań (photo by K. Dudzic-Gyurkovich)



Fig. 4.a. Preserved fragments of fortifications set realistic limits of the Old Town in Toruń (photo by K. Dudzic-Gyurkovich)



Fig. 4.b. The name and course of Podmurna street (Polish: *near the walls*) in Toruń testifies to the presence of fortifications whose fragments have been preserved to date (photo by K. Dudzic-Gyurkovich)



Fig. 4. Milan, view from the historic city towards Porta Ticinese, a place that commemorates one of the gates in the now non-existent city walls. The course of the walls is still legible in the tissue of the city; it is determined by two parallel streets forming characteristic narrow quarters (photo by K. Dudzic-Gyurkovich)

address the new lifestyle. This fact, as well as the development of warfare techniques, led to a situation where existing fortification systems, most of all dating back to the Middle Ages, now not surrounding entire cities, but only their central parts, became an undesirable barrier hampering and obstructing territorial development. In many cases, they were disassembled in order to allow for harmonious development of city centres, or for their reconstruction. The resulting areas were developed in compliance with the then needs, frequently as boulevards constituting an important element of the emerging transport systems and municipal greenery¹¹.

Another important change that had far-reaching effects in the spatial organisation of cities was the appearance and popularisation of railway transport used for transporting goods as well as passengers. At that time, it became necessary to consider it and plan its routes in the operating structure. Changes, and sometimes obstacles in the previously established system of local traffic, relating predominantly to the auxiliary infrastructure, such as embankments, excavations, railway tracks and tractions, from the contemporary point of view, could be classified as barriers with a significant effect on the continuity and coherence of space.

¹¹ A perfect example are Parisian fortifications of Thiers; falling into decay until the end of the 19th century, eventually disassembled in the 1920s. They were replaced by a ring of roads, the so-called Les Boulevards des Maréchaux, which until the construction of the parallel Boulevard Périphérique in the 1970s functioned as a ring road of the city. Similar actions were undertaken e.g. in Vienna, by creating in the years 1858–1872 the Ring and Gürtel boulevards in the place of disassembled fortifications.



Fig. 5. Milan, view from a parking lot above railway tracks leading to the Porta Garibaldi railway station. The railway tracks, as well as well-developed systems of parking lots constitute a barrier for the surrounding tissue (photo by K. Dudzic-Gyurkovich)

Buildings of railway stations, and most of all railway lines, once intensely utilised, constituted very clear edges, forming the tissue of the city and dividing it. The development of railway progressed over subsequent decades, being an easily accessible as well as mass transportation system¹². These days, we face a challenge, which is the adjustment of this type of transport to the current needs¹³. The existing, extended systems of railway junctions and sidings are usually utilised to a minor extent, and the grounds occupied by them are closed and excluded from the urban use, still constituting real spatial barriers in the city.

3.3. Late 19th century, early 20th century – new theories of space organisation

the appearance of contemporary urban settlements was influenced in a very special way by activities belonging to broadly understood modernism. This trend, developing partially as a negation of the historic, excessively dense tissue, which was no longer able to meet the

¹² 12 As late as in the 1950s, that is until the moment of rapid development of car traffic, railway used to be the dominating means of transport in European cities. Over subsequent decades it was losing its dominance to cars in terms of the transport of people, as well as goods. In socialist states, as a result of definitely slower development of the network of motorways and the activities of the planned economy, comprising the volumes and directions of railway transport, as well, the dominance of railway lasted longer – until the 1970s [18].

¹³ 13 A developing branch of this type of transport is the high-speed rail, which for several decades now has been gaining in importance, not only in Europe; cf. e.g. [54, 18].

needs of the then society, resulted in a revolutionary reevaluation of the concept of the city, and solutions implemented at the time frequently evoke controversies and call for revision. Postulates of providing decent living and working conditions, as well as of creating an urban form corresponding more to the modern, dynamic reality, found their reflection in realistic, as well as utopian concepts¹⁴. The common quality of the sometimes quite different ideas was the principle of functional division, which was given its most radical form in flagship projects by Le Corbusier¹⁵. According to the new planning doctrine, sanctioned with the deliberations of the CIAM congress and the provisions of the Athens Charter, the city should be functional, i.e. it should have specific areas allocated to residential, industrial, office-related purposes, as well as vast green areas able to provide the designed conditions for leisure and pastimes. The road structure appeared as the superior structure, intended to link individual parts of the city, as well as the city centre with the suburbs. New technical opportunities brought about the actual tiered utilisation of space – wharfs, tunnels, and grade-separated junctions served the purpose of effective separation of functions and improvement of the flow of all types of traffic. In this model, which was implemented over subsequent decades in different forms¹⁶, barriers disturbing the coherence of the urban tissue were no longer single elements. The previous relations between the open space and buildings were reversed [40, 30]. Freestanding structures were located in the open space, limited merely by the edge formed by a transport route or green areas. The continuity of the form of the city was disturbed programmatically.

4. Summary – contemporary problems of urban planning

development and transformations of contemporary cities are characterised by the multitude of directions and issues, which, due to the so far never encountered scale of urbanisation¹⁷, concentrate in urban settlements. From the perspective of transformations of the physical form of the city, the continuity of the urban tissue, and the appearance of barriers, several phenomena seem to be particularly important. Centuries of the development of industrial production-based economy have influenced the urban structure of European cities, leaving behind industrial areas

¹⁴ Starting from the concept of ‘industrial city’ of T. Garnier, remaining in the sphere of plans, or ‘garden city’ of E. Howard, which has been implemented in numerous European countries, through F.L. Wright’s deglomeration ‘broadacre city’ or A. Soria y Mata’s and A. Milutin’s ‘linear city’, to the aforementioned designs by Le Corbusier, in all concepts one can notice a pursuit of clear division of the main functions of the city. Cf. e.g. [33, 6].

¹⁵ E.g. *Ville contemporaine de trois millions d’habitants*, (1922), *Ville radieuse*, (1924), and the never implemented plans for Paris and Barcelona: the *Voisin Plan* (1925), the *Macia Plan* (1932), the latter executed in collaboration with a Catalan architect, Joseph Lluís Sert [10].

¹⁶ Recommendations of the Athens Charter, published as late as in 1943, had a significant effect on urban planning in the post-war period, not only in Europe. Concepts of modernism, sometimes in their quite grotesque version, were manifested in e.g. large-scale urban projects, wasteful land development, or mass housing construction.

¹⁷ According to the data of the World Health Organisation in 2014 54% of all people lived in urban areas; it is estimated that in 2030 it will be even 66%. http://www.who.int/gho/urban_health/situation_trends/urban_population_growth_text/en/ (access: 05.02.17).

and facilities, which, in the era of post-industrial economy, have become useless. As P. Lorens observes, 'the effect of deindustrialisation processes are also dramatic social consequences, such as very high unemployment rates, immense growth of delinquency, and physical degradation of entire vast areas of the urban space' [32, p. 13]. Revitalisation or re-development of such territories constitutes a serious task, which can have a positive effect on the harmonisation and coherence of the city's appearance. Improvement of the quality of grounds that used to be invested into, in global terms, is inscribed in tendencies, which aim to prevent excessive spread of unstructured suburban development, today referred to as 'the urban sprawl'. The development of advanced means of transport, especially the constant increase in the number of passenger cars, is the result as well as one of the causes of the urban sprawl and of locating satellite housing estates further and further from the city centre. Cities on the American continent were one of the first – already in the 1950s – to experience the phenomenon referred to above, which is connected not only with the expansion of extensive forms of development, but also with the dispersion and degradation of downtown areas¹⁸ [24, 46]. The lack of continuity in the land development constitutes an inseparable quality of this development system, which currently refers to the majority of European cities, as well [16]. Strategies that are to stop or tame this development model assume different forms, from the concept of 'compact city'¹⁹, which is oriented towards the form of the city, through 'smart city', 'eco-city', 'creative city', to 'connected city', which is a vision of a coherent city of the 21st century.

The dominance of individual transport, regarded as a priority for many decades of conscious planning, is a complex problem, with multiple consequences. One of them is the creation of barriers inside the urban structure in places where extended transportation routes dominate other types of land use. Heavy car traffic contributes to the marginalisation of the role of public space, and areas adjacent to motorways often are degraded or remain undeveloped due to multiple issues, such as noise, exhaust fumes, or difficulty in crossing the barrier. These are not the only phenomena that create 'the dead edges' of the urban tissue. The group of broadly understood barriers within an urban form includes e.g. fenced residential enclaves or large-scale shopping malls. In each of those cases, a part of the space is demarcated and separated – excluded from public use. Today, privatisation of public space is a broadly encountered phenomenon, manifesting itself very strongly in contemporary spaces of consumption, which compete with the city, assuming social activities traditionally undertaken within the urban environment. Phenomena relating to the imminent globalisation, development of the knowledge-based economy and information society, also contribute to breaking traditional relations within the built space [48]. The return to the concept of urbanity, postulated for many years now, is manifested in a tangible way in the compactness of structure, the block development, or the hierarchical sequence of streets and squares [41]. The actual public space, despite its sometimes quite surprising transformations, or even despite the announcement of its fall, still constitutes the most natural and accessible field of study devoted to the condition of the contemporary city.

¹⁸ Which has been already tackled by J. Jacobs, who pointed out that once compact areas with diversified functions change and degenerate in the direction of homogenous, unfriendly structures [24].

¹⁹ Cf. e.g. [26, 38].





Fig. 6. Barcelona, the main road (Gran Via de les Corts Catalanes) running nearly across the entire city, intersects the neighbouring areas of compact urban development (photo by K. Dudzic-Gyurkovich)



Fig. 7. Szczecin – a grade-separated junction of Nadodrzańska Artery (built right after World War II) and Zamkowa Route generates nobody's land in the very city centre, which dangerously hampers the creation of any compositional and functional link between both parts of the Old Town (photo by K. Dudzic-Gyurkovich)



Fig. 8. Milan, part of a fenced and guarded complex of residential buildings 'City Life', under construction. The buildings visible in the picture have been designed in the studio of Daniel Liebeskind (photo by K. Dudzic-Gyurkovich)

References

- [1] Augé M., *Nie-miejsca: wprowadzenie do antropologii nowoczesności*, PWN, Warszawa 2011.
- [2] Batty M., Longley P.A., *Fractal cities: A geometry of form and function*, Academic Press, San Diego CA 1994.
- [3] Batty M., *New Science of Cities*, MIT Press, Cambridge MA 2013.
- [4] Benevolo L., *Miasto w dziejach Europy*, Wydawnictwo Krag, Oficyna Wydawnicza Wolumen, Warszawa 1995.
- [5] Billert A., *Założenia, modele i planowanie polityki rozwoju miast. Próba konfrontacji dwóch światów Unii Europejskiej*, [in:] Derejski K., Kubera J., Lisiecki S., Macyra R. (ed.), *Deklinacja odnowy miast*, Wydawnictwo Naukowe Wydziału Nauk Społecznych, UAM, Poznań 2012.
- [6] Böhm A., *O czynniku kompozycji w planowaniu przestrzeni*, Wydawnictwo PK, Kraków 2016.
- [7] Brugemann R., *Sprawl – a compact history*, University of Chicago Press, Chicago 2006.
- [8] Burgers, J., *De Gefragmenteerde Stad [The Fragmented City]*, Boom, Amsterdam 2002.
- [9] Burgess E.W., *Growth of the City, Introduction to a Research Project*, [in:] Park R.E., Burgess E.W., McKenzie R.D., (ed.) *The City*, The University Of Chicago Press, Chicago, London 1925.
- [10] Cohen J.-L., *Le Corbusier, la planète comme chantier*, Textuel, Paris 2005.

- [11] Deakin M., (red.), *Cerating Smart-er Cities*, Oxon, Routledge 2013.
- [12] De Cauwer L., *The Capsular Civilization: On the City in the Age of Fear*, NAI Pub, Rotterdam 2004.
- [13] Duany A., Plater-Zyberk E., Speck J., *Suburban Nation. The Rise of Sprawl and the Decline of American Dream*, North Point Press, New York, 2000.
- [14] Dymnicka M., *Przestrzeń publiczna a przemiany miasta*, Wydawnictwo Naukowe Scholar, Warszawa 2013.
- [15] Elin N., *Postmodern Urbanism*, Princeton Architectural Press, New York 1999.
- [16] European Environment Agency EEA, *Urban sprawl in Europe: the ignored challenge. EEA Report No 10/2006*, European Environment Agency, 2006.
- [17] Fainstein S., Gordon I., Harloe M., *Divided cities: New York and London in the contemporary world*, Basil Blackwell, Cambridge, MA 1992.
- [18] Garlikowska M., *Czynniki wpływające na postrzeganie transportu kolejowego w kategoriach niezawodności*, [in:] *Problemy Kolejnictwa*, Vol. 165 (XII 2014), pp. 35–49.
- [19] Harris C.D., Ullman E.L., *The nature of cities*, [in:] *Annals of the American Academy of Political and Social Science*, 242, 1945, pp. 7–17.
- [20] Häussermann H., *The End of European City?*, [in:] *European Review*, Vol. 13, 2005, No. 2, pp. 237–249.
- [21] Hillier B., *Space is the machine: a configurational theory of architecture*, Space Syntax, London 2007, E-book, <http://spaceisthemachine.com> (access: 02.02.2016).
- [22] Hoyt H., *The Structure and Growth of Residential Neighborhoods in American Cities*, Federal Housing Administration, Washington DC 1939.
- [23] Isin E.F., *Theorizing the European city*, [in:] Delanty G. (ed.) *Handbook of Contemporary European Social Theory*, Routledge 2006.
- [24] Jacobs J., *The Death and Life of Great American Cities*, Modern Library Editions Random House Inc, New York 1961.
- [25] Jencks Ch., *The Story of Post-Modernism: Five Decades of the Ironic, Iconic and Critical in Architecture*, John Wiley & Sons, Chichester 2011.
- [26] Jenks M., Burton E., Williams K., *The Compact City; A Sustainable Urban Form?*, E & FN Spon, London 1996.
- [27] Koch F., *The European City as a Transdisciplinary Concept: contradictions and potentials*, [in:] *Boletín de la Asociación de Geógrafos Españoles*, No. 67, 2015, pp. 457–463.
- [28] Kostof S., *The city assembled : the elements of urban form through history*, Thames and Hudson, London 1999.
- [29] Kosiński W., *Preliminaria badań nad problematyką: Piękno miasta*, [in:] *Przestrzeń i Forma*, No. 10/2008 pp. 13–42.
- [30] Krier L., *The Architecture of Community*, Island Press, Washington DC 2009.
- [31] Lorens P., *Porządek architektoniczny i urbanistyczny jako element przestrzennego zagospodarowania kraju*, [in:] *Studia Regionalne i Lokalne*, No. 3(21)/2005.
- [32] Lorens P., Martyniuk-Pęczek J. (ed.), *Wybrane zagadnienia rewitalizacji miast*, Wydawnictwo Urbanista, Gdańsk 2009.

- [33] Lorens P., Mironowicz I., (ed.), *Wybrane teorie urbanistyki współczesnej*, Wydawnictwo Urbanista, Gdańsk 2013.
- [34] Lynch K., *Obraz miasta*, Archivolta, Kraków 2010.
- [35] Marcuse P., van Kempen R., *Of states and cities: The partitioning of urban space*, Oxford University Press, Oxford 2002.
- [36] McKenzie R.D., *The Ecological Approach to the Study of the Human Community*, [in:] Park R.E., Burgess E.W., McKenzie R.D., (ed.) *The City*, The University Of Chicago Press, Chicago, London 1925.
- [37] Mollenkopf J.H., Castells M., *Dual City: Restructuring New York*, Russell Sage Foundation, New York 1991.
- [38] OECD, *Green Growth Studies: Compact City Policies: A Comparative Assessment*, OECD Publishing: Paris 2012.
- [39] OECD, *The Metropolitan Century: Understanding Urbanisation and its Consequences*, OECD Publishing, Paris 2015.
- [40] Panerai P., Castex J., Depaule J-C., Samuels I., *Urban Forms: The Death and Life of Urban Block*, Architectural Press, Oxford 2004.
- [41] Paszkowski Z., *Miasto idealne w perspektywie europejskiej i jego związki z urbanistyką współczesną*, Universitas, Kraków 2012.
- [42] Rowe C., Koetter F., *Collage City*, MIT Press, Cambridge MA 1983.
- [43] Salingeros N., *Principles of Urban Structure*, Techne Press, Amsterdam 2005.
- [44] Sennett R., *The Fall of Public Man*, Penguin Books, London, 2002.
- [45] Tołwiński T., *Urbanistyka T.1 – Budowa miasta w przeszłości*, Wydawnictwo Zakładu Urbanistyki Politechniki Warszawskiej, Warszawa 1939.
- [46] Trancik R., *Finding Lost Space: Theories of Urban Design*, Van Nostrand Reinhold Company, New York 1986.
- [47] United Nations, Department of Economic and Social Affairs, *Population Division*, 2014.
- [48] van Kempen R., *Divided cities in the 21st century: challenging the importance of globalisation*, [in:] *Journal of Housing and the Built Environment*, 2007, 22, pp. 13–31.
- [49] Weber M., *The Nature of the City*, [in:] Sennett R. (ed.), *Classic Essays on the Culture of Cities*, Prentice, Hall Inc., Englewood Cliffs, New York 1969.
- [50] Whitehand J.W.R., *British Urban Morphology: The Conzenian Tradition*, [in:] *Urban Morphology*, 2001, 5(2), pp. 103–109.
- [51] Williams K., *Urban form and infrastructure: a morphological review*, *Future of cities: working paper*, Foresight, Government Office for Science, 2014.
- [52] Wirth L., *Urbanism as a Way of Life*, *The American Journal Of Sociology*, Vol. XLIV, No. 1, 1938, pp. 2–24.
- [53] *World Urbanization Prospects: The 2014 Revision, Highlights (ST/ESA/SER.A/352)*.
- [54] Załuski D., *Przekształcenia dworców kolejowych i terenów kolejowych na nowe funkcje miejskie*, Politechnika Gdańska, Studio DZ, Gdańsk 2010.
- [55] Zuziak Z.K., *The Idea Of The City And Planning Theories*, *Technical Transactions*, 12-A/2015, pp. 9–27.
- [56] www.urbanform.org/glossary.html (access: 20.05.2017).



- [57] www.ectp-ceu.eu (access: 20.05.2017).
- [58] www.who.int/gho/urban_health/situation_trends/urban_population_growth_text/en (access: 20.05.2017).
- [59] www.fhwa.dot.gov/interstate/history.cfm (access: 20.05.2017).
- [60] <http://spaceisthemachine.com> (access: 20.05.2017).
- [61] <http://libeskind.com/work/city-life> (access: 20.05.2017).

Eliza Szczerek (eszczerek@pk.edu.pl)

Division of Public Spaces for Movement, Institute of Urban Design,
Faculty of Architecture, Cracow University of Technology

INTERNATIONAL STUDENT WORKSHOPS AS AN IMPORTANT ELEMENT IN ARCHITECTURAL EDUCATION

MIĘDZYNARODOWE WARSZTATY STUDENCKIE JAKO ISTOTNY ELEMENT EDUKACJI ARCHITEKTONICZNEJ

Abstract

Workshops as one of the paths in the process of architectural education seem to constitute an important element in the development of competence and skills, mostly of students, but they can also considerably enrich the didactic and scientific competence of people who assume the role of teachers. This pertains especially to students of Ph.D. courses, who, as teaching assistants, are standing at the threshold of their teaching careers. Due to the fact that workshops have a different character than the formula of course projects, on the one hand, they are a diversion in the regular courses, and on the other, they enrich them to a considerable extent, especially if they are international.

Keywords: international students workshops, architectural education

Streszczenie

Warsztaty, jako jedna ze ścieżek w procesie edukacji architektonicznej, mogą stanowić istotny element rozwoju kompetencji i umiejętności studentów, ale także mogą wzbogacić warsztat pracy dydaktycznej i naukowej osób, które występują w roli prowadzącego. Dotyczy to szczególnie słuchaczy studiów doktoranckich, którzy jako asystenci stoją u progu swojej kariery dydaktycznej. Warsztaty studenckie, ze względu na swoją odmienną formę w stosunku do formuły projektów kursowych, stanowią niejako ich uzupełnienie. Z jednej strony są odskocznią od regularnego trybu studiów, a z drugiej w znaczący sposób mogą go wzbogacić, szczególnie jeśli ich charakter jest międzynarodowy.

Słowa kluczowe: międzynarodowe warsztaty studenckie, edukacja architektoniczna

Workshops as one of the paths in the process of architectural education seem to constitute an important element in the development of competence and skills, mostly of students, but they can also considerably enrich the didactic and scientific competence of people who assume the role of teachers. This pertains especially to students of Ph.D. courses, who, as teaching assistants, are standing at the threshold of their teaching careers.

Due to the fact that workshops have a different character than the formula of course projects, the former, as it were, supplement the latter, and constitute an important element in the process of architectural education. A feature that makes workshops stand out is, above all, the working time, which is much shorter, translating into the manner and nature of work. Workshops most often last several days and predominantly focus on the development of guiding ideas. The works usually are performed in teams, which implies the need of close and intense cooperation between participants.

Both properly conducted workshops and course projects develop the skills and knowledge necessary to exercise the profession, which are referred to as the so-called hard competence, and the so-called soft competence, connected with personal psychophysical properties and interpersonal predispositions.

It seems that the difference between both forms of teaching resides predominantly in the extent to which a specific type of skills is developed. The curriculum of the university courses composed as a whole aims at guiding students through its individual stages, so as to allow them to develop the knowledge necessary to move on to the next one. Course projects, by 'guiding' to more and more complex issues, enable to obtain and consolidate students' knowledge and competence, focusing most of all on the development of the hard skills.

The formula of an architectural workshop is, on the one hand, a diversion in the regular courses, and on the other, it enriches them to a considerable extent. Most often, the tackled subjects pertain to up-to-date problems, which increases sensitivity to specific aspects, but also boosts the students' professional knowledge. The importance of this form of expanding knowledge of architecture students is well illustrated by the international workshop of Eco Rehab 3 – Future of the City (Cracow 2012)¹ and 'Cracow Zakrzówek – Inner City Edge (Cracow 2013)². Within the scheme of the Eco Rehab 3 workshop, the subject of housing estates consisting of buildings made of prefabricated concrete panels and options of their revitalization was tackled. The workshop devoted to Zakrzówek in Cracow focused on the issue of aggressive developers' policy in the city, in the context of creating the city edge, which is a place of contact between urbanized and green areas. Demographic and spatial problems of the currently poorly developing small Italian town were the subject matter of another equally valuable workshop: Canzo International Design Workshop (Canzo 2011)³.

¹ International Student Workshop, Eco Rehab 3 – Future of the City. Workshop organized by the Institute of Urban Design, Faculty of Architecture, Cracow University of Technology, on 17–28 April 2012 in Cracow.

² Workshop: Design Seminar 'Cracow Zakrzówek – Inner City Edge', organized by the Institute of Urban Design, Faculty of Architecture, Cracow University of Technology, on 15–17 November 2013 in Cracow.

³ Canzo International Design Workshop: projects for the touristic-environmental redevelopment of the Valassina district, held within the framework of a cycle of workshops "Territori in Evoluzione". It was held on 11–20.09.2011 in Canzo (Italy).

The task of investigating the subject matter of a workshop, and later on of searching for a solution and development of the concept, requires strong commitment on the part of the students, as well as communication skills, creativity, dynamism of action, ability to work in a team, time management, etc. Therefore, it could be stated that workshops develop mostly the so-called soft skills to a great extent.

Workshops are also the time for the verification and utilization of the skills acquired so far. A short working time forces to act and make decisions quickly, as well as to organize oneself well. This calls for regular activities and closing subsequent stages 'step by step', securing constant progress. At this stage, an important role could be played by the group leader, who assists the team in going through subsequent stages of the project, moving them in the right direction.

For the team leader, it is also an opportunity to quickly confront and verify his/her teaching methods. A short duration of a workshop forces intensive work, thanks to which the effects of individual stages are visible on a constant basis. Therefore, workshops can also serve as a kind of experimental field where various approaches are tested.

A very important aspect of workshops is setting free and developing creativity. A characteristic and extremely important stage is brainstorming, which actually stands for setting abstract thinking free, overcoming limits, and verifying various variants of solutions, breaking the widespread preconceived notions. It is extremely important in the creative process, which, in case of students of architecture and urban planning, has a special significance. A valuable aspect of the operations of the teacher (team leader) could be the improvement of the team's sensitivity to adopting an appropriate operational strategy in the creative process. It is worth pointing out that the question 'how this could be done', especially in the initial designing phase, should not be dominated with questions 'what I want to do', 'what could be done here'. An inappropriate order can result in a blockade and become a barrier for creative thinking.

The most common workshop formula is teamwork. At the same time, it is an opportunity to develop the skill of presenting one's views, of defending them, of discussing ideas, as well as of reaching a consensus. Cooperation with other people broadens horizons and allows to perceive a specific topic from a different perspective.

Teamwork consists in the mutual symbiosis and allows to reach the effect of synergy. Individuals form a structure, where everybody is different and has their weaknesses and strengths. Therefore, it is important to diagnose the potential that resides in individual persons and to develop the strategy for benefitting from it so as to enable everybody to contribute. In this case, the role of the teacher can also prove to be helpful; the teacher can guide the team to secure synergy of the work of its members.

Teamwork and the feeling of belonging to a group constitute key elements that motivate a person to reach the target, which is the development of a specific solution. The feeling of isolation and lack of good relations hinders cooperation and reduces commitment. Therefore, it is important to take care of building relationship between team members, as well as creating appropriate atmosphere. A great role in this respect is played by additional activities beyond the workshop, aiming at socializing workshop participants. This allows to get to know each other, to establish closer relations, and in doing so, to build the feeling of belonging to the group.



Additional socializing events, as well as lectures and meetings that accompany workshops, are also an important element of education, enabling to explore the subject matter. In case of the workshop held in Goerlitz⁴, where the main tool of the students of architecture was film, one of the most important elements of the workshops were meetings with employees of the Babelsberg movie studio in Berlin and visiting this facility. The movie studio has produced numerous distinguished masterpieces of film art, such as e.g. *The Cabinet of Dr. Caligari* (1920) or *Metropolis* (1927), as well as contemporary movies, such as *V Like Vendetta* (2006) or *Inglourious Basterds* (2009). The goal of the workshop was to create a several minutes' film illustrating the dichotomy of the city that functions on both sides of the border: Goerlitz – Zgorzelec, presenting its spatial aspects connected with its urban development. Examining the issues of a double city, grasping its everyday life and complicated past, required thorough investigation. Therefore, a very important item on the agenda was participation of the workshop attendees in a lecture devoted to the history of the city, as well as experiencing it physically. Visiting its nooks and spending time with its residents became a valuable source of inspiration.

A similar assumption connected with additional activities accompanied the INTBAU workshop⁵, the main idea of which was to investigate the principles of traditional and contextual design. Emphasis on designing in a strictly defined historical and cultural context most of all calls for thorough investigation and knowledge of the local building tradition. In order to understand these issues better, within the scheme of the workshop, a study visit to Zakopane was organized – a city of rich history and culture, with a strong identity of building and architecture. Besides experiencing the city and learning about its history, the workshop participants had an opportunity to learn about traditional craftsmanship, as well as about contemporary methods applied in the traditional building process. It aimed at the improvement of sensitivity to the aspect of tradition and context in the designing process so as to start to design space, which requires such an approach. The obtained knowledge and inspirations became the foundation for undertaking the main topic of the workshop, which is the development of a spatial concept for Sikorskiego Square in Cracow. Placing the workshop in a tenement house located at the square, as well as meetings with experts, allowed to fathom the knowledge about the history of this place, as well as to experience it more personally. Talks with the local community also proved to be very helpful. As a result, two valuable proposals of spatial solutions came into being. One was more traditional in its style, and the other was more contemporary in its form, both strongly connected with the context and referring to the historical conditions of the place.

Workshops that are international in character additionally enrich the path of the development of architectural education of students, as well as of their teachers. Working with people from various cultural environments is a form of approaching the problem from a different perspective.

⁴ *City and a Film – Zgorzelec – Goerlitz – Workshop for Students in Architecture and Urban Design*. 20–28 September 2013; organized by HAWK Hildesheim (Germany) and CUT Krakow (Poland) on 20–28 September 2013 in Goerlitz.

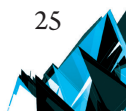
⁵ International training workshop devoted to contextual design and place creation, organized by INTBAU Polska and the Cracow University of Technology, in cooperation with INTBAU Italia and the Allerhand Institute on 8–16 May 2014 in Cracow.

Functioning in a specific community defines certain patterns of behaviour, ways of thinking and approaching a given problem, and this in turn imposes a specific optics of perception, which easily becomes a strongly subjective point of reference. Cooperation with persons from other cultures allows to change this perspective and to see elements, which so far have been absent from one's own cultural references. This is particularly important with regard to a specific new place and space. People 'from the outside', with a different perspective and experience, are able to perceive a specific place in a different way. They can notice different values, different characteristic features, different relations, different connections embedded in them.

For a Ph.D. candidate, working in an international environment is a perfect opportunity to develop his/her teaching skills. Contact with people representing various schools has a considerable importance here, as they often demonstrate different approaches and philosophies in the process of teaching and project management. For the teaching staff, workshops are also a forum for the exchange of experience and an opportunity to observe one another, thanks to which everyone can learn something new and introduce new elements to their working methods. It is important for Ph.D. candidates because they can improve their teaching skills considerably in a short time. It also pertains to the ways of integrating a team, of motivating students, as well as of organizing team work and assuming a substantive approach to the subject matter. Numerous matters that are important for the teacher can be provided by students themselves, whom, being educated at different universities, present different ways of thinking. Contact with a different perspective and optics of perceiving the ways of developing the skills of creative activities of students constitutes a very important experience for the teacher, and for Ph.D. candidates in particular, as it allows them to get to know the diversity of approaches to this issue right at the beginning of their teaching career.

International cooperation also stands for the exchange of experience in a similar field. The Eco Rehab 3 workshop focused on housing estates consisting of buildings made of prefabricated concrete panels, which is a topic that most European cities, especially from the former Eastern Bloc, have been familiar with. The workshop became an arena for the exchange of thoughts and experience connected with them, and for the joined search for ways to revitalize them. It pertained to the design and spatial solutions for specific housing estates in Cracow, located in Czyżyny, in the vicinity of a former runway. Students from Italy, Spain, Romania, Germany and Poland were looking together for ways to create attractive public spaces in the housing estate. Their work resulted in the formulation of 8 concepts for the development of this area, and the diversity of the developed concepts demonstrated a number of possibilities of interpreting this place and its solutions. The designs were strongly founded in the context of the city and were taking the specificity of the place into account. However, despite this fact, due to the nature of this type of urban formations, it was possible to find certain universal solutions for them. The workshop constituted a perfect place for the exchange of observations and mutual inspiration of students, as well as the teaching staff. The comments of the jurors proved to be very valuable, too.

The examples listed above demonstrate that workshops enable to obtain and develop skills, which are necessary in the professional activities of an architect or an urban planner. One of the necessary skills is cooperation with specialists from a related, but not the same field, as in



fact working on a design usually comprises multi-faceted activities, especially in case of urban design, which requires comprehensive strategies. Design workshops with the participation of students from different specialties enable them to cooperate and look for solutions to problems on numerous planes. Such a formula was adopted during a double edition of the Cracow-Vienna workshop⁶. The subject matter of the study was an area located within the borders of Zakrzówek, limited from the north and east by the Vistula River, and from the south and west by the route of the planned Relief Channel. The cooperation of students from Cracow from the majors of Architecture and Urban Planning, as well as from the Technical University of Vienna, predominantly from the major of Spatial Planning, resulted in the development of four interesting concepts of the development of this area. One of them pertained to its development in the context of Cracow as the capital of culture in 2020. The starting point for adopting an appropriate strategy for its selected area was confronting the immense potential of Cracow, resulting from its historic and cultural heritage, with the needs of the contemporary knowledge society. In this respect, there appeared concepts that gave rise to a more detailed planning of this area. It was assumed that the city should develop as a dynamic complex structure. The historic city should be an integral part of the entire urban structure of the city, and not a mummified reserve. In this respect, changes that occur in historic cities should be based on the constant search of balance, harmony and compromise between the economic reality and the principles pertaining to the integrated approach to heritage protection.

As a result, there appeared a concept according to which the area of Dębniki was to become a new stage for arts, culture and knowledge. This area offers a lot of opportunities and freedom of operation and experimenting, unlike the historic tissue of the city, which naturally imposes numerous architectural and urban limitations. There is more space for innovative activities and experiments, maintaining a great potential of this terrain: there are areas located close to the city centre and, at the same time, areas, which exhibit a diversified structure, combining attractive green areas with a water reservoir and developed areas of a different character.

Cooperation of students of architecture and urban planning with students of spatial planning also allowed to develop a concept of the spatial development and a development strategy for these areas. Operations were divided into 2 stages; key activities necessary to be performed by 2016, and then by 2020, were described.

A very interesting and instructive form are workshops which consist in the cooperation of students of the 1st and 2nd degree courses, students of Ph.D. courses and professors, during which all participants work together and develop a common concept. It is close to the formula of working in an architectural office, which could be a valuable experience for students. The teacher does not act as an outsider who only evaluates, but he/she actively participates in the designing process. This formula was adopted in the aforementioned workshop devoted to the area of Zakrzówek in Cracow. Its goal was to create the city edge, which is a place of contact of green and urban areas. For the city of Cracow, this subject is particularly sensitive because there are very attractive areas due to their natural and recreational value. At the same

⁶ Vienna-Cracow International Design Workshop, organized by the Institute of Urban Design, Faculty of Architecture, Cracow University of Technology, and TU Wien; 1st edition: 8–12 September 2010 (Cracow), 2nd edition: 16–22 May 2011 (Vienna).

time, they are under a great pressure of developers. The goal of the workshop was to find a compromise solution that would maintain the green character of this space, but which simultaneously would enable to introduce a safe investment there, which is an investment that would not have any effect on the degradation of these areas. The final effect had a form of 5 concepts demonstrating different possible solutions.

An interesting approach to the organization of workshops is the issuance of topics to be developed by students prior to the commencement of the workshop. In such an event, the workshop begins with thematic presentations prepared by students. This allows not only to fathom the subject matter more quickly and efficiently, but also to get to know the predispositions of persons who are to cooperate. Opportunities offered by the Internet communication enable us to cooperate with people from different parts of the world; geographical distance is not an issue any more. In case of the 'Goerlitz – Zgorzelec' workshop, the pre-workshop work resulted in a thematic foundation of the workshop in the form of presentations pertaining to the town, as well as to the history of cinema.

Within the Eco-Rehab workshop, a formula of earlier preparation of presentations connected with the set topics was also adopted. The attending students from different European universities presented the problem from the point of view of their countries. The task faced by students from Cracow, where the workshop was held, was to conduct thorough analyses of the place that was the subject of the workshop – housing estates consisting of buildings made of prefabricated concrete panels in Czyżyny. The analyses presented during the public presentation, as well as the studies published as brochures, were to be the basis for further exploration of the area and its problems and for finding a concept for its development.

Due to the limited working time compared to semester projects, the workshop studies devoted to architectural and urban issues are most frequently focused on communicating a concept and an idea. This pertains especially to more complex large-scale designs. Therefore, it frequently happens that a workshop is a starting point of a course project conducted later on. They constitute a perfect substantive foundation for them, but, at the same time, they serve as a kind of exercise for further designing activities.

For Ph.D. candidates, architectural workshops are not merely a valuable experience from the point of view of teaching, but they can also become a sort of a field for inquiries for their research work. As far as the author of this commentary is concerned, it referred to e.g. the topic of architecture made of prefabricated concrete panels, which is the subject of her Ph.D. dissertation. Her participation in the Eco-Rehab 3 workshop, which was fully devoted to this kind of architecture, and in the Cracow-Vienna workshop, which touched upon this issue as well, although to a lesser extent, allowed most of all to confront the adopted approach to this research topic with concepts of students, sometimes too abstract, but usually fresh, created with considerable imagination. The discussion demonstrated that students' concepts and solutions could be beneficial for creative verification of proposed solutions to a given problem. In this case, the emphasis was put on the role of revitalization of such housing estates in the creation of continuity and complementarity of public spaces in the city. Selected housing estates in Cracow became a field of the search for new forms of space of a housing



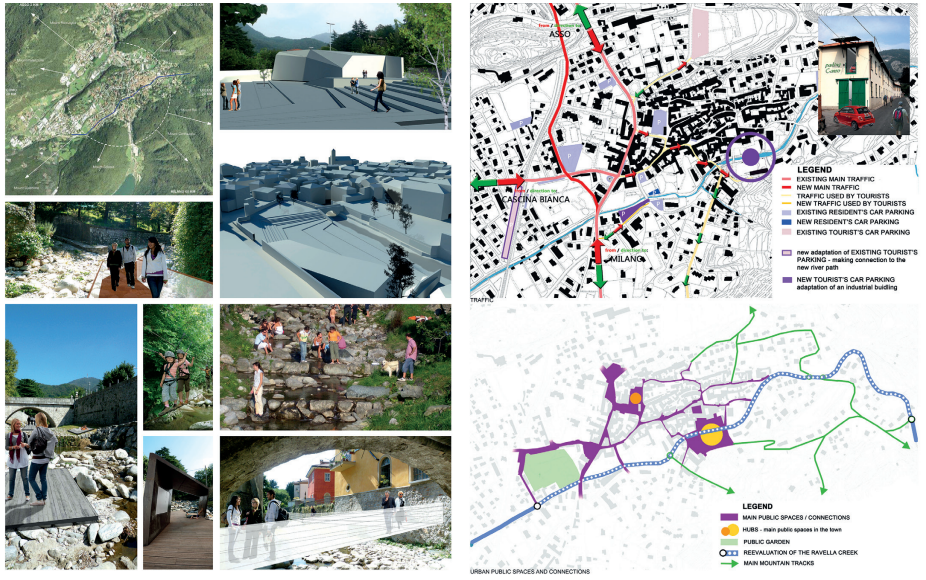
estate, taking into account the context of the place and its values, as well as its affiliation with the system of urban spaces.

Due to the fact that there constantly emerge new opportunities of cooperation between universities or their individual units, within the scheme of international programmes, bilateral agreements, etc., workshops, especially over the last few years, have become a more and more popular and common element in the process of architectural education. Their number, and at the same time their diversity in the sense of the adopted formula or subject matter, provides students as well as Ph.D. candidates with an opportunity to choose the ones that seem to be the most useful and close to their interests. It is particularly important for Ph.D. candidates, since besides developing their teaching skills, they can also support their scientific research.

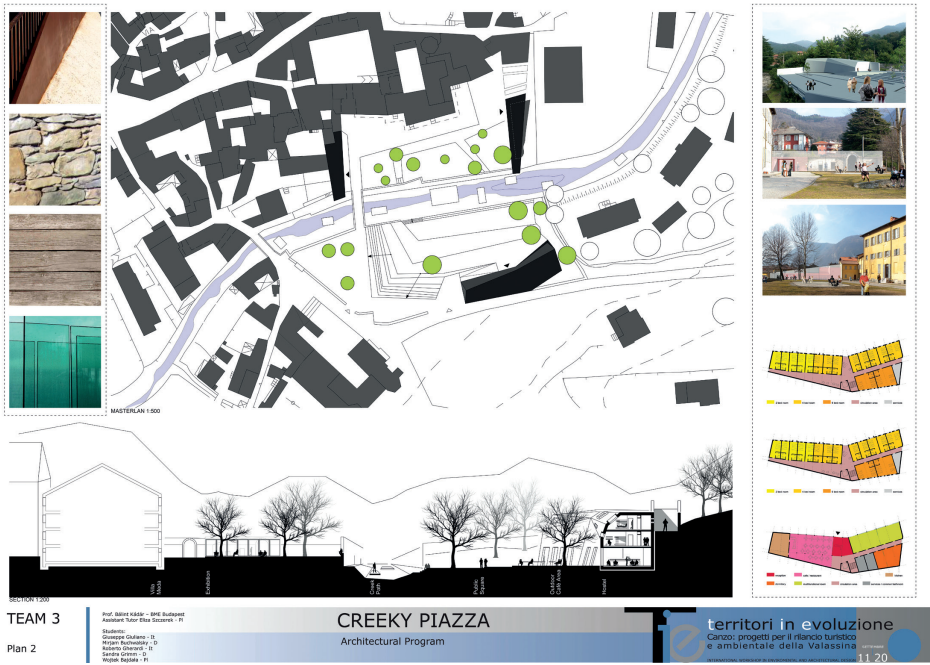
The author's experience gained so far proves that workshops can play a significant role in the process of architectural education of students. They also offer new knowledge to the teaching staff, especially to young academics, both in terms of the methodology of teaching and creative discussions devoted to the research problems solved by them. Regular participation in workshops, which nowadays is becoming more and more possible due to their multitude, allows to constantly improve one's teaching competence. Furthermore, in the knowledge society, characterized by a quick information flow, the possibility of moving around, and generally speaking a more mobile lifestyle, contact with representatives of other cultures and expanding one's thinking horizons by confronting experiences in the international environment constitute very important aspects of development for people who study and are engaged in scientific activities.



Fig. 1. Different activities within Canzo International Design Workshop – “Territori in Evoluzione” (11–20.09.2011, Canzo, Italy): bike tour around the town, site visit, working in studio



TEAM 3 Prof. Bálint Kádár - DE Buchwald Roberto - IT Elia Scaccini - IT
Plan 1 Studenti: Giuliano - IT, Gherardi - IT, Buchwaldsky - DE, Grimm - DE, Bajdala - PL; Tutor: Bálint Kádár - HU, Tutor Assistant: Eliza Szczerek - PL; Canzo International Design Workshop - "Territori in Evoluzione" (11-20.09.2011, Canzo, Italy)



TEAM 3 Prof. Bálint Kádár - DE Buchwald Roberto - IT Elia Scaccini - IT
Plan 2 Studenti: Giuliano - IT, Gherardi - IT, Buchwaldsky - DE, Grimm - DE, Bajdala - PL; Tutor: Bálint Kádár - HU, Tutor Assistant: Eliza Szczerek - PL; Canzo International Design Workshop - "Territori in Evoluzione" (11-20.09.2011, Canzo, Italy)

Fig. 2, Fig. 3. Final presentation boards of Team No. 3 (Students: Giuseppe Giuliano – IT, Roberto Gherardi – IT, Mirjam Buchwaldsky – DE, Sandra Grimm – DE, Wojtek Bajdala – PL; Tutor: Bálint Kádár – HU, Tutor Assistant: Eliza Szczerek – PL); Canzo International Design Workshop – “Territori in Evoluzione” (11–20.09.2011, Canzo, Italy)

References

- [1] M. Gyurkovich (ed.), *Future of the city. Mass housing estates of multifamily housing complexes?*, Eco Rehab 3, Kraków 2012,
- [2] Szczerek E., *Adjusting Prefabricated Housing Estates to Contemporary Conditions and Local Specificity in Revitalization Processes–German Experiences*, „Future of the city. Mass housing estates of multifamily housing complexes?”, Eco Rehab 3, Kraków 2012, M. Gyurkovich (ed.), p. 128–135.
- [3] Szczerek E., *Discovering the city and placemaking. Canzo case study*, 6 ULAR : The Urban Landscape Renewal: City–People Friendly Places: ideas–projects–realisations: proceeding of International Scientific Conference Silesian University of Technology: monograph. Vol. 2, N. Juzwa, A., Sulimowska-Ociepka (eds.), Gliwice 2012, p. 387–392.
- [4] Fredriksson U., *Quality Education: The Key Role of Teachers*, Education International Working Papers No. 14, September 2004; http://glotta.ntua.gr/posdep/Dialogos/Quality/ei_workingpaper_14.pdf (access: 04.05.2017).

Bożena Hoła

Tomasz Nowobilski (tomasz.nowobilski@pwr.edu.pl)

Department of Construction Methods and Managements, Faculty of Civil Engineering,
Wrocław University of Science and Technology

Jarosław Rudy

Faculty of Electronics, Wrocław University of Science and Technology

Ewa Borowa Błazik

Faculty of Civil Engineering and Architecture, Lublin University of Technology

DA

NIEBEZPIECZNE ZDARZENIA ZWIĄZANE Z UŻYTKOWANIEM RUSZTOWAŃ BUDOWLANYCH

Abstract

The majority of construction works are carried out at height; these are works that carry a high risk of accident. This paper presents an analysis of dangerous events associated with scaffolding. Information about these events was obtained from online resources. The collected data not only allowed analysis of occupational accidents but also accidents involving third parties and near-miss events. The paper presents particular examples of these events.

Keywords: scaffolding, Internet, occupational accident, potentially accidental event

Streszczenie

Znaczna część robót budowlanych, wykonywana jest na wysokości. Są to prace, z którymi związane jest duże ryzyko zagrożeń. W artykule zawarto analizę zdarzeń niebezpiecznych związanych z rusztowaniami budowlanymi, uzyskanych z zasobów internetowych. Pozyskany w ten sposób materiał badawczy umożliwił przeanalizowanie nie tylko wypadków przy pracy, ale również zdarzeń wypadkowych z udziałem osób trzecich oraz zdarzeń potencjalnie wypadkowych. W artykule przedstawiono charakterystyczne przykłady takich zdarzeń.

Słowa kluczowe: rusztowanie, internet, wypadek przy pracy, zdarzenie potencjalnie wypadkowe

1. Introduction

The majority of construction works are carried out at height. According to the general regulations on occupational health and safety included in the Regulations of the Minister of Labour and Social Policy from 26th September 1997 [1], work at height is classified as particularly dangerous and is associated with a high risk of accident e.g. falling from a height or being hit by falling material.

To present the scale of this phenomenon, statistical data regarding the total number of people injured in occupational accidents in the construction industry in the years 2007–2015 and the amount of people injured as a result of falling from height, being hit by falling material and also being pulled from below, are included in Figure 1. In the analysed time period, 72,733 people were injured in all occupational accidents in the construction industry.

From the above number, 7657 people were injured as a result of falling from a height, 7768 as a result of being hit by falling material, while 1723 people were pulled down from below. Between them, these three events have caused injuries to more than 23% of all people injured in accidents at work in the construction industry. It is known that a significant number of these incidents are directly connected with working on construction scaffolding. However, on the basis of published statistical data, it is not possible to accurately determine the scale of risk associated with work carried out on these structures.

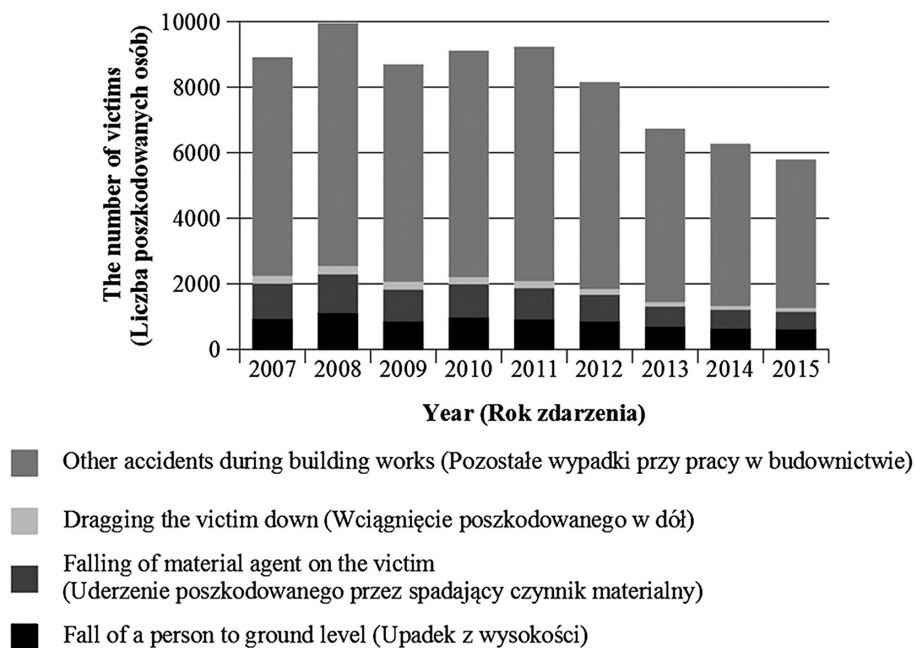


Fig. 1. The number of people injured in occupational accidents in the construction industry in the years 2007-2015 in relation to events causing physical trauma, data source: Central Statistical Office (data source: [2])

Inspections carried out by state institutions, including the National Labour Inspectorate and the State Construction Supervision, have shown a number of irregularities and deviations from the provisions of occupational health and safety during the use of scaffolding [3]. Detailed analysis of such events can help to determine the types of hazards and their scale and also help to define the factors that contribute to accidents occurring during work on scaffolding.

Information about dangerous events in the construction industry can be obtained from many sources, such as: the archives of the National Labour Inspectorate (PIP); National Construction Supervision (GNP) and Central Statistical Office (GUS); the press; online resources. In this article, the Internet is the source of information on such events. It was decided that websites would be searched because it provided the opportunity to not only find information on occupational accidents but also on other hazardous events involving scaffolding which are not included in the archives of PIP, GUS and GNP.

2. Research methodology and examples of hazardous events involving scaffolding

In order to find information on the Internet about dangerous events involving scaffolding, the Google search engine was used. A number of keywords were entered in the searches such as: 'scaffolding', 'accident', 'fall', 'disaster', 'collapse' and 'potentially accidental event'. As a result of the set of queries, several thousand results were obtained. Due to the high repetition of results, pre-processing was used during queries and the repeated results (i.e. the same websites) were removed. However, it was still possible to get two different websites describing the same event, which in some cases, helped to obtain additional information about an event. At this stage, some of the results were rejected due to inaccessibility or error pages. At the end of this stage about 600 websites with results were obtained.

In the next stage, the number of websites was reduced to sequences of words that were then searched regarding the number of occurrences of certain keywords and then divided into two groups. The first group concerned words that are typical for the described events (e.g. 'accident' or 'scaffolding'), and the second group referred to words that are less common and depend on the specific event (e.g. 'fall', 'security', 'victim', 'injuries', 'accident', 'hit', 'injury' etc.). The obtained data was used to support the manual verification of results in the third stage. After the final verification, it was found that the websites have information about 190 dangerous events involving scaffolding. The events happened all over Poland during the period from 2007 to 2015. Some specific examples of such events are presented below:

- ▶ on 23rd August 2010 in Gostyn, a strong gust of wind caused the collapse of scaffolding situated next to a wall of a multi-storey building [4]. The 'curtains' attached to the scaffolding that were supposed to protect pedestrians from falling objects made the entire structure act like a large sail. During a violent storm, a strong gust of wind caused such a large pressure on the scaffolding structure that it pulled out the anchorages of

the walls of the building and overturned the scaffolding. Fortunately, the collapsing structure did not result in any injuries to people.

- ▶ on 6th May 2012 in Białystok, a section of scaffolding located next to a four-storey building collapsed [5]. The main reason for this event, according to the National Labour Inspectorate [6], were mistakes made during the assembly of the structure which caused the collapse of a section of scaffolding with a length of approximately 45 m and a height of 15.5 m as a result of a gust of wind. Despite this occurring during the afternoon in an area with heavy pedestrian traffic, the collapsing structure caused only material damage.
- ▶ on 29th July 2011, there was an accident during the construction of the North Bridge in which one person died and four others were injured [7, 8]. The event was caused by errors in the attachment of the scaffolding to the construction of the bridge, which resulted in the destruction of the scaffolding and the victims falling from approximately 20 m into the Vistula River.
- ▶ on 7th August 2007 in Bielsko-Biala, an accidental event resulted in the injury of a three year old girl [9]. A moment of inattention by a babysitter led to a situation where the child went onto scaffolding and fell off it. The child was taken to hospital unconscious and with serious injuries.
- ▶ on 16th November 2010 on Piotrkowska Street in Lodz, an accidental event occurred involving third parties [10]. Badly attached scaffolding collapsed on two pedestrians. As a result of this event, a 24-year-old woman was crushed by the collapsing structure. Medical tests confirmed that the victim had a spinal vertebral fracture, head injuries and general bruising.

3. Research results – the classification of dangerous events

The above-mentioned examples show that dangerous events involving scaffolding can be divided into three basic groups: occupational accidents; accidental events involving third parties; potentially accidental events.

According to the law regarding social insurance due to occupational accidents and occupational diseases [11], an occupational accident is: “a sudden event caused by an external factor that results in injury or death and which takes place in relation to work:

- 1) during or in connection with an employee carrying out ordinary activities or instructions of superiors;
- 2) during or in connection with an employee carrying out activities for a superior, even without being instructed;
- 3) when an employee remains at the disposal of an employer and on the way between the employer’s office and the place of carrying out work due to the obligation arising from the employment agreement.”

An accidental event involving third parties is understood as a sudden event which takes place in connection with work and causes the injury or death of a bystander.

In turn, according to the PN-N 18001:2004 standard [12], a potentially accidental event is a “dangerous event that is related to work and in which there is no injury or health deterioration” due to there being no people within range of the hazard. Figure 2 shows the percentage share of individual hazardous events in relation to the total number of examined events.

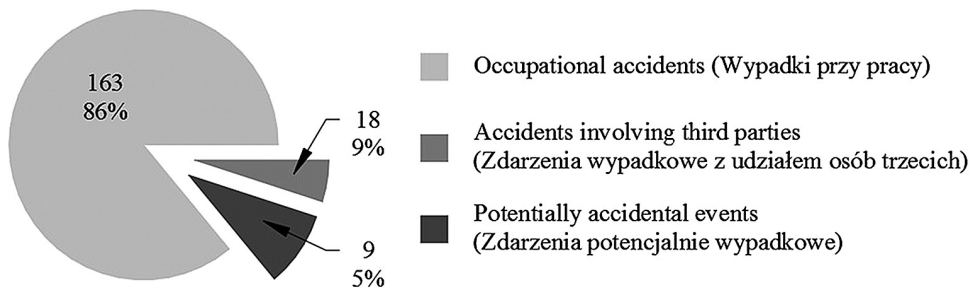


Fig. 2. Percentage share of event types in the tested statistical sample (source: author’s archive)

3.1. Occupational accidents

When analysing events classified as occupational accidents, it can be stated that the injuries of victims were usually caused by falling from a height either down to the ground or down to lower levels of scaffolding. This type of event occurred in the case of 92% of victims. In the case of 4% of victims, the direct cause of injury was an electric shock, and in the case of 3%, falling material. The remaining 4% were other events such as, for example, crushing. The effects of falling from scaffolding are illustrated in Figure 3.

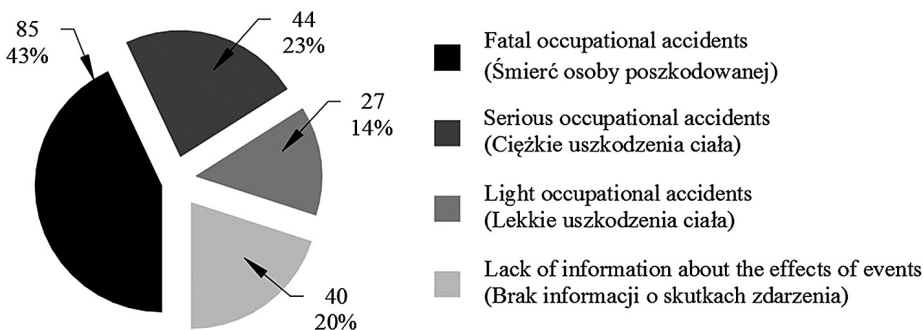


Fig. 3. The number and percentage of the particular consequences of occupational accidents (source: author’s archive)

3.2. Accidental events involving third parties

Scaffolding and works that are carried out on them also pose a threat to third parties. In the analysed statistical sample, a total of 19 people were affected. In nine cases, the cause of injury was falling from a height, and in eight cases, a person was injured by falling materials. The items involved were scaffolding that collapsed as a result of insufficient stability, an object or a building object used during the course of works. The number and the percentage share of the effects of events on the injured third parties are shown in Figure 4.

It should be noted that many of the above events could have been prevented by, among other precautions, appropriate anchoring of scaffolding, security of the danger zone or by preventing bystander entry. According to the Regulation on Occupational Health and Safety during construction works [13], a danger zone is calculated on the plane of a building structure and cannot be less than 1/10 of the height from which there is a risk of falling objects, and at the same time, must be equal to at least 6 m.

In exceptional situations, if it is not possible to designate the danger zone in such a way (e.g. in a dense urban area) the legislator allows a reduction of this zone “on condition that other technical or organisational solutions are in place that protect against falling objects”, e.g. nets and roof overhangs.

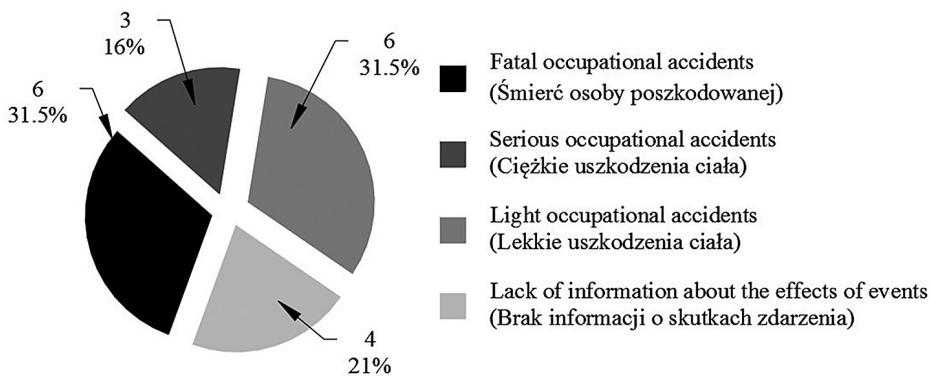


Fig. 4. The number and percentage of the particular consequences of accidents involving third parties (source: author's archive)

3.3. Potentially accidental events

Potentially accidental events, and thus events in which there were no injured people, very often occur during the execution of building works. However, information about such events is very limited because the obligation of recording them only applies to organisations that have an occupational safety management system (e.g. according to the series of standards PN-N 18000). According to the regulation from Construction Law [14], only events that are defined as building disasters must be reported.

Other events that do not show signs of being a construction disaster are not recorded and are sometimes even covered up by employers. However, if there is an occupational accident, there is a duty to report such events to the relevant institution but only if the accident is fatal, severe or collective. Since there is no obligation to report light accidents, they are also very often covered up by employers. Such actions mean that there is no complete picture of accident phenomenon in the construction industry.

Previous studies of American scientists have shown that every accident that results in an injury is preceded by the occurrence of many similar events that do not cause injury [15, 16]. Research of Heinrich and Bird showed the presence of a constant ratio between the different effects of accidents. And so, according to a study of Heinrich, for each single serious or fatal accident there are 29 light accidents and 300 accidents without injury. In turn, according to a study by Bird, for 630 events without injury there are 30 events that generate losses, 10 accidents which cause minor injury and one which results in serious injury. These relationships are shown in Figures 5a and 5b. Analysis of such events and timely learned lessons could prevent an accident or minimise its consequences.

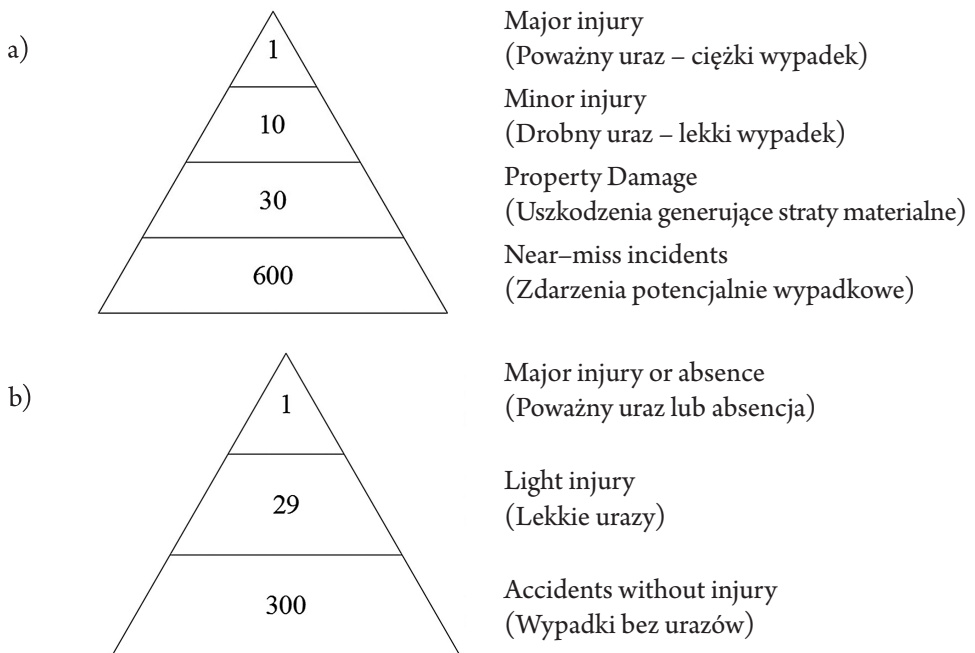


Fig. 5. a) Bird's triangle; b) Heinrich's triangle (source: author's archive)

In the analysed research set, which had 190 dangerous events involving scaffolding, only nine potentially accidental events were identified. However, it should be expected that their number was much larger, but information about them was not made available on the Internet.

4. Summary

Based on the conducted survey of online resources, it should be stated that works on scaffolding are associated with a high risk of danger to the life and health of workers and bystanders. The most common cause of injury in the case of workers is falling from scaffolding, and in the case of bystanders it is being hit by falling material, e.g. elements of scaffolding, tools or other building products.

The effects of occupational accidents that involve scaffolding are very serious. In the assessed sample, up to 43% of accidents resulted in the death of a victim and 23% ended in severe injury. The most common injuries include fractures of legs and arms and also head injuries. Accidents involving third parties were often associated with unauthorised entry to a building site. Other events should also be noted, especially potentially accidental events – these are often wrongly underestimated; however, details about them are a very rich source of information that can be used in and preventative measures.

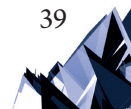
A potentially accidental event often involved the collapsing of scaffolding caused by a strong gust of wind. It is worth mentioning that safety nets, which are used on scaffolding, significantly increase the aerodynamic resistance of such a construction, which affects its overall stability and increases the forces generated in anchorages.

The article is the result of the implementation by the authors of research project No. 244388 “Model of the assessment of risk of the occurrence of building catastrophes, accidents and dangerous events at workplaces with the use of scaffolding”, financed by NCBiR within the framework of the Programme for Applied Research on the basis of contract No. PBS3/A2/19/2015.

References

- [1] Rozporządzenie Ministra Pracy i Polityki Socjalnej z dnia 26 września 1997 r. w sprawie ogólnych przepisów bezpieczeństwa i higieny pracy (Dz.U. z 2003 r. Nr 169, poz. 1650)
- [2] Główny Urząd Statystyczny, *Wypadki przy pracy 2007–2015*, Warszawa 2008–2016.
- [3] Hoła B., Sawicki M., Szóstak M., Błazik-Borowa E., Czarnocki K., Szer J., *Badania rusztowań na placu budowy*, „Builder” 2016(12), 80–83.
- [4] Elka.tv, http://elka.tv/index.php?option=com_hwdvideoshare&task=viewvideo&Itemid=63&video_id=1061 (access: January 2017).
- [5] Onet.pl, <http://bialystok.onet.pl/runelo-rusztowanie-przy-bloku-na-ul-gajowej/mtjh4> (access: January 2017).
- [6] Państwowa Inspekcja Pracy, <https://www.pip.gov.pl/pl/pod-inspektorska-lupa/16978,-clle-zmontowane-rusztowanie-przy-budynku-mieszkalnym-w-biac-ymstoku-nie-wytrzymac-o-silniejszych-podmucha-w-wiatru-inspektorzy-pracy-stwierdzili-m-in-c-e-przy-stawianiu-konstrukcji-nie-przeznaczono-pochodzc-cej-od-producent-.html> (access: January 2017).

- [7] Polskie Radio, <http://www.polskieradio.pl/5/3/Artykul/410864,Rusztowanie-z-robotnikami-spadlo-do-Wisly> (access: January 2017).
- [8] Polskie Radio, <http://www.polskieradio.pl/5/3/Artykul/412797,Zmarl-robotnik-tory-spadl-z-Mostu-Polnocnego> (access: January 2017).
- [9] Gazeta.pl, <http://wiadomosci.gazeta.pl/wiadomosci/1,114873,4371684.html> (access: January 2017).
- [10] Naszemiasto.pl, <http://lodz.naszemiasto.pl/artikul/na-piotrkowskiej-rusztowanie-przygniotlo-kobiete,659760,art,t,id,tm.html> (access: January 2017)
- [11] Ustawa z dnia 30 października 2002 r. o ubezpieczeniu społecznym z tytułu wypadków przy pracy i chorób zawodowych (Dz.U. z 2002 r. Nr 199, poz. 1673).
- [12] PN-N 18001:2004 Systemy zarządzania bezpieczeństwem i higiena pracy. Wymagania.
- [13] Rozporządzenie Ministra Infrastruktury z dnia 6 lutego 2003 r. w sprawie bezpieczeństwa i higieny pracy podczas wykonywania robót budowlanych (Dz.U. z 2003 r. Nr 47, poz. 401).
- [14] Ustawa z dnia 7 lipca 1994 r. Prawo Budowlane (Dz.U. z 2016 r., poz. 290, z późn. zm.).
- [15] Heinrich H. W., *Industrial Accidents Prevention*. McGraw-Hill Book Company, INC., New York, Toronto, London 1959.
- [16] Bird F., *Management Guide to Loss Control*, International Safety Academy, Houston, TX 1974.



Krzysztof Ostrowski (kostrow@agh.edu.pl)

Faculty of Mining and Geoen지니어ing, AGH University of Science and Technology

THE INFLUENCE OF CFRP SHEETS ON THE STRENGTH OF SPECIMENS
PRODUCED USING NORMAL CONCRETE AND HIGH-PERFORMANCE
CONCRETE ASSESSED USING UNIAXIAL COMPRESSION TESTS

WPLYW WŁÓKIEŃ WĘGLOWYCH NA WYTRZYMAŁOŚĆ PRÓBEK Z BETONU
ZWYKŁEGO I WYSOKOWARTOŚCIOWEGO ŚCISKANYCH JEDNOOSIOWO

Abstract

This article presents the results of an experimental investigation on the influence of carbon-fibre-reinforced polymer (CFRP) sheets on the strength of short concrete columns constructed from normal concrete (NC) and high-performance concrete (HPC). The results show that external confinement can significantly improve the ultimate strength and strain of the specimens. The stress-strain response of confined concrete depends largely on the type of concrete with regard to its compressive strength. The results demonstrate that composite columns constructed from normal concrete work in an elastic-plastic range with strengthening, whereas strengthening of columns constructed from high-performance concrete did not occur. The study indicates that the confinement.

Keywords: composite column, normal concrete, high-performance concrete, carbon reinforced polymer material, stress-strain

Streszczenie

W artykule przedstawiono rezultaty eksperymentalnych badań poświęconych wpływowi mat z włókien węglowych na wytrzymałość krótkich kolumn betonowych wyprodukowanych z betonu zwykłego i wysokowytrzymałościowego. Wyniki wskazują, iż stosowanie CFRP może w znaczący sposób zwiększyć wytrzymałość i odkształcalność próbek. Charakterystyka naprężenie-odkształcenie wzmocnionych kolumn zależy w istotny sposób od wytrzymałości betonu. Wyniki przeprowadzonych badań wskazują na sprężysto-plastyczną z wzmocnieniem charakterystykę pracy wzmocnionych kolumn z betonu zwykłego, w przeciwieństwie do betonu wysokowartościowego, gdzie wzmocnienie nie występuje. Badania wskazują, iż efektywność wzmocnienia kolumn zespolonych spada wraz ze wzrostem wytrzymałości na ściskanie rdzenia betonowego.

Słowa kluczowe: słup zespolony, beton zwykły, beton wysokowytrzymałościowy włókna węglowe, naprężenie-odkształcenie.

1. Introduction

With recent advances in composite materials technology, fibre-reinforced polymers (FRP) have reached a new level in the field of civil engineering to repair and retrofit existing infrastructures or to design new infrastructures [2].

Retrofitting of concrete columns using FRP jackets with fibres predominately oriented in the hoop direction has become popular within the structural engineering community [5]. FRP-confinement could increase both the compressive strength and the ultimate strain of concrete columns [6, 7]. The confinement of concrete columns is thus an application where the external wrapping by glass- or carbon-fibre-reinforced polymers is particularly effective [1]. CFRP has high strength and a high Young's modulus, it has good resistance to aggressive environments, a high strength-to-weight ratio and good fatigue properties [8].

Epoxy resins are most commonly used in strengthening by FRP – these resins are examples of organic polymer matrices. Epoxy resins have disadvantages including: their fairly high costs; the hazards they pose for the manual worker; their incongruity at low temperatures or with humid surfaces; their lack of permeability to vapour, the obstacle they pose when assessing the post-earthquake damage of reinforced concrete behind (intact) composite jackets; their weak performance in high-temperature conditions. Besides epoxy resin, it is possible to use inorganic matrices – these are more adaptable, more cost-effective – they are eco-friendly substitutes for epoxy resin and the efficiency of the bond between the concrete surface and the cement-based composites in confined mode is acceptable [12,13].

The use of CFRP sheets can be of significant importance for the strengthening of historical buildings and monuments where change of use is considered as this often causes an increase in loads. The many historical buildings were often constructed from low-performance concrete which corresponds to the current C15/20 class. Strengthening with CFRP confinement can increase the bearing capacity of a construction and the maximum strains [10].

For more than twenty years, high-performance concrete has been increasingly applied in structural engineering due to its superior material properties related to strength, stiffness, and durability. One of its major drawbacks is that the ductility of HPC generally decreases as compressive strength increases. High strength concrete structural members therefore generally exhibit a lack of ductile behaviour and hence brittle failure. Using CFRP can be an effective method for improving the ductility of confined concrete columns constructed from HSC [3].

This article is based on selected results of the author's work [9, 10] on the basis of which, a comparative analysis of the influence of CFRP sheets on the strength of the specimens produced by normal concrete and high-performance concrete was performed.

2. Experimental programme

The specimens and materials

In total, twelve specimens were analysed covering two different concrete mixtures (NC – normal concrete and HPC – high-performance concrete). All specimens were manufactured in a local laboratory and tested under uniaxial compression. The mix design of each mixture is displayed in Table 1. In this study, the constituent materials making up the concrete mixtures were as follows: Portland-fly ash cement type I – CEM I 42.5R (in case of HPC); Portland-fly ash cement type II – CEM II/B-V 32.5R (in case of NC) [16]. SikaFume was used as a concrete additive in fine-powder form based on silica fume technology [15]. Sika ViscoCrete-5-600 was used as a superplasticiser. Diabase ($\phi 2-8$) and fine sand ($\phi 0-2$) were used as aggregate.

Six samples were made of each type of concrete. All specimens were divided into four groups: normal concrete columns (NCC); high-performance concrete columns (HPCC); normal concrete columns reinforced with CFRP (NCC-CFRP); high-performance concrete columns reinforced with CFRP (HPCC-CFRP). Each of these groups was represented by three samples.

The specimens had a 150mm diameter and were 400mm in height. The concrete specimens were ripened in a water bath at a temperature of 20°C for twenty-eight days.

Table 1. Proportions of concrete mixture ingredients

Mix type	Cement [kg/m ³]	Sand [kg/m ³]	Coarse aggregate [kg/m ³]	Water [kg/m ³]	SikaFume [kg/m ³]	Superplasticiser [kg/m ³]	w/c ratio [-]
NC	366	942	942	183	–	–	0.5
HPC	500	650	1000	200	60	10	0.4

Preparation of specimens

After the maturation of the samples in the water bath, they were dried out for seven days. The efficiency of the CFRP confinement depends on the preparation of the concrete surface before the lamination process. To ensure adequate bond strength in this study, the concrete surface was sanded, cleaned and dried. The concrete surface before and after the sandblasting process in the case of HPC is shown in Fig. 1. As a result of adding a superplasticizer and SikaFume to the concrete mixture, the concrete surface was very tight and glassy. This surface provides a very weak level of adhesion to the epoxy resin and prevents its penetration into the concrete. This is why it is so important to emphasise the proper preparation of the resin-concrete contact surface.

According to the resin manufacturer, the moisture content of the concrete surface should be approximately 5% – this condition was satisfied. The confined cylinders were wrapped with Sikawrap301c carbon fibres by using Sikadur330 epoxy resin using the manual dry layup process. In all cases, the principal fibres were oriented perpendicular to the column axis, in a so-called 0° orientation. The fibre sheets were overlapped by 150 mm. The age of



Fig. 1. The concrete surface before (left) and after sandblasting process (right) in the case of HPC

the concrete specimens at the moment of testing was six weeks. The strength parameters of Sikawrap301c and Sikadur330 were in accordance with the manufacturer's specifications as shown in Tables 2 and 3, respectively.

Table 2. Characteristic parameters of Sikawrap301c [15]

Areal Weight	304 g/m ² ± 10 g/m ²	
Fabric Design Thickness	0.17 mm (based on carbon content)	
Fibre Density	1.80 g/cm ³	
Dry Fibre Properties	Tensile E-modulus	230 000 MPa (nominal)
	Tensile strength	4 900 MPa (nominal)
	Elongation at the break	2.1% (nominal)

Table 3. Characteristic parameters of Sikadur330 epoxy resin [15]

Density	Mixed resin: 1.3 ± 0.1 kg/dm ³ (at + 23°C)		
Tensile Strength	30 MPa (7 days at + 23°C)		(PN-EN ISO 527-3)
Bond Strength	Concrete fracture (> 4 N/mm ²) on sandblasted substrate:		(PN-EN ISO 4624)
E-Modulus	Flexural:	3 800 MPa (7 days at + 23°C)	(PN-EN 1465)
	Tensile:	4 500 MPa (7 days at + 23°C)	(PN-EN ISO 527-3)
Elongation at Break	0.9% (7 days at + 23°C)		(PN-EN ISO 527-3)

Instrumentation and loading conditions

Specimens were loaded under a monotonic uniaxial compression loading. The tests were performed using a servo-controlled MTS Rock and Concrete Mechanics Testing System. The load was applied at a quasi-static displacement rate of $5 \times 10^{-5} \text{ [s}^{-1}\text{]}$. The measurement of the axial force was carried out by means of a force transducer and the displacements were measured using linear variable differential transformer (LVDT) sensors. Radial and axial displacements were determined through the measurement of the whole columns' dimension changes, where the LVDT sensors were mounted directly between compression plates (Fig. 2).

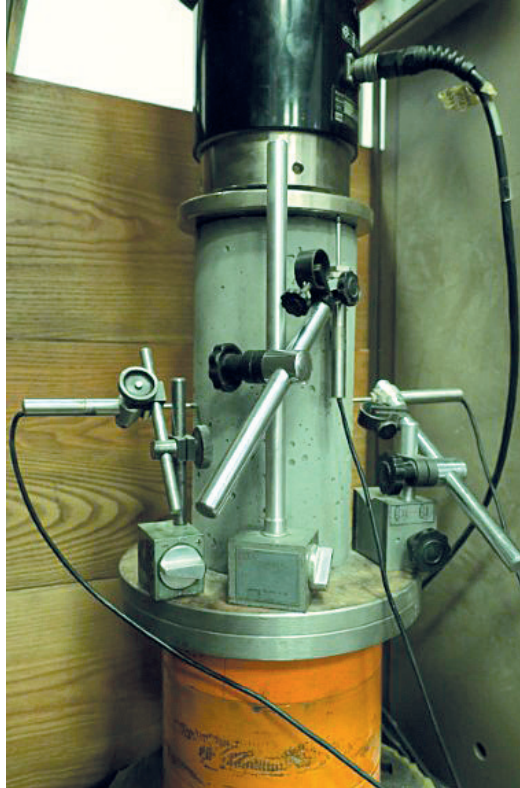


Fig. 2. Measurement system for specimens

3. Results and discussion

The test results described in Table 4 show that CFRP confinement can significantly enhance the specimens' ultimate strengths and strains. All the CFRP confined specimens failed due to the hoop tensile rupture of the CFRP jacket in the weakest location of the specimen, with a sudden explosive noise. Figs. 3 & 4 show the typical failure modes of both the unconfined and the confined specimens.

Table 4. Experimental results

Specimen	Ultimate load [kN]	Nominal compressive strength [MPa]	Axial strain during fracture of columns [‰]	Axial strain during fracture of concrete [‰]	Transverse strain during fracture of concrete [‰]	Modulus of elasticity E_1 [GPa]	Modulus of elasticity E_2 [GPa]
Normal Concrete Columns							
NCC1	520	30.25	3.95	3.95	1.04	8.52	–
NCC2	622	35.69	3.73	3.73	1.98	12.20	–
NCC3	517	29.28	3.78	3.78	3.77	10.12	–
High-Performance Concrete Columns							
HPCC1	1312	74.25	4.29	4.29	3.50	17.42	–
HPCC2	1115	63.12	4.40	4.40	3.85	13.48	–
HPCC3	1000	57.36	4.79	4.79	3.81	14.97	–
Normal Concrete Columns reinforced with CFRP							
NCC-CFRP1	1290	72.99	25.69	5.44	2.75	12.72	1.36
NCC-CFRP2	1255	71.97	25.21	6.34	4.11	10.30	1.36
NCC-CFRP3	1236	71.87	22.86	5.01	3.57	14.40	1.40
High-Performance Concrete Columns reinforced with CFRP							
HPCC-CFRP1	1414	80.04	6.16	–	–	16.46	–
HPCC-CFRP2	1635	92.50	5.17	–	–	22.58	–
HPCC-CFRP3	1515	85.70	5.52	–	–	18.09	–
Summary							
Group of specimens	Average compressive strength [MPa]	Standard deviation of the mean [MPa]	Average axial strain during fracture of columns [‰]	Average axial strain during fracture of concrete [‰]	Average transverse strain during fracture of concrete [‰]	Average modulus of elasticity E_1 [GPa]	Average modulus of elasticity E_2 [GPa]
NCC	31.74	2.63	3.82	3.82	2.26	10.28	–
HPCC	64.91	7.01	4.68	4.68	3.72	15.29	–
NCC-CFRP	72.28	0.48	24.59	5.60	3.48	12.47	1.37
HPCC-CFRP	86.08	4.28	5.62	–	–	19.04	–



Fig. 3. Failure modes of NCC (left) and HPCC (right)



Fig. 4. Failure modes of NCC-CFRP (left) and HPCC-CFRP (right)

Axial stress–strain response

The experimental axial stress-axial strain and axial stress-lateral strain curves of CFRP-confined columns are shown in Figure 5. The nominal axial stresses were defined by dividing the axial loads by the total cross-sectional areas of the columns – the small thickness of the CFRP was insignificant in this evaluation. The modulus of elasticity E_1 and E_2 were calculated without preloading cycles; therefore the results are qualitative. The modulus of elasticity E_1 and E_2 were identified in the range of stress ranging from 15% to 33% [4] and from 75% to 95% value of maximum stress, respectively. The point of inflection on the stress-strain curve was the moment of determination of the axial and transverse strains during the fracture of concrete in the case of CFRP columns.

The average compressive strength of NCC is 31.74 MPa; standard deviation in this case is 2.63 MPa. The average longitudinal and transverse strains of NCC at the time of destruction

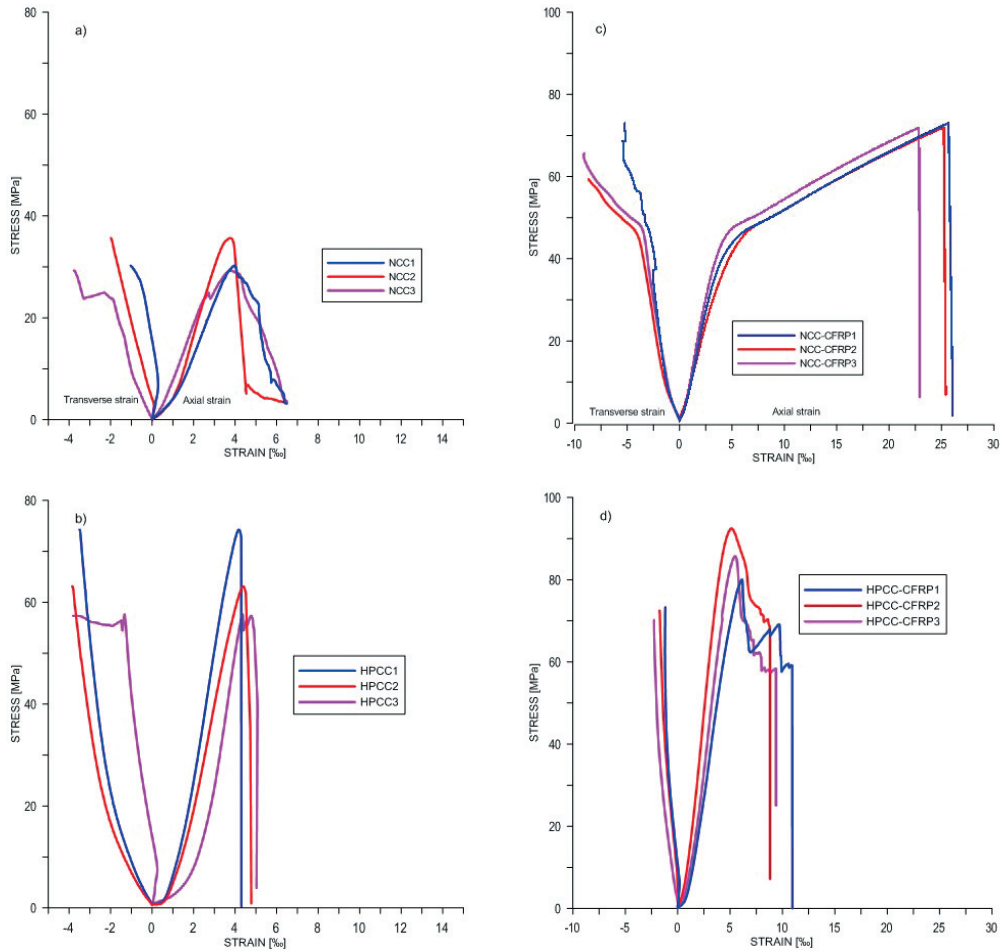


Fig. 5. Axial stress–strain relationships for specimens: NCC (a), HPCC (b), NCC-CFRP (c), HPCC-CFRP (d)

were 3.82‰ and 2.26‰, respectively. The average modulus of elasticity E_1 is 10.28 GPa. The average compressive strength after retrofitting with CFRP increases by 128%. The average maximum axial strains in the case of NCC-CFRP are 24.59‰, the modulus of elasticity E_1 is 12.47 GPa. It is worth noting the standard deviation, which is a mere 0.48 MPa. The modulus of elasticity E_2 is 1.37 GPa. The NCC-CFRP columns may be treated as a composite material working as elastic-plastic with strengthening.

The average compressive strength of HPCC is 64.91 MPa; standard deviation in this case is 7.01 MPa. The average longitudinal and transverse strains of HPCC at the time of destruction were 4.68 ‰ and 3.72‰, respectively. The average modulus of elasticity E_1 is 15.29 GPa. The use of CFRP sheets in the covering of HPCC increases the compressive strength and axial strain by 33% and 20% respectively. The modulus of elasticity E_1 for HPCC-CFRP is 19.04 GPa. The behaviour of HPCC-CFRP is close to being linearly elastic. After exceeding the load capacity, we observe a step loss of stiffness leading to the destruction of the element – this is not observed in the case of NCC-CFRP.

Adhesion of CFRP confinement to the concrete surface

The aspect of the resin-concrete contact area is often overlooked in the interpretation of the test results. It is, however, a very significant role in determining the performance of CFRP, especially in the new generation of concrete, in which the surface is specific and different from normal concrete. Figure 6 shows the laminate which was breaking away from the normal concrete (left) and the high-performance concrete (right). We can observe that the Sikadur330 epoxy resin thoroughly adhered to the concrete surface of NC. The coarse

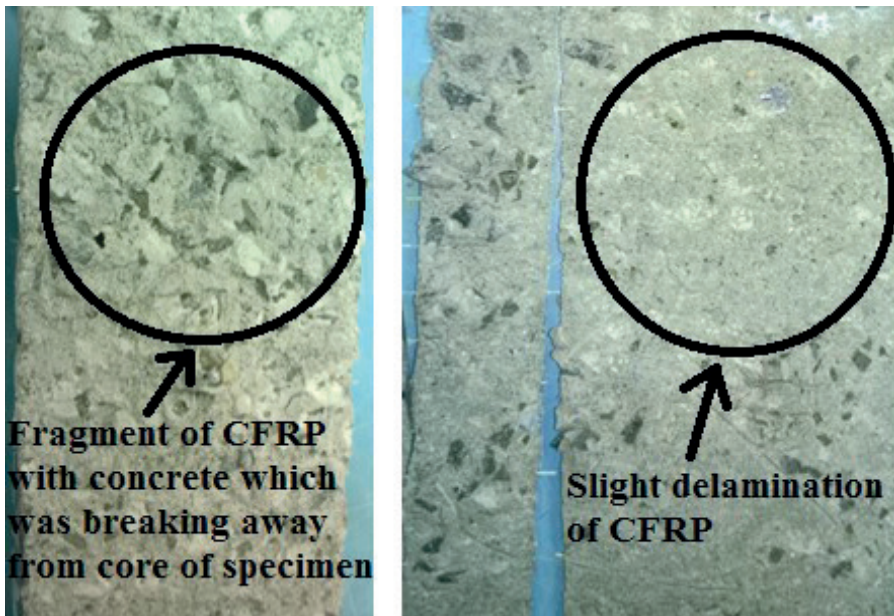


Fig. 6. CFRP sheets torn from NCC-CFRP (left) and HPCC-CFRP (right)

aggregates and cement paste were torn from the concrete core in the case of NCC-CFRP; however, in the case of HPC a small amount of aggregate and a surface layer of cement paste were detached from the surface of the HPCC-CFRP. This indicates a worse co-operation of the epoxy resin with the surface of high-performance concrete; however, it should be emphasised that this is a phenomenon reported in the literature [11, 14].

4. Conclusions

An experimental program was carried out to study the axial compression behaviour of normal concrete and high-performance concrete columns of circular cross-section confined externally with CFRP sheets. The main conclusions of the tests are noted below:

1. The stress–strain curves of the NCC-CFRP can be divided into two separate regions: firstly, the elastic stage involved with the transfer of stresses by the concrete; secondly, the strengthening stage, where stresses are transferred by CFRP confinement – this provides the columns with post-yield stiffness for load carrying;
2. The stress–strain curves of the HPCC-CFRP is close to being linearly elastic. After exceeding the load capacity, we observe a step loss of stiffness leading to the destruction of the element – this is not observed in the case of NCC-CFRP;
3. The failure of all CFRP columns occurred in a sudden and explosive manner and was preceded by typical creeping sounds;
4. The ultimate capacity of the confined concrete, given in terms of ultimate strength and axial strain, depends on the concrete core strength;
5. The confinement efficiency drops when the compressive strength of the concrete core increases. In the cases of NCC-CFRP and HPCC-CFRP, confinement caused a 130% and 33% increase in load capacity, respectively;
6. The adhesion of the epoxy resin to the concrete surface and its penetration depth depends on the type of the concrete with regard to strength. It is possible that the rupture of the jacket could be accompanied by a slight delamination of the layers.

The author would like to thank Mr Marek Kawalec, MSc. Eng., from SIKA Poland, for his donation of the strengthening materials and for the technical support provided.

This thesis was conducted within the framework of the regulation researches of AGH University of Science and Technology, Poland No 15.11.100.009.

References

- [1] Berthet J.F., Ferrier E., Hamelin P., *Compressive behavior of concrete externally confined by composite jackets*, Part A: experimental study. *Construction and Building Materials*, 2005.
- [2] Chikh N., Gahmous M., Benzaid R., *Structural Performance of High Strength Concrete Columns Confined with CFRP Sheets*, *Proceedings of the World Congress on Engineering*, 2012.
- [3] Daiyu Wang, Zhenyu Wang, Scott T. Smith, Tao Yu, *Seismic performance of CFRP-confined circular high-strength concrete columns with high axial compression ratio*, *Construction and Building Materials*, 2017.
- [4] EN 12390-13:2013 *Testing hardened concrete, Part 13: Determination of secant modulus of elasticity in compression*.
- [5] Jiang S., Fernando D., Ho J.C.M., Heitzmann M., *Behavior of FRP confined ultrahigh-strength concrete columns under axial compression: An experimental study*, *Mechanics of Structures and Materials: Advancements and Challenges*, 2017.
- [6] Jiang T., Teng J.G., *Analysis-oriented stress-strain models for FRP-confined concrete*, *Engineering Structures*, 2007.
- [7] Lim J.C., Ozbakkaloglu T., *Confinement model for FRP-confined high-strength concrete*, *Journal of Composites for Construction*, 2013.
- [8] Mayer P., Kaczmar J., *Właściwości i zastosowania włókien węglowych i szklanych*, *Tworzywa Sztuczne i Chemia*, 2008.
- [9] Ostrowski K., Kinasz R., Cieślak J., Wałach D., Ahmida B., *Nośność elementów osiowo ściskanych na przykładzie kolumn z betonu i fibrobetonu wysokowartościowego wzmocnionych włóknami węglowymi*, *Czasopismo Inżynierii Lądowej, Środowiska i Architektury*, 2016.
- [10] Ostrowski K., Kinasz R., Cieślak J., Wałach D., *The influence of CFRP sheets on strength of short columns produced from normal strength concrete and fibre reinforced concrete*, *Technical Transaction*, 2–B/2016.
- [11] Sadowski Ł., Mathia T. G., *Multi-scale metrology of concrete surface morphology: fundamentals and specificity*, *Construction and Building Materials*, 2016.
- [12] Sadowski Ł., Czarnecki S., Hoła J., *Evaluation of the height 3D roughness parameters of concrete substrate and the adhesion to epoxy resin*, *International Journal of Adhesion and Adhesives*, 2016.
- [13] Sadrmomtazi A., Khabaznia M., Tahmouresi B., *Effect of Organic and Inorganic Matrix on the Behavior of FRP-Wrapped Concrete Cylinders*, *Journal of Rehabilitation in Civil Engineering*, 2016.
- [14] Xiao Y., Wu H., *Compressive behavior of concrete confined by various types of FRP composite jackets*, *Journal of Reinforced Plastic and Composites*, 2003.
- [15] www.sika.com (access: 07.04.2017).
- [16] www.gorazdze.pl (access: 17.03.2017).

Elżbieta Pilecka (epilecka@pk.edu.pl)

Institute of Structural Mechanics, Cracow University of Technology

Krystyna Stec

The Central Mining Institute

Renata Szermer-Zaucha

Design Studio of the General and Industrial Construction, Ltd

THE INFLUENCE OF THE KŁODNICA FAULT TECTONIC ZONE
ON THE DEGREE OF DAMAGE TO BUILDINGS RESULTING FROM HIGH
MAGNITUDE TREMORS

WPLYW STREFY TEKTONICZNEJ USKOKUKŁODNICKIEGO
NA WIELKOŚĆ USZKODZEŃ W BUDYNKACH SPOWODOWANYCH
WYSOKOENERGETYCZNYM WSTRZĄSEM

Abstract

On 18 April 2015, a regional tremor with an energy $E=4 \cdot 10^9$ J occurred in the main saddle of fault VIa. This phenomenon emerged as result of summing up of stresses caused by underground exploitation conducted in the vicinity of natural faults with unrelaxed tectonic stresses, which resulted in the very strong influence of this tremor on the surface infrastructure and on the emotional well-being of local people. This analysis suggests that there is a statistical relationship between these values. Diversity of location both of the size of measured vibration parameters, damages in the buildings and of feelings of the vibrations prove an unequal radiation of the seismic waves caused by the amplifying influence of the fault zone.

Keywords: mining tremors, tectonic faults, mining damage

Streszczenie

18 kwietnia 2015 r. w strefie uskokuwej uskoku VIa w siodle głównym wystąpił wstrząs regionalny o energii $E=4 \cdot 10^9$ J. Zjawisko to miało miejsce w wyniku sumowania się naprężeń wywołanych podziemną eksploatacją prowadzoną w otoczeniu naturalnych uskokuw z niezrelaksowanymi naprężeniami tektonicznymi, co miało przełożenie na bardzo silne oddziaływanie tego wstrząsu na infrastrukturę powierzchniową i odczucia przez ludzi. Przeprowadzona analiza wykazała, że istnieje statystyczny związek między tymi wielkościami. Zróżnicowanie położenia zarówno wielkości pomierzonych parametrów drgań, uszkodzeń w budynkach, jak i odczuć wstrząsów świadczą o nierównomierniej radiacji fal sejsmicznych spowodowanej amplifikującym oddziaływaniem strefy uskokuwej.

Słowa kluczowe: wstrząsy górnicze, uskoki tektoniczne, szkody górnicze

1. Introduction

In the Upper Silesian Coal Basin, mining induced seismic events of varying intensities occur, from weak events which go unnoticed to people, to very strong events of a tectonic character which are described as being regional [5, 9]. Regional seismic events cause numerous instances of damage to buildings and surface infrastructure. The connection between regional tectonics and damage to buildings resulting from high-intensity mining tremors has been the subject of studies carried out since 2011 by Renata Szermer-Zaucha and Elżbieta Pilecka. The studies were carried out using statistical methods verified using selected archive materials from coal mines and they explicitly showed that there is such a connection. The results are presented in works [6–8].

The present article focuses on the results of research referring to the determination of statistical dependence between the distance of the damaged buildings from the tectonic zone of the Kłodnica fault (dk) or accompanying faults (d) and the amplitude of horizontal vibration velocity PGV_{Hmax} , (determined as the horizontal maximum length of the ground vibration vector) of the tremor of 18 April 2015 of energy $E=4 \cdot 10^9$ J, calculated for the foundation place of the building.

The epicenter of this tremor belonging into “regional events”, was located in the zone of the VIa fault. This fault is situated is a meridional of the Kłodnica fault zone which is situated of latitudinal.

The Kłodnica fault zone and the accompanying faults are located in a region in which for years, strong tremors of 10^8 and even 10^9 J have occurred as a result of the accumulation of exploitation stresses caused by coal exploitation carried out and the tectonic stresses. Exploitation stresses are an additional factor which triggers the energy in tectonic structures. The occurrence of tectonic stresses in this region is documented by studies [1, 2]. A fault is usually a zone in which the orogenic belt is strongly cracked. When a seismic wave approaches the fault, various phenomena take place in it. The fault is the border of two centres which have different acoustic impedences; thus, in accordance with Snellius’ law, reflection and refraction of the seismic wave follows.

In article [3], it was claimed that the results of refraction studies of consolidated substrate in Poland provide evidence that even at depths of several kilometres, changes to the velocity occur in the faulting zones. Assuming that open fissures do not occur in dislocation zones, it has to be taken into account that there is a strong probability of the zones being filled with dislocation material of different elastic properties – this has been proven by making exploratory boreholes. Velocity diversification also occurs and this creates favourable conditions for the formation of waves reflected from the plane of the fault zones. The border of layers in the orogenic belt and cracked layers in the fault fissure is then the border of reflected waves and form an additional hazard for building objects in the vicinity of the faults.

2. Characteristics of the scope of studies

The area of studies encompasses the Panewniki exploitation field, which is located in the northern part of the Upper Silesia Coal Basin, in the southern wing of the main saddle. The main saddle is a structure with a very complex nature – it is a row arranged in a sequence of elevations and dome folds. In the main saddle area, there are many fault structures (Fig. 1). The majority of large faults cutting the main saddle and the main basin come from the Variscan age. Some of them were rejuvenated later in the Mesozoic and Tertiary ages. Many new faults (so-called Alpine faults) appeared in the discussed area during those period. One of such fault is the Kłodnica fault – a several-kilometre-long fault zone stretching in the east-west direction.

In the eastern and western part the fault, it changes its direction to south-east. The discussed fault generally throws the layers to the south. Throw amplitude reaches 40–160 m in the eastern part, about 360 m in the middle part and further to the west, the throw amplitude decreases to about 15–20 m. The Kłodnica fault is accompanied by a number of smaller faults of a few to several metre throws, arranged in steps or fan-shaped and faults of throws of several to a few dozen meters. The Kłodnica fault is also accompanied by non-continuous deformations of small lengths of up to 150 m and throws of 2–3 m faults. The described faults have different azimuths as well as throws. It can be observed in the zones and junctions that when smaller faults reach the Kłodnica fault, their throws accumulate. The Kłodnica fault fissures and the accompanying faults are filled with breccia in the form of sandstone, mudstone, carbonaceous substances and sandstone blocks.

In the area of research, there is also a system of meridional faults. The size of their throws is changeable and fluctuates from 5–120 m and the layers of the orogenic belt are thrown to the west or the east. Similarly varied is the dip angle of the planes of these faults (40–90°). The most important characteristics are:

- ▶ Fault IV – a natural eastern border of the Panewniki field. The fault runs from NNE to SSW and throws the layers towards the NW by about 50–70 m. Fault IV reaches the Kłodnica fault and continues in a northerly direction as fault VII.
- ▶ Fault V runs from north to south. At the beginning a single fault zone to the south separates into a number of fissures following different course azimuths from NE to SW, through N to S and NW to SE and of different throws, forming a characteristic fan-shaped structure in the vicinity of the Kłodnica fault. The fault throws layers to the E by 40–50 m in the northern part of the discussed area. In the southern part, a number of dislocations forming the fault V zone has throws from 1–6 m and changeable angles of plane inclinations from 60–80°. This fault ends at the Kłodnica fault.
- ▶ Fault Jakub is in the southern part of the Panewniki field on the extension of fault V. This is a meridional fault, throwing layers to the west from 40 m at Kłodnica fault to 70 m south of it, that is in Panewniki field. What is characteristic about this fault is that its inclination angle changes from 60–90°. Two echelon fault zones accompany this fault their throws being 3–4 m and a number of small faults in generally sub-meridional directions, and seldom of parallel latitude.
- ▶ Fault VIa runs a parallel course to that of fault IV and throws its layers to the south-east. The size of the throw is $h \sim 50$ m. In the northern part, the discussed fault crosses the

Kłodnica fault and goes meridionally through the Panewniki field throwing layers to the east by about 70–90 m. In the southern part, the fault diverts into a westerly direction.

- ▶ Faults VII and VIa form a common zone in a northerly direction from the Kłodnica fault and further separate into two independent faults of large throws of 60 m and 70 m. In the area of the Kłodnica fault, they join into one zone again consisting of a number of faults of different directions and sizes of throws. On the other side of the Kłodnica fault, that is in Panewniki field, the faults continue as two independent exploitation zones with large throws of 80 m and 110 m.
- ▶ Fault VIII is a fault which follows a course close to meridional. It forms a zone of the width extend in the southern direction from several meters on the north to about 23 m on the south in the area of Kłodnica fault. Fault VIII at Kłodnica fault separates into a number of faults that have dip from a few to 45 m. The fault plane inclination angle is changeable and fluctuates from 60–80°. The fault throws layers towards the west.

The described system of lower-order multidirectional faults which accompany the Kłodnica fault has caused the studied area to be cut into a number of tectonic blocks of different sizes, differently shifted with regard to one another, both horizontally and vertically. Thus, this is an area prone to all kinds of deformations due to both past and present coal mining exploitation which is accompanied by numerous tremors of the order of $10^8 - 10^9$ J.

The tremor from 18 April 2015 occurred during exploitation of coal bed 409 in the western part of the Panewniki coalfield and was localised in the footwall of the Kłodnica fault in the region of the VIa fault.

The coal seam in this area is rated as the III degree of the rockburst hazard in years 2003–2008 was exploited in two longwalls of its western part by a longitudinal system with the roof fall. Moreover, in the eastern part of the field, coal seam 409 was also exploited in two longwalls in the years 2009–2012 by a lateral system with a roof fall. At the beginning of October 2013, in the western part of the field, the next longwall was exploited by a longitudinal system with a roof fall. During the exploitation of this longwall the analysed regional tremor occurred with a energy $E=4 \cdot 10^9$ J. Coal seam 409 in the longwall lies at a depth of about 1040 m (786 mbsl) up to about 1097 m (844 mbsl) with an average inclination of 4–7°, in southerly and south-westerly directions and its seam thickness fluctuates between 2.2 m and 3.1 m, with the interlayer of clay slate with a seam thickness of up to about 0.3m. In the roof of the coal seam lies a layer of clay slate with a seam thickness of 4.7 m. Above this seam lies light grey sandstone of various grains with a seam thickness of 5.2 m, below this seam there is a layer of sandstone with a thickness of 3.7 m. In this area there have not been exploitation events so there are no edges, remains or abandoned workings which are mining factors which most often cause stress concentration zones. High seismicity in Panewniki field appeared at the very beginning of exploitation. There were many low-energy phenomena (750 tremors below 10^5 J) and 113 tremors of energy higher than 10^5 J, including five tremors of 10^7 J energy, one of 10^8 J energy and the strongest one which was $4 \cdot 10^9$ J and is the subject of the present analysis.

3. Soil vibration parameters and damage to buildings due to the tremor of 18 April 2015

Seismic measurements constitute the most precise and direct information which is indispensable for the evaluation of surface vibrations; they also allow for the empirical correlation of the effects of vibrations with measurement sizes. Registration of vibration parameters of the tremor from 18 April 2015 with an energy $E=4 \cdot 10^9$ J was carried out at five surface seismic stations. Table 1 shows parameter values of soil vibrations from measurement stands on the basis of publication [10] containing soil vibration analysis made according to the methodology used for the GSI_{GZWKW} -2012 scale [12].

After the occurrence of the analysed tremor, the inhabitants of Katowice and the neighbouring towns reported numerous instances of damage to buildings and reported their resulting feelings of anxiety, fear and discomfort.

Table 1. Parameters of 18 April 2015 tremor vibrations as registered at surface seismometric stations [10]

Seismic station	Epicentral distance [m]	Velocity, PGV_{Hmax} [mm/s]
A 4 – Bałtycka	1253	20
A 3 – Panewnicka (wall)	887	100.3
A 3 – Panewnicka (soil)	890	61
A 2 – Kalinowa	2670	12.8
A 7 – Piłsudskiego	2428	14.7
A7 – Mikołowska	6147	3

Table 2 displays the instances of damage to buildings caused by the analysed tremor. These cases were reported right after the tremor and they were then evaluated by personnel from the mining damages department – this was essential for the reliability of such information. On the basis of the measurement data, the dependence describing regional relations between seismic energy, hypocentral distance and maximum velocity parameters of horizontal vibrations registered on the bedrock [4] distribution was calculated of the forecast component amplitudes of the horizontal velocity of vibrations. Next, having taken the vibration amplification factor in this region into consideration, vibration velocity isolines PGV_{Hmax} were plotted. On the basis of the received map of vibration velocity PGV_{Hmax} , the values of vibration velocity for the location of the buildings damaged as a result of the analysed tremor were calculated (Table 2). The location of these buildings and tectonic structures are shown on the PGV_{Hmax} vibration velocity map in Fig. 1.

Table 2. List of damage to buildings following the tremor of 18 April 2015; intensity $E = 4 \cdot 10^9$ J; velocity PGV_{Hmax} ; distance from Klodnica fault dk ; distance from closest fault d

Nr *	Town street	Type of building**/ Description of damages	Distance from epicentre [m]	Distance from the nearest fault [m] - d	Distance from Klodnica fault [m] - dk	Velocity PGV_{Hmax} [mm/s]
3	Katowice, Tysiąclecia	A/ scratches on the walls	7290	1096	4359	0
6	Świętochłowice, Topolowa	A/ scratches on the ceiling	6145	1481	4359	0
7	Chorzów, Sępolowska	A/ scratches on the ceiling	5065	883	2980	0.9
8	Ruda Śląska, Radoszowska	A/ scratches on the wall	3474	40	2089	2.6
9	Ruda Śląska, Radostowska	A/ fallen roof tile	3450	309	2196	2.6
10	Katowice, Lompy	A/ garage door seizure	8191	2774	2774	0
11	Ruda Śląska, Cegielniana	A/ scratches on the walls	2744	0	1570	3.7
12	Katowice, Ogrodowa	A/ building tilt, uplift of floor tiles	3200	227	227	4.3
13	Katowice, Ogrodowa	A/ cracks of ceiling plaster and plaster coves in two rooms	3134	158	158	4.5
14	Katowice, Heweliusza	B/ numerous cracks in all rooms, cracks and loosening of wall tiles	3313	122	122	4.5
15	Katowice, Orkana	A/ cracks on elevations and walls	4882	185	185	2
16	Katowice, Braci Wieczorków	A/ cracks on elevations and walls	3079	22	22	4.9
17	Katowice, Braci Wieczorków	A/ cracks on elevations , walls and floor tiles	3130	60	60	4.9
18	Katowice, Panewnicka	A,C/ numerous cracks on elevations, walls and ceilings, cracks of window lintels, dilatation of flight of stairs from the building	578	188	188	24
19	Katowice, Panewnicka	B/ crack on walls and ceilings, separation of gable wall from the floor and interior load bearing wall, coming off plaster, door frame relocation	970	178	178	18

20	Katowice, Kuźnicka	A/ numerous cracks on elevation, walls and ceilings	534	235	235	15
21	Katowice, Panewnicka	C/ numerous scratches on walls and ceiling, cracks of floor tiles	1389	214	214	17
22	Katowice, Panewnicka	Church – crack of interior wall, crack of lintel	917	221	221	19
		B/ numerous cracks on elevation, walls and ceilings				
23	Katowice, Kuźnicka	A/ cracks on fencing, elevation and cellar walls	549	307	307	13
24	Katowice, Łąkowa	A/ crack around windows, scratches in joints of floor tiles in the bathroom, , door deformation	533	319	319	25
25	Katowice, Bałtycka	A/ cracks on elevation and walls, twist of door frame	1037	336	336	23
26	Katowice, Koszykowa	A, B/ cracks on elevation, walls and ceilings, cracks of floor tiles, loosening of skirting on the terrace, lowering and deformation of the terrace sett	347	501	501	32
27	Katowice, Bałtycka	B/cracks on walls and ceilings, deformation of balcony window and door joinery	1120	535	535	20
28	Katowice, Bałtycka	B/ cracks on elevation, wall, ceilings in many rooms, scratches of dilatation wall corners	1179	521	521	21
29	Katowice, Koszykowa	B/ cracks on elevation, walls and ceilings, loosening and cracks of the tiles	316	565	565	33
30	Katowice, Poleska	A/ cracks on walls and tiles	3624	779	779	3.7
31	Katowice, Huculska	A/ cracks on elevation, stairs and fence, twist of door frame	3634	717	717	3.7
32	Katowice, Huculska	A/ cracks on walls and ceilings	3659	749		3.5



33	Katowice, Huculska	A/ numerous cracks on elevation, walls, ceilings and fence base	3551	760		3.4
34	Katowice, Wczasowa	C/ cracks on balcony, walls, scratches on plaster cove in the bathroom	3153	1212		4
35	Katowice, Żołnierska	A/ cracks on elevation, tiles, entrance door deformation	3853	1445		3
36	Katowice, Komasa	A/ scratches on the walls	4845	2356		1.5
37	Katowice, Sępia	A/ scratches on the walls	4144	2474		2.3
38	Katowice, Armii Krajowej	A/ entrance door deformation	5689	3905		0.5
39	Katowice, Stabika	Collapse of ground floor in the cellar (about 5 cm) (after verification – no connection)	5326	3595		0.8
40	Mikolów, Przyjaźni	A/ cracks on elevation	4653	740		1
41	Katowice, Norblina	A/ cracks on external elevation	6145	3811		0.4

* No – the object number on the map

** Type of building : A – (single family house); B – (single family terraced or twin houses); C – (multifamily building)

4. Statistical analysis of the relationship between the distance of the damaged buildings' from the fault and soil vibration velocity PGV_{Hmax}

To determine the influence of the amplification of the Kłodnica fault zone on the amount of damage to buildings caused by high-energy tremors, statistical analysis was used. For the purpose of statistical analysis, two variables were taken into consideration: distance of the buildings from the nearest fault – dk ; maximum amplitude of horizontal vibrations velocity PGV_{Hmax} at the location of the foundations of the damaged buildings. The first step in the analysis was to check whether the distribution of parameters taken into analysis is a normal distribution. The statistical analysis was carried out by the STATISTICA software program. To check whether the distribution of the variables is normal, Shapiro-Wilk's test was used – this showed that neither variable has a normal distribution; therefore, Spearman's correlation coefficient was used to check correlation. The Spearman correlation coefficient takes values from the interval $[-1; 1]$. If there is no correlation between the variables, the returned value is 0. The critical values of the Spearman correlation coefficients are given in the statistics tables (Kendall test). The null hypothesis H_0 was tested – this states that there is no correlation between the variables. The alternative hypothesis H_1 states that there is a correlation if the calculated correlation coefficient at a specific level of significance (usually $\alpha = 0.05$) is greater than the critical value given.

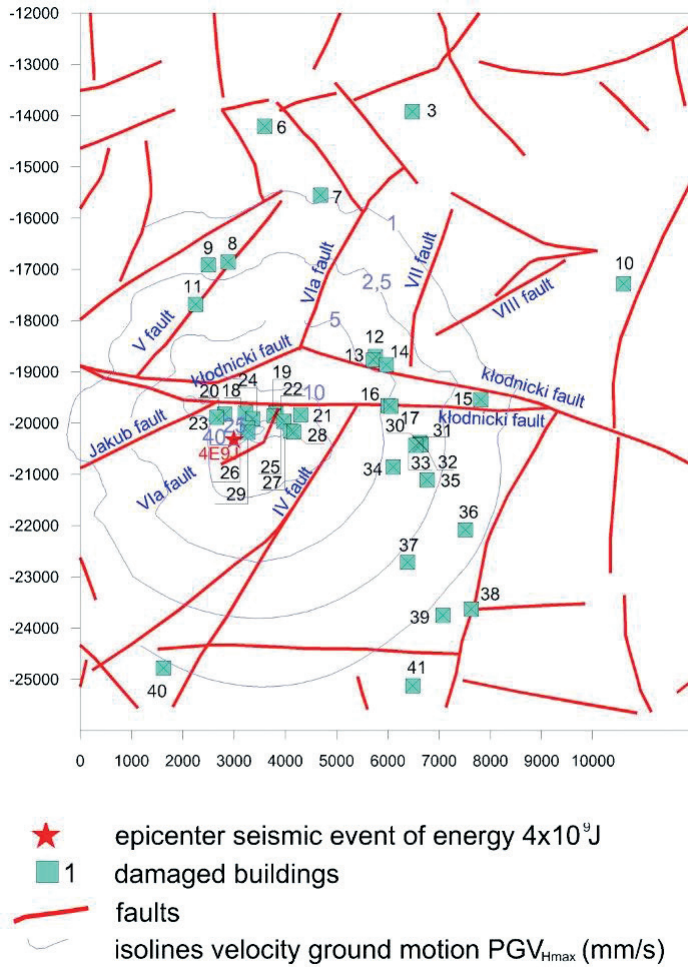


Fig. 1. Location of damaged buildings and tectonic structures on the map of vibration velocities PGV_{Hmax} from the tremor of 18 April 2015 with seismic energy of $E=4 \cdot 10^9$ J

Table 3. Correlation matrix PGV_{Hmax} and dk for the tremor of 18 April 2015 of seismic energy $E=4 \cdot 10^9$ J

	PGV_{Hmax} [mm/s]	dk [m]
PGV_{Hmax}	1	-0.74
dk [m]	-0.74	1

As a result of calculations, the statistically essential correlation coefficient $R = |-0.74| = 0.74$ for level of significance 0.05 was obtained (Table 3). In order to establish the significance of the correlation coefficient for the given level of significance, a method of

hypothesis testing (test t – Student’s) was applied. It appeared that the correlation coefficient is essential. Thus, with a 95% level of probability both variables, that is PGV_{Hmax} – horizontal velocity of ground vibrations [mm/s] in the foundation place of a building and dk – distance of the damaged building from Klodnica fault [m], are related to each other.

In the second analysis, the influence of the fault on damage to buildings located closest to it was investigated. As in the first analysis, two variables were taken into consideration in statistical tests: distance of the buildings from the nearest fault – d ; the maximum amplitude of horizontal vibrations velocity PGV_{Hmax} at the location of the foundations of the damaged buildings. The first step in the analysis was to check whether the distribution of parameters taken into analysis is a normal distribution. The statistical analysis was carried out by the STATISTICA software program. To check whether the variables have normal distributions, Shapiro-Wilk’s test was used – this showed that neither variable is of a normal distribution; therefore, Spearman’s correlation coefficient was used to check correlation.

Table 4. Correlation matrix PGV_{Hmax} and dk for the tremor of 18 April 2015 of seismic energy $E=4 \cdot 10^9$ J

	PGV_{Hmax} [mm/s]	d [m]
PGV_{Hmax}	1	-0.57
d [m]	-0.57	1

As a result of calculations, a statistically essential correlation coefficient of $R = |-0.57| = 0.57$ for level of significance 0.05 was obtained (Table 4). In order to check the significance of the correlation coefficient for the given level of significance, a method of hypothesis testing (test t – Student’s) was applied. It appeared that the correlation coefficient is essential. Thus with a 95% level of probability both variables, that is PGV_{Hmax} – horizontal velocity of ground

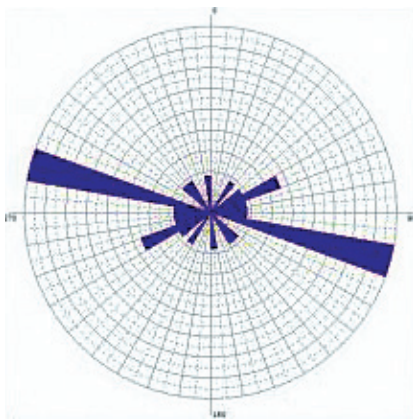


Fig. 2. Direction diagram of mining damage for tremor of 18 April 2015 of seismic energy $E=4 \cdot 10^9$ J

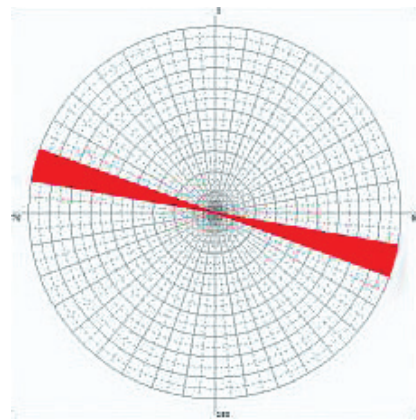


Fig. 3. Direction diagram of the Klodnica fault zone for tremor of 18 April 2015 of seismic energy $E=4 \cdot 10^9$ J

vibrations [m/s] in the foundation place of a building and dk – distance of the damaged building from Kłodnica fault [m], are related to each other. Taking into consideration the values of the obtained correlation coefficients, it can be stated that the influence of the Kłodnica fault on the occurrence of damage to the buildings was larger than that of the other faults, in spite of the fact that the buildings are located in their vicinity in some cases. Therefore, for the buildings in the Kłodnica fault region, a statistical analysis of their location direction was carried out. The analysis was performed according to a method described in work [11]. To obtain direction diagrams of mining damage, straight lines were drawn through each of the two closest instances of mining damage in the studied area. The obtained distribution direction of the analysed mining damage and the zone of the Kłodnica fault is presented in Figures 2 & 3.

The performed analysis shows that when evaluating the influence of vibrations on the buildings except tremor energy, the epicentre distance, the vibration amplification coefficient, and the location of the buildings in relation to the tectonic zones also has to be considered. From the data set in Table 2, it appears that damage found in the buildings is, in some cases, located even at a distance of over 3.5km from the centre of the tremor. These buildings, however, are located up to 0.8km from the fault zone (Table 2 – number of buildings from 12–33).

5. Summary

The analysis focused on the influence of the Kłodnica fault zone on the size of damage in the buildings caused by the regional tremor of 18 April 2015 of seismic energy $E=4 \cdot 10^9$ J. On the basis of statistical analysis of the relationship between the distance of the damaged buildings' from the tectonic zone of Kłodnica fault (dk) or the nearest fault (d) and the maximum amplitude of horizontal vibrations velocity PGV_{Hmax} (at the locations of foundations of these buildings), it was shown that the influence of the Kłodnica fault in this region on damage caused to these buildings is of key importance.

As a result of the performed calculations, statistically essential values of correlation coefficients were obtained, wherein the correlation value of PGV_{Hmax} velocity with the distance of the damaged buildings from the Kłodnica fault is larger than with the distance of the buildings from the nearest fault – this is also proved by the analysis of the distribution direction of the damaged buildings.

From the analysis, it can be seen that the dominant direction of mining damage distribution is the direction of the Kłodnica fault zone, which is close to being latitudinal. This is also a dominant direction of tectonics in the southern wing of the main saddle.

On the basis of the performed analysis, it can be stated that when evaluating or forecasting the influence of vibrations on buildings – apart from seismic energy of the tremors, epicenter distance and amplification coefficient of the vibration – the location of buildings in relation to the tectonic zones also has to be taken into consideration; this is extremely essential when designing buildings and in site planning.

References

- [1] Czarnogórska M., Graniczny M., Kowalski Z., Wegmuller U., *Usung ALOS PALSAR nad ERS data for monitoring of subsidence and related ground failures in Upper Silesian Coal Basin*, Southern Poland EGU General Assembly Conference Abstracts, Vol. 11/2009, 13792.
- [2] Jura D., *Young-Alpine Kłodnica Fault scarps of the metacarpathian in the Silesian Upland*, Techn. Posz. Geol. Geosynoptyka i Geotermia, No. 1/99, Kraków, 52–56.
- [3] Krynicki T., *Wybrane zagadnienia metodyki prac polowych w badaniach geologicznych utworów paleozoicznych metodą refleksyjną*, Kwartalnik Geologiczny, Vol. 26/1982, 217–229.
- [4] Mutke G., *Metoda prognozowania parametrów drgań podłoża generowanych wstrząsami górnymi w obszarze GZW*, rozprawa doktorska, Główny Instytut Górnictwa, Katowice 1991.
- [5] Pilecka E., Pilecki Z., *Analysis of relation between induced seismic activity and satellite data*, 19th Symposium on Application of Geophysics to Engineering and Environmental Problems SAGEEP, EEGS, 2–6 April 2006, Seattle 346–355.
- [6] Pilecka E., Szermer-Zaucha R., *Analiza lokalnej tektoniki w powiązaniu z uszkodzeniami budynków wynikającymi z wystąpienia wysokoenergetycznego wstrząsu w dniu 9 lutego 2010 roku w KWK „Piast”*, Prace Naukowe GIG 4/2/2011, 366–382.
- [7] Pilecka E., Szermer-Zaucha R., *Wnioski wynikające z analizy szkód górniczych po wysokoenergetycznych wstrząsach w powiązaniu z tektoniką na terenie górniczym KWK „Piast”*, Przegląd Górniczy 3/2013.
- [8] Pilecka E., Szermer-Zaucha R., *Analiza wpływu uskoju Rydułtowskiego na szkody górnicze spowodowane wstrząsami z dnia 21.04.2011 i 07.06.2013 lokalnej tektoniki w powiązaniu z uszkodzeniami budynków wynikającymi z wystąpienia wysokoenergetycznego wstrząsu w dniu 9 lutego 2010 roku w KWK „Piast”*, Przegląd Górniczy 6/2014, 60–66.
- [9] Pilecka E., Piątkowska A., Stec K., Buła Z., Pilecki Z., Król M., *Związek lineamentów z sejsmicznością indukowaną na terenach górniczych Górnośląskiego Zagłębia Węglowego*, Pilecka E. (ed.), Wyd. IGSMiE PAN, Kraków 2006.
- [10] Stec K., Mutke G., *Mechanizm ognisk i intensywność oddziaływania na środowisko powierzchniowe wstrząsów regionalnych z obszaru Katowice-Panewniki*, Górnicze No. 1, 11–20, 720.
- [11] Szermer-Zaucha R., *Wpływ silnych wstrząsów górniczych na uszkodzenia budynków w powiązaniu z budową geologiczno-tektoniczną*, praca doktorska, Politechnika Krakowska, Kraków 2016.
- [12] Uszko M., Barański A., Kowal T., Mutke G., *Zagrożenia naturalne w kopalniach Kompanii Węglowej SA. Część II. Oddziaływanie wstrząsów górniczych na powierzchnię*, Wiadomości Górnicze 12/2013, 708–720.

Anna Śpiewak (aspiewak@bud.czest.pl)

Małgorzata Ulewicz

Department of Organization and Technology Building, Faculty of Civil Engineering,
Czestochowa University of Technology

ANALYSIS OF THE IMPACT OF CORROSION ON LOSS OF LOAD CAPACITY
AND TIME BETWEEN FAILURES OF A BRIDGE IN THE TOWN OF WISLA

ANALIZA WPŁYWU KOROZJI NA SPADEK NOŚNOŚCI ORAZ CZAS
BEZAWARYJNEJ PRACY MOSTU W WIŚLE

Abstract

This article presents guidelines developed by the Research Institute of Roads and Bridges for estimating the loss of the load capacity and determining the time between failures of steel road bridges resulting from corrosion. Mathematical relationships which enable the determination of load capacity and durability of bridge structures were discussed. Reduction coefficients required to calculate the percentage decrease of the load bearing capacity of the corroded structure and reduction coefficients that are significant in determining the degree to which lifespan of the structure is shortened were defined. Mathematical algorithms of presented method made it possible to obtain information, that are necessary for further maintenance and possible modernization of the bridge in Wisla.

Keywords: corrosion, steel girders of bridge structures, loss of load capacity of a bridge structure, time between failures of structure due to corrosion

Streszczenie

W artykule przedstawiono wytyczne opracowane przez Instytut Badawczy Dróg i Mostów dotyczące szacowania utraty nośności oraz określania czasu bezawaryjnej pracy stalowych, drogowych obiektów mostowych z uwzględnieniem zjawiska korozji. Omówiono zależności matematyczne pozwalające na wyznaczenie nośności i trwałości konstrukcji mostowych. Scharakteryzowano współczynniki redukcyjne niezbędne do obliczenia procentowego spadku nośności skorodowanej konstrukcji oraz istotne współczynniki zmniejszające pozwalające na określenie czasu bezawaryjnej pracy konstrukcji. Algorytmy matematyczne przedstawionej metody pozwoliły na uzyskanie danych, które są niezbędne do dalszego utrzymania oraz ewentualnej modernizacji mostu w Wiśle.

Słowa kluczowe: korozja, stalowe dźwigary główne obiektów mostowych, utrata nośności konstrukcji mostowych, czas bezawaryjnej pracy konstrukcji

1. Introduction

Technical inspections are very important in the context of bridge maintenance. Technical inspections, maintenance and servicing of bridges need to be performed in order to determine safety risks to users, to maintain the appropriate technical condition and esthetic design of the bridge, to prevent deterioration of the mechanical properties and ensure the efficiency of the durability of bridge structures. The system of inspection of road and bridge structures include: ongoing reviews, annual fundamental reviews, extended reviews every five years and detailed reviews. To analyse the percentage loss of the load capacity of steel girders and determine the time between structural failures due to corrosion, it is necessary to carry out a detailed inspection. Detailed inspections and visual inspection of all elements of construction and execution of basic measurements and tests provide data and information which is necessary for analysing the capacity and durability of the steel girders of the bridge structure. The detailed review report of the technical condition of the bridge on the Wisla (shared by the Management for Provincial Roads in Katowice) allowed for calculations according to the method of the Research Institute of Roads and Bridges (IBDiM). Calculations made using the method of the Road and Bridge Research Institute provided results that are complementary to detailed inspection and additional information on the load bearing capacity (strength of the structure, the stress and loss of material) and durability of structural steel elements. Calculations can help to provide the methods necessary for the modernisation of the bridge or can help in choosing the corrosion protection of structures. In addition, the results of calculations enable the determination of the time between failures of all bridge structures due to corrosion and this results of calculations also enables the identification of strategies that will ensure the ongoing safe use of the bridge structure [1].

2. An analytical approach to assessing the load capacity of a bridge structure which has been damaged by corrosion

The decrease in structural load bearing capacity related to the reduction of the cross-sectional area of a steel member is caused by the corrosive loss of steel. The loss of material in the solid-web girder cross-section is calculated by measuring the thickness reduction of the cross-section in the upper and lower flanges of the girders and their webs. Measurement of the corrosion loss in bridge members and decks in the form of a steel orthotropic plate is taken considering the width of the deck subpanel defined in accordance with PN-EN 1993-2:2010 standard [2]. When the load bearing capacity reduction of corroded structure is being calculated the corrosion phenomena should be taken into account as it is often developed in the orthotropic plate longitudinal and transversal stiffeners. The reduction measurement is taken when the u_7 – reduction coefficient is applied. Estimating the loss resulting from the undesirable influence of corrosion on the thickness of the cross-sections subjected to bending moments consists of measuring the extent of the identified calibration distance (Fig. 1), where, according to the structural analysis, there is the maximum stress. The result

of the measurement is the smallest value of the cavity in the 25 mm measuring points, which they must be cleaned of corrosion products on the circuit of the element [3–6]. Corrosion phenomenon changes the cross-sectional geometry which is why the second moment of area and indicators of the corroded cross-sectional resistance should be calculated taking into account another position of the neutral axis of a steel profile. In accordance with the method recommended by the Road and Bridge Research Institute, it is important to determine the corrosion value of the i -th bridge girder – this is calculated relative to the upper and lower fibres of the cross-section with formulas [3]:

$$w_{id} = \frac{W_{id_cor}}{W_{id_nom}} \quad (1)$$

$$w_{ig} = \frac{W_{ig_cor}}{W_{ig_nom}} \quad (2)$$

where:

- w_{id}, w_{ig} – is the corrosive girder parameter i ;
- W_{id_cor}, W_{ig_cor} – is the flexural resistance indicator (elastic section modulus) of a corroded girder i to the upper and lower fibre, [m³];
- W_{id_nom}, W_{ig_nom} – is the flexural resistance indicator (elastic section modulus) of a corrosion-free girder i to the upper and lower fibre, [m³].

For further calculations, the minimum value of each corrosive parameters, should be applied. In addition, the cross-sectional areas of the corroded web of girders and transverse stiffeners located at the support points should be determined and then, according to the formula (3), they should be compared with the areas of uncorroded cross-sections. For further analysis assumes the smallest value of the parameter a_i the most corroded girders [3–4].

$$a_i = \frac{A_{i_cor}}{A_{i_nom}} \quad (3)$$

where:

- a_i – is the corrosive parameter of the cross-section in the support i ;
- A_{i_cor} – is the area of the corroded cross-section in the support i , [m²];
- A_{i_nom} – is the area of the not corroded cross-section in the support i , [m²].

The next stage is to select reduction coefficients which are characterised by susceptibility to changes with regard to the geometry and strength of the cross-sections of the steel elements of the bridge structures. The load capacity of a structure depends on the degree of corrosion of each girder and their interaction when the service load is being transferred. The presented analytical method describes seven dependencies to which the Road and Bridge Research Institute developed reduction coefficients. Of equal importance are: the number of main girders (u_1); the spacing of main girders in their cross-section (u_2); deck type (u_3); transversal bracing type (u_4); transversal bracing concentration along the structure length excluding

support bracing (u_s); degree of corrosion in transversal bracing (u_δ); corrosion degree in transversal stiffeners orthotropic plate longitudinal (u_σ). The chosen coefficients enable the identification of the percentage of decrease of the load capacity of a steel road bridge structure (S_M) due to the bending moment with particular consideration to corrosion [3]:

$$S_M = \left[1 - \frac{\min(\sum_{(i=1)}^k w_{id}, \sum_{(i=1)}^k w_{ig})}{k} \cdot \prod_{(j=1)}^n u_j \right] \cdot 100\% \quad (4)$$

where:

S_M – is the load capacity decrease due to the bending moment, [%];

w_{id}, w_{ig} – is the corrosion parameters of the girder $i = 1, \dots, k$;

u_j – is the reduction coefficient $j = 1, \dots, n$;

k – is the number of girders.

To determine the ultimate loss of the structural load bearing capacity caused by corrosion, the load decrease associated with the support's reaction needs to be determined (S_p) [3] – this is achieved using the formula:

$$S_p = \left[1 - a_i \cdot \prod_{j=1}^n u_j \right] \cdot 100\% \quad (5)$$

where:

S_p – is the load capacity decrease due to the support reaction, [%];

a_i – is the corrosion parameter of the most corroded girder i ;

u_j – is the reduction coefficients $j = 1, \dots, n$.

Formulas (4) and (5) enable the identification of a decrease to the total load capacity of a bridge with solid web steel girders (S_U) resulting from the destructive phenomenon of corrosion [3], which is described with the formula (6):

$$S_U = \max\{S_M, S_p\} \quad (6)$$

where:

S_U – is the load capacity decrease of the solid web girder due to corrosion phenomenon, [%].

An analytical approach to assessing the durability of a bridge structure which has been damaged by corrosion

Estimation of the impact of corrosion on the durability of bridge structures requires, above all, the analysis of the object and determining the type and extent of corrosion on the construction. It is important to determine the location of corrosion on the surface of the load bearing capacity steel elements because irregular distribution of corroded elements and the resulting decreases in the mass of the material in cross-sections of the bearing elements causes concentration of stresses. Variable tensions intensify the corrosion process, which accelerates

the fatigue of structural material. In the method developed by the Road and Bridge Research Institute, the reduction coefficients of durability and mathematical formulas are used – this enables the lifetime of a corroded bridge to be determined [3, 7, 8]. To determine the reduction coefficients, it is necessary to analyse technical and material data relating to the steel-concrete bridge structure, because reduction coefficients are related to: the level of aggressiveness of the environment (S_A); bridge location; type of corrosion in the load capacity structure (K_R); the technical condition of bridge drainage system (T_W), dilatation system (T_D) and insulation system (T_I). The appropriate selection of reduction coefficients enables calculation of the degree to which the lifespan of the construction has been shortened by corrosion (S_T) [3]:

$$S_T = K_R \cdot S_A \cdot \frac{T_W + T_I + T_D}{3} \quad (7)$$

where:

S_T – is the degree of shortening of the lifespan of the construction;
 K_R, S_A, T_W, T_I, T_D – is the reduction coefficients.

The next step is to determine the β coefficient related to the road class and the age of the analysed bridge (W). It is also obligatory to the projected life span of the bridge (T_m). According to the Polish procedure developed by the Road and Bridge Research Institute, these parameters (S_T, β, W and T_m) are used to determine the time between failures of the structure due to corrosion (T_c), during which corrosion proceeds with a probability of about 90% [3]:

$$T_c = T_m \cdot S_T \cdot \beta - W \quad (8)$$

where:

T_c – is the time between failures of structure due to corrosion, [years];
 T_m – is the projected lifespan of the bridge structure, [years];
 S_T – is the degree of shortening of the lifespan of the construction;
 β – is reduction coefficient;
 W – is the age of the analysed bridge structure, [years].

Analysis of the load capacity and durability of the steel girders of the bridge structure in Wisla.

The triple-span beam bridge shown below was analysed. This bridge is located in Wisla and is situated over the Mailnka steam (Fig. 1). This bridge is part of the inter-regional road DW942 managed by the Management for Provincial Roads in Katowice.

The load capacity structure of this bridge is made up of steel beams comprising a rolled profile connected to a concrete slab. In the cross-section, there are four IN340 girders spaced every 1.80m. The bridgeheads and pillars of the bridge are reinforced concrete, solid-wall structures. Additional elements of the bridge are steel safety barriers, the road surface comprised of asphalt concrete, and the bridge drainage system [9].

Based on an analysis of the detailed review report of the technical condition of the bridge on the Wisla [9] and the local detailed inspection of this bridge (Fig. 2 a–d), the values of



Fig. 1. The analysed bridge in Wisla (photo by authors)

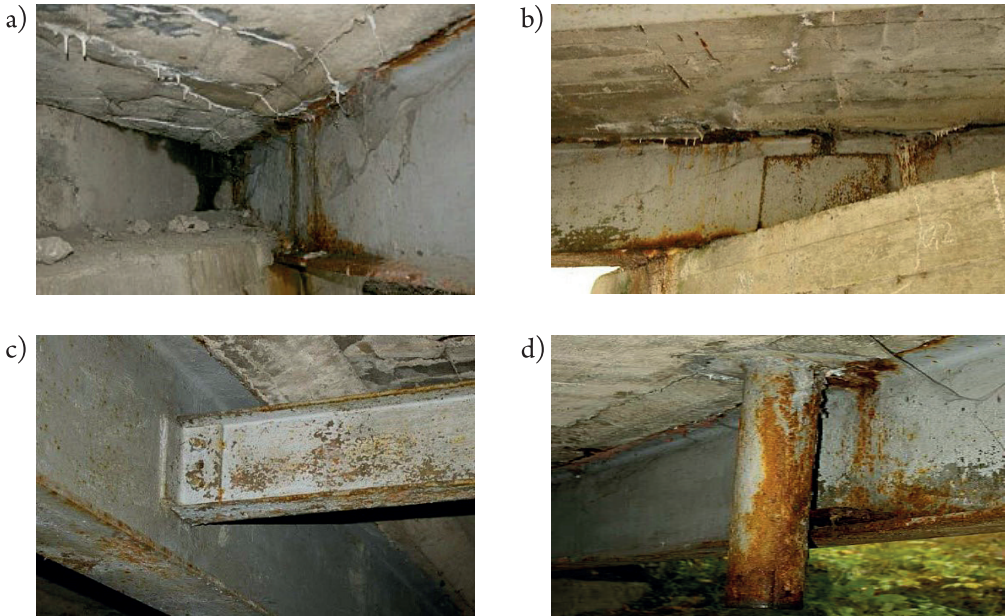


Fig. 2. a) Support of the extreme girder on the bridge abutment with corroded top and bottom flange; b) The corroded steel girder is supported by bridge pillar; c) Corrosion of the connection between the cross beam and the main girder; d) Corroded drain pipe which forms part of the drainage system (photo by authors)

the reduction coefficients to the bearing capacity and durability of the analyzed object were taken into account and Tables 1 and 2 were developed. These values defined the percentage structural load bearing capacity decrease due to corrosion and the time between failures of the structure due to corrosion.

Table 1. Data for the bearing capacity of the bridge in Wisla

Reduction coefficient of load capacity					
u_1	u_2	u_3	u_4	u_5	u_6
0.98	1.10	1.00	1.00	0.95	0.98
Load capacity decrease due to the bending moment				S_M	7.36%
Load capacity decrease due to the support reaction				S_P	1.04%
Load capacity decrease of the solid web girder due to corrosion				S_U	7.36%

Table 2. Data for the durability of the bridge in Wisla

Reduction coefficient of durability						
S_A	K_R	T_W	T_i	T_D	β	W
0.98	0.923	0.98	0.90	–	0.96	54
Degree of shortening time between failures of structure				S_T	0.850	
Time between failures of structure due to corrosion				T_e	27 years	

The analysis of the bridge in Wisla showed that the higher value takes the value of the load bearing capacity due to the bending moment than the value of the load bearing capacity due to the support reaction. The load bearing capacity decrease of the solid web girder due to corrosion was 7.36%. The load capacity decrease of the bridge structure and time between failures of the structure due to corrosion depended on the type of corrosion located on the surface of girders. Additionally, the aggressiveness of the environment had the greatest impact on the durability of the bridge structure. The preceding analysis has shown that the time between failures of structure due to corrosion until this calculation was 27 years. This can only be good news for the functional longevity of this bridge. However, this method does not take into account the ongoing corrosion of the structure. The amount of corrosion very dynamically rises from year to year. The amount of corrosion products is increasing year by year due to the air pollution, the aggressive environment in which the bridge is located and the concentration and amount of salt used for the winter maintenance of roads. The corroded girders are damaged above the ultimate limit state and their durability has consequently been compromised. Therefore, this method allows estimation of the load bearing capacity and durability only with regard to the current state of the bridge structure.

3. Conclusion

The analytical method of estimating the effect of corrosion on the percentage loss in load bearing capacity and the time between failures of the bridge operation allows for easy and rapid determination of important parameters related to the strength and durability of steel bridge girders taking into account the destructive corrosion process. The use of this method is justified though the opportunity it presents to extend the functional longevity of the structure. The results of such an analysis constitute a valuable addition to the detailed

reports of technical inspections of steel-concrete bridge structures. The results of this analysis enabled the determination of the approximate date for modernisation of the bridge and the development of a plan for renovation and technical improvement. This approach enables the identification of the loss of load capacity of bridges and the time between structural failures – this allows the formulation of optimal construction schedules for possible bridge reconstructions. The preceding analysis document that the bridge located in Wisła does not require repair and reconstruction prior to the next detailed review. However, the technical condition of the bridge in Wisła should be monitored accurately during the ongoing reviews.

The research was supported by scientific grant SK-EN-2015-0004

References

- [1] Janas L., Jarominiak A., Michalak E., *Załącznik do Zarządzenia nr 14 Generalnego Dyrektora Dróg Krajowych i Autostrad z dnia 7 lipca 2005r. Instrukcje Przeprowadzania Przeglądów Drogowych Obiektów Inżynierskich*, Warszawa, Wydawnictwo SliTK RP, Oddział w Rzeszowie, Rzeszów 2005.
- [2] PN-82/S-10052 *Obiekty mostowe. Konstrukcje stalowe. Projektowanie*.
- [3] Czerepak A., Czudek H., Pryga A., Wysokowski A., *Metoda szacowania wpływu korozji na nośność konstrukcji stalowych mostów drogowych. Zalecenia GDDKiA*, Wydawnictwo IBDiM, Żmigród 2003.
- [4] Chwastek A., Ulewicz M., Vician J., *Assessing the corrosion impact on bearing capacity of steel girder bridges in Poland. Transcom Proceedings, 11th European Conference of Young Researchers and Scientists, Section 7 Civil Engineering, Žilina 2015*, 76–81.
- [5] Wysokowski A., *Limitation of corrosion effect on the reduction of load capacity of steel bridges by thermal spraying*, Surface Engineering, No. 1, 2007, 39–47.
- [6] Vičan J., Odrobiňák J., *Steel structures*, Wydawnictwo University of Žilina, Žilina 2008.
- [7] Wysokowski A., *Trwałość mostów stalowych w funkcji zjawisk zmęczeniowych i korozyjnych*, praca habilitacyjna, Wydawnictwo IBDiM, Warszawa 2001.
- [8] PN-EN 1993-2:2010 *Eurokod 3. Projektowanie konstrukcji stalowych. Część 2: Mosty stalowe*.
- [9] Wawrzacz J., Kotowicz-Kulka K., Białecki T., *Ocena aktualnej nośności wraz z raportem z przeglądu szczegółowego*, Zarząd Dróg Wojewódzkich w Katowicach, Katowice 2010.

Yaroslav Kovivchak (ya_kovivchak@yahoo.com)

Department of Automated Control Systems, Lviv Polytechnic National University

AN ANALYSIS OF ELECTROMAGNETIC PROCESSES IN A TURBOGENERATOR
WITH A REAL ROTOR AND A STATOR TOOTH STRUCTURE
IN THE NO-LOAD MODE

ANALIZA PROCESÓW ELECTROMAGNETYCHNYCH W TURBOGENERATORZE
ZE STRUCTURAMI REALNYMI ROTORA I STATORA NA BIEGU JAŁOWYM

Abstract

The results of the research presented in this article are 2-D mathematical field models of a turbogenerator in the no-load mode with real tooth structures on the rotor and stator in the rotor coordinate system and in the physical systems of reference. The results of the computer simulation of the electromagnetic field in the cross-sectional zones of the device in the no-load mode transition process are pre-sented.

Keywords: electromagnetic field, vector potential, turbogenerator, tooth zones, movable and immovable me-dia, systems of coordinates

Streszczenie

W artykule przedstawiono model 2-D polowy matematyczny turbogeneratorsa na biegu ja-lowym ze strukturami realnymi zębów rotora i statora w systemie koordynat rotora i fizycznych systemach współrzędnych rotora i statora jednocześnie. Przedstawiono rezultaty symulacji komputerowej pola elektromagnetycznego w płaszczyźnie przekroju urządzenia dla procesu przejściowego na biegu jałowym.

Słowa kluczowe: kpole elektromagnetyczne, potencjał wektorowy, turbogenerator, strefy zębów, środowiska poruszające się i stacjonarne, układy współrzędnych

1. Introduction

The practicality of the possibilities to perfect properties, improve characteristics, and optimise parameters of electrical engineering equipment directly depends on the depth of a multi-aspect, versatile analysis of the peculiarities of electromagnetic phenomena in the elements of the given device. Thus, in the world scientific and technical literature, much attention has been paid to the development of theoretical and methodological approaches to solving the problems arising when developing mathematical models of electric objects. In these approaches, efforts are made to take the construction of objects into account to as great an extent as possible and apply real physical laws of electromagnetic phenomena occurring in the device media [1–12]. One of the more advanced strategies for successfully tackling this problem is to develop mathematical models of electric objects exclusively based on the theory of electromagnetic fields. This article summarizes the results obtained while conducting research into the development of the mathematical field model of turbogenerators in no-load modes with different levels of detail of the tooth structures of the rotors and stators both in the rotor's own coordinate system, and in the physical reference systems of the rotor and stator simultaneously [13].

The aim of the proposed publication is the search for theoretically reasoned, practical and effective ways of solving problems that may arise while developing the mathematical field models of electrodynamic objects. The following problems are some of the most important to be solved:

- ▶ achievement of correctness of mathematical and physical justification of the methods chosen for calculating an electromagnetic field in moving and fixed media of electric devices in different systems of reference;
- ▶ the need for improved strategies for identifying boundary and initial conditions for the field equations on the basis of matching the first and higher spatial derivatives of a vector potential function with certain magnetic properties of the media on both sides of the separation line;
- ▶ the need to identify optimal ways of taking into account the non-linear characteristics of the magnetic materials with deep saturation. These provide both necessary numeric stability of the models and practical implementation of the effective algorithm for the calculation of electromagnetic processes in the complex construction of electrodynamic devices based on the models developed.

Despite certain limitations of the proposed models [13], the main limitation being the performance of field calculation in 2-D space and the necessity to use some abstract coefficients applied in the theory of circuits. The values of the coefficients may be in rather a wide range of different modes, the approaches to the design of the 2-D models that are the focus of this research have opened up the possibility to develop effective 3-D models of this class of physical objects by using the methods described.

As a result of the computer simulation of electromagnetic processes in the moving and fixed media of the turbogenerator, it can be confirmed that it is impossible to develop a single 2-D mathematical field model of any electric device that will calculate various modes of its operation. The simulation of each mode requires the development of a separate model, each of which taking into consideration the construction of the device and describing the real

physical characteristics and parameters of the object media to a degree, which is sufficient for reproducing a particular given mode under simulation.

Currently, one of the significant additional disadvantages of the mathematical field models of electric devices is the time-consuming computer simulation of the transition processes. This is often used as the strongest argument against using mathematical field models without emphasizing the fact that the particularly mathematical field models are a reliable source of true, comprehensive, and detailed information on the electromagnetic phenomena in the objects. The rapid development of modern computational engineering and software in the near future will eliminate the urgency for a solution to the indicated problem; furthermore, theoretical and algorithmic issues concerning the development of the 3-D models will become much more pressing.

2. Statement of the problem

The proposed mathematical field models of the turbogenerator with real rotor and stator tooth structures both in a single moving coordinate system of the rotor, and in the physical systems of reference are based on the equations of electromagnetic field with respect to potentials in quasi-stationary approximation. They imply a direct time integration of the formed system of equations.

In the developed models of the turbogenerator, there is no summand $\mathbf{v} \times \mathbf{B}$ in the equations of electromagnetic field for moving media. In work [13], it is theoretically substantiated that the given summand can only be used to transfer determined values of the field vectors from one inertial system to another – it cannot help in calculating unknown electromagnetic quantities in moving media of electrodynamic devices.

The calculation of the electromagnetic field in the models is conducted for a no-load mode of the turbogenerator at the given voltage of the rotor power supply winding.

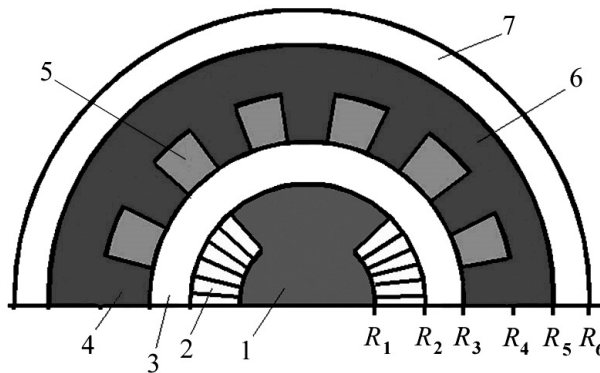


Fig. 1. Calculated zones of the turbogenerator cross section

On the pole division of the device, in the models, we reproduce twenty-four stator slots and teeth and eight slots with an excitation winding in the left and right parts of the rotor – as specified by the technical parameters of the object. The angular segment in which all rotor slots are located in each part of the winding ('2' in Fig. 1) on the pole division of the turbogenerator is approximately 60° . Practically in the same segment, there are 8 stator slots. That is why to simplify the models, the number of rotor slots at both winding sides on the stator pole division is also chosen to be equal to 8.

With regard to paying consideration to achieving accurate reconstruction of the tooth zones, it is necessary to choose the minimum possible discretisation grid size – this enables a more detailed description of the real structure of the device. Another possible way to achieve accurate reconstruction is through the application of separate rotor and stator grids and performing the recalculation of unknown electromagnetic quantities at their boundaries.

Fig. 1 shows a virtual image of the turbogenerator cross section, where 1 is the massive rotor body; 2 denotes the rotor tooth zone; 3 is the air gap between the rotor and stator; 4 is the stator tooth; 5 is slot with the stator winding; 6 is the laminated stator body; 7 is the air zone outside the turbogenerator.

The geometric dimensions of the zones formed in the models (see Fig. 1) correspond to the geometric dimensions of the construction of the real TGV-500 turbogenerator that are presented in Fig. 2.

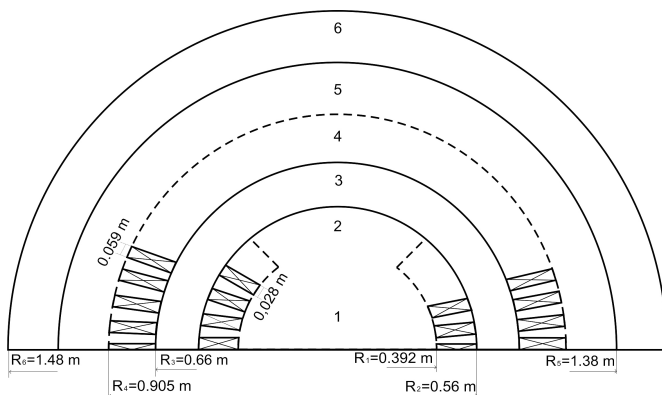


Fig. 2. Main geometric zone dimensions of the turbogenerator cross section

While developing the mathematical field models of the turbogenerator with real tooth rotor and stator structures, as with descriptions of previous works, the following main assumptions were made:

- ▶ emission currents in the device media are disregarded;
- ▶ the electromagnetic field in the turbogenerator can be considered to be plane-parallel;
- ▶ the electromagnetic phenomena on the butt are not taken into consideration;
- ▶ the hysteresis characteristics of the magnetic material of the rotor and stator are not taken into consideration.

3. Mathematical model of a turbogenerator with real rotor and stator tooth zones in the coordinate system of the moving rotor

The given model implies that the calculation of the electromagnetic processes in the turbogenerator in a no-load mode is achieved using a single moving coordinate system of the rotor. The electromagnetic phenomena in the model are considered in terms of quasi-stationary approximation in the case of a plane-parallel field. In order to obtain the minimum number of calculated equations and to simplify the task of determining boundary and initial conditions, the mathematical field model is designed on the basis of electromagnetic field potentials using the Weil's gauge $\nabla\varphi = 0$.

Work [13] shows that the calculation of electromagnetic processes in moving and fixed media can be performed both in the own coordinate systems of moving and fixed bodies, and in the transformed systems of reference. The only condition is that all the variables present in the equations must belong to the same system of coordinates.

In the suggested model, the analysis of the electromagnetic phenomena in the body, teeth and slots of the rotor – as well as in the air gap between the rotor and stator – is performed using the coordinate system of the moving rotor. The calculation of the electromagnetic field in the body and teeth of the rotor is performed using the following equation:

$$\frac{\partial \mathbf{A}}{\partial t} = -\gamma^{-1} \nabla \times (\nu \nabla \times \mathbf{A}) \quad \mathbf{A} = A_z \mathbf{z}_0 \quad (1)$$

where \mathbf{A} is the vector potential of the electromagnetic field; γ is the static matrix of electric conductions; ν denotes the matrix of the static inverse magnetic penetrability of the medium; ∇ is the Hamiltonian operator.

In this equation, the component of the vector potential of the electromagnetic field A_z belongs to the rotor coordinate system.

To describe the electromagnetic phenomena in the slots with the excitation winding connected to an external voltage source, we use the following equation:

$$\frac{\partial \mathbf{A}}{\partial t} = -\gamma^{-1} (\nu_0 \nabla \times \nabla \times \mathbf{A} \pm \boldsymbol{\delta}) \quad \mathbf{A} = A_z \mathbf{z}_0 \quad \boldsymbol{\delta} = \delta_z \mathbf{z}_0 \quad (2)$$

where ν_0 is the inverse magnetic copper penetrability; δ_z is the axis component of the extraneous current density vector.

The value of the current density in the rotor slots can be found through the relationship:

$$\delta_z = \frac{w_f i_f}{S} \quad (3)$$

where w_f , i_f are the number of windings and current of the excitation winding; S is the integral area of the rotor winding slots.

In the air gaps between the rotor and stator, the electromagnetic field can be calculated by using the relationship:

$$0 = \nu_0 \nabla \times \nabla \times \mathbf{A}; \quad \mathbf{A} = A_z \mathbf{z}_0 \quad (4)$$

where ν_0 is the inverse magnetic air penetrability.

The electromagnetic processes in the body, slots and teeth of the stator, as well as outside of the turbogenerator, are considered in the reference system of the stator fixed to that of the rotor.

As conduction currents are absent in the stator slots with a winding enclosed when the turbogenerator operates in a no-load mode, the electromagnetic field in the zone is determined by the following relationship:

$$0 = \nu_0 \nabla \times \nabla \times \mathbf{A}'; \quad \mathbf{A}' = A'_z \mathbf{z}_0 \quad (5)$$

where \mathbf{A}' is the vector potential of the electromagnetic field in the coordinate system connected to the rotor.

In the laminated body and teeth of the stator, the electromagnetic phenomena are described by the following relationship:

$$0 = \nabla \times \nu \nabla \times \mathbf{A}'; \quad \mathbf{A}' = A'_z \mathbf{z}_0 \quad (6)$$

The electromagnetic field outside the turbogenerator is determined by dependence (5).

In the model, a fuller reproduction of the laws of electromagnetic phenomena on the external boundaries of the pole division of the turbogenerator cross section – and consequently, the improvement of numeric stability of the formed system of equations – were provided by applying an advanced approach to the formation of boundary conditions. This implies matching the first and second spatial derivatives of the function of vector potential on the external separation lines of the calculated zones and their periodicity along the angular coordinate [13]. To find the boundary conditions of the corresponding internal boundaries of the turbogenerator cross-sectional zones, we use the following known dependencies [13]:

$$H_r^- = H_r^+; \quad H_\alpha^- = H_\alpha^+ \quad (7)$$

where H_r, H_α are the radial and tangential components of the vector of magnetic force on both sides of the medium separation line, respectively.

The relationships

$$A_{z,(k)} = \frac{\nu_{r,(k-1)} \Delta \alpha_2 A_{z,(k-1)} + \nu_{r,(k+1)} \Delta \alpha_1 A_{z,(k+1)}}{\nu_{r,(k-1)} \Delta \alpha_2 + \nu_{r,(k+1)} \Delta \alpha_1} \quad (8)$$

$$A'_{z,(k)} = \frac{\nu_{r,(k-1)} \Delta \alpha_2 A'_{z,(k-1)} + \nu_{r,(k+1)} \Delta \alpha_1 A'_{z,(k+1)}}{\nu_{r,(k-1)} \Delta \alpha_2 + \nu_{r,(k+1)} \Delta \alpha_1}$$

where v_r, v_α are the levels of static inverse magnetic penetrability of the medium in the radial and tangential directions respectively; $\Delta r_1, \Delta r_2, \Delta \alpha_1, \Delta \alpha_2$ are the steps of the discretisation grids in the respective coordinates, are used to find the value of the vector potential of the electromagnetic field on the internal boundaries of the device along the radial coordinate.

The expressions

$$A_{z,(i)} = \frac{v_{\alpha,(i-1)} \Delta r_2 A_{z,(i-1)} + v_{\alpha,(i+1)} \Delta r_1 A_{z,(i+1)}}{v_{\alpha,(i-1)} \Delta r_2 + v_{\alpha,(i+1)} \Delta r_1} \quad (9)$$

$$A'_{z,(i)} = \frac{v_{\alpha,(i-1)} \Delta r_2 A'_{z,(i-1)} + v_{\alpha,(i+1)} \Delta r_1 A'_{z,(i+1)}}{v_{\alpha,(i-1)} \Delta r_2 + v_{\alpha,(i+1)} \Delta r_1}$$

are used to calculate the value of A_z on the internal boundaries along the angle α , with the index i corresponding to the nodes of the grids along the radii, and k corresponding to the nodes of the grids along the angular coordinate.

In terms of the other objective physical condition of the spatial periodicity of the electromagnetic field on the pole division of the turbogenerator [13]

$$\left. \frac{\partial H_r}{\partial \alpha} \right|_{\alpha=0} = - \left. \frac{\partial H_r}{\partial \alpha} \right|_{\alpha=180} \quad (10)$$

we obtain the following calculated dependencies for determining boundary conditions along the radii:

$$A_{z,(k=1)} = 2A_{z,(k=2)} + 2A_{z,(k=n-1)} - A_{z,(k=3)} - A_{z,(k=n-2)} - A_{z,(k=n)} \quad (11)$$

$$A_{z,(k=n+1)} = A_{z,(k=2)} + A_{z,(k=4)} + A_{z,(k=n-1)} - 2A_{z,(k=3)} - 2A_{z,(k=n)}$$

$$A'_{z,(k=1)} = 2A'_{z,(k=2)} + 2A'_{z,(k=n-1)} - A'_{z,(k=3)} - A'_{z,(k=n-2)} - A'_{z,(k=n)}$$

$$A'_{z,(k=n+1)} = A'_{z,(k=2)} + A'_{z,(k=4)} + A'_{z,(k=n-1)} - 2A'_{z,(k=3)} - 2A'_{z,(k=n)}$$

where k is the index corresponding to the nodes of the discretisation grid along the angular coordinate.

By the equation:

$$A'_{z,(i=m+1)} = 2A'_{z,(i=m)} - A'_{z,(i=m-1)} \quad (12)$$

we determine the boundary conditions for the equations of the field on the external boundary of the calculated air zone, with i being the index corresponding to the spatial grid nodes in the cylindrical system of coordinates along the radius.

As the results of the computer calculation of the no-load mode transition processes based on the models developed in [13] showed, numerical stability of the solutions also depends on the way in which the non-linear characteristics of magnetic material are presented in the models. For this, using the following cubic splines proved to be the most effective:

$$v(B) = \sum_{m=0}^3 a_m^{(k)} (B - B_k)^m, \quad k = 1, 2, \dots, n \quad (13)$$

where n is the number of segmentations along the axis B . The module value of the magnetic induction vector in the nodes of the discretisation grid of the cylindrical system of coordinates in the corresponding systems of reference is found from the given relationships:

$$B_r = \frac{1}{r} \frac{\partial A}{\partial \alpha}; \quad B_\alpha = -\frac{\partial A}{\partial r}; \quad B = \sqrt{B_r^2 + B_\alpha^2} \quad (14)$$

where B_r, B_α, B are the radial and tangential components and the module of a magnetic induction vector in the grid nodes of both the physical reference system of the rotor, and the transformed coordinate system of the stator, respectively.

The non-linear electromagnetic characteristics of the rotor and stator materials in the model are considered by means of expression (13) with respective coefficients for the specified media.

The recalculation of the magnetic characteristics of the equivalent medium of the laminated stator body was performed on the basis of the following relationship:

$$v_\alpha = v_r = \frac{d_f + d_0}{d_f + v_f \cdot d_0 / v_0} \cdot v_f \quad (15)$$

where v_f, v_0 are the inverse magnetic penetrability of the ferromagnetic sheet and isolation of the laminated stator; d_f, d_0 are the width of the sheet and isolation, respectively.

To remove ambiguity in the balance of electrical and magnetic quantities in the case of non-linear variants of the models, an equation for the excitation winding is formed in the form:

$$\frac{di_f}{dt} = \left(u_f - r_f i_f - \frac{d\psi_f}{dt} \right) / L_f \quad (16)$$

where

$$\frac{d\psi_f}{dt} = w_f k_f l_r \sum_{i=1}^n \frac{\partial A_{zRi}}{\partial t} \quad (17)$$

with w_f being the number of the rotor winding turns; l_r is the axis length of the winding; A_{zRi} is the value of the vector potential function in the rotor coordinate system in the grid

nodes being located in the winding zone; and k_f being the coefficient involving the number of nodes along the angle α which are found in the rotor winding zone.

The equations for determining the stator winding voltages have the following form:

$$u_i = \frac{d\Psi_i}{dt} = w_i k_i l \sum_{m=1}^n \frac{\partial A'_{zSi}}{\partial t}, \quad i = A, B, C. \quad (18)$$

where w_i is the number of the stator windings in each phase; l denotes the axis winding length; k_i being the coefficient involving the number of nodes along the angle α , which is found in the stator winding zone; A'_{Si} is the value of the vector potential function in the nodes of the spatial discretization grid connected with the coordinate system of the moving rotor within the stator windings.

Equations (1)–(18) make up the basis of a mathematical field model designed for calculating the no-load mode of the turbogenerator with the real tooth zones of the rotor and stator at the specified voltage of the excitation winding in the reference system of the moving rotor.

4. Mathematical model of a turbogenerator with real tooth zones of the rotor and stator in the rotor and stator systems of coordinates simultaneously

One of the most important directions of research into the peculiarities of electromagnetic phenomena is creating mathematical field models of electrodynamic devices in physical systems of coordinates of moving and stationary bodies.

This section deals with the development of a mathematical field model for calculating the no-load mode of the turbogenerator at the pre-set voltage of the excitation winding with the real tooth zones of the rotor and stator in the physical systems of reference.

The mathematical modelling of the electromagnetic field in the massive body of the rotor, teeth and slots with the rotor winding, and in the air gap between the stator and rotor is performed in the system of coordinates connected to the moving rotor. At the same time, in the slots with the stator windings, teeth and stator body, and in the air gap outside the turbogenerator, this is performed in the reference system of the static stator. The given model provides a positional relationship of the rotor construction elements relative to the media of the stator along the angular coordinate.

The analysis of electromagnetic phenomena in the cross section of the body and teeth of the rotor is performed using equation (1); analysis of phenomena in the slots with electrically conductive rotor winding connected to the external source of voltage by using expression (2); analysis in the air gap between the rotor and stator by means of ratio (4). In all the zones mentioned, an axis component of the function of vector potential of the electromagnetic field A_z belongs to the physical coordinate system of the moving rotor.

As the device is in a no-load mode, there are no conduction currents in the stator winding, the calculation of the electromagnetic field in the zone is performed by using the following equation:

$$0 = \nu_0 \nabla \times \nabla \times \mathbf{A}; \quad \mathbf{A} = A_z \mathbf{z}_0 \quad (19)$$

To describe the electromagnetic phenomena in the teeth and body of the stator, we use the equation below:

$$0 = \nabla \times \nu \nabla \times \mathbf{A}; \quad \mathbf{A} = A_z \mathbf{z}_0 \quad (20)$$

We also find the value of the function of the vector potential \mathbf{A} outside the turbogenerator by means of expression (20).

The boundary conditions for the main system of equations on the external perimeter of the calculated zones in the physical coordinate systems along the radii are used in the form of equation (11).

On all the formed internal boundaries of the cross sectional zones of the turbogenerator between the media with different electromagnetic characteristics in the physical systems of reference, the boundary conditions are determined on the basis of relations (8), (9).

The non-linear characteristics of the magnetic materials of the rotor and stator in the model are considered by using dependence (13). At the same time, the values of the module and the components of the magnetic induction vector in the nodes of the rotor and stator grids are determined using (14). The magnetic characteristics of the equivalent anisotropic medium of the stator body are calculated using expression (15).

Equation (16) is used to determine the values of the current in the excitation winding of the turbogenerator; the values of the stator phase voltages are obtained by means of relationship (18).

The mathematical field model of the turbogenerator designed for calculating the no-load mode at the pre-set voltage of the excitation winding with the real rotor and stator tooth zones implies a reciprocal displacement of the grid nodes along with the corresponding physical media of the moving and stationary system of coordinates if the following condition is satisfied:

$$\Delta\alpha = \omega\Delta t \quad (21)$$

where $\Delta\alpha$ is the step of the discretisation grids along the angular coordinate; Δt represents the step of the time integration of the system of differential equations; ω denotes the angular speed of the rotor rotation.

5. Results of computer simulations

Computer simulations of the transition process in no-load mode were conducted at a level of at $u_f = 141$ V (u_f denotes the voltage of the excitation winding) using the mathematical field model of the turbogenerator with the real tooth zones of the rotor and stator. The model was developed in the reference system connected to the moving rotor, taking the parameters of the real TGV-500 turbogenerator in to consideration. To perform a more comprehensive analysis of the electromagnetic processes occurring in the no-load mode of turbogenerator

at the chosen step of the discretisation grid along the angular coordinate, it is sufficient to calculate the field for eight possible cases of the reciprocal location of the rotor and stator, since the given number corresponds to the number of grid discretization individually for a slot and a tooth of the stator in the tangential direction.

As a result of the computer calculations of the transition process of the no-load mode, using the model described above we obtained spatial-time values of the \mathbf{E} , \mathbf{H} , \mathbf{B} , \mathbf{D} , and so comprehensive information on the character of the electromagnetic processes in the zones of the device cross section.

The spatial distributions of electromagnetic quantities shown in Fig. 4–12 correspond to the following nodes of the coordinate grid of the turbogenerator cross-sectional zones: 0–54 (along the angular coordinate of the ferromagnetic rotor body zone); 54–75 (the rotor tooth zone); 75–87 (the air gap zone between the rotor and stator); 87–117 (the stator tooth zone); 117–174 (the stator body zone); 174–186 (the air gap outside the turbogenerator); 4–8 (along the angular coordinate of the rotor tooth structure); 12–16; 20–24; 28–32; 36–40; 44–48; 52–56; 60–64 (slots on the right side of the winding); 132–136; 140–144; 148–152; 156–160; 164–168; 172–176; 180–184; 188–192 (slots on the left side of the winding); 2–4; 8–12; 16–20; 24–28; 32–36; 40–44; 48–52; 56–60; 136–140; 144–148; 152–156; 160–164; 168–172; 176–180; 184–188; 192–194 (rotor teeth); 64–132 (large rotor tooth); 2–4 (along the angular coordinate of the stator tooth structure); 8–12; 16–20; 24–28; 32–36; 40–44; 48–52; 56–60; 64–68; 72–76; 80–84; 88–92; 96–100; 104–108; 112–116; 120–124; 128–132; 136–140; 144–148; 152–156; 160–164; 168–172; 176–180; 184–188; 192–194 (laminated teeth of the stator body); 4–8; 12–16; 20–24; 28–32; 36–40; 44–48; 52–56; 60–64; 68–72; 76–80; 84–88; 92–96; 100–104; 108–112; 116–120; 124–128; 132–136; 140–144; 148–152; 156–160; 164–168; 172–176; 180–184; 188–192 (stator slots).

Figure 3 depicts a time dependence of the excitation winding current of the turbogenerator rotor in the transition process in a no-load mode.

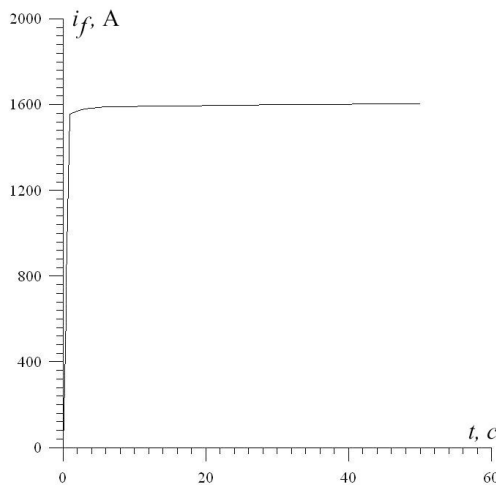


Fig. 3. Calculated values of the current in the turbogenerator excitation winding

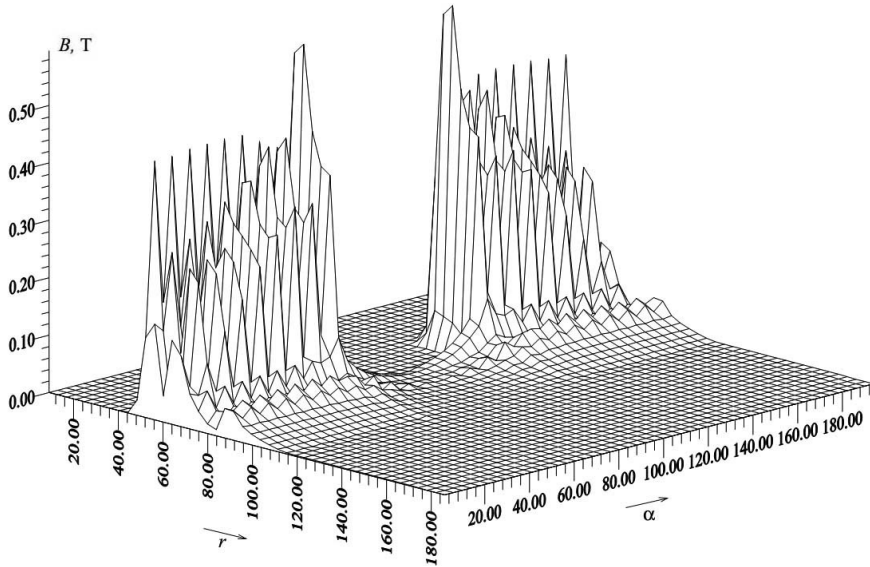


Fig. 4. Spatial distribution of the magnetic induction vector module in the rotor coordinate system on the turbogenerator pole division at $t = 1$ s of the transition process in a no-load mode

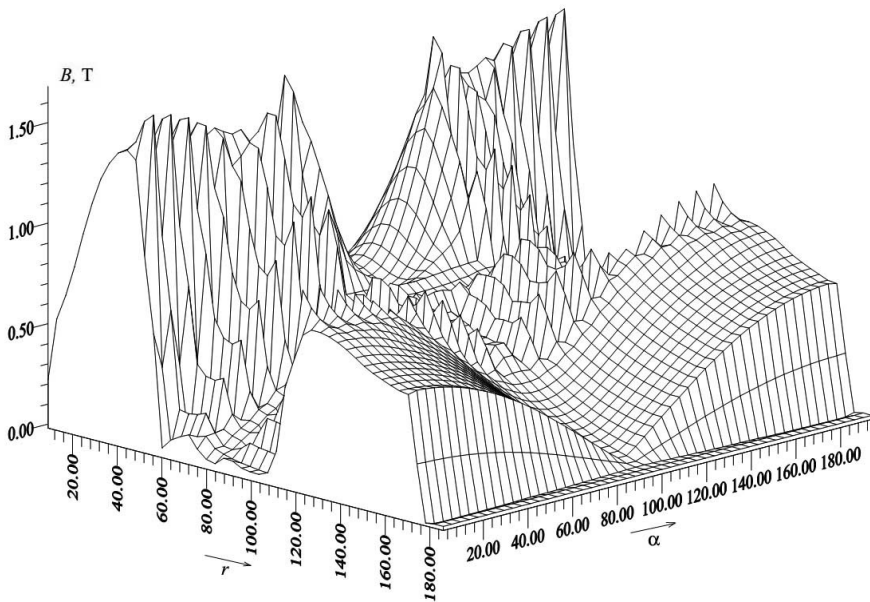


Fig. 5. Spatial distribution of the magnetic induction vector module in the rotor coordinate system on the turbogenerator pole division at $t = 100$ s of the transition process in a no-load mode

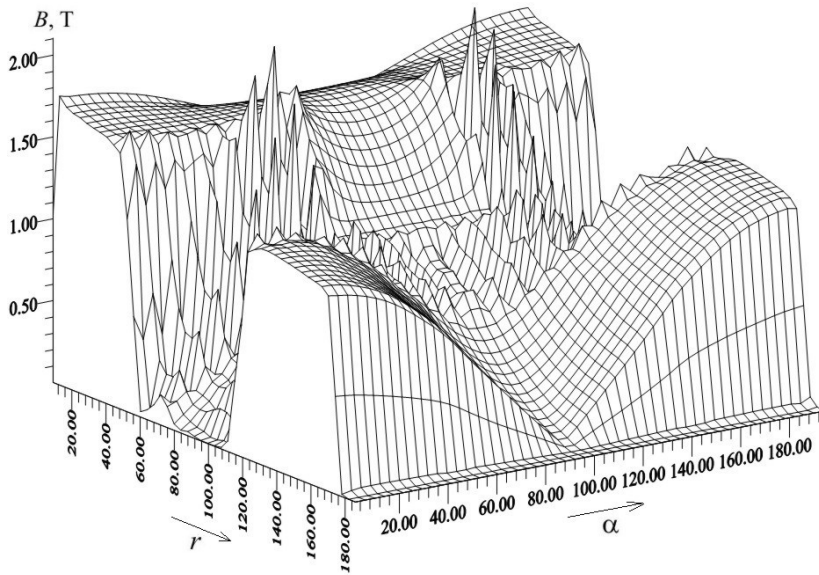


Fig. 6. Spatial distribution of the magnetic induction vector module in the rotor coordinate system on the turbogenerator pole division at $t = 650\text{s}$ of the transition process in a no-load mode

Figure 4 shows spatial distributions of the magnetic induction vector module on the turbogenerator pole division at the point of time $t = 1\text{s}$ of the no-load mode transition process. This was obtained on the basis of the mathematical field model developed in the coordinate system of the moving rotor.

Figure 5 demonstrates a spatial distribution of the magnetic induction vector module on the turbogenerator pole division at the point of time $t = 100\text{s}$ of the no-load mode transition process. This was obtained on the basis of the mathematical field model developed in the moving rotor coordinate system.

Figure 6 illustrates a spatial distribution of the module of a magnetic induction vector on the turbogenerator pole division at the point of time $t = 650\text{s}$ of the no-load transition process. This was obtained on the basis of the mathematical field model developed in the moving rotor coordinate system.

Figure 7 represents a spatial distribution of the vector potential of electromagnetic field in the rotor system of coordinates on the turbogenerator pole division at the point of time $t = 650\text{s}$ of the no-load mode transition process. This was obtained on the basis of the mathematical field model developed in the moving rotor coordinate system.

Figure 8 depicts a spatial distribution of the radial component of the vector of electromagnetic field induction in the rotor system of coordinates on the turbogenerator pole division at the point of time $t = 650\text{s}$ of the no-load mode transition process. This was obtained on the basis of the mathematical field model in the moving rotor coordinate system.

Figure 9 shows a spatial distribution of the tangential component of the vector of electromagnetic field induction in the rotor system of coordinates on the turbogenerator pole division at the point of time $t = 650$ s of the no-load mode transition process. This was obtained on the basis of the mathematical field model in the moving rotor coordinate system.

The character of time variation of the excitation current in the rotor winding in the no-load mode transition process (see Fig. 3), and the spatial-time distributions of the module of a magnetic induction vector (see Figs. 4-6) demonstrate different periods of electromagnetic phenomena duration both in the electric winding of the rotor and in the magnetic system of the turbogenerator.

Having analysed the results of the of electromagnetic quantities distribution in real tooth zones of the rotor and stator calculated using the proposed model and compared them with those obtained employing the mathematical field models of the turbogenerator suggested in previous articles [13] where the tooth structures were substituted for the equivalent media, one may notice a discrepancy in the physical processes in the equivalent zones and the electromagnetic phenomena in the real tooth structures. This again confirms the conclusion that there is the necessity for full consideration of the existing construction of the devices while developing their mathematical field models.

The model developed in the reference systems of the rotor and stator, and the values of the electromagnetic field vector potential obtained on the basis of the model in the rotor coordinate system contributed to the calculation of the no-load mode transition process of the turbogenerator in the physical reference systems. Having the spatial-time values of the electromagnetic field vector

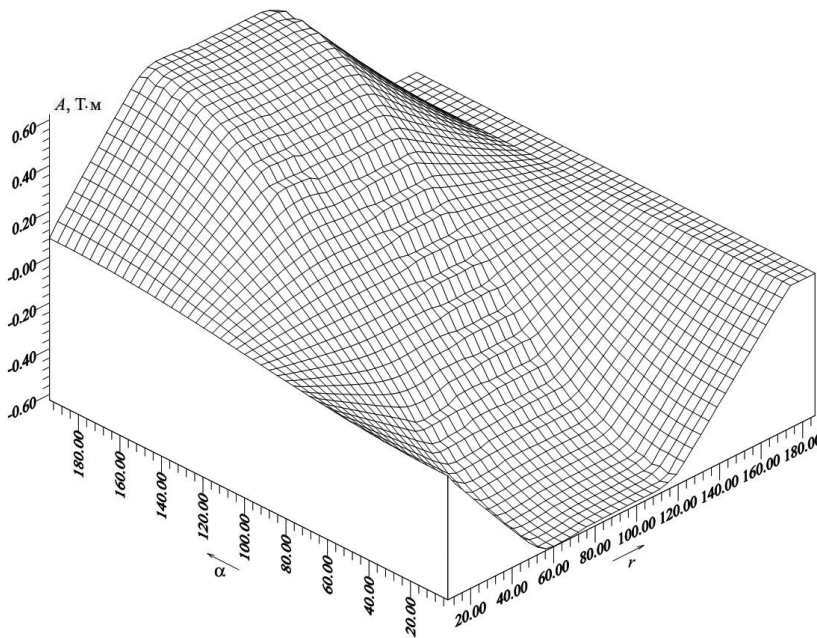


Fig. 7. Spatial distribution of the vector potential of electromagnetic field in the rotor system of coordinates on the turbogenerator pole division at the point of time $t = 650$ s of the no-load mode transition process

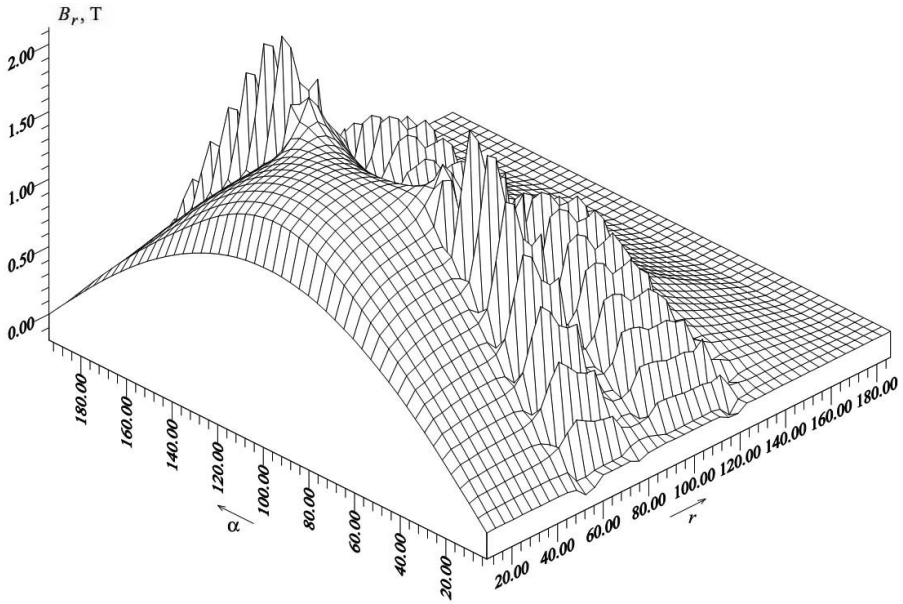


Fig. 8. Spatial distribution of the radial component of the vector of electromagnetic field induction in the rotor system of coordinates of the turbogenerator pole division at the point of time $t = 650$ s of the no-load mode transition process

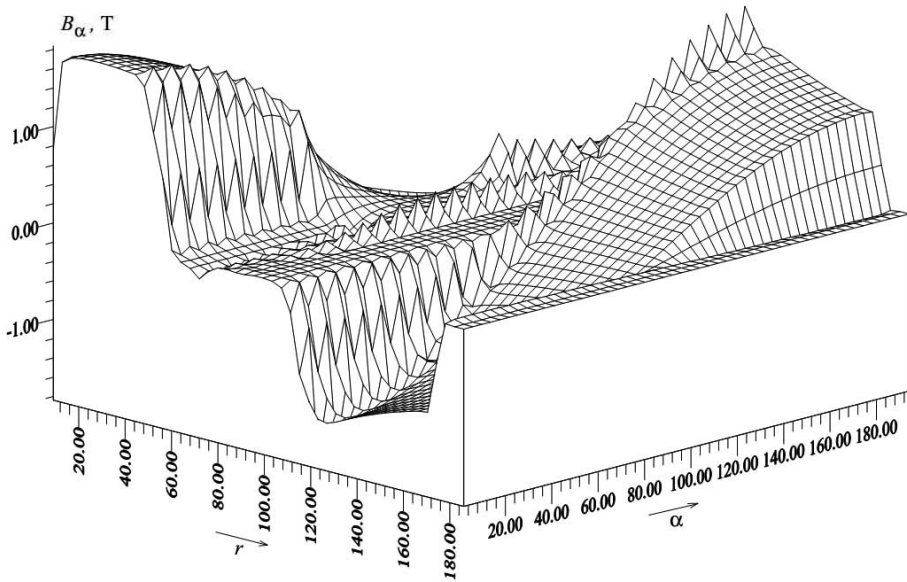


Fig. 9. Spatial distribution of the tangential component of the vector of electromagnetic field induction in the rotor system of coordinates of the turbogenerator pole division at the point of time $t = 650$ s of the no-load mode transition process

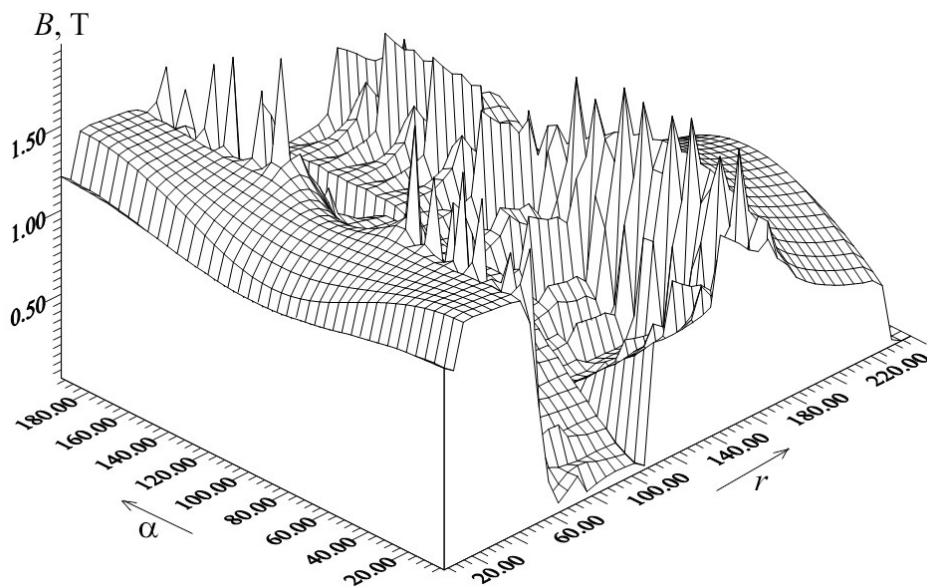


Fig. 10. Spatial distribution of the magnetic induction vector module in the phase coordinate systems of the rotor and stator simultaneously on the turbogenerator pole division at $t = 645.01325$ s of the transition process in a no-load mode

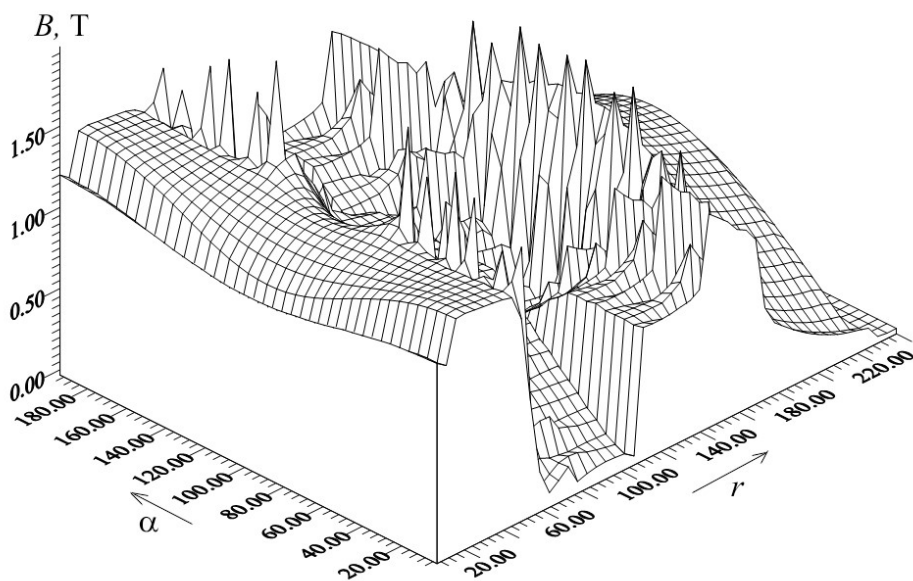


Fig. 11. Spatial distribution of the magnetic induction vector module in the phase coordinate systems of the rotor and stator simultaneously on the turbogenerator pole division at $t = 645.01548$ s of the transition process in a no-load mode

potential in the systems of coordinates of movable and immovable media enabled calculation of the values of the current in the excitation winding and those of the phase voltages of the stator windings in the transition process. Some of the obtained results are given in Figs. 10–12.

Figure 10 presents the spatial distribution of the module of a magnetic induction vector on the pole division of the turbogenerator at the point of time $t = 645.01325$ s of the no-load mode transition process. This was obtained on the basis of the mathematical field model developed in the coordinate systems of the rotor and stator simultaneously.

Figure 11 shows the spatial distribution of the module of a magnetic induction vector on the pole division of the turbogenerator at the point of time $t = 645.01548$ s of the no-load mode transition process. This was obtained on the basis of the mathematical field model developed in the coordinate systems of the rotor and stator simultaneously.

Figure 12 demonstrates the spatial distribution of the module of the magnetic induction vector on the pole division of the turbogenerator with a conductive tooth zone of the stator at the point of time $t = 645.01216$ s of the no-load mode transition process. This was obtained on the basis of the mathematical field model developed in the physical reference systems.

When comparing the results displayed in Figs. 6, 10 and 11, it may be observed that the spatial distribution of the module of the magnetic induction vector in the tooth zone and the rotor body (see Fig. 6) is displaced relative to the angular coordinate. The value of the displacement corresponds to the real relative positions of the rotor and stator at a prescribed fixed moment of time (see Fig. 10 & 11). In actuality, this is clear evidence of compatibility of the results obtained with the help of the models developed in different reference systems.

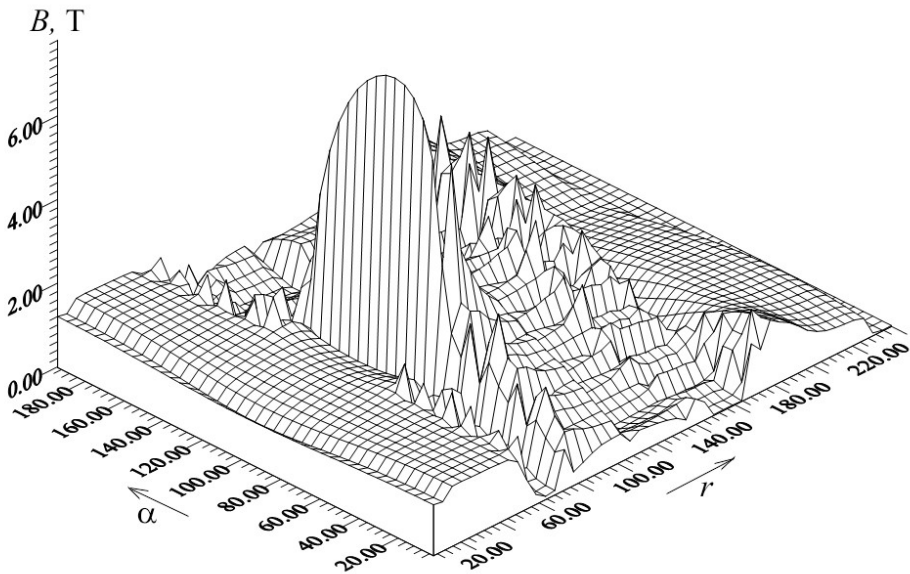


Fig. 12. Spatial distribution of the module of a magnetic induction vector on the pole division of the turbogenerator with a conductive tooth zone of the stator in phase coordinate systems at the point of time $t = 645.01216$ s of the no-load mode transition process

In the considered Figures, we can see that there is a sharp change in spatial distributions in the values of the magnetic induction in the angular points of the slots with copper rotor and stator windings. Such changes are caused by an insufficient number of segments on the grid of the slot and tooth zones of the rotor and stator. This results in insufficient stability with regard to numerical solutions in the angular nodes on the boundary of nonlinear media. However, even a slight increase in the number of nodes is the cause of a significant increase in the basic system of calculation equations of the mathematical field model; furthermore, it affects the accuracy and quality of general calculation results.

Attention should especially be paid to the spatial distribution of the module of the magnetic induction vector depicted in Fig.12. The given distribution was obtained on the basis of the mathematical field model of the turbogenerator developed in phase systems of coordinates implying a reciprocal mechanical displacement of the rotor media relative to that of the stator. In this variant of the device model, we used equation (1), and not equation (4) to calculate electromagnetic processes in electrically conductive slots of the stator tooth zone. The achieved result demonstrates that in the case of calculating an electromagnetic field in the stator slots by means of expression (1), the model reproduces a short circuit mode of the stator winding rather than a no-load mode. A significant rise in the magnetic induction on the surface of the rotor, on the internal surface of the tooth zone of the stator, and in the air gap between the rotor and stator, as well as a fall of magnetic induction in the body of the stator (as the stator becomes demagnetised) can be seen in Fig. 12. These fluctuations are characteristic of the processes in the devices operating in a short-circuit mode of the stator windings and are not unusual for turbogenerators in a no-load mode. Such an effect is a direct result of the mechanical motion of the electrically conductive zone of the rotor slots relative to the magnetised stator body and does not conflict with the physical nature of electromagnetic phenomena. A detailed analysis of this discovered law is presented in work [13].

The calculations of the no-load device mode at equal values of the excitation winding voltage were carried out with the use of the developed mathematical field modes of the TGV-500 turbogenerator with different levels of tooth structure detailing and in different systems of reference. This provided all the developed models with equal by value magnetomotive forces ($w_j i_j$). The results show that for all the models, the character of the change in the current value of the excitation winding in the transition process remains both quantitatively and qualitatively equal. However, there is a considerable difference in the spatial distributions of the electromagnetic field vectors in each group of the developed models.

With the level of detail of the mathematical descriptions of electromagnetic phenomena in the turbogenerator construction, there is a change in the character of reproducing the peculiarities of the electromagnetic processes occurring in separate zones of the device. This is evidence of the direct dependence of the results obtained while calculating the mathematical field models on the extent to which the turbogenerator construction details are taken into consideration in the models. It also serves as evidence of the discrepancy between the electromagnetic phenomena in the equivalent media of the models and the processes in the real tooth structures.

For simplifying the obtained results, the mathematical field models of the turbogenerator with equivalent zones of the rotor and stator are labelled M1. Models with the equivalent

tooth zones of the rotor and the real tooth structure of the stator are labelled M2. Those with equivalent tooth zones of the stator and real tooth structures of the rotor are labelled M3, and the turbogenerator mathematical models that take into consideration the tooth structures of the device are labelled M4 [13].

The amplitude values of the phase voltages in the stator windings of the real TGV-500 turbogenerator in the no-load mode equal 16300 V.

The calculated values of the established amplitude phase voltages of the stator in the no-load mode determined on the basis of the models developed are presented in Table 1.

Table 1. Amplitudes of stator winding phase voltages (B)

Turbogenerator mathematical model	Linear variant of the model	Nonlinear model
M1	22000	20000
M2	21500	18250
M3	16340	16315
M4	16050	15950

Table 2 contains the relative errors of the amplitude values of the stator phase voltages, which were obtained on the basis of the developed models, with regard to the specified voltages of a real turbogenerator in the mode under investigation.

Table 2. Values of relative errors of the models

	Turbogenerator mathematical model							
	Linear variant				Nonlinear variant			
	M1	M2	M3	M4	M1	M2	M3	M4
Relative error (%)	35	31.9	0.1	1.5	23	11.9	0.01	2.1

Table 2 shows that an increase in the degree to which the real construction of the device tooth zones is taken into account (if the current flowing in an excitation winding is of the same value) causes a decrease in the value of electromagnetic quantities in the zones of the device cross section and, unsurprisingly, in the stator winding voltage, with the calculation accuracy being enhanced.

Given the data presented in Table 2, we also can observe that M4 (being the most detailed model of the turbogenerator) demonstrates a 1.5–2.1% error, and this error is greater than that of model M3. To identify the causes of such a discrepancy, it is necessary to analyse the initial parameters used in the computer simulation by involving the models developed.

Calculation results are always directly influenced by all linear and nonlinear coefficients present in the equations of mathematical models, in this particular case, this refers to the coefficients that are involved in the expressions of the main equations of the field and the auxiliary relations. Such parameters as γ , ν , ν_0 characterise the physical properties of the media, their values are precise and well-known – this is why they cannot be the cause of the obtained errors. The parameters w_j , w_i are the constants. The coefficients k_j , k_i and the values Δr_1 , Δr_2 , $\Delta \alpha_1$, $\Delta \alpha_2$ depend only on the number of nodes in discretisation grids. In the eight models presented, these parameters are identical. As the series of calculations showed, an increase in the number of nodes is substantial up to a certain value only, after which, a decrease in the grid step values has an insignificant influence on the results (within a few per cent).

Let us enlarge on other parameters.

The coefficient L_f in the developed models enabled considering the flows of dispersion of the front parts of the rotor winding. This parameter is often used in the mathematical description of electromagnetic processes in electric windings of devices by employing the theory of electromagnetic circuits. The range of possible values of L_f is fairly broad and depends on the mode being modelled. In the considered mode, the flows of dispersion of the excitation winding are low. Moreover, the value of L_f does not affect the established spatial distribution of the electromagnetic field in the zones of the device in no-load mode. The value of L_f was equal for all the models; consequently, this coefficient cannot cause a difference in the computer simulation results.

The assumption on the field's plane-parallelism in the device zones along its axis coordinate is a weakness of 2-D models. As far as we know, electromagnetic processes in the end parts of a turbogenerator differ from those in the cross section of the device in the middle of its length. The peculiarity mentioned can be taken into consideration only by using 3-D models.

In the real turbogenerator, the axial length of the rotor winding is $l_r = 5.44\text{m}$, and that of the stator is $l_s = 6.2\text{m}$. Since in the presented mathematical field models, the electromagnetic processes are considered the same throughout the length of the device, the values of l_r and l_s used for the calculations are relative approximate quantities. In all the cases of computer simulation of transition processes occurring in the turbogenerator in a no-load mode, the values of those parameters were $l_r = l_s = 5.44\text{m}$.

If we accept that the assumed length of the rotor winding is $l_r = 5.44\text{m}$, the assumed value of l_s is then within 5.44–6.2m. The parameter of l_s makes it possible to calibrate the developed 2-D mathematical field models of the turbogenerator in the no-load mode. If $l_s = 5.56\text{m}$, miscalculation of the nonlinear models will consequently be equal to M4 – 0%; M3 – (0.01+2.1)%; M2 – (11.9+2.1)%; M1 – (23+2.1)% at the same (unchanged) values of the spatial distributions of the electromagnetic field.

Certainly, for the models M1, M2, M3 it is also possible to select such nonlinear dependences of the values of γ and ν in continuous and equivalent media such that the miscalculation with respect to integral variables is equal to 0%. However, the character and the parameters of the electromagnetic phenomena reproduced by the developed models in the device zones would not correspond to the processes in the media of the real turbogenerator.

It is necessary to emphasise that in mathematical models of electric devices developed on the basis of the theory of circuits, there exists a much larger number of abstract coefficients – when manipulated, these coefficients make it possible to reach the necessary level of accuracy with the calculation. In the proposed mathematical field models of the turbogenerator and in the majority of the completed mathematical field models of other electric devices, the number of these quantities (abstract coefficients) is minimised.

6. Conclusion

The results obtained from the computer simulation of electromagnetic processes in the turbogenerator in a no-load mode based on the developed models clearly demonstrate both a theoretical and practical necessity for taking into account the systems of coordinates of moving and stationary bodies when developing mathematical field models of electrodynamic devices. It is impossible to either avoid or evade this issue in practical calculations because one of the components of the essence of an electromagnetic phenomenon is the movement of the media that are the sources of an electric or magnetic field and consequently, it is inadmissible to ignore the physical systems of reference of such media when analysing electromagnetic phenomena.

Both the developed mathematical field models of the turbogenerator with real tooth structures and the model considered in previous works [13] have proved that to analyse a no-load mode similar to the other states of electrodynamic devices in which the sources of electromagnetic fields are present in the construction elements in one reference system only, it is optimum to build the mathematical field models in this very same system of coordinates. Such an approach would considerably simplify the model because we would eliminate mechanical movement of the media, and at the same time, achieve a fairly high level of calculation accuracy.

In the case of more comprehensive research into electromagnetic phenomena in electrodynamic devices, it would be necessary to design the mathematical field models in physical systems of reference. The computer simulation of electromagnetic processes in the turbogenerator using models of this class affirms that while developing the models, it is necessary to take into consideration the coordinate systems of both moving and stationary elements of their construction and devise an appropriate way of describing characteristics and properties of the media with respect to the mode under analysis.

To overcome the present weaknesses of the proposed mathematical models of the turbogenerator, it is necessary to take the next logical step, namely to move on to the development of 3-D mathematical field models of an electrodynamic object.

References

- [1] Faiz J., Babaei M., Zadeh J. N., Ebrahimi B. M., Amini S., *Diagnosis and Magnetic Field Analysis of Small Power Saliient-Pole Synchronous Generator with Static Eccentricity Using Time-Stepping Finite-Element Method*, "Electromagnetics", Vol. 31, Issue 3, 2011, 173–191.
- [2] Gholizad H., Fuieru B., Binder A., *Direct Modeling of Motional Eddy Currents in Highly Saturated Solid Conductor by the Magnetic Equivalent Circuit Method*, "IEEE Transactions on Magnetics", Vol. 45, No. 3, 2009, 1016–1019.
- [3] Kazan E., Onat A., *Modeling of Air Core Permanent-Magnet Linear Motors with a Simple-Field Nonlinear Magnetic Analysis*, "IEEE Transactions on Magnetics", Vol. 47, No. 6, 2011, 1753–1762.
- [4] Lubin T., Mezani S., Rezzoug A., *2-D Exact Analytical Model for Surface-Mounted Permanent-Magnet Motors With Semi Closed Slots*, "IEEE Transactions on Magnetics", Vol. 47, No. 2, 2011, 479–492.
- [5] Pfister P.D., Perriard Y., *Slot Less Permanent-Magnet Machines: General Analytical Magnetic Field Calculation*, IEEE Transactions on Magnetics, Vol. 47, No. 6, 2011, 1739–1751.
- [6] Rosseel E., Gersen H., Vandewalle S., *Spectral Stochastic Simulation of a Ferromagnetic Cylinder Rotation at High Speed*, "IEEE Transactions on Magnetics", Vol. 47, No. 5, 2011, 1182–1185.
- [7] Saied S. A., Abbaszadeh K., Fadaie M., *Reduced Order Model of Developed Magnetic Equivalent Circuit in Electrical Machine Modeling*, "IEEE Transactions on Magnetics", Vol. 46, No. 7, 2010, 2649–2655.
- [8] Shekh-Ghalavand B., Vaez-Zadeh S., Isfahani A. H., *An Improved Magnetic Equivalent Circuit Model for Iron-Core Linear Permanent-Magnet Synchronous Motors*, "IEEE Transactions on Magnetics", Vol. 46, No. 1, 2010, 112–120.
- [9] Wang L. L., Shen J. X., Kluk P. C., Fei W. Z., Wang C. F., Hao H., *Development of a Magnetic-Geared Permanent-Magnet Brushless Motor*, "IEEE Transactions on Magnetics", Vol. 45, No. 10, 2009, 4578–4581.
- [10] Wang X., Xie D., *Analysis of Induction Motor Using Field-Circuit Coupled Time-Periodic Finite Element Method Taking Account of Hysteresis*, "IEEE Transactions on Magnetics", Vol. 45, No. 3, 2009, 1740–1743.
- [11] Wu L. J., Zhu Z. Q., Staton D., Popescu M., Hawkins D., *An Improved Subdomain Model for Predicting Magnetic Field of Surface Mounted Permanent Magnet Machines Accounting for Tooth-Tips*, "IEEE Transactions on Magnetics", Vol. 47, No. 6, 2011, 1693–1704.
- [12] Yamazaki K., Suzuki A., Onto M., Takakura T., Nakagawa S., *Equivalent Circuit Modeling of Induction Motors Considering Stray Load Loss and Harmonic Torques Using Finite Element Method*, "IEEE Transactions on Magnetics", Vol. 47, No. 5, 2011, 986–989.
- [13] Kovivchak Ya. V., *Mathematical Modelling of Electromagnetic Processes in Moving Anisotropic Media of Electric Devices*, Monograph, Lviv: Publishing House of Lviv Polytechnic National University, 2015, 352.

Andrzej Bielski (abielski@riad.usk.pk.edu.pl)

Faculty of Environmental Engineering, Cracow University of Technology

DIFFERENT OPTIMISATION TASKS
USED IN WATER QUALITY MANAGEMENT

WYBRANE ZADANIA OPTIMALIZACYJNE
DLA POTRZEB ZARZĄDZANIA JAKOŚCIĄ WÓD

Abstract

This study presents a methodology for the management of surface water quality which guarantees that the concentrations of pollutants remain within acceptable levels. The paper presents different optimisation tasks that can be used for managing the quality of surface waters. The paper presents calculations for a hydrographic network with both point and non-point pollution sources. The calculations include the total BOD and the dissolved oxygen concentrations. The author shows how different types of optimisation tasks affect the chemical profiles of the receiving water.

Keywords: management, water quality, optimisation, pollution transformation models

Streszczenie

Celem pracy jest przedstawienie metody zarządzania jakością wód powierzchniowych umożliwiającą zagwarantowanie stężeń zanieczyszczeń na dopuszczalnym poziomie. Przedstawiono różne typy zadań optymalizacyjnych umożliwiających zarządzanie jakością wód powierzchniowych. Zaprezentowano przykładowe obliczenia dla sieci hydrograficznej z punktowymi i obszarowymi źródłami zanieczyszczeń. W obliczeniach uwzględniono całkowite biochemiczne zapotrzebowanie tlenu i ilość rozpuszczonego w wodzie tlenu. Pokazano, jak różne typy zadań optymalizacyjnych wpływają na profile chemiczne wody w ciekach.

Słowa kluczowe: zarządzanie, jakość wód, optymalizacja, modele przekształcania zanieczyszczeń

1. Introduction

This study presents a methodology for the management of surface water quality which guarantees that the concentrations of pollutants remain within acceptable levels. Frequently, as a result of pollution loads coming from various sources, substances identified as quality indicators exceed their allowable values in the aquatic environment. To reduce their levels of concentration, the decision to reduce their discharge to the environment should be made. Such decisions should be optimised and be a compromise between the amount of pollutants produced by the source and the amount of pollutants that may be released into surface water; thus, it is necessary to perform optimisation calculations to help improve water quality. Different classes of optimisation tasks are solved in optimisation calculations. These can be tasks in which the objective functions are single-criterion [1, 2] and which concern, for example, costs of wastewater treatment or multicriteria [3] and take into account costs of wastewater treatment, frequency or magnitude of violation of the allowable water quality values, water-quality parameters, costs of wastewater treatment and pollutant loads [4]. The optimisation task with a single objective function can be accomplished by finding extreme points of the objective function against properly defined constraints. In the case of multi-objective tasks, the extreme points are sought in a number of functions while satisfying the properly set constraints. There are many methods used for solving optimisation tasks; they have been described in detail in publications such as: [5–9].

Another approach for the management of water quality is fuzzy programming—this is not analysed in this paper [10–12].

Pollutants present in surface waters can originate from single sources, so-called point sources, or they can originate from sources distributed along the watercourse. Since the pollutant discharge along the watercourse may occur by means of the flow of groundwater to the river, runoff, or a series of concentrated point source discharges, in the following paragraphs, sources in the form of multiple discharges distributed along a stream are referred to as non-point sources.

2. Optimal water-quality management

To determine the discharge of pollutants to surface waters by both individual point sources and non-point sources, specific optimisation tasks have to be solved. Each optimisation task consists of the objective function and the constraint functions (constraints) [5], [8]. The objective function represents a certain criterion, due to which, water quality should be improved. Constraints define the so-called area of feasible solutions in a multi-dimensional space – this includes the independent parameters of the objective function. Optimisation is based on the search for extremes (maximum or minimum) of the objective function in the area of feasible solutions. Optimisation tasks may refer to an entire hydrographic network or just a part of it for which the discharge of pollutants into receiving water from point or non-point sources has to be limited (Fig.1).

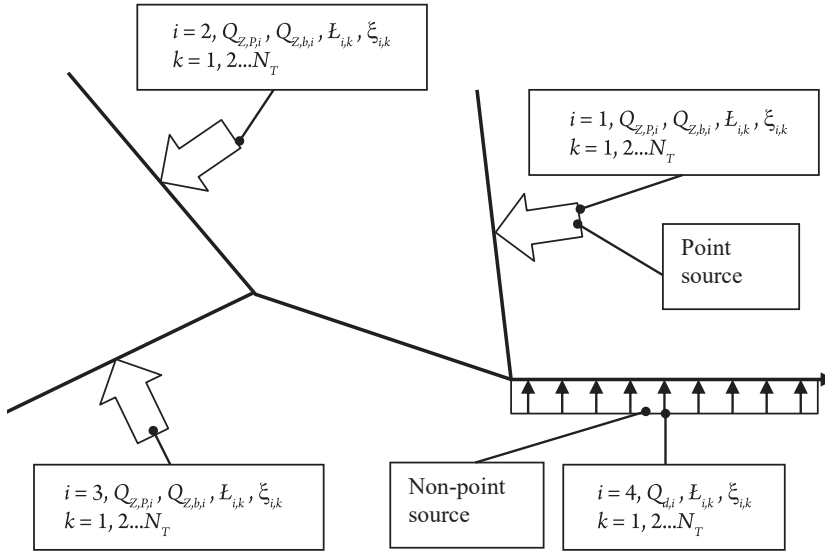


Fig. 1. A hydrographic network with point and non-point pollution sources. (Q_{z,p_i} – capacity of the plant associated with i -th source, Q_{z,b_i} – balance output of i -th source as a flow difference between points upstream and downstream from i -th source, $L_{i,k}$ – k -th pollutant load from i -th source, N_T – number of types of pollutants, $\xi_{i,k}$ – coefficient of level of pollution reduction for i -th source and k -th pollutant).

If water quality is managed, the objective function can be defined in different ways, such as the function of wastewater treatment costs and/or the function of the cost of water treatment, the total pollutant load, the sum of the coefficients of levels of pollution reduction and the sum of the coefficients of concentration variations [1–4, 13–16]. Depending on the objective function its maximum or minimum value is searched within the area of feasible solutions. The constraints are equalities and inequalities developed for concentrations of substances – these are water quality indicators, and decision variables, e.g. coefficients of levels of pollution reduction and efficiency of wastewater treatment. Constraints for concentrations may be associated with one or more water monitoring points i.e. cross sections of the watercourse where measurements are taken. Constraints functions for decision variables define the acceptable range of values for these variables.

3. Optimisation tasks

3.1. The objective function : Total wastewater treatment costs

The optimisation task (OT) with a cost function attempts to minimise this function against some constraints [1, 2, 13, 15, 16]. The task has the following form:

$$ZO : \min K = \sum_{i=1}^{N_z} K_i(\xi_i) \quad (1)$$

$$C_j \begin{cases} \leq \\ \\ \geq \end{cases} C_{\lim,j} \quad j=1,2,\dots,N_p \quad (2)$$

$$\xi_{\min,i} \leq \xi_i \leq \xi_{\max,i} \quad i=1,2,\dots,N_z \quad (3)$$

where:

- i – index for pollution source number
- K – total treatment costs [PLN/year]
- K_i – treatment costs for i -th source [PLN/year]
- N_z – number of pollution sources
- j – index for cross section number
- C – concentration in j -th cross section [g/m^3]
- $C_{\lim,j}$ – limiting concentration in j -th cross section [g/m^3]
- N_p – number of cross sections
- ξ_i – level of pollution reduction from i -th pollution source
- $\xi_{\min,i}$ – minimum level of pollution reduction for i -th pollution source
- $\xi_{\max,i}$ – maximum level of pollution reduction for i -th pollution source

The optimisation task allows performing calculations for practically one type of pollutant. The general formula of the cost function for i -th source (associated with a wastewater treatment plant) can be presented as the following relationship [1]:

$$K_i = aQ_{z,p,i}^b \left(\frac{1-\xi_i}{\xi_i} \right) = aQ_{z,p,i}^b \left(\frac{\eta_i}{1-\eta_i} \right) \quad (4)$$

where:

- a, b – parameters
- $Q_{z,p,i}$ – capacity of the plant associated with i -th pollution source [m^3/s]
- ξ_i – level of pollution reduction for i -th pollution source
- η_i – efficiency of wastewater treatment for i -th source ($\eta_i = 1-\xi_i$)

The costs associated with a reduction of discharged pollutants vary and sometimes can be difficult to determine because they depend on the magnitude of level of pollution reduction ξ_i or treatment efficiency $\eta_i = 1-\xi_i$ and treatment plant capacity $Q_{z,p,i}$. Reduction of pollutant discharges can also be achieved in other ways, by, for example:

- ▶ change of production technology at the plant discharging the pollutants
- ▶ closed water circuits
- ▶ elimination of pollution sources (closure of the industrial plant), etc.

The costs related to pollution discharges also concern non-point sources and the structure of sewage systems; therefore, they are affected by:

- ▶ less intense fertilisation of farmland (compensation for farmers)
- ▶ reduction of breeding and grazing (compensation for farmers)
- ▶ construction or modernisation of sewage network
- ▶ construction of sewage pumping stations, etc.

Therefore, the costs will be generally determined by the method used to reduce pollutant discharge. With regard to the pollution source, it is possible to use one or more methods of pollution control; thus, for some sources, the cost estimations may be very complicated.

Complications arise also in situations in which the cost function for a number of pollution indicators has to be determined. Indeed, if there is a need to determine the treatment cost for two parameters (e.g. BODt and ammonia nitrogen) then a function that combines both BODt removal and nitrification efficiencies has to be defined. In the biological process, the reduction of BODt is accompanied by the growth of microorganisms. These microorganisms assimilate ammonium nitrogen, which is both oxidised and absorbed by nitrifying bacteria in the same biological reactor where oxidation of organic compounds takes place. In addition, the BODt removal efficiency is closely related to the efficiency of nitrification. In this situation, some increases of the BODt removal efficiency increases the nitrification efficiency too, and if so, only one efficiency will impact the costs. There may be, however, a situation when the nitrification efficiency is not satisfactory and has to be increased due to the required ammonia nitrogen removal. In this case, the cost will depend on the nitrification efficiency, which should be recalculated with respect to BODt efficiency; however, in more complex cases, the costs may depend on efficiencies of many other processes (biochemical oxidation, nitrification, denitrification, phosphorus removal). In extreme cases, the higher efficiency of one process (e.g. nitrification) may suppress the other unit processes (e.g. biochemical oxidation of organic compounds due to an ammonia nitrogen shortage for protein synthesis in heterotrophs organisms cells.). Thus, the use of the cost function for a number of indicators is possible, but sometimes it can be very difficult. Furthermore, estimation of operating costs for the treatment plant may be difficult since they depend on unknown parameters, such as treatment efficiency when the technological system has yet to be selected (the system is designed once the required process efficiency is known).

Therefore, the cost function, as the objective function, should preferably be formulated only for the point sources related to a given treatment plant and a single pollution parameter. A number of constraints functions (2) concerning concentrations may be high (many cross section) – such instances make the optimisation calculations much more complicated. Conditions (2) may include some restrictions for oxygen. The oxygen concentration is unlikely to affect the value of the objective function; however, taking its impact into account is possible.

3.2. The objective function: total pollution load

In the optimisation task (OT) where the objective function takes a form of a total pollution load the function is maximised against some constraints. The task may have the following form:

$$ZO: \max L = \sum_{i=1}^{N_z} \xi_i \mathcal{L}_i \quad (5)$$

$$C_j \left\{ \begin{array}{l} \leq \\ \\ \geq \end{array} \right\} = C_{\text{lim},j} \quad j = 1, 2, \dots, N_p \quad (6)$$

$$\xi_{\text{min},i} \leq \xi_i \leq \xi_{\text{max},i} \quad i = 1, 2, \dots, N_z \quad (7)$$

where:

L – total pollution load discharged to receiving water [g/s]
 \mathcal{L}_i – total pollution load discharged to water by i -th source [g/s]
 (other abbreviations are as defined above)

The task (5, 6, 7) allows carrying out a calculation for only one type of pollutant. It is not possible to add different types of loads, e.g. g O₂ BODt / s and g N_{NH₄⁺} / s. Obviously, such a sum would be a value of unspecified unit; however, the coefficients of level of pollution reduction obtained after maximisation of objective function would depend on sensitivity of the sum (5) on changes of pollution loads. To some extent, this problem may be solved through the introduction of weighting factors $w_{i,k}$ for each type of pollutant. The objective function in this case assumes the form:

$$ZO: \max A = \sum_{i=1}^{N_z} \sum_{k=1}^{N_T} w_{i,k} \xi_{i,k} A_{i,k} \quad (8)$$

where:

k – index for type of pollutant
 $w_{i,k}$ – weighting factor for i -th source and k -th pollutant
 N_T – number of pollutant types

(other abbreviations are as defined above)

The determination of the weighting factors can be a very subjective process; consequently, the obtain optimisation result may be not objective. As with the task with the cost function, task (5, 6, 7) can be comprised of a number of constraints (6) for the concentrations calculated in many cross sections. Maximisation of the sum of the coefficients of levels of the pollution reduction tends to lower the treatment efficiency, thereby lowering treatment costs and all other costs incurred while reducing pollution loads discharged to water.

3.3. The objective function: total level of pollution reduction

In the optimisation task (OT) where the objective function takes the form of a sum of levels of pollution reduction, the function is maximised against some constraints. The task may have the following form:

$$ZO: \max \Xi = \sum_{i=1}^{N_Z} \sum_{k=1}^{N_T} \xi_{i,k} \quad (9)$$

$$C_{j,k} \begin{cases} \leq \\ = \\ \geq \end{cases} C_{\lim j,k} \quad j=1,2,\dots,N_p, k=1,2,\dots,N_T \quad (10)$$

$$\xi_{\min,i,k} \leq \xi_{i,k} \leq \xi_{\max,i,k} \quad i=1,2,\dots,N_Z, k=1,2,\dots,N_T \quad (11)$$

where:

- Ξ – sum of coefficients $\xi_{i,k}$
- $\xi_{i,k}$ – coefficient of level of pollution reduction for i -th source and k -th pollutant
- $C_{j,k}$ – concentration of k -th pollutant in j -th check point [g/m^3]
- $C_{\lim,j,k}$ – limiting concentration of k -th pollutant in j -th check point [g/m^3]

(other abbreviations are as defined above)

Task (9, 10, 11) has been developed for many water-quality parameters. This procedure is possible because $\xi_{i,k}$ is dimensionless and can be summed (9). The weighting factors can also be introduced to the objective function if necessary, then:

$$ZO: \max \Xi = \sum_{i=1}^{N_Z} \sum_{k=1}^{N_T} w_{i,k} \xi_{i,k} \quad (12)$$

Just as with the preceding tasks, task (9, 10, 11) may be comprised of many constraints functions (10) for the concentrations calculated in numerous cross sections. Maximisation of the sum of the coefficients of pollution reduction levels tends to lower the treatment efficiency, thereby reducing treatment costs and all other costs incurred while reducing pollutant loads discharged to water.

3.4. The objective function: sum of coefficients of variation (CVs)

In the optimisation task (OT) where the objective function takes the form of a sum of CVs, the function is minimised against some constraints [11]. The task may have the following form:

$$ZO: \min v = \sum_{k=1}^{N_T} v_k \left(\xi_{1,k}, \xi_{2,k}, \dots, \xi_{N_Z,k} \right) \quad (13)$$

$$C_k \left\{ \begin{array}{l} \leq \\ = \\ \geq \end{array} \right\} C_{\lim,k} \quad k = 1, 2, \dots, N_T \quad (14)$$

$$\xi_{\min,i,k} \leq \xi_{i,k} \leq \xi_{\max,i,k} \quad i = 1, 2, \dots, N_Z, \quad k = 1, 2, \dots, N_T \quad (15)$$

where:

- v – sum of coefficients of variation $v_k(\xi_{1,k}, \xi_{2,k}, \dots, \xi_{N_z,k})$
- $v_k(\xi_{1,k}, \xi_{2,k}, \dots, \xi_{N_z,k})$ – CVs for concentrations for k -th pollutant
- C_k – concentration of k -th pollutant in the lowest cross section [g/m³]
- C_k – the limiting concentration of k -th pollutant in the lowest cross section [g/m³]
- $C_{\lim,k}$ – limiting concentration of k -th pollutant in the lowest cross section [g/m³]

(other abbreviations are as defined above)

Coefficients of concentration variation v_k are dimensionless and therefore can be summed. They are determined for the entire hydrographic network. By definition, the CVs are the ratio of the concentration σ_k deviation from the average value and the average \bar{C}_k value:

$$v_k = \frac{\sigma_k}{\bar{C}_k} \quad (16)$$

The average and the standard deviation for the concentration of the k -th pollutant is calculated from the formulas:

$$\bar{C}_k = \frac{1}{\sum_{jj=1}^{N_L} L_{jj}} \sum_{jj=1}^{N_L} \int_0^{L_{jj}} C_{k,jj}(x) dx \quad (17)$$

$$\sigma_k = \sqrt{\frac{1}{\sum_{jj=1}^{N_L} L_{jj}} \sum_{jj=1}^{N_L} \int_0^{L_{jj}} (C_{k,jj}(x) - \bar{C}_k)^2 dx} \quad (18)$$

where:

- jj – index of segment number
- N_L – number of segments of hydrographic network
- L_{jj} – length of segment jj [m]
- $C_{k,jj}(x)$ – concentration function related to a distance coordinate x for k -th pollutant and segment jj [g/m³]

In this optimisation task, it is possible to significantly reduce the number of constraints functions for concentrations; they simply require defining for the most distant (lowest) cross section in the hydrographic network. Such a procedure is acceptable because minimisation of v_k promotes a concentration equalisation in the hydrographic network. Moreover, minimisation of the sum of v makes the average concentrations rather high (is in a denominator); furthermore, the sum of the pollutant loads discharged into water remains high. Accordingly, the coefficients of levels of pollution reduction are as high as possible so the costs of limiting pollution load discharged to water are minimised.

3.5. Modification of the objective function in optimisation tasks

Objective functions in optimisation tasks can be defined in different ways. Also, the optimisation problem itself may be modified in numerous ways. Three different tasks (OT) with a modified objective function are shown below:

OT 1:

$$ZO: \min v^* \quad (19)$$

$$v_k^*(\xi_{1,k}, \xi_{2,k}, \dots, \xi_{N_z,k}) \leq v^* \quad k = 1, 2, \dots, N_T \quad (20)$$

$$v_k^*(\xi_{1,k}, \xi_{2,k}, \dots, \xi_{N_z,k}) = \frac{v_k(\xi_{1,k}, \xi_{2,k}, \dots, \xi_{N_z,k})}{v_k(\xi_{1,k} = 1, \xi_{2,k} = 1, \dots, \xi_{N_z,k} = 1)} \quad k = 1, 2, \dots, N_T \quad (21)$$

$$C_k \begin{cases} \leq \\ = \\ \geq \end{cases} C_{\lim,k} \quad k = 1, 2, \dots, N_T \quad (22)$$

$$\xi_{\min,i,k} \leq \xi_{i,k} \leq \xi_{\max,i,k} \quad i = 1, 2, \dots, N_z, k = 1, 2, \dots, N_T \quad (23)$$

$v_k(\xi_{1,k} = 1, \xi_{2,k} = 1, \dots, \xi_{N_z,k} = 1)$ – CVs for k -th pollutant for an initial state (all coefficients of levels of pollution reduction for the i -th pollution source and the k -th pollutant $\xi_{i,k} = 1$)

(other abbreviations are as defined above)

In task OT 1, coefficients of variation are normalised. A new coefficient v^* was introduced, the values of which vary in the range of $\langle 0, 1 \rangle$. The coefficient v^* is an additional and unknown variable. It was assumed that once the optimisation task was solved, fluctuations of the concentrations of the water quality parameters around their average values were lower than the ones at the initial state i.e. for the primary water quality. Although the CVs are dimensionless and can therefore be compared with each other, their range of variation can be



very large – theoretically, they can be between $< 0, +\infty >$. The CVs for different water quality parameters can take a different order of magnitude. Minimising the sum of these factors does not lower concentration fluctuations of all parameters due to solving the optimisation task. The sum of the coefficients may indeed decrease; however, some of them may take values greater than those observed at the initial state. If one wants to assure lower fluctuations for all parameters, a normalisation is necessary and then all v_k^* stay in the range $< 0, 1 >$; therefore, the coefficients of variation are $v_k(\xi_{1,k}, \xi_{2,k} \dots \xi_{N_z,k}) \leq v_k(\xi_{1,k} = 1, \xi_{2,k} = 1 \dots \xi_{N_z,k} = 1)$.

OT 2:

$$ZO: \min v^* = \sum_{k=1}^{N_T} v_k^*(\xi_{1,k}, \xi_{2,k} \dots \xi_{N_z,k}) \quad (24)$$

$$v_k^*(\xi_{1,k}, \xi_{2,k} \dots \xi_{N_z,k}) = \frac{v_k(\xi_{1,k}, \xi_{2,k} \dots \xi_{N_z,k})}{v_k(\xi_{1,k} = 1, \xi_{2,k} = 1 \dots \xi_{N_z,k} = 1)} \quad k = 1, 2 \dots N_T \quad (25)$$

$$C_k \begin{cases} \leq \\ = \\ \geq \end{cases} C_{\lim,k} \quad k = 1, 2 \dots N_T \quad (26)$$

$$\xi_{\min,i,k} \leq \xi_{i,k} \leq \xi_{\max,i,k} \quad i = 1, 2 \dots N_z, k = 1, 2 \dots N_T \quad (27)$$

(other abbreviations are as defined above)

The task OT 2 is similar to the task OT 1. This task also uses the standardised CVs but their sum is minimised. Despite the significant similarities of the tasks, the results of calculations may vary. It is difficult to predict in advance which solution is better or more satisfying for a decision-maker. The decision will ask for additional assumptions e.g. the real values of level of pollution reduction.

$$OT 3: \quad ZO: \min \alpha \quad (28)$$

$$1 - \xi_{i,k} \leq \alpha \quad i = 1, 2 \dots N_z, k = 1, 2 \dots N_T$$

$$v_k^*(\xi_{1,k}, \xi_{2,k} \dots \xi_{N_z,k}) \leq \alpha \quad k = 1, 2 \dots N_T \quad (29)$$

$$v_k^*(\xi_{1,k}, \xi_{2,k} \dots \xi_{N_z,k}) = \frac{v_k(\xi_{1,k}, \xi_{2,k} \dots \xi_{N_z,k})}{v_k(\xi_{1,k} = 1, \xi_{2,k} = 1 \dots \xi_{N_z,k} = 1)} \quad k = 1, 2 \dots N_T \quad (30)$$

$$C_{j,k} \left\{ \begin{array}{l} \leq \\ = \\ \geq \end{array} \right\} C_{\text{lim},j,k} \quad j=1,2,\dots,N_p, k=1,2,\dots,N_T \quad (31)$$

$$\xi_{\text{min},i,k} \leq \xi_{i,k} \leq \xi_{\text{max},i,k} \quad i=1,2,\dots,N_Z, k=1,2,\dots,N_T \quad (32)$$

Task OT 3 is a combination of task OT 1 and minimisation of the sum of the levels of pollution reduction, as discussed earlier. Task OT 3 has two objectives and employs two different types of functions: standardised coefficients of variation v_k^* ; complements to unity of the levels of pollution reduction $(1-\xi_{i,k})$. Task OT 3 is basically a multi-criteria task since both the standardised CVs and the expression $(1-\xi_{i,k})$ refer to different parameters of water quality. All the functions of this task must be either expressed in the same units or be dimensionless since α is common for all the criteria. Task OT 3, like many others, enables solving multi-criteria problems in the Pareto efficiency [4, 5].

Solving task OT 3 it is essentially striving to achieve the ideal point in which $\alpha = 0$.

The above examples do not exhaust all the possibilities of optimisation tasks used in water– quality management.

4. Analysis of the results from different optimisation tasks

4.1. Model of transport and transformation in the water used in the optimisation tasks

To illustrate the changes of concentrations of some water-quality indicators along the watercourses of the hydrographic network, an advective mass transport model was assumed. The model takes into account the kinetics of changes in the total biochemical oxygen demand and changes in the dissolved oxygen (DO) and has the form [17]:

$$V_x \frac{\partial C_B}{\partial x} = -k_1 C_B \frac{C_T}{K_T + C_T} + R_L (C_{B,d} - C_B) \quad (33)$$

$$V_x \frac{\partial C_T}{\partial x} = k_2 (C_T^* - C_T) - k_1 C_B \frac{C_T}{K_T + C_T} + R_L (C_{T,d} - C_T) \quad (34)$$

where:

C_B – total biochemical oxygen demand (BODt) [g O₂ BODt / m³]

C_T – DO concentration [g O₂ / m³]

C_T^* – saturation concentration of DO [g O₂ / m³]



- $C_{B,d}$ – total biochemical oxygen demand (BODt) for a non-point pollution source [g O₂ BODt / m³]
 $C_{T,d}$ – DO concentration in a saturation state for a non-point pollution source [g O₂ / m³]
 V_x – flow velocity along river (x–axis), (average value for the segment) [m/s]
 k_1 – biochemical oxidation rate constant [1/s]
 k_2 – rate constant of oxygen absorption from the atmosphere [1/s]
 K_T – Michaelis–Menten constant for oxygen [g O₂ / m³]
 R_L – dilution rate constant [1/s]
 x – distance coordinate [m]
 t – time [s]

A non-point pollution source (distributed along the watercourse) results in changes of concentrations in water. A local value of a dilution rate constant is [17]:

$$R_L(x) = \frac{q_L(x)}{A(x)} = \frac{q_L(x)}{Q(x)/V(x)} \quad (35)$$

- $q_L(x)$ – side flow per unit length of watercourse in cross section x [m²/s]
 $A(x)$ – cross section area at a certain water level at cross section x (m²)
 $V(x)$ – average velocity in cross section x [m/s]
 $Q(x)$ – flow in cross section x [m³/s]

With some simplifying assumptions [17], the average value of the dilution rate constant in the whole segment can be calculated with the formula:

$$R_L = \frac{1}{L/V_x} \text{Ln} \left(\frac{Q_0 + q_L \cdot L}{Q_0} \right) = \frac{1}{t_k} \text{Ln} \left(\frac{Q_0 + Q_d}{Q_0} \right) \quad (36)$$

where:

- L – length of segment [m]
 Q_0 – flow at the initial cross section of segment [m³/s]
 q_L – average side flow per unit length of watercourse [m²/s]
 Q_d – total side flow to segment [m³/s]
 t_k – flow time on section of watercourse [s]
 Ln – natural logarithm

(other abbreviations are as defined above)

After the numerical integration of equations (33) and (34) the value of R_L changes along the watercourse, then [17]:

$$R_L(x + \Delta x) = \frac{1}{\Delta x / V_x} \text{Ln} \left(\frac{Q(x) + Q_d \cdot \Delta x / L}{Q(x)} \right) = \frac{1}{\Delta t} \text{Ln} \left(\frac{Q(x) + Q_d \cdot \Delta t / t_k}{Q(x)} \right) \quad (37)$$

Δx – distance step [m]
 Δt – time step [s]
 t_k – flow time along the segment [s]
 $Q(x)$ – flow in the cross section x [m³/s]

(other abbreviations are as defined above)

Assuming that the average side flow per unit length is constant then:

$$Q(x) = Q_0 + q_L \cdot x \quad (38)$$

(other abbreviations are as defined above)

To solve the different optimisation tasks, equations (33) and (34) were integrated numerically by the Newton method with a step $\Delta t = \Delta x/V_x = 0.001d$. The hydrographic network is shown in Figure 2.

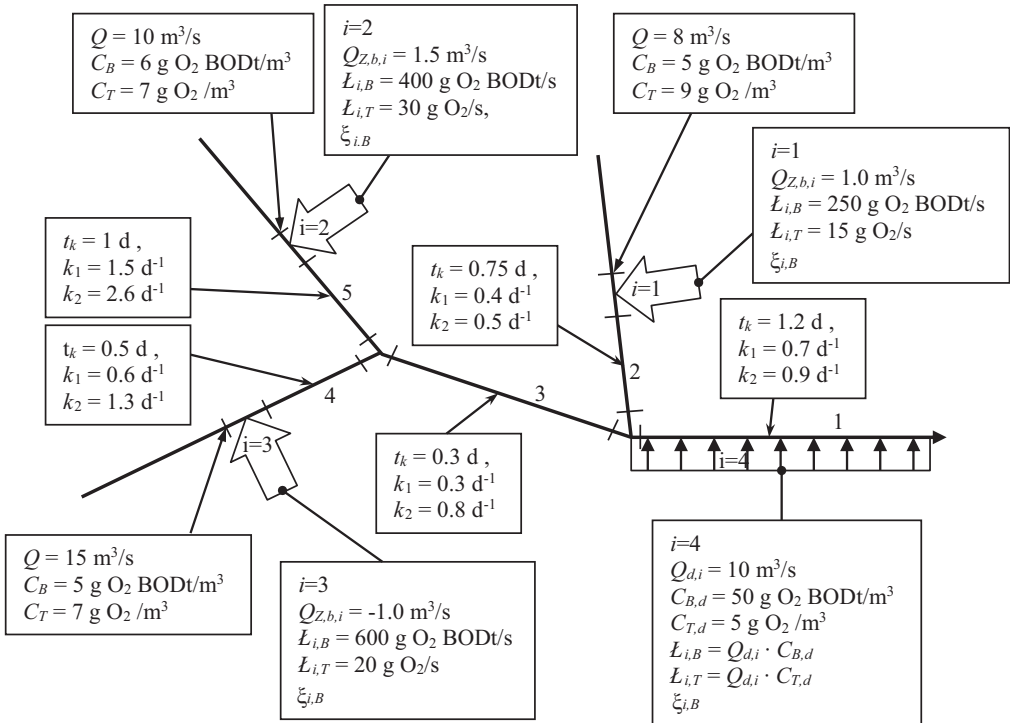


Fig. 2. The hydrographic network with the values describing: point sources; non-point sources; segments of watercourses; cross sections. Parameters for the whole network: the Michaelis-Menten constant for oxygen $K_T = 0.01$ g O₂/m³; DO at the saturation state $C_T^* = 12$ g O₂/m³ (from now on a level of pollution reduction $\xi_{i,B}$ for BODt is marked as ξ_i)

4.2. Solution of optimisation tasks

Optimisation tasks (5–7), (9–11), (13–15), (19–23), (24–27) and (28–32) were solved and coefficients of the pollution reduction levels were identified in order to compare improvements in the water quality. The coefficients of pollution reduction levels $\xi_{i,B}$ for BODt associated with i-th source were sought in all tasks. It was assumed that $\xi_{i,B}$ would change within the range of 0.05 to 0.95. In real life, the range must be separately specified for each source of pollution. Additionally, it was assumed that in the final cross section of segment 1 $C_B \leq 6g O_2 \text{ BODt} / m^3$ while $C_T \geq 7g O_2 / m^3$

In the particular hydrographic network, the limiting concentration values may be different for different water quality parameters and can be defined for multiple cross sections.

The optimisation calculations are summarised in Table 1. The curves showing the total biochemical oxygen demand (C_B) and the DO concentration (C_T) in the five segments of the hydrographic network for six optimisation tasks are shown in Figs. 3 & 4.

Table 1. Solutions to the optimisation tasks: (5–7), (9–11), (13–15), (19–23), (24–27) and (28–32)

Parameter	$\max \sum L$ r. (5... 7)	$\max \sum \xi$ r. (9... 11)	$\min \sum v$ r. (13... 15)	$\min v'$ (ZO 1) r. (19... 23)	$\min \sum v'$ (ZO 2) r. (24... 27)	$\min \alpha$ (ZO 3) r. (28... 32)
$\xi_{1,B} =$	0.0500	0.4709	0.2060	0.4430	0.2878	0.7440
$\xi_{2,B} =$	0.9500	0.9500	0.0500	0.0500	0.0500	0.1944
$\xi_{3,B} =$	0.0500	0.0500	0.2401	0.2456	0.2499	0.2122
$\xi_{4,B} =$	0.8038	0.5193	0.6873	0.5192	0.6175	0.3222
$\sum L = [g O_2 \text{ BODt/s}]$	824.3773	787.4016	559.2351	537.6607	550.6722	552.1565
$v_B =$	0.4515	0.3675	0.1366	0.1319	0.1335	0.1646
$v_T =$	0.1376	0.16104	0.0476	0.0622	0.0523	0.0893
	$\max \sum L = [g O_2 \text{ BODt/s}]$	$\max \sum \xi =$	$\min \sum v =$	$\min v' =$	$\min \sum v' =$	$\min \alpha =$
	824.3773	1.9903	0.1842	0.6454	0.9876	0.8056

Solutions of different optimisation tasks, at the same constrains for the decision variables i.e. level of pollution reduction coefficients and the same constrains for BODt and DO showed that different total BODt loads ($\sum L$) would be introduced to the water in the hydrographic network (Table 1). The largest BODt loads are associated with the tasks (5–7) and (9–11) and are 824.38 and 787.40g O_2 BODt/s, respectively (Table 1). These are tasks that attempt to maximise the pollution loads introduced to the network – they allow to utilise the transformation possibilities of the analysed pollutants through the aquatic environment to the highest extent. The solutions of the remaining four tasks: (13–15); (19–23); (24–27); (28–32) show a slightly lower total load, it ranges from 537.66 to 559.24g O_2 BODt / s (Table 1). Tasks (5–7) and (9–11) however, provide an unfavorable distribution of BODt and DO in the hydrographic network. Significant changes in BODt and DO in the network were observed

(Figs. 3 & 4). Deviations of BODt values comparing to the average value reached, in these tasks, respectively 45.15% and 36.75%, while for DO they were respectively 13.76% and 16.10%, (Table 1). Furthermore, these tasks show little sensitivity to pollutants originating at locations far from the lowest check point, for which the limiting conditions for BODt and DO were formulated. The curves obtained for these two parameters are similar to curves for initial conditions observed in the aquatic environment, and thus in all $\xi_{i,k}=1$ (Figs. 3 & 4, segment 5).

The state of the aquatic environment was not substantially improved in segment 5. The BOD_t values are still high and the oxygen concentrations reach the minimum ($0.65g O_2 / m^3$), which is only slightly higher than the initial value ($0.25g O_2 / m^3$) (Fig. 4, segment 5).

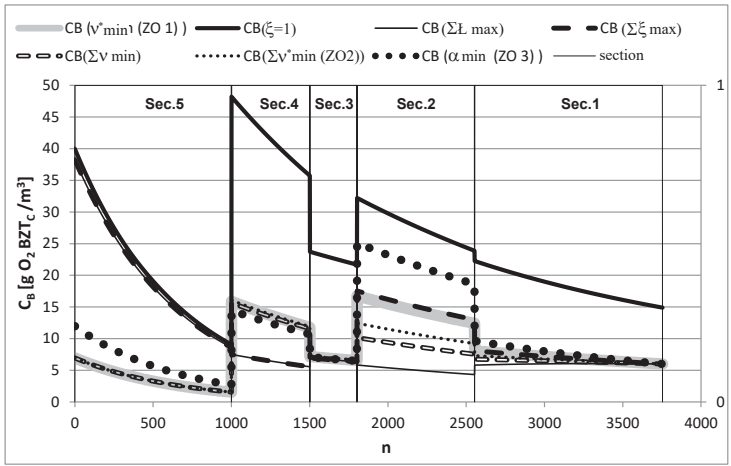


Fig. 3. Changes of BODt along all segments of the hydrographic network resulting from solving different optimisation tasks (Sec. – section of the river)

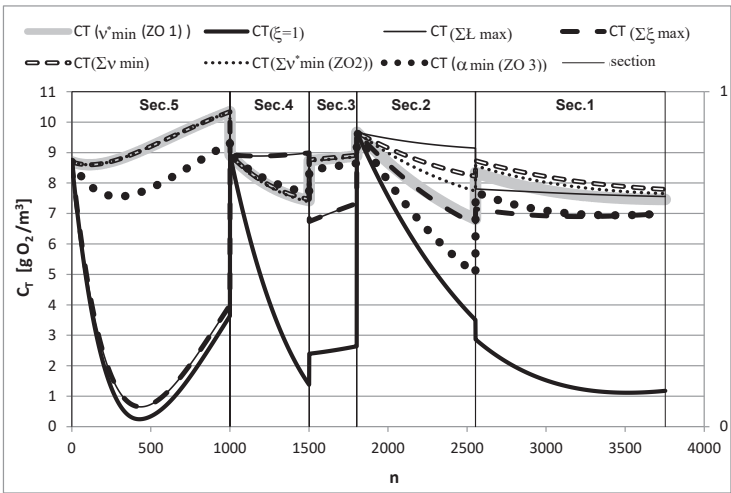


Fig. 4. Changes of the DO concentration along all segments of the hydrographic network resulting from solving various optimisation tasks (Sec. – section of the river)



Of course, this disadvantage can be eliminated by setting additional constraints to the optimisation task. It is a simple operation in the case of a small network. In a large hydrographic network, additional constraints in one segment may result in poor concentration distributions in other segments. In extreme cases, the constraints functions for concentrations have to be set in all segments. Such action makes the optimisation task more complicated and the total pollution load lower than that obtained from the optimisation task with a small number of constraints functions for concentrations. Additional constraints for the concentrations may result in a possible conflict of constraints. It may indeed prove that at the assumed ranges of $\xi_{i,k}$, neither sufficiently low pollutant concentrations nor sufficiently high DO concentrations can be achieved. In such cases, the optimisation task cannot be solved.

Tasks (13–15), (19–23), (24–27) and (28–32) show much better concentration distributions. In these tasks, the coefficient of concentration variation contributes to the equalisation of concentrations in the entire network (Figs 3 & 4). Deviations between BOD_t values and the average value varied in the range of 13.19% to 16.46%, while for oxygen, it changed from 4.76% to 8.93% (Table 1). The values were much lower than those found in tasks (5–7) and (9–11). The additional concentration reducing features should be introduced to OT (13–15), (19–23), (24–27) and (28–32) only in exceptional situations. In these tasks, both low concentrations of dissolved oxygen and minimum of this concentration could be eliminated with no additional constraints functions (Fig. 4). It should be noted that in segment 5, the minimum oxygen concentration remained but increased up to the value from range 7.56–8.60g O_2 / m^3 , depending on the task.

It should also be noted that the minimum shifted in time with respect to the initial minimum – it happens earlier and closer to the upper cross section of segment 5 (Fig. 4). The limiting conditions for oxygen in the upper and lower cross section of segment 5 in tasks (5–7) and (9–11) assure a proper level of the DO but its minimum concentration may be too low for aquatic organisms. Therefore, the minimum oxygen concentration with a variable location along a segment should be sought in optimisation calculations; it should not be lower than the limiting value. Such conditions would solve the problem of extremely low oxygen concentrations; however, looking for location of the minimum oxygen concentration makes the solution more complex. Additionally, it is difficult to determine the actual limiting minimum concentration of DO. In OT, employing the CVs for concentrations, the problem of the acceptable concentration minimum virtually does not exist.

Levelling concentration fluctuations around the average value results in a lower total pollution load discharged.

While solving four tasks (13–15), (19–23), (24–27) and (28–32) similar total pollution loads discharged to the watercourse and similar CVs for water quality parameters are obtained; however, the decision variables $\xi_{i,B}$ may differ significantly (Table 1). The OT (28–32) seems to be the best although it gives the highest CVs and the average total load (Table 1). The distinctive feature of this task is that CVs and levels of pollution reductions are together considered as a separate criterion; such a task becomes more universal and safer due to the maximization of sum of the pollution reduction levels.

The other three tasks do not have such a feature, which may be advantage at the complex hydrographic networks, with large number of different pollution sources and different pollutants. Their results may be beneficial for both the environment users (people, an industrial plant etc.) and the aquatic environment itself.

5. Conclusions

Water quality management requires setting the upper limit load of pollutants that can be discharged into surface water is determined. The acceptable loads may vary slightly depending on the optimisation task. The tasks where the costs of water protection are minimised are difficult to define with respect to one pollutant only. In the case of many pollutants, the cost function can be virtually impossible to determine and be economically unjustified; furthermore, cost assessments may be far from certain. For projects designed to improve water status in the distant future, the solutions may become far from optimal due to changes in economic and administrative conditions within the region.

The study proposes a number of alternative optimisation tasks for water quality management.

The optimisation tasks involving the maximisation of total load discharged into watercourses give different solutions (against the same constraints) to those where total levels of pollution reductions are maximised, though similar total loads will be discharged. Such tasks require that a number of constraints functions are considered – this guarantees a proper level of parameters in the water. For a large number of constraints functions, the optimisation task cannot be solved due to the existing conflict and should not be used for equalisation of concentrations in the hydrographic network. The objective function representing the total pollutant load discharged into water can be formulated for one pollutant only. The objective function which is the sum of levels of pollution reduction (the sum of the dimensionless coefficients) can be used for multiple parameters, simultaneously.

The optimisation tasks that use CVs for concentrations ensure a considerable equalisation of concentration distributions along a given watercourse, at a small number of constraints functions for concentrations. As a result, a lower total pollution load is discharged compared to loads from tasks with the objective functions based on the loads or levels of pollution reduction. The tasks with CVs can carry out optimisation calculations simultaneously on many water quality parameters.

All alternative optimisation tasks described in the paper tend to minimise the prospective costs involving water-quality improvement.

The optimisation tasks together with models of pollutant transformations try to utilise the assimilative capacity of a watercourse in a rational manner. If only mass transport models were considered without transformation, the limiting pollution loads would be smaller while the efficiency of treatment would be higher. Such effects are observed while carrying out calculations for low water temperatures which slow down the transformation of pollutants to a significant degree.

References

- [1] Qin X.S., Huang G.H., Zeng G.M., Chakma A., Huang Y.F., *An interval-parameter fuzzy nonlinear optimization model for stream water quality management under uncertainty*, European Journal of Operational Research 180, 2007, 1331–1357.
- [2] Egemen Aras, Vedat Togan, Mehmet Berkum, *River water quality management model using genetic algorithm*, Environ Fluid Mech 7, 2007, 439–450.
- [3] Huapeng Qin, Jingjing Jiang, Guangtao Fu, Ying Zheng, *Optimal water quality management considering spatial and temporal variations in a tidal river*, Water Resour Manage 27, 2013, 843–858.
- [4] Chih-Sheng Lee, Shui-Ping Chang, *Interactive fuzzy optimization for an economic and environmental balance in a river system*, Water Research 39, 2005, 221–231.
- [5] Coleman Th, Branch M.A., Grace A., *Optimization Toolbox for use with Matlab*, 1999, MathWorks, Inc.
- [6] Białas-Heltowski K., *Determination and evaluation of polyoptim solutions based on the selected technical system*, University of Zielona Góra, 2006.
- [7] Masatoshi Sakawa, Kosuke Kato, *An interactive fuzzy satisficing method for multiobjective nonlinear integer programming problems with block-angular structures through genetic algorithms with decomposition procedures*, Hindawi Publishing Corporation, Advances in Operations Research, 2009, Article ID 372548.
- [8] Horst R., Pardalos Panos M., *Handbook of Global Optimization*, Springer 1995.
- [9] Lee C.S., Wen C.G., *Application of Multiobjective Programming to Water Quality Management in a River Basin*, Journal of Environmental Management 47, 1996, 11–26.
- [10] Sakawa M., *Fuzzy sets and interactive multiobjective optimization*, Plenum Press, New York 1993, 149–173.
- [11] Liu J., Li Y.P., Huang G.H., *Mathematical modeling for water quality management under interval and fuzzy uncertainties*, Hindawi Publishing Corporation, Journal of Applied Mathematics, 2013, Article ID 731568.
- [12] Zhu H., Huang G.H., Guo P., *SIFNP: Simulation – Based interval – Fuzzy nonlinear programming for seasonal planning of stream water quality management*, Water Air Soil Pollution 223, 2013, 2051–2072.
- [13] Biedugnis S., Miłaszewski R., *Optimization methods in water supply and sewerage*, Wydawnictwo Naukowe PWN, Warszawa 1993.
- [14] Bielski A., *Application of optimization methods in the design of protection zones for surface water intakes*, Politechnika Krakowska, Zeszyt Naukowy nr 3, Kraków 1997.
- [15] Biswas A. K., *Models for Water quality management*, McGraw-Hill Inc. 1981.
- [16] Haimes Y. Y., *Hierarchical analyses of water resources systems*, McGraw-Hill Inc. 1977.
- [17] Bielski A., *Equilibrium, kinetics of change and transport of substances in the aquatic environment*, Politechnika Krakowska, Kraków 2010.

Monika Szłapa (monika.szłapa@iigw.pk.edu.pl)

Paweł S. Hachaj

Institute of Water Engineering and Water Management, Faculty of Environmental Engineering, Cracow University of Technology

THE IMPACT OF PROCESSES OF SEDIMENT TRANSPORT ON STORAGE RESERVOIR FUNCTIONS

WPLYW PROCESÓW TRANSPORTU SEDYMENTU NA FUNKCJONOWANIE ZBIORNIKÓW RETENCYJNYCH

Abstract

Maintaining the good condition of water reservoirs is always one of the main tasks of water management. This is especially vital when the reservoir serves as a water supply and/or a facility for recreational activities. Not only what goes into the lake but also everything that is stored within the area needs to be considered. In a case of dam reservoirs, one of the important issues is the transport and storage of sediment. This paper focuses on the sediment which is characteristic of the Dobczyce Reservoir and considers situations which may potentially generate problems from the point of view of maintaining good condition of the water body.

Keywords: sediment transport, retention reservoir, numerical modelling, hydrodynamic, water quality

Streszczenie

Utrzymanie dobrego stanu zbiorników wodnych jest zawsze jednym z najważniejszych zadań gospodarki wodnej. Jest tak zwłaszcza, gdy wśród funkcji rezerwuaru znajduje się zaopatrzenie w wodę i/lub rekreacja. Z jednej strony należy zwrócić uwagę na materię dostarczaną do zbiornika, z drugiej zaś na to, co w tej przestrzeni jest deponowane. Ta praca skupia się na charakterystyce osadów zbiornika Dobczyckiego i rozważeniu scenariuszy mogących generować sytuacje problemowe dla utrzymania dobrego stanu zbiornika wodnego.

Słowa kluczowe: transport sedymentu, zbiornik retencyjny, modelowanie numeryczne, hydrodynamika, jakość wody

1. Introduction

Building storage reservoirs by blocking rivers with dams is a method of water management that civilisations have used since ancient times and is still used today. These reservoirs may have many vital functions that meet a lot of needs. The most common functions nowadays are: water supply; power generation; flood/drought protection; recreation. The local environment changes as a result of human impact; thus, it needs continuous monitoring and treatment. In the case of a reservoir which is a source of potable water, maintaining the water quality is the primary task. There are several important points that need to be considered, these are not limited to the kind of contamination that may enter the water source but also includes everything that is already present within the area. In the case of a dam reservoir, the dam itself is a physical obstacle for flowing water and it makes the river current slow down within the lake. In such a case, some important sediment transport phenomena occur; these are most visible in the backwater areas resulting in sediment accumulation.

With regard to sediment transport phenomena, storage reservoirs are primarily considered to be accumulation zones within the course of rivers (for a good overview, see [14]). In such cases, relatively simple and robust 1D models may be used; however, when it comes to sediment transport within reservoirs, there is a need for multidimensional models. The significant increase of computing power that has occurred in recent years has made such calculations feasible to perform within a reasonable timeframe. A review of models in use can be found in [17], while a comprehensive approach to applying mathematical methods of sediment movement in an around reservoirs is presented in [24].

This paper focuses on the problem of sediment transport and storage in a dam reservoir using the example of the Dobczyce Lake.

2. Research area

The area of research is the Dobczyce reservoir located in the south of Poland in the Lesser Poland voivodeship (Fig. 1). The lake was created by building a dam on the 60th kilometre of the Raba river – the Raba is one of the tributaries of the Vistula. The parameters of the Dobczyce reservoir are presented in Table 1, the shape of the reservoir and its principal objects are shown in Fig. 2.

Knowledge regarding the propagation of pollution in this reservoir is as important as the main function of the Dobczyce Lake itself – the lake is the primary water source for the nearby city of Cracow. Therefore, the issue of water quality is among the top priorities and currently, the whole lake is a protected area. However, allowing limited recreation activities in some parts of the lake has been discussed many times in the past. It is likely that some kind of recreation will be allowed there in the future. Thus, the potential sources of pollution and contamination propagation should be inspected, both for the sake of keeping the recreation areas clean and to minimise the impact of these areas on the water supply system.

Table 1. Reservoir parameters [7, 19, 22]

Capacity [mln m ³]	min	23.23
	max	137.95
Surface [km ²]	min	3.35
	max	10.65
Water discharge [m ³ /s]	min	1.8
	most probable	2.03
	yearly average	10.6
	mean ($Q_{50\%}$)	200
	highest observed	1150
Water surface elevation [m a.s.l.]	min	256.7
	max	272.6
Depth [m]	max	30
Catchment area [km ²]		768

The subject of the propagation of pollutants dissolved in storage reservoir water has been considered in previous articles [8, 9, 10]. In this paper, the authors focus on the sediment-based constituents including those entering the reservoir as well as those already present. Preliminary studies on both the direct and the indirect impact of sediment gathering and transport on the condition of the reservoir are analysed.

The sediment transport phenomena are most intensive and most visible in the backwater region. This is the zone where the borders between the river and the lake are blurry – in fact, they change along with the water surface elevation in the reservoir. In this area, the velocity of water decreases and its potential for carrying rubble and suspended particles also decreases. Conditions like these are favourable for the settling of sedimentary grains on the bed of the lake.

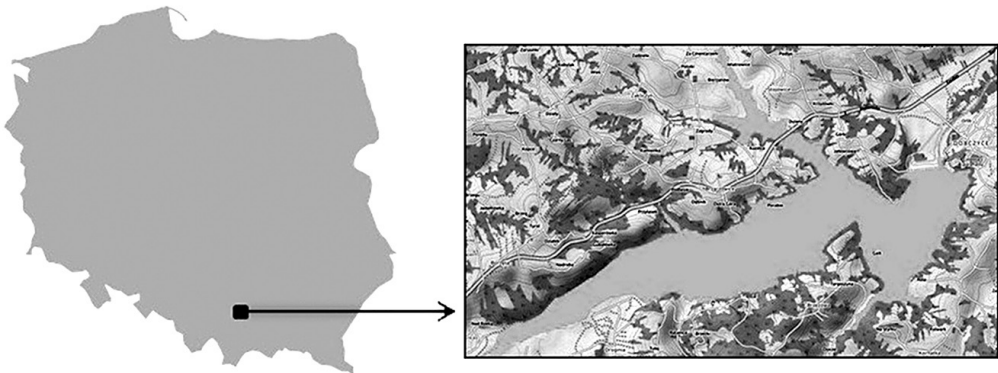


Fig. 1. Geographical location of the Dobczyce Lake and its shape

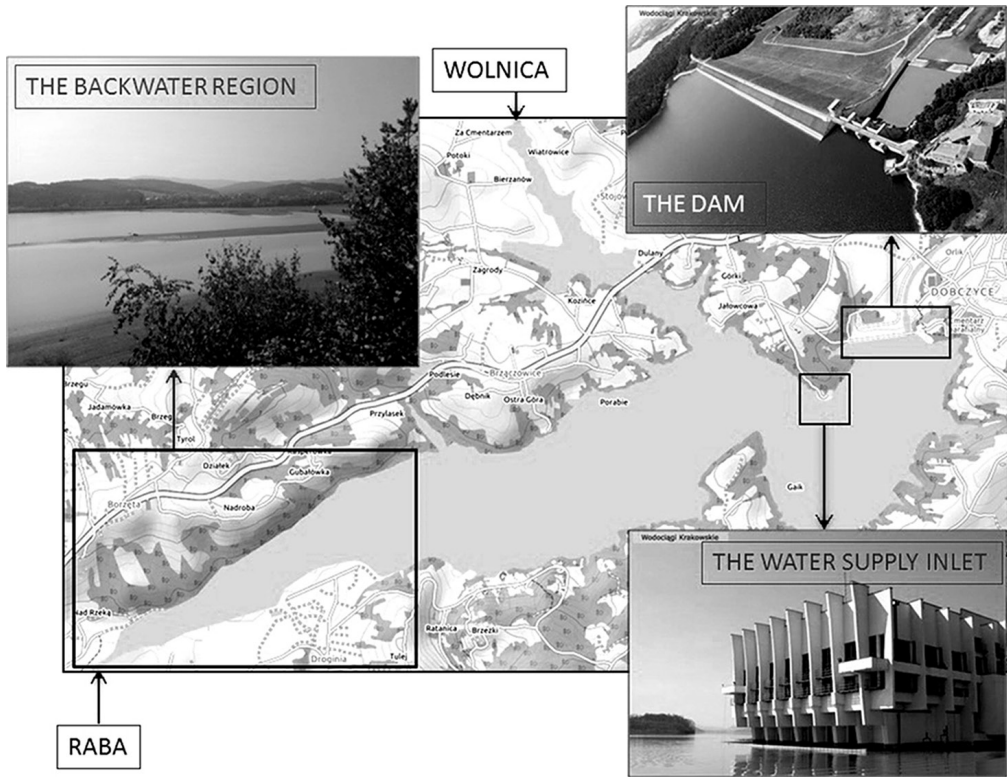


Fig. 2. Location of the strategic areas of the Dobczyce Reservoir (Photos: MPWiK Kraków)

3. Backwater region analysis

In considering the direct impact of the sediment on the lake, it is worth following the transformation of this area through the years. The aerial photos presented below (Figs. 3 & 4) show the seventeen-year history of changes to the backwater environment as sediments have built up to form land.

Figure 3 depicts the process of transformation of the estuary area from 1997 to 2014. The main process that occurs is the deposition of material transported by the river – this is marked by solid black lines on the subsequent photos. The only region where deepening of the water is visible is the area where the river material was artificially removed (region marked with a white line on the 2009 part of Fig. 3). Even following the large flood that occurred in this area in 2010, the effect of the deposition process is more significant than the flushing out of material from this area. The high discharge that time made new river channels cut within the newly created land (in the area marked by the long white ellipse in the photo from 2010). However, the total area of dry regions simultaneously increased after that flood. Some of the previously gathered material was certainly flushed out to deeper areas of the lake that time, although this effect was less significant than the deposition process. The marked area visible in Fig. 4 is about 1.5km long area of land and wetland with plants such as grass, small trees and

shrubs. The annual average amount of sediment gathered in the reservoir is about 185,000 m³ – this value is close to that which was predicted when the reservoir was designed [3].

As shown, most of the sediment is deposited in the shallow western region of the reservoir, close to the inflow of the Raba river. To get more information about the properties of the material deposited in the backwater area, and to obtain some knowledge about the intensity of the process in this region, a local investigation and a laboratory analysis have been conducted. The initial in-situ research included local observations of the actual state of the reservoir with regard to siltation, the choosing of places for sediment sampling and measurements as well as the macroscopic classification of material deposited in the backwater region; preliminary observations indicated the presence of fine and very fine (clay-like) material there.

All local measurements were performed in the moderately dry season when the water surface in the reservoir was low, thus uncovering large areas of the backwater region of the lake. The water surface elevation was approximately 267 m a.s.l. – this is 3 m lower than the average state desired in standard hydrometeorologic conditions. The exposed area provided evidence that intensive deposition processes occurred there. The terrain there is flat – this results in long and broad shallows when the water level is high enough to cover it.

In the backwater area, the samples were collected at five points on both the southern and northern sides of the reservoir (Fig. 5). The sampling collection indicated that the thickness of the sedimentary layer is variable and can even exceed 3m in depth. The accumulated material can be classified as ‘fine fractions’ as defined in [18]. The sediment was well hydrated and organic matter was visibly present.

The laboratory research included sieve and aerometric analyses as well as identification of the contribution of mineral and organic fractions in the samples. Table 2 presents the average grain size at each sampling point at specified depths. The research confirmed the macroscopic in-situ observations – the material deposited within the research area could be classified as clay or clay silt. The proportion of organic matter in the dry mass was between 3.75% and 6.75%. This proportion is relatively small but it should be noted that organic matter contributes much towards the total volume when it is hydrated. It was observed that the average grain size was larger for locations close to the main current (northern bank, locations 4 and 5) than in the regions far from it. There seems to be no direct correlation between the grain size and the depth level of the sample; this appears to be random. The most probable explanation for this is that the pattern of the main current was different for previous episodes of high discharge (i.e. floods) and this resulted in the occasional depositing of coarser sediment in seemingly random places. Traces of stronger current appear at measuring point 1, starting at a depth of 1.4m. For point 2 – further inside the reservoir – bigger grains start to appear at a depth of approximately 1m. It is noteworthy that for the third measuring point (which is placed on the newly created land), the coarse fraction is scarce up to at least 3.2 m (which was the depth limit of the drilling performed there).

There is no evident dependence between the percentage of organic matter and either the position or depth of the sampling with the exception that in the upper layers of sites 4 and 5 (that are presently located in the strong current zone), the organic fraction is lower than anywhere else (3.75%–4.5% versus 5.15%–6.75% elsewhere).



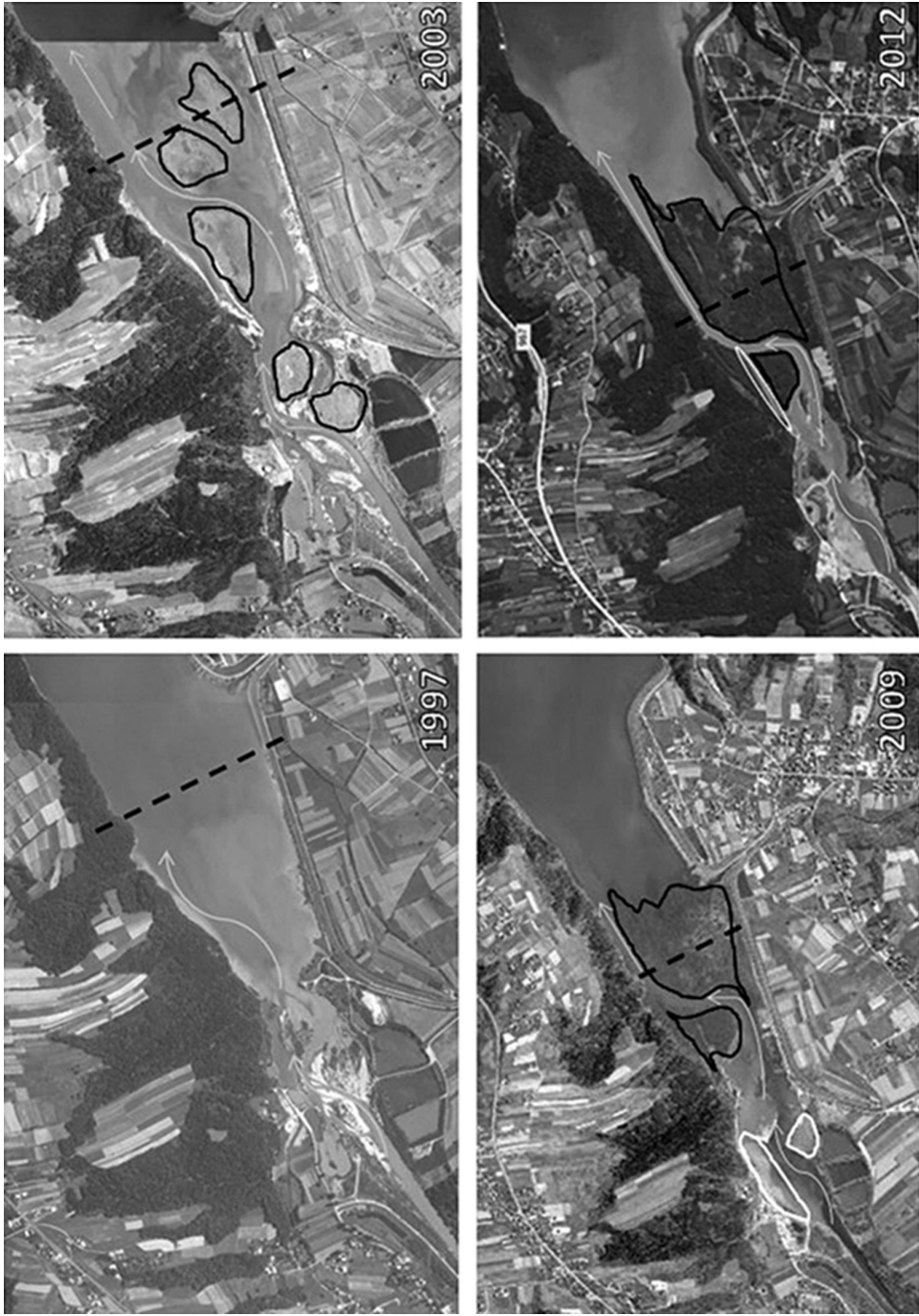


Fig. 3. History of changes in the backwater region of the Dobczyce Reservoir [Photos: Google, 3]



Fig. 4. Siltation of the backwater region 1997–2014



Fig. 5. Locations of sampling

Table 2. Grain diameter at various depths in the sampled locations

h[m]\pt.	Average grain diameter d_{s0} [mm]				
	1	2	3	4	5
0.0-0.2	0.016	0.014	0.016	0.030	0.020
0.2-0.4	0.014	0.019	0.018	0.130	0.034
0.4-0.6	0.018	0.016	–	–	0.050
0.6-0.8	0.026	–	0.014	0.026	–
0.8-1.0	0.014	0.024	–	0.020	0.026
1.0-1.2	0.016	0.034	0.015	–	0.017
1.2-1.4	0.017	0.040	–	0.018	0.019
1.4-1.6	0.036	0.029	0.014	0.024	0.024
min	0.014	0.014	0.014	0.018	0.017
max	0.036	0.040	0.018	0.130	0.050

4. Numerical modelling of the processes of the sediment transport

To model the sediment transport processes, the PTM (Particle Tracking Model) [16] was used. This model was created by US Army Corps of Engineers [23] and is one of the simulation tools integrated within the SMS (surface water modeling solution) [1].

The basic procedure of the PTM is as follows: a region (geometry) with bathymetric and sediment data is defined; flow (and wave data if applicable) are entered into the model; virtual particles are released into the flow. The geometry data is usually prepared within the SMS environment. The flow data may originate from various hydrodynamic models that create their output as planar velocity fields (with the vertical velocity component neglected) – these are then interpolated with the geometry mesh (grid) used by the PTM.

The computations model the behaviour of the particles over the course of time (entrainment, advection, diffusion, settling, deposition, burial, etc.). Two types of calculations are performed at each time-step of PTM. Eulerian (mesh-based) calculations are required to determine the local characteristics of the environment, and Lagrangian (particle-based) calculations are required to determine the behaviour of each tracked particle.

Within the Eulerian calculations, the PTM requires potential transport rates to determine the likelihood of the burial of a sediment particle once deposited, as well as to get a particle from the bed moving again. This can be done using either one of two techniques, namely Soulsby-van Rijn [21] and van Rijn [25]. The authors of the model recommend the first of these as it is significantly faster. The Soulsby-van Rijn total load sediment transport equation [21] is:

$$q_t = A_s \bar{U} \left(\left(\bar{U}^2 + \frac{0.018 \bar{U}_w^2}{C_D} \right)^{1/2} - U_{cr} \right)^{2.4} \quad (1)$$

where:

q_t – total transport rate;

A_s – coefficient dependant on grain size;

\bar{U} – depth averaged planar velocity;

\bar{U}_w – average wave orbital velocity;

C_D – wave drag coefficient;

U_{cr} – critical (threshold) velocity for motion/suspension regimes U.

The coefficient $A_s = A_{sb} + A_{ss}$, with the terms for bedload and suspended load respectively, is given by:

$$A_{sb} = \frac{0.005h \left(\frac{D_{s0}}{h} \right)^{2.4}}{(g(s-1)D_{s0})^{1.2}} \quad (2)$$

$$A_{ss} = \frac{0.0012D_{s0}D_{gr}^{-0.6}}{(g(s-1)D_{s0})^{1.2}} \quad (3)$$

where:

h – local depth;

D_{s0} – median surficial sediment grain size;

D_{gr} – dimensionless grain size;
 g – gravitational acceleration;
 s – relative local density.

The critical velocity is calculated separately for particles considered to be ‘large’ or ‘small’:

$$U_{cr} = \begin{cases} 0.19D_{50}^{0.1} \log_{10} \left(\frac{4h}{D_{90}} \right) & \text{for } D_{50} < 0.5 \text{ mm} \\ 8.5D_{50}^{0.6} \log_{10} \left(\frac{4h}{D_{90}} \right) & \text{for } D_{50} \geq 0.5 \text{ mm} \end{cases} \quad (4)$$

where:

D_{50}, D_{90} – appropriate percentiles of surficial grain size.

It should be noted that the wave term in the sediment transport equation can be omitted for calculations relating to lakes and rivers; thus, it was not used in the modelling described in this article ($\bar{U}_w = 0$); therefore, there was no need to find the value of the wave drag coefficient C_D .

For the Lagrangian calculations regarding positions of the simulated sediment particles, the PTM uses a second-order, predictor-corrector technique to identify particle position at time $t + dt$ for each of the three orthogonal dimensions x , y , and z .

For example, for the dimension x , the first stage of the procedure uses information relating to the particle’s present position and time to predict the particle’s position half a time-step into the future, x' , as:

$$x' = x_n + 0.5(u_A + u_D)dt \quad (5)$$

where:

x' – new position along the x axis;
 x_n – x position in the previous, n -th, step;
 u_A – advection velocity in the x dimension;
 u_D – diffusion velocity in the x dimension.

The second stage of the procedure scheme uses information regarding velocity components from this location over a full time-step:

$$x_{n+1} = x_n + (u'_A + u'_D)dt \quad (6)$$

where the velocity components u_A and u_D are determined in the middle point (calculated above).

For the advection velocity, the local horizontal velocity at the elevation of the particle, u^* , is taken (according to vertical velocity distribution) – this may then be adjusted to account for bed-interaction.



For the diffusion velocity, in the absence of information on eddy diffusivity from the hydrodynamic model, the PTM estimates lateral diffusivity itself. As presented in [7] and as applied in [20] amongst others, the turbulent diffusion coefficient, E_t , is estimated to be:

$$E_t = K_{E_t} hu. \quad (7)$$

where the empirical coefficient K_{E_t} relates the turbulent diffusion to the local shear velocity and water depth. Typically, K_{E_t} ranges from 0.15 to 0.6.

The diffusion velocity for the given time step is then calculated as a part of a random walk process:

$$u_D = \Psi \sqrt{\frac{6E_t}{dt}} \quad (8)$$

where Ψ is a random number between -1 and 1 with the uniform distribution.

5. Application of the model and its results

There have been a number of simulations of water dynamics performed for the Dobczyce Lake so far – these simulations used models contained in the SMS package, e.g. FESWMS [6], RMA [4, 15]. On the basis of findings from previous studies [8, 11, 12, 13, 26] flow simulations were performed using the AdH model [2]. An AdH simulated velocity field was chosen as the hydrodynamic background for the PTM models runs. The simulation process was carried out for the hydrodynamic conditions corresponding to the annual average flow ($Q_{av} = 10.6 \text{ m}^3/\text{s}$) as a representative ‘low discharge’ and a flow with a probability level of 50% ($Q_{50\%} = 200 \text{ m}^3/\text{s}$) as the representative ‘high discharge’. The water surface level was set as the average (269.6 m a.s.l.) and high (272.6 m a.s.l.) values for the reservoir. A ‘stationary state’ assumption (inflow=outflow) was made. Incoming and outgoing discharge were both split – the inflow between the Raba and Wolnica rivers; the outflow between the dam facilities and water supply inlet – this is close to the actual conditions in the reservoir. Wave impact was neglected as it has little impact on the water dynamics. Bank abrasion was also considered as a negligible source of sediment compared to the load carried by the Raba river.

The modelling process included tracking the behaviour of the sediment sample with the parameters of diameter distribution, specific gravity, loading time and location remaining the same for all the simulation runs. The physical parameters were as close as possible to the measured ones. In the simulations, a localised source of particles (‘point source’) was used with a one-metre horizontal and vertical dispersion radius. This was located in the main current of the Raba, where the river enters the lake in order to mimic material entering the backwater region from the main river inflow. The source was active for one hour, the simulation was then carried out over subsequent days; as a result, the evolution of the material carried into the lake over the course of one hour was observed.

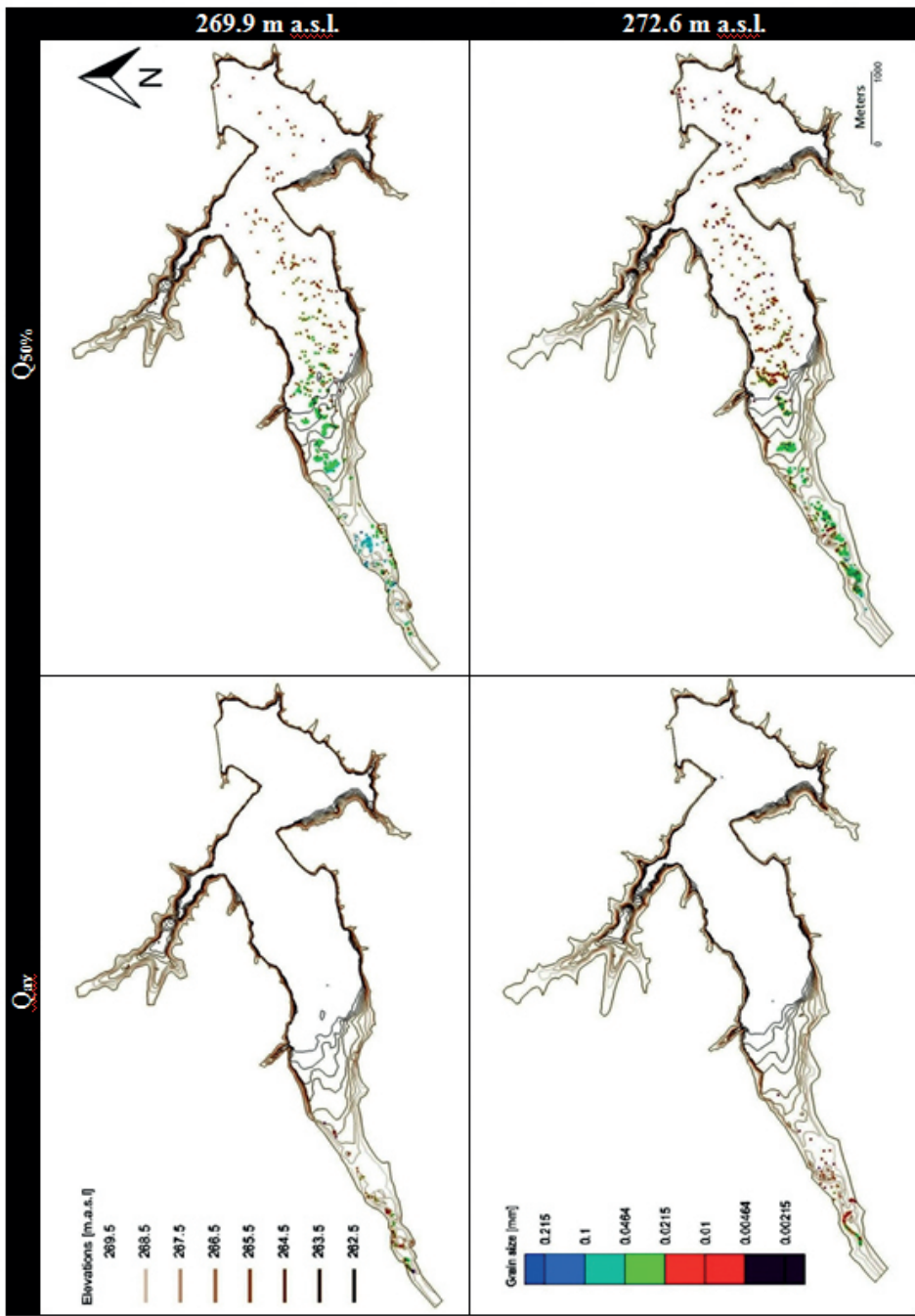


Fig. 6. Deposited particle positions and sizes for various conditions (model results)

The simulations were run until all the modelled sediment particles were either settled on the reservoir bed or moved all the way to the lake outflow; the latter accounted for only a small proportion of the sediment and only applied in the case of high discharge conditions and for the smallest particles ($d < 0.01 \text{ mm}$). Figure 6 depicts the spatial distribution of the particles after seven days of simulation. Coloured dots represent deposited particles of various grain sizes. It can be seen that for Q_{iv} , almost all the grains are deposited in the backwater region of the reservoir. For the higher discharge value, the sediment particles, especially the smaller particles, are often carried further down the reservoir.

When comparing the sub-figures relating to the low discharge and different water surface elevation values, one can see that the shape of the current is slightly different in the westernmost part of the reservoir. Coarse grains settle along the appropriate path. As the current slows down more rapidly for the higher water level, larger particles are deposited closer to each other than for the lower water surface elevation. By contrast, particles that pass that zone and float up to the deeper parts of the reservoir have more space around for further dispersion when the water level is high.

For higher discharge, it is clearly visible that the finer the particle, the further it is carried within the lake. This is true both for both the higher and lower water surface level. However, for the lower level, when the velocities are higher and when the current bends and whirls more, another effect is visible – some medium-sized and fine particles are carried close to the banks and settle there. The larger grains fall closer to the centre of the local bed cross section. This is consistent with the measurements of real grain sizes mentioned in section 3.

6. Summary, conclusions and future possibilities

To sum up the first part of research on the Dobczyce backwater area, it can be said that the process of sediment deposition is intensive there. Sediment material transported by the Raba has been deposited in this area over the years and has continuously changed its character. The whole region has been generally levelled. Shallow bays and banks with a gentle slope appeared on the southern side. The river channel is close to the northern bank. In that kind of area, almost all the discharge is carried out by the main current and the flow of water in the southern backwater part is extremely slow. Therefore, under the considered conditions, only the smallest particles are able to reach the southern part of the backwater region and settle there. Larger and medium-sized particles settle closer to the main current area; this is visible in both actual sediment samples and in numerical simulations. This leads to the conclusion that the grain size of the deposited material decreases along with the distance from the main current.

The next finding from the sediment sampling is that there is no straightforward dependence between the average grain diameter and the depth of sampling in a given location. Fine and coarse layers seem to lay randomly on one another – this may lead to the conclusion that the process of deposition in the backwater region depends upon the hydrodynamic conditions which become volatile over the course of time in each part of the reservoir (especially during episodes of high discharge).

The material deposited in the lake is not only made of mineral grains but also of organic matter which is able to store and transport substances in an aquatic environment; this means that biogenic substances or other constituents that pose threats for the good condition of the water reservoir may also be transported. The presence and possible movement of pollution carried by sediment is one of the research areas targeted towards water engineering and water management; conditions favouring the advection of the deposited material and triggering its polluting potential have to be considered.

The obtained results are consistent; the simulation outcome concurs with the results of the in-situ measurements. This indicates that the PTM model may be used to some future more sophisticated simulations regarding transport phenomena in the Dobczyce reservoir. Further research is planned which is aimed especially towards siltation processes and water quality issues.

References

- [1] AQUAVEO, <http://www.aquaveo.com/adh>, (access: 03.01.2014).
- [2] Berger R.C et al., *Adaptive hydraulics users manual*, AQUAVEO, 2010.
- [3] Bojarski A. et al., *Wykorzystanie zbiornika Dobczyce w perspektywie krótko i długoterminowej*, Kraków, 2012.
- [4] Donnell B., et al., *Users Guide RMA2Version 4.5*, Valhalla, NY 2009.
- [5] Fischer H. B., et al., *Mixing inland and coastal waters*, Academic Press, San Diego, CA 1979, 483.
- [6] Froelich DC., *Two-Dimensional Depth-Averaged Flow and Sediment Transport Model*, Federal highway administration, Mc Lean, Virginia 2003.
- [7] Gałek M., *Analiza czułości modelu FESWMS na zmienność jego parametrów na przykładzie Zbiornika Dobczyckiego*, Politechnika Krakowska, Kraków 2010.
- [8] Gałek M, Hachaj P., *Application of the RMA2/RMA4 Models to Simulate Pollution Transport in a Retention Reservoir*, [in:] *GeoPlanet: Earth and Planetary Science*, Springer-Verlag, ed. P. Rowiński, Berlin Heidelberg 2013, 301–313.
- [9] Hachaj P., *Numerical modelling of pollution transport phenomena in the lake of Dobczyce*, Publications of the Institute of Geophysics. E, Hydrology (formerly Water Resources), Warszawa 2008, 47–54.
- [10] Hachaj P. et al., *Efektywność modeli hydrodynamicznych w ocenie dynamiki zbiornika zaporowego*, Gospodarka Wodna, Warszawa 2014, 286–288.
- [11] Hachaj P., Tutro M., *Flow patterns for drying and wetting of a retention reservoir bed – numerical modeling*, *Infrastructure and Ecology of Rural Areas*, 4/3, 2014, 1407–1419.
- [12] Hachaj, P. *Modelling of a two-dimensional velocity field for the water flow in the lake of Dobczyce.*, [in:] *Publs. Inst. Geophys. Pol. Acad. SC. E-7 (401)*, ed. P. Rowiński, Warszawa 2007.
- [13] Hachaj P., *Modelowanie pola prędkości wody w zbiorniku dobczyckim – budowa siatki obliczeniowej i wstępne wyniki*, *Czasopismo Techniczne*, 1-Ś/2006.
- [14] International Sediment Initiative, *Sediment Issues & Sediment Management in Large River Basins; Interim Case Study Synthesis Report*, UNESCO, Beijing 2011.



- [15] Letter J. et al., *Users Guide for RMA4 Version 4.5*, Valhalla, NY 2008.
- [16] Niel J. et al., *PTM: Particle Tracking Mode*, Coastal and Hydraulics Laboratory, U.S. Army Corps of Engineers, Vicksburg 2006.
- [17] Papanicolaou, A., et al., *Sediment transport modeling review – Current and future developments*, Journal of Hydraulic Engineering, 134(1), 1–14.
- [18] Polski Komitet Normalizacji, *Miar i Jakości*. PN-86/B-02480 Grunty budowlane. Określenia, symbole, podział i opis gruntów, Warszawa 1986.
- [19] RZGW, <http://www.krakow.rzgw.gov.pl> (access: 11.04.2017).
- [20] Shen H. T. et al., *A mathematical model for oil slick transport and mixing in rivers*, Special Report 93-21. U.S. Army Cold Regions Research and Engineering Laboratory, Hanover, NH 1993. 78.
- [21] Soulsby R. L., *Dynamics of marine sands – A manual for practical applications*, Thomas Telford Publications, London 1997, 249.
- [22] Starmacha J., Mazurkiewicz-Boroń G., *Zbiornik Dobczycki; ekologia – eutrofizacja – ochrona*, Zakład Biologii Wód PAN, Kraków 2000.
- [23] U.S. Army Corps of Engineers, <http://www.usace.army.mil/> (access: 07.01.2016).
- [24] USSD Committee on Hydraulics of Dams, *Modeling Sediment Movement in Reservoirs*, USSD, Denver 2015.
- [25] van Rijn L. C., *Principles of sediment transport in rivers, estuaries and coastal seas*, The Aqua Publications, Netherlands 1993.
- [26] Witek K., *Symulacje przepływu wody w zbiorniku retencyjnym Tresna za pomocą modelu numerycznego ADH*, Politechnika Krakowska, Kraków 2013.



Marcin Hojny (mhojny@metal.agh.edu.pl)

Department of Applied Computer Science and Modeling, Faculty of Metals Engineering and Industrial Computer Science, AGH University of Science and Technology

HYBRID MODEL OF LIQUID METAL FLOW AND SOLIDIFICATION

HYBRYDOWY MODEL PRZEPŁYWU CIEKŁEGO METALU I KRZEPNIĘCIA

Abstract

The article presents a hybrid model dedicated to simulations of liquid metal flow and its solidification. The developed solution is a key component of the developed integrated modelling concept, which combines the advantages of physical and computer simulations, while the concept itself is the foundation of a scientific workshop oriented at high-temperature processes (close to solidus lines). Examples of test simulation results are presented, indicating that the adopted model assumptions are correct.

Keywords: smoothed particle hydrodynamics (SPH), finite element method (FEM), extra-high temperatures, solidification, fluid flow

Streszczenie

W artykule przedstawiono hybrydowy model dedykowany symulacjom przepływu ciekłego metalu i krzepnięcia. Opracowane rozwiązanie jest kluczowym elementem rozwijanej koncepcji zintegrowanego modelowania łączącego zalety symulacji fizycznej i komputerowej, zaś sama koncepcja stanowi fundament warsztatu naukowego zorientowanego na procesy wysokotemperaturowe (bliskich linii solidus). Przedstawiono przykładowe wyniki symulacji testowych, wskazujących na poprawność przyjętych założeń modelowych.

Słowa kluczowe: metoda cząstek rozmytych, metoda elementów skończonych, ekstrawysokie temperatury, krzepnięcie, przepływ cieczy

1. Introduction

In particle methods, the fluid flow modelled, or the heat flow, is represented by a set of points. Each point has an assigned set of descriptors. These descriptors determine the point's properties in the model concerned (e.g. mass, temperature, thermal conductivity, location or speed). A point, together with its descriptors is called a particle. A set of particle descriptors depends on the model used in the simulation and may vary from a few to over ten components. Particle methods are a typical example of a problem related to interaction of a finite number of bodies. In the fluid flow, modelling interactions between particles are computed, and the results serve as the basis for tracking particle trajectory and speed. For phenomena coupled with thermal effects also, for instance, temperature changes are tracked. One of particle methods, widely used in issues involving fluid flow or modelling metal solidification processes, is known as the smoothed particle hydrodynamics (SPH). This method is opposite to methods that use meshes for discretisation of the area modelled (e.g. the finite element method). In meshfree methods, neither imposed restrictions nor any constraints limiting degrees of freedom within the system exist. Particles in these methods may move in any directions, and interactions between them only depend on their parameters and distances between them. Forces defined by the adopted interaction model act between each particle couple. Computer simulation is a sequence of iterations, where forces with which particles interact in each iteration are computed for each particle couple. Next, on the basis of the resultant force which has effect on the particle, acceleration of the particle in a given iteration is computed for each particle. This is the basis for computing a correction of particle velocity. The last step is computing a new particle position on the basis of the current position and computed velocity.

In this paper, the results of two test simulations are presented. They were carried out with a new generation 3D solver, included in the original simulation package DEFFEM. The main objective of the numerical tests was to check the implemented thermal solutions in the context of possibilities to simulate heat conduction or solidification processes. The developed model concept constitutes one of the foundations of the scientific workshop developed, focused on high-temperature processes. The term "high-temperature processes" defines two classes of issues, namely the processes of steel deformation modelling within a temperature range near the solidus line, and within a temperature range between the solidus and liquidus temperatures. Thus, the defined research and scientific area force alternative model solutions (which often have a complex nature) to be applied and developed. These solutions are dedicated to the analysis of the following, specific effects: mechanical, thermal, fluid mechanics, density changes or microstructure development. These issues are strictly related to the *soft-reduction* technology, or integrated strip casting and rolling processes. The modelling of effects occurring during both processes requires – due to its complexity – the use of solutions of many differential equations describing individual physical phenomena.

2. Hybrid model of liquid metal flow and solidification

The developed and implemented hybrid model combines advantages of the finite element method (FEM) and the smoothed particle hydrodynamics (SPH). The governing equations of fluids in the SPH method are based on the Navier-Stokes equations in the Lagrangian form. The main equations are given by [1, 2]:

$$\frac{d\rho}{d\tau} = -\rho \nabla \cdot v \quad (1)$$

$$\rho \frac{dv}{d\tau} = -\nabla p + \nabla \cdot \theta + \rho F \quad (2)$$

where: τ is time, v is velocity, p is pressure, F is external force, θ is a second-order tensor containing τ_{ij} stresses. Equation (1) is the continuity equation which describes the evolution of fluid density over time and Eq. (2) is the momentum equation which describes the acceleration of fluid medium. By employing the SPH interpolation given by:

$$\langle \nabla f(r_i) \rangle \approx \sum_{j=1}^N \frac{m_j}{\rho_j} f_j \nabla_i W(r_i - r_j, h) \quad (3)$$

to Eq. (1), the SPH representation of the continuity equation can be written as follows [1, 2]:

$$\frac{d\rho_i}{d\tau} = \sum_{j=1}^N m_j (v_i - v_j) \cdot \nabla_i W_{ij} \quad (4)$$

where: m_j and ρ_j are the mass and the density for particle j , respectively, W is the smoothing kernel, index j corresponds to any neighbouring particle of particle, i , f_j is the value of f for particle, j , N is the total number of particles, h is the smoothing length that defines the radius of influence around the current particle i . The momentum equation can be rewritten in the SPH formalism as:

$$\frac{dv_i}{d\tau} = -\sum_{j=1}^N m_j \left(\frac{p_j}{p_j^2} + \frac{p_i}{p_i^2} + \Pi_{ij} \right) \cdot \nabla_i W_{ij} + F \quad (5)$$

The viscous force used in this implementation is the viscosity term which was introduced by Monaghan [1] and denoted ij Equation (5) shows that the change of the motion of a particle is due to the pressure field, viscosity and body forces acting on the fluid. An equation of state is required to calculate pressure in Eq. (5). The equation of state used in the presented model is a quasi-compressible form which is calculated by means of the density calculation from Eq. (4) and is given by [1]:

$$p = \beta \left[\left(\frac{\rho}{\rho_{ref}} \right)^\gamma - 1 \right] \quad (6)$$

where: ρ_{ref} is the reference density, c is the speed of sound, β is the magnitude of pressure, $\gamma=7$ for liquid steel. The dynamic particle was selected as a definition of boundary conditions [3]. These kinds of particles have the same properties as fluid particles except that the equation of momentum is not solved for them.

Heat exchange between the particles occurs by considering heat conduction. The model of heat conduction is based on the enthalpy method which is given by:

$$\frac{dH}{d\tau} = \frac{1}{\rho} \nabla(\lambda \nabla T) \quad (7)$$

where: H is enthalpy, λ is thermal conductivity, and T is temperature. The SPH formulation of this equation is approximated by [4]:

$$\frac{dH_i}{d\tau} = \sum_j \frac{m_j}{\rho_i \rho_j} \frac{4\lambda_i \lambda_j}{(\lambda_i + \lambda_j)} (T_i - T_j) \frac{(r_i - r_j) \cdot \nabla_i W_{ij}}{(r_i - r_j)^2 + \eta^2} \quad (8)$$

where: η is a small parameter to prevent singularity when $(r_i - r_j)$ goes to zero. If the specific heats to be constant then the relationship between enthalpy and temperature can be written as [4]:

$$H = \begin{cases} c_{p_s} T & , T \leq T_s \\ c_{p_s} T_s + \frac{L}{(T_l - T_s)} (T - T_s) & , T_s < T \leq T_l \\ c_{p_s} T_s + \left(\frac{L}{(T_l - T_s)} \right) (T_l - T_s) + c_{p_l} (T - T_l) & , T > T_l \end{cases} \quad (9)$$

The latent heat L describes the energy released by a particle to change the phase from liquid to solid. T_l and T_s : are the liquidus and solidus temperatures, respectively, and c_{p_l} and c_{p_s} are the specific heats in the liquid and solid phases, respectively. The temperature of each particle is then calculated by means of this relation in the temperature term [4]:

$$T_i = \begin{cases} \frac{H_i}{c_{p_s}} & , H_i \leq H_s = c_{p_s} T_s \\ T_s + \frac{H_i - H_s}{\left(\frac{L}{(T_l - T_s)} \right)} & , H_s < H_i \leq H_l = H_s + \left(\frac{L}{(T_l - T_s)} \right) (T_l - T_s) \\ T_l + \frac{H_i - H_l}{c_{p_l}} & , H_i > H_l \end{cases} \quad (10)$$

Phase transition (from liquid to solid) occurs when particle temperature is below the solidus temperature T_s . In the proposed solution, solid particles are modelled as a viscous pseudo fluid. It means that the behaviour of solid particles is like that of fluid particles but they move under very high viscosity. This approach is used to keep the forces acting on the solid particles and fluid particles.

The solution in the form of temperature field for the FEM model was searched by solving the Fourier equation, which in the general form can be written as follows:

$$\nabla^T (\lambda \nabla T) + \left(Q - c_p \rho \frac{\partial T}{\partial \tau} \right) = 0 \quad (11)$$

where:

- T – absolute temperature,
- λ – thermal conductivity coefficient,
- Q – heat generation rate for volume unit,
- c_p – specific heat,
- ρ – density,
- τ – time.

The model coupling both domains (FE+SPH) is based upon a solution of coupling by fixing particles to the FE nodes.

3. Example results

As a part of test simulations, computing was carried out for two variants, focusing on the assessment of the implemented thermal solutions. C45 grade steel [5] is the material used in both simulations. Thermal properties (temperature dependent) necessary for the simulation were calculated by means of commercial JMatPro software [5]. The liquidus T_l and solidus T_s temperatures of the investigated steel are 1494.79°C and 1412.42°C, respectively. The first

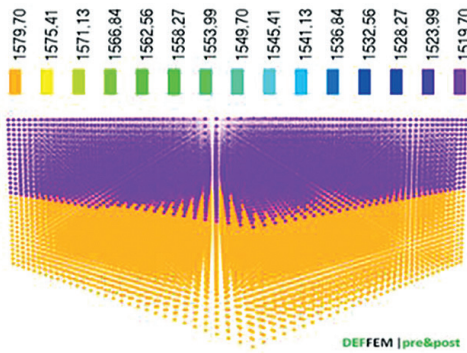


Fig. 1. Initial temperature of the computational domain

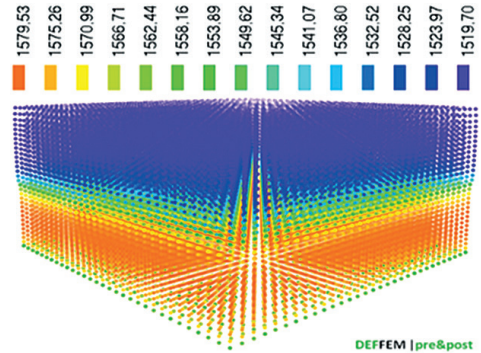


Fig. 2. Example temperature distribution of the computational domain

numerical simulation consisted in a free fall of a box (simulation domain) onto a substrate defined by dynamic particles. The simulation domain in the form of a box was divided in equal proportion into particles, to which temperatures of 1580°C and 1520°C were assigned respectively (Fig.1). The substrate temperature of 20°C was assumed in the computing process. Solutions domain consisting of 29 791 moving particles and 61 206 dynamic particles represents the boundary condition. The initial drop height for free fall case was set to 0.01 m. Other parameters were adopted as follows: initial smoothing length = 0.007 m, speed of sound 30 m/s and simulation time: 7.0 s. In the simulation no heat transfer to the environment was assumed. Figure 2 presents an example of temperature field distributions within the liquid steel volume for the simulation time equal to 1.0046051658706517E-002 second of the free fall. Analysing Fig. 2, one may observe temperature transfer within the liquid steel volume and first contact with heat transfer between the interface substrate–solution domain.

In Fig. 3, an example of temperature distribution of the boundary domain is presented. The maximum temperature reaches about 1292°C and is located in the centre of interface contact liquid steel-substrate, where an intensive area of solidification occurs. In the subsequent stages of the simulation (Fig. 5 and Fig. 6), as a result of contact with the ground, there is a free flow

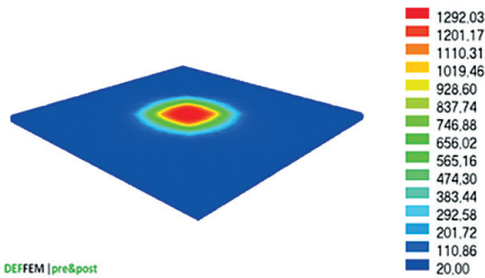


Fig. 3. Example temperature distribution of the boundary domain (time 0.23005412588462504 s.)

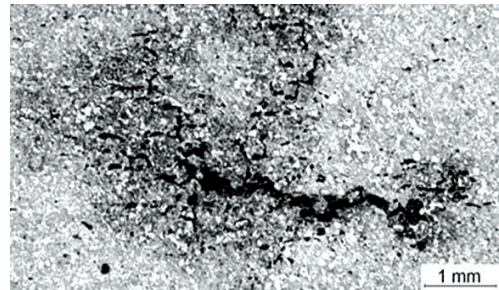


Fig. 4. Macrostructure of the sample centre with visible defects area after re-melting process at 1430°C

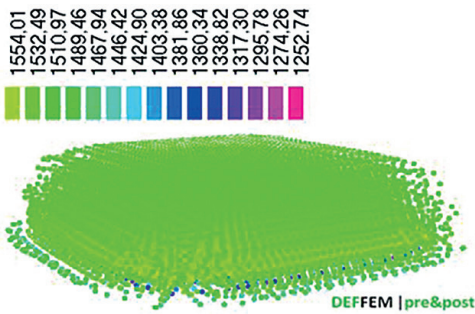


Fig. 5. Example temperature distribution of the computational domain (time 8.0122210271315705E-002 s.)

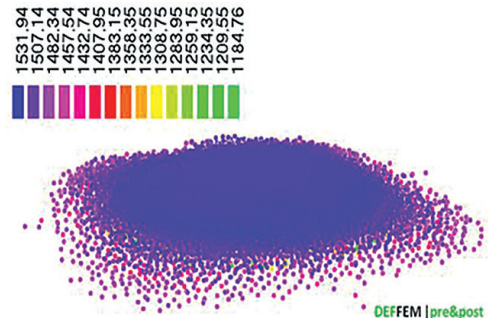


Fig. 6. Example temperature distribution of the computational domain (time 0.18009102709323876 s.)

of liquid steel on the substrate surface together with simultaneous solidification. The second simulation variant was oriented for a test hybrid solver and possibility to predict defects (porous zone formation) within the volume of a sample (see Fig. 4) as well as robustness of the hybrid solver. Cylindrical specimens with a diameter of 10 mm and a length of 125 mm were tested with a Gleeble 3800 thermo-mechanical simulator [5]. A specimen was heated by resistance heating, with an automatically controlled alternating current being introduced into the specimen through cooper grips.

At the first stage of a physical simulation, the specimen was rapidly heated up to 1350°C at the heating rate of 20°C/s. At the second stage, the specimen was slowly heated up to 1430°C at the heating rate of 1°C/s and held at this temperature for 30 seconds. Finally, the specimen was cooled down to nominal temperature and after holding for 10–60 seconds (this time depends on simulation variant) cooled down to ambient temperature. To prevent oxidation, the specimen was located in a vacuum chamber. A transparent quartz sleeve was used to protect against potential leakage of metal during re-melting. In order to find out the temperature distribution along the heating zone within the specimen, temperatures are continuously measured at several locations of the sample. A special thermocouple was mounted in the core of the specimen and gave access to the radial temperature gradient. More details about experimental methodology can be found in [5]. The hybrid methodology of numerical modelling consists of three main steps:

- 1) In the first stage (resistance heating process), a classic DEFFEM thermal solver based on FEM is applied in order to estimate temperature distribution within the volume of a sample [5].
- 2) In the second stage, a hybrid DEFFEM solver is used. The mesh is re-built and particles are generated within the volume of a sample together with their temperature initialization based on interpolation temperature from FEM mesh nodal results (Fig. 7).

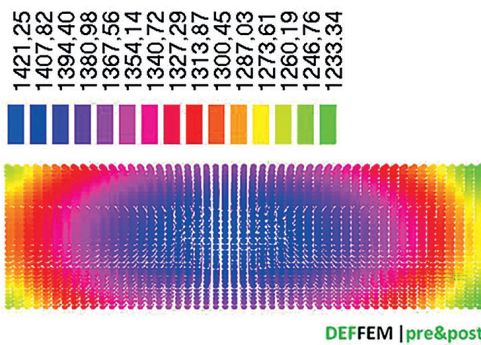


Fig. 7. Particles temperature distribution in the longitudinal-section of a sample after interpolation based on FEM mesh nodal results, just before cooling down to ambient temperature

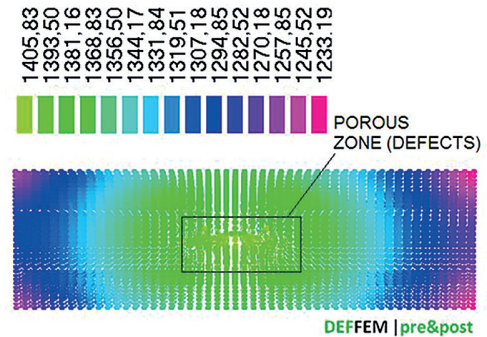


Fig. 8. Particles temperature distribution in the longitudinal-section of a sample after finishing solidification process with visible defects within the sample volume

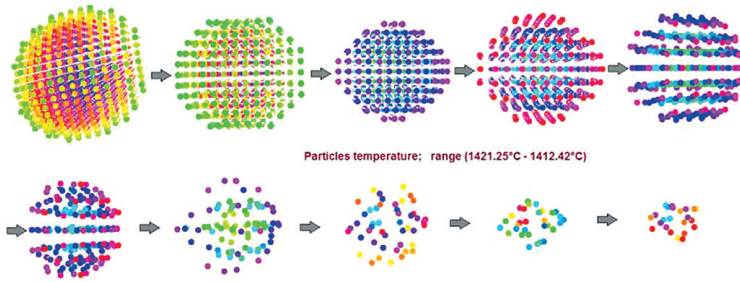


Fig. 9. Mushy zone evaluation over the simulation time of solidification process

- 3) In the third stage, the solidification process is performed (hybrid solver). The particles temperature distribution after finishing solidification is presented in Fig. 8. While analysing Fig. 8, one may observe that particles temperature drops below the solidus temperature and in the centre of the sample a porous zone (defects area) was formed. The obtained results are similar to the results received from physical simulations. The computer simulation results are promising, however the DEFFEM hybrid solver required further validation tests based on physical simulations.

The maximum temperature of 1421.5°C occurs in the sample centre and is higher than the solidus temperature of about 9°C (Fig. 7). The surface temperature on the FEM mesh equals 1380°C [5]. The total gradient temperature in the cross-section of the sample is 41.25°C . Based on such temperatures as references temperatures, a mushy zone can be estimated within the volume of the sample (Fig. 9). The volume of the mushy zone decreases over the simulation time to reach the minimum volume after 0.3 seconds from the start of solidification process.

Such result is nearly half faster than the results obtained from the physical simulation. In Fig. 10, the temperatures changes versus time for the experiment and a hybrid model is presented. According to physical results, the solidification process lasts 0.6 seconds. At the beginning of solidification process within about 0.2 seconds, temperature changes between the

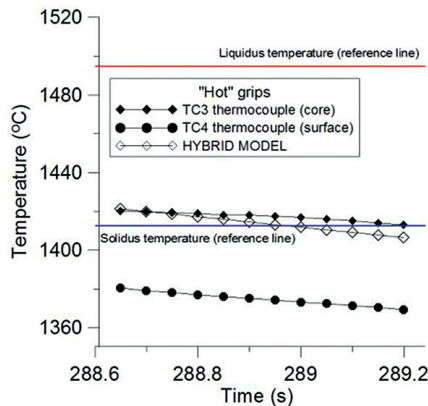


Fig. 10. Temperatures changes versus time (experiment and hybrid model)

computer and physical simulations were very convergent. The whole process of solidification was finished 0.35 seconds faster for the computer simulation than during the physical simulation. The main reason of such differences is the admission of linear approximation of enthalpy changes versus temperatures in the numerical model and adoption of a constant heat exchange coefficient in the FEM model [5]. The impact of these simplifications will be examined in the next research project.

4. Conclusions

The article presents test simulations allowing the quality and capabilities of a hybrid solver as regards fluid flow simulation, taking into account thermal effects or simulation of the solidification processes in terms of their further development by subsequent sub-models to be evaluated. The solidification process was calculated by applying the enthalpy method in the SPH formulation to solve a heat transfer problem. The phase transition model from liquid to solid was treated by considering the effect of latent heat and non-isothermal phase change on the model of heat transfer. The conducted simulations indicate that the assumed and implemented model solutions (shrinkage cavity and heat transfer during liquid mixing) are correct. Further work related to the developed solution will focus on making the liquid-solid phase interaction model more specific by adding a particular force between the mushy and solid phases, or the procedure of particle grouping and taking into account its movement within the mixed zone (liquid and solid phases).

The project has been supported by the Polish National Science Centre, Decision number: DEC-2011/03/D/ST8/04041.

References

- [1] Monaghan J.J., *Smoothed particle hydrodynamics*, Annual Review of astronomy and Astrophysics, Vol. 30, 1992, 543–574.
- [2] Monaghan J.J., *Simulating free surface flows with SPH*, Journal of Computational Physics, Vol. 110, 1994, 399–406.
- [3] Crespo A.A.J.C., et al., *Boundary conditions generated by dynamic particles in sph methods*, Cmc -Tech Science Press, Vol. 5, 2007, 173–184.
- [4] Cleary P.W., Monaghan J.J., *Conduction modelling using smoothed particle hydrodynamics*, J Comput Phys, vol. 148, 1999, 227–264.
- [5] Hojny M., *Modeling of Steel Deformation in the Semi-Solid State*, Advanced Structured Materials, vol. 78, Springer 2017.

Małgorzata Kowalczyk (kowalczyk@mech.pk.edu.pl)
Faculty of Mechanical Engineering, Cracow University of Technology

CUTTING FORCES DURING PRECISE TURNING OF NiTi SHAPE MEMORY ALLOY

POMIAR SIŁ SKRAWANIA PODCZAS TOCZENIA PRECYZYJNEGO STOPU Z PAMIĘCIĄ KSZTAŁTU NiTi

Abstract

The selected indicators of machinability of NiTi based shape memory alloys has been examined. The paper presents research of possibilities of shape memory alloy like low-temperature (austenitic) Ni53Ti47 (Nitinol) with a coated cemented carbide tool, cutting force components (F_f – the feed force, F_p – the passive force, F_c – the main cutting force). In the work, a special attention was paid on the main cutting force components at variable cutting speed (v_c).

Keywords: machinability, Nitinol, precise turning, cutting force

Streszczenie

Wybrane wskaźniki skrawalności stopu z pamięcią kształtu NiTi były przedmiotem badań. W artykule przedstawiono wyniki pomiarów sił skrawania (F_f – siła posuwowa, F_p – siła odporowa, F_c – główna siła skrawania) podczas toczenia precyzyjnego stopu z pamięcią kształtu w fazie nisko temperaturowej (martenzyt) Ni53Ti47 (Nitinol) ostrzem z pokrywanych węglików spiekanych. Szczególną uwagę zwrócono na analizę składowych głównej siły skrawania dla zmiennej prędkości skrawania (v_c).

Słowa kluczowe: skrawalność, Nitinol, toczenie precyzyjne, siły skrawania

1. Introduction

TiNi alloys are an important class of shape memory alloys. In 1938 Greninger and Mooradian¹ first observed the shape memory effect for copper-zinc alloys (Cu-Zn) and copper-tin alloys (Cu-Sn). Yet nearly 30 years elapsed until Buehler and his colleagues applied in 1965 for the first patent for a nickel-titanium alloy, called Nitinol, from the Naval Ordnance Laboratory. They exhibit not only shape memory effect SME, but also unusual pseudoelasticity and high damping capacities. These properties along with their superior ductility, fatigue strength, and corrosion resistance, have resulted in many applications.

The microstructure characteristic of Nitinol is that it is in a martensitic phase at lower temperatures, but in an austenitic phase at elevated temperatures. Nitinol exhibits two unique mechanical behaviors: thermal shape memory and superelasticity, which are illustrated in the stress-strain-temperature diagram in Fig. 1.

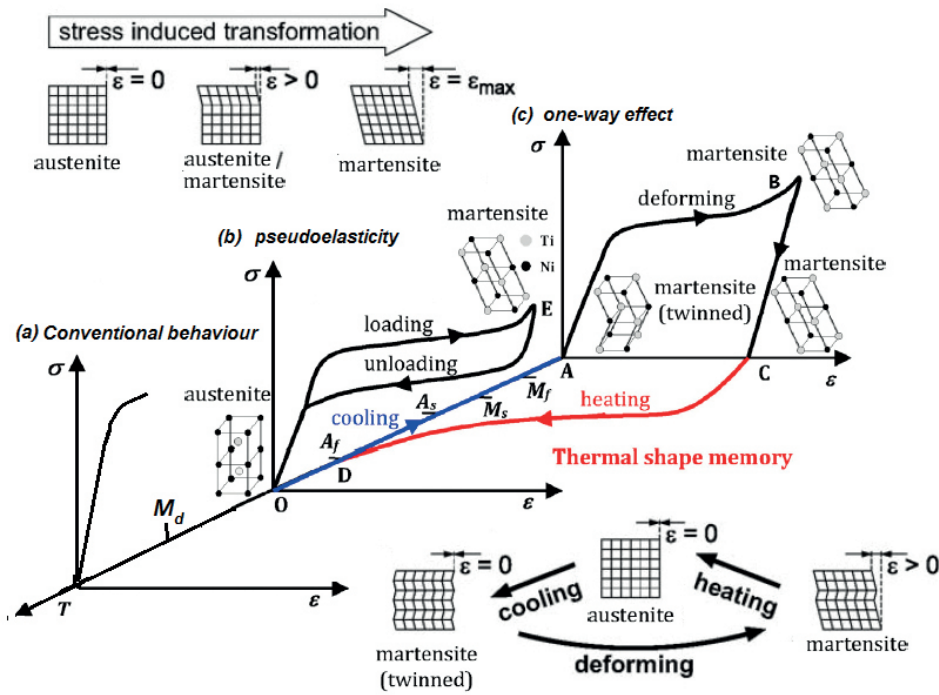


Fig. 1. Temperature dependent stress-strain behaviour of shape memory alloys [4,10]

The phase transformation that occurs in Nitinol is depended on the start and final thermal transitions of the austenite and martensite crystalline phases. It is important to understand the diffusionless transformation to predict the mechanical behavior.

Fig. 1 shows the path that thermal shape memory takes place. Assuming Nitinol initially is in an austenitic state at the origin point O. With no applied stress as Nitinol is cooled

along path $O \rightarrow A$ below martensite finish temperature (M_f), complete transformation from austenite to martensite (twinned) will occur. The material is deformed through reorientation and detwinning of martensite along path $A \rightarrow B$. Then, load releasing on path $B \rightarrow C$ will cause elastic unloading of the reoriented detwinned martensite and the material stays deformed. On heating above the austenite finish temperature (A_f), the material transforms from martensite to austenite and recovers the pseudoplastic deformation “remembering” its former shape. The austenitic Nitinol can be loaded along the path $O \rightarrow E$ (Fig. 1) above the austenite finish temperature (A_f) through a stress-induced transformation to martensitic state. A large elastic strain up to 11% can be achieved. Upon unloading along the path $E \rightarrow O$, the material will transform back to austenitic state and the superelastic deformation will be recovered, demonstrating a hysteresis loop in the stress–strain diagram [5, 13].

Nitinol, a nearly equiatomic nickel–titanium shape memory alloy, has wide applications in cardiovascular stents, microactuators, and high damping devices. Nitinol alloy is used both in the construction of parts of machines and equipment as well as in medicine. In the first case usually are made portions of the temperature of safety valves, fire detectors, the regulatory systems in the radiators of regulating the flow of fuel and air in carburetors, automatic systems, opening windows in greenhouses, etc. And in the second case of nitinol are made specialized implants for surgery, orthopedics and orthodontics for the treatment of spinal diseases, osteoporosis, fractures rib, malocclusion. Another sphere of application is the arms industry, military and aerospace industry, and industrial robots [2, 4].

In the present study, we aim to investigate the machinability of NiTi alloy by using a mechanical cutting test. In the work, a special attention was paid on the main cutting force components and finish surfaces at variable cutting speed (v_c).

2. Current state of knowledge of the machinability of NiTi alloy

Shape memory alloys are metals, which exhibit two very unique properties, pseudoelasticity and the shape memory effect. The nickel–titanium (NiTi) alloys are one type of these materials; they present additional advantages such as biocompatibility, high ductility, and high strength to weight ratio, good fatigue and corrosion resistance, high damping capacities.

Due to their specific properties NiTi alloys are known to be difficult-to-machine materials particularly by using conventional techniques. Their high ductility, high degree of strain hardening, poor thermal conductivity, very low “effective” elastic modulus and unconventional stress–strain behavior are the main properties responsible for their poor machinability.

As shown in Fig. 2a, machining causes severe tool wear. The machinability of NiTi significantly depends on the cutting speed and feed rate, which should be chosen high enough. Poor chip breaking and the formation of burrs is another problem that can be attributed to the high ductility as well as unconventional stress–strain behavior (Fig. 2b). Despite the optimization of machining parameters, tool wear still remains a problem in machining of these alloys [1, 5, 7–9, 12–13].

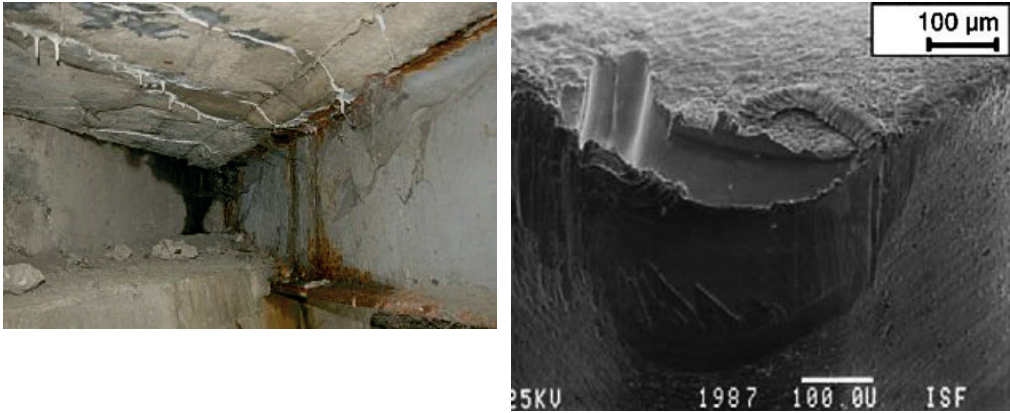


Fig. 2. Major drawbacks in machining NiTi shape memory alloys: a) formation of burrs after turning
b) tool wear [4, 13]

3. Experimental procedure

The nominal composition of the examined binary–NiTi shape memory alloy was slightly off-stoichiometry with 52.85 at.% Ni. The austenite finish temperature was, $A_f = 60^\circ\text{C}$. Table 1 shows the spectroscopy (EDS) analysis. The thermal and mechanical properties of the material are shown in Table 2, respectively.

Table 1. The spectroscopy (EDS) analysis [own results]

$\beta\text{-TiNi}$		
Element	wt.%	at.%
TiK	42.12	47.15
NiK	57.88	52.85
Total	100	100

Table 2. Physical, mechanical and thermal properties of $\text{Ni}_{53}\text{Ti}_{47}$ shape memory alloy [6, 10, 13]

$\beta\text{-TiNi}$	Hardness [HV]	Thermal conductivity [W/m \cdot C]	Density [kg/m 3]	Structure (phase)	The tensile Strength [MPa]	The tensile Strength Yield [MPa]	Modulus of Elasticity [GPa]
	231	18	6500	hi-temp B2	1364	649	28

A positive 7° clearance 80° rhombic insert with hole made from uncoated carbide was used for research. Fig. 3. The CCGT 060202 – AS insert produced by Iscar has an overall dimension (Fig. 4): $d_1 = 2.8$ mm, $d_i = 6.35$ mm, $l = 6.4$ mm, $S = 2.38$ mm. Geometry of tool was following: $\alpha_o = 7^\circ$; $\gamma_o = 26^\circ$; $\kappa_r = 90^\circ$. The literature recommends cutting conditions for NiTi alloy; cutting speed $v_c = 10\text{--}50$ m/min; feed rate $f < 0.2$ mm/rev; depth of cut $a_p < 0.5$ mm.

The test stand for research of the cutting force components during NiTi alloy turning was consisted of the: precise lathe, work piece (hi – temperature – NiTi), tool holder SCACR 1616K – 06S, insert produced by Iscar, Kistler dynamometer. The values of the cutting force components



Fig. 3. The photo of insert type CCGT 060202 – AS [14]

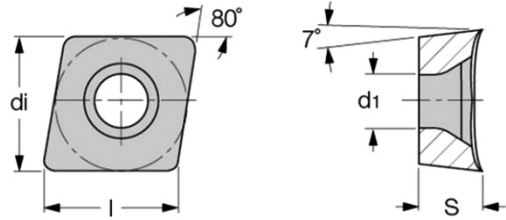


Fig. 4. The overall dimensions of the rhombic insert with hole [14]

(F_f, F_p, F_c) were recorded by the dynamometer and next, the dependence characteristics between the cutting force components and time were in DynoWare software processed.

4. Results of the cutting force components measurements

This work focuses on the study of the cutting force components values (F_f, F_p, F_c) generated during TiNi alloy turning with carbide insert.

The cutting force values for four tests were analyzed and next, the suitable diagrams were generated. The parameters of precise turning process are shown below (Table 3). The diagrams (Fig. 5–6) show dependences between values of the components of cutting forces (F_f, F_p, F_c) and time t [s] for the test1. Also, the tables 4–7 present the average, the lowest and the highest values of cutting forces for selected ranges. The Fig. 6 shows the result of cutting forces components for cutting speed $v_c = 50$ m/min. In the “range 2” it could be see a sudden increase in cutting forces. This is probably due to formation of burrs after turning (Fig. 2a)

Table 3. The parameters of TiNi alloy turning with carbide insert

Number of research	Cutting speed v_c [m/min]	Feed f [mm/rev]	Depth-of-cut a_p
1	20	0.053	0.2
2	30		
3	40		
4	50		

Table 4. The average, the lowest and the highest cutting force values, for selected ranges during precise turning for cutting speed $v_c = 20$ m/min

Force component	Average value	Min value	Max value
F_c [N]	43.07	33.87	47.47
F_f [N]	15.92	11.98	17.45
F_p [N]	9.42	8.3	11.01

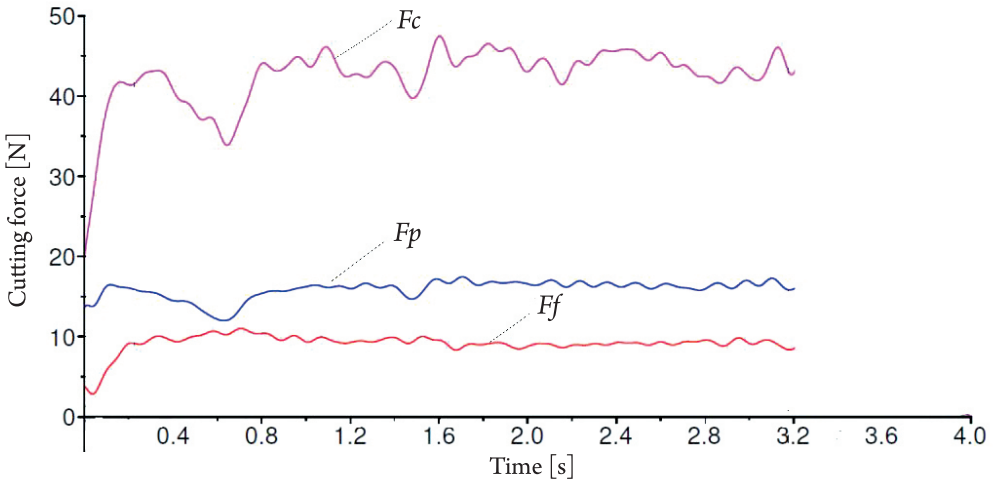


Fig. 5. The result of cutting forces components for cutting speed $v_c = 20$ m/min

Table 5. The average, the lowest and the highest cutting force values, for selected ranges during precise turning for cutting speed $v_c = 30$ m/min

Force component	Average value	Min value	Max value
F_c [N]	38.53	26.72	46.8
F_f [N]	14.92	11.92	16.65
F_p [N]	5.81	4.83	6.87

Table 6. The average, the lowest and the highest cutting force values, for selected ranges during precise turning for cutting speed $v_c = 40$ m/min

Force component	Average value	Min value	Max value
F_c [N]	13.1	11.08	15.54
F_f [N]	19.5	17.77	20.78
F_p [N]	8.87	7.48	10.24

Table 7. The average, the lowest and the highest cutting force values, for selected ranges during precise turning for cutting speed $v_c = 50$ m/min

Force component	Average value	Min value	Max value
F_c [N]	32.42	30.49	33.69
F_f [N]	9.02	7.75	10.6
F_p [N]	9.69	8.53	10.97

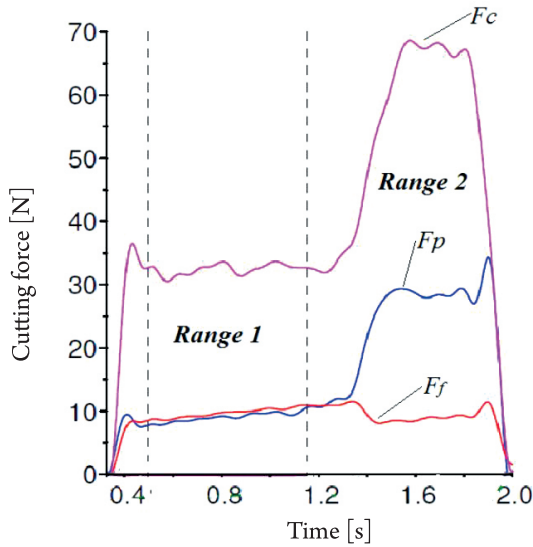


Fig. 6. The result of cutting forces components for cutting speed $v_c = 50$ m/min

In a next step the influence of the cutting speed on the machinability of NiTi was examined by turning experiments. Figures 7–9 shows the cutting force (F_f – the feed force, F_p – the passive force, F_c – the main cutting force) with respect to its dependence on the cutting speed. The machinability can be classified by three different ranges. At low cutting speeds ($v_c = 20$ m/min) the main cutting force is the highest ($F_c = 44$ N – first range – Fig. 7). With increasing cutting speeds the main cutting force decrease. For cutting speeds ($v_c = 40$ m/min) the feed force is the highest ($F_f = 20$ N – range 2 – Fig. 8). With increasing cutting speeds the feed force increase also. At high cutting speeds ($v_c = 50$ m/min) the passive force is the highest ($F_p = 10$ N range 3 – Fig. 9).

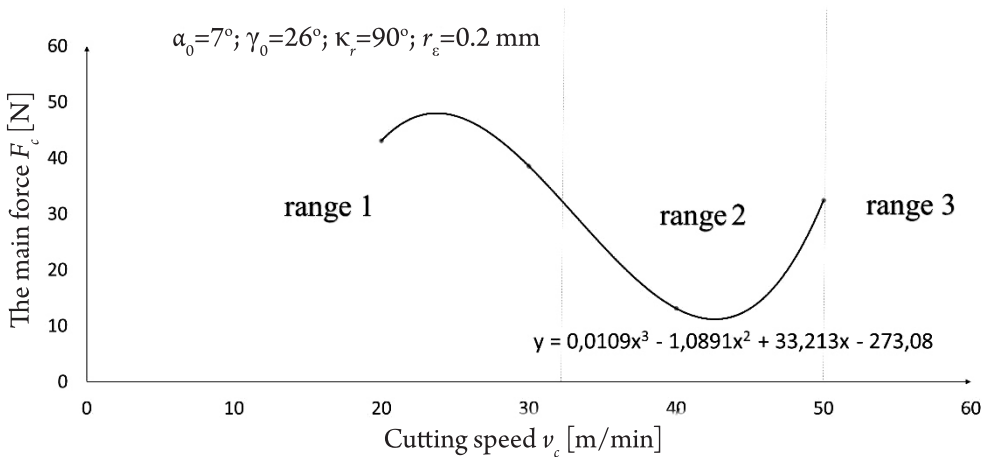


Fig. 7. The main cutting force with respect to its dependence on cutting speed (workpiece: NiTi; cutting parameters: $f = 0.053$ mm/rev; $a_p = 0.2$ mm; cutting tool: CCGT 060202 – AS)

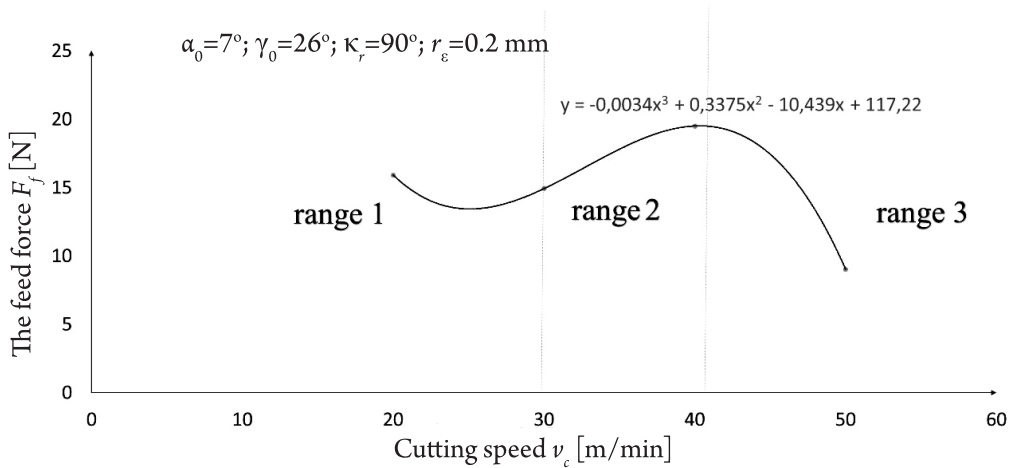


Fig. 8. The feed force with respect to its dependence on cutting speed (workpiece: NiTi; cutting parameters: $f = 0.053 \text{ mm/rev}$; $a_p = 0.2 \text{ mm}$; cutting tool: CCGT 060202 – AS)

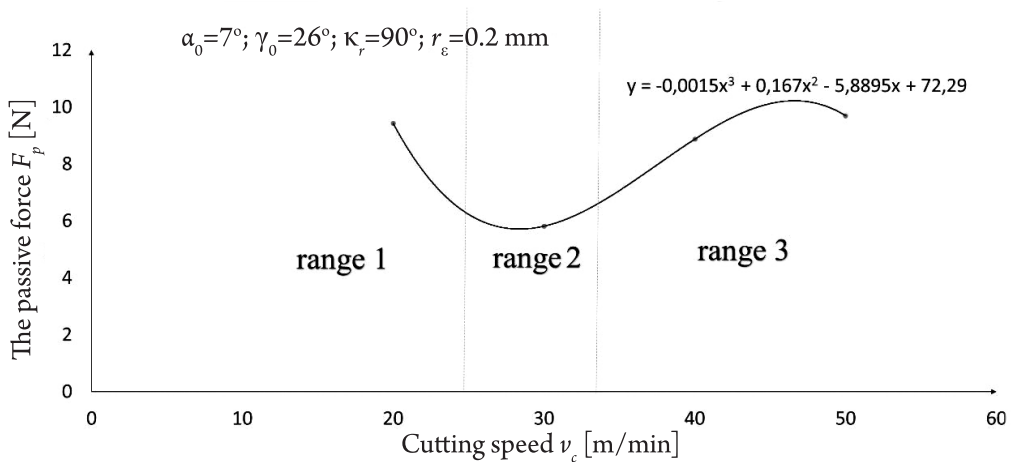


Fig. 9. The passive force with respect to its dependence on cutting speed (workpiece: NiTi; cutting parameters: $f = 0.053 \text{ mm/rev}$; $a_p = 0.2 \text{ mm}$; cutting tool: CCGT 060202 – AS)

5. Conclusion

Shape memory alloys based on NiTi are difficult to process. Experiments concerning precise turning, to examine the cutting force. The results of obtained values of cutting force during sintered carbides turning for different cutting speeds, constant feed and depth of cut were analyzed. Key findings are as follows:

- 1) The lowest the main cutting force is for cutting speed $v_c = 40 \text{ m/min}$ (average value: $F_c = 13.1 \text{ N}$);
- 2) The highest the main cutting force is for cutting speed $v_c = 20 \text{ m/min}$ (average value: $F_c = 43.07 \text{ N}$);

- 3) The lowest the feed force is for cutting speed $v_c = 50\text{m/min}$ (average value: $F_f = 9.02\text{ N}$);
- 4) The highest the feed force is for cutting speed $v_c = 40\text{m/min}$ (average value: $F_f = 19.5\text{ N}$);
- 5) The lowest the passive force is for cutting speed $v_c = 30\text{m/min}$ (average value: $F_p = 5.81\text{ N}$);
- 6) The highest the passive force is for cutting speed $v_c = 50\text{m/min}$ (average value: $F_p = 9.69\text{ N}$).

Cutting speed has twofold impact on the whole cutting process. First – direct as a ratio of occurring deformations, second – indirect influencing cutting temperature. The indirect impact definitely overrides, that is why the course of the main cutting force during precision turning of NiTi alloy can be described according to Rosenberg and Jeremin basing on so called typical curves [3]. In the speed range $v_c = 20\text{ m/min}$ to 40 m/min the main cutting force decreases due to increase of real rake angle (by built up edge) so deformation level decreases. When the cutting speed is getting higher to $v_c = 50\text{ m/min}$ main cutting force increases due to vanishing of accretion and decreasing of real rake angle down to the value of rake angle on the cutting edge as well as increase of the friction coefficient. Similar relation were observed in 10 (Fig. 10). Further research would require testing higher cutting speeds.

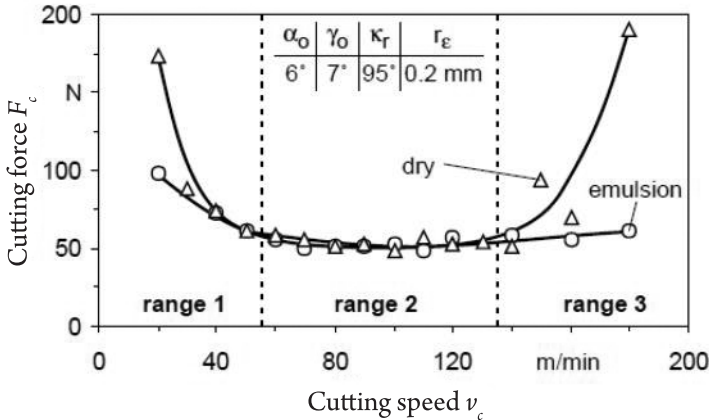


Fig. 10. Cutting force with respect to its dependence on cutting speed and cooling lubricant concept (workpiece: β -NiTi; cutting parameters: $f = 0.05\text{ mm/rev}$; $a_p = 0.2\text{ mm}$; cutting tool: HC TiCN/TiAlN) [10]

References

- [1] Biermann D., Kahleyss F., Krebs E., Upmeier T., *A Study on Micro-Machining Technology for the Machining of NiTi: Five-Axis Micro-Milling and Micro Deep-Hole Drilling*, JMEPEG, vol. 20, 2011, 745–751.

- [2] Elahinia M. H., Hashemi M., Tabesh M., Bhaduri S. B., *Manufacturing and processing of NiTi implants: A review*, Prog. in Mater. Sci., Vol. 57, 2012, 911–946.
- [3] Kaczmarek J., *Podstawy skrawania metali*, PWT., Warszawa 1956.
- [4] Guo Y., Klink A., Fu Ch., Snyder J., *Machinability and surface integrity of Nitinol shape memory alloy*, CIRP Annals – Manu. Tech., Vol. 62, 2013, 83–86.
- [5] Kaynak Y., Robertson S. W., Karacac H.E., Jawahir I.S., *Progressive tool-wear in machining of room-temperature austenitic NiTi alloys: The influence of cooling/lubricating, melting, and heat treatment conditions*, J. Mater. Process. Tech., Vol. 215, 2015, 95–104.
- [6] Kaynak Y., Karaca H.E., Noebe R.D., Jawahir I.S., *Tool wear analysis in cryogenic machining of NiTi shape memory alloys: A comparison of tool wear performance with dry and MQL machining*, Wear, Vol. 306, 2013, 51–63.
- [7] Kłaput J., *Studies of selected mechanical properties of nitinol – shape memory alloy*, Archives of Foundry Engineering, Vol. 10, Issue 3, 2010, 155–158.
- [8] Lin H.C., Lin K.M., Chen Y.C., *A study on the machining characteristics of TiNi shape memory alloys*, J. Mater. Process. Tech., Vol. 105, 2000, 327–332.
- [9] Piquard R., Acunto A. D, Laheurte P., Dudzinski D., *Micro-end milling of NiTi biomedical alloys, burr formation and phase transformation*, Prec. Eng., Vol. 38, 2014, 356–364.
- [10] Weinert K., Petzoldt V., Kotter D., *Turning and Drilling of NiTi Shape Memory Alloys*, CIRP Annals – Manuf. Technol., Vol. 53, Issue 1, 2004, 65–68.
- [11] Weinert K., Petzoldt V., *Machining of NiTi based shape memory alloys*, Mater, Sci. and Eng., Vol. 378, 2004, 180–184.
- [12] Weinert K., Petzoldt V., *Machining NiTi micro-parts by micro-milling*, Mater, Sci. and Eng., Vol. 481–482, 2008, 672–675.
- [13] Wu S.K., Lin H.C., Chen C.C., *A study on the machinability of a Ti 49,6 Ni 50,4 shape memory alloy*, Mater. Letters 40, 1999, 27–3.
- [14] <http://iscar.pl> (access: 03.10.2016).

Artur Krowiak (krowiak@mech.pk.edu.pl)

Institute of Computer Science, Faculty of Mechanical Engineering, Cracow University of Technology

Jordan Podgórski

Student of Applied Informatics, Faculty of Mechanical Engineering, Cracow University of Technology

THE ADAPTATION OF THE CROSS VALIDATION APPROACH FOR RBF-BASED COLLOCATION METHODS

ADAPTACJA PODEJSCIA KRZYŻOWEGO SPRAWDZANIA DO METOD BAZUJĄCYCH NA FUNKCJACH RBF

Abstract

The paper shows the adaptation of the cross validation approach, known from interpolation problems, for estimating the value of a shape parameter for radial basis functions. The latter are involved in two collocation techniques used on an unstructured grid to find approximate solution of differential equations. To obtain accurate results, the shape parameter should be chosen as a result of a trade-off between accuracy and conditioning of the system. The cross validation approach called “leave one out” takes these aspects into consideration. The numerical examples that summarize the investigations show the usefulness of the approach.

Keywords: radial basis functions, shape parameter, cross-validation approach

Streszczenie

W artykule pokazano adaptację algorytmu krzyżowego sprawdzania, znanego z zagadnień statystyki i interpolacji, do wyznaczenia wartości współczynnika kształtu w radialnych funkcjach bazowych. Funkcje te użyto w dwóch typach technik kolokacyjnych stosowanych na nieregularnej siatce do przybliżonego rozwiązywania równań różniczkowych. Aby otrzymać rezultaty o odpowiedniej dokładności, współczynnik kształtu powinien być dobrany na bazie kompromisu pomiędzy dokładnością a uwarunkowaniem układu równań. Przedstawiony algorytm, zwany “leave one out”, bierze te aspekty pod uwagę. Podsumowaniem artykułu są numeryczne testy, które pokazują użyteczność tego podejścia.

Słowa kluczowe: radialne funkcje bazowe, współczynnik kształtu, algorytm cross-validation

1. Introduction

In recent years a significant development of numerical methods for solving differential equations with the use of an unstructured grid has been observed. All these techniques are called meshless or meshfree methods as opposed to well-known mesh based methods such as finite element, finite difference, or finite volume method. The meshless methods can overcome some drawbacks of mesh based techniques associated with grid distortion, remeshing in adaptation approaches and handling problems characterized by complicated geometries. There are several formulations of meshless methods [1, 2]. Among them, one can distinguish methods that apply interpolant composed of radial basis functions (RBF) and use the collocation technique in order to discretize a differential problem – the Kansa method and RBF-based pseudospectral method (RBF-PS). There are many papers devoted to these methods [3–7]. The problem of choosing a respective value of the shape parameter for RBF is the issue which appears in almost all of these papers. This parameter is responsible for the flatness of RBF and influences the accuracy of the methods as well as conditioning of the system of algebraic equations that follows from the discretization procedure. To achieve high accuracy, the value of the parameter should be large but this leads to an ill-conditioned system, which cannot be easily solved [8]. To estimate a respective value, a trade-off is needed. This value is estimated mostly on the base of researcher’s experience, but there are also a few more sophisticated approaches [9, 10].

The present paper shows the adaptation of a kind of cross validation algorithm to this end. The latter is called “leave one out” and it has been used in statistics and interpolation problems [5]. The paper presents an easy implementation of the approach in the Kansa method and demonstrates that the same value of the parameter is valid for the RBF-PS method. The layout of the paper is as follows: in section 2 two RBF-based numerical techniques are briefly described, in section 3 the use of the “leave one out” algorithm is demonstrated and finally in section 4 the numerical tests are shown.

2. RBF-based collocation methods for partial differential equations

There are several numerical methods for solving boundary-value problem. The latter can be written in a general form as:

$$Lu = f \quad \text{in } \Omega, \quad (1)$$

$$Bu = g \quad \text{on } \partial\Omega$$

where L and B denote linear differential operators imposed on the sought function u in the domain Ω and on the boundaries $\partial\Omega$, respectively, and f, g are known functions. Among the methods that take advantage of irregularly distributed nodes for domain discretization, one can distinguish collocation techniques that employs interpolant consisting of RBF. Such interpolant has a general form, which is as follows:

$$u(\mathbf{x}) = \sum_{j=1}^N \alpha_j \varphi(\|\mathbf{x} - \mathbf{x}_j\|) \quad (2)$$

where $\mathbf{x}_j, j = 1, \dots, N$ represent a set of irregularly distributed nodes in the domain as well as on the boundary. Among them one can distinguish interior nodes $\mathbf{x}_i^I, i = 1, \dots, N^I$ and the nodes imposed on the boundary $\mathbf{x}_i^B, i = 1, \dots, N^B$. In Eq. (2) $\varphi_j(\mathbf{x}) = \varphi(\|\mathbf{x} - \mathbf{x}_j\|)$ represents RBF and α_j are the interpolation coefficients.

One of the approach which falls into the mentioned category called the Kansa method, introduces function (2) to problem (1) and by the collocation technique transforms differential problem into a set of algebraic equations. Another one uses the RBF interpolant to determine discrete approximation of derivatives included in , thereby obtaining algebraic approximation of the considered problem – the RBF- PS method. The details of these methods are given below.

2.1. Kansa method

By introducing interpolation function described by Eq. (2) into Eq. (1) and by collocating at each node in the domain including boundaries, one gets:

$$\begin{aligned} \sum_{j=1}^N \alpha_j \left[L\varphi(\|\mathbf{x} - \mathbf{x}_j\|) \right]_{\mathbf{x}=\mathbf{x}_i^I} &= f(\mathbf{x}_i), \quad i = 1, \dots, N^I, \\ \sum_{j=1}^N \alpha_j \left[B\varphi(\|\mathbf{x} - \mathbf{x}_j\|) \right]_{\mathbf{x}=\mathbf{x}_i^B} &= g(\mathbf{x}_i), \quad i = 1, \dots, N^B \end{aligned} \quad (3)$$

Using matrix notation one can put Eq. (3) in the following way:

$$\mathbf{A}_{LB} \boldsymbol{\alpha} = \mathbf{b} \quad (4)$$

In Eq. $\mathbf{A}_{LB} = \begin{bmatrix} \mathbf{A}_L \\ \mathbf{A}_B \end{bmatrix}$, $\mathbf{b} = \begin{bmatrix} \mathbf{f} \\ \mathbf{g} \end{bmatrix}$, where $(\mathbf{A}_L)_{ij} = \left[L\varphi(\|\mathbf{x} - \mathbf{x}_j\|) \right]_{\mathbf{x}=\mathbf{x}_i^I}, i = 1, \dots, N^I, j = 1, \dots, N$

$$(\mathbf{A}_B)_{ij} = \left[B\varphi(\|\mathbf{x} - \mathbf{x}_j\|) \right]_{\mathbf{x}=\mathbf{x}_i^B}, i = 1, \dots, N^B, j = 1, \dots, N$$

$$\mathbf{f}_i = f(\mathbf{x}_i^I), i = 1, \dots, N^I, \mathbf{g}_i = g(\mathbf{x}_i^B), i = 1, \dots, N^B$$

The interpolation coefficients are obtained from Eq. if only \mathbf{A}_{LB} is invertible:

$$\boldsymbol{\alpha} = \mathbf{A}_{LB}^{-1} \mathbf{b} \quad (5)$$

The study on the invertibility of the Kansa matrix (\mathbf{A}_{LB}) can be found in several papers. One can conclude that although there are numerical examples showing that the matrix can be singular for arbitrary center locations [11], these cases are rare and many other works [12] indicate a successful application of the method.

Since the interpolation coefficients are determined, the approximate solution is described by interpolant (2).

2.2. RBF-PS method

RBF-PS is a combination of RBF interpolation with the pseudospectral technique. In this approach, the interpolant in the form of (2) is used to determine the discrete approximation of differential operator from Eq. (1). To this end, the interpolation conditions are taken into account:

$$\sum_{j=1}^N \alpha_j \varphi(\|\mathbf{x}_i - \mathbf{x}_j\|) = u_i, \quad i = 1, \dots, N \quad (6)$$

It allows for presenting the coefficients α_i in terms of the values of the sought function, which can be put in the matrix notation in the following way:

$$\boldsymbol{\alpha} = \mathbf{A}^{-1} \mathbf{u} \quad (7)$$

where $\boldsymbol{\alpha} = [\alpha_1 \quad \dots \quad \alpha_N]^T$, $\mathbf{u} = [u_1 \quad \dots \quad u_N]^T$ and $\mathbf{A}_{ij} = \varphi(\|\mathbf{x}_i - \mathbf{x}_j\|)$, $i, j = 1, \dots, N$.

Then, by imposing an appropriate differential operator on the interpolant and evaluating it at each interior as well as boundary node, one gets:

$$\mathbf{u}_L = \mathbf{A}_L \boldsymbol{\alpha} \quad (8)$$

$$\mathbf{u}_B = \mathbf{A}_B \boldsymbol{\alpha} \quad (9)$$

where $\mathbf{u}_L, \mathbf{u}_B$ are discrete representation of appropriate derivatives and $\mathbf{A}_L, \mathbf{A}_B$ are the same matrices that appear in Eq. (4).

Using Eq. (7) one can express derivatives \mathbf{u}_L and \mathbf{u}_B in Eqs. (8) and (9) in terms of the sought function values from the whole domain as:

$$\mathbf{u}_{LB} = \mathbf{A}_{LB} \mathbf{A}^{-1} \mathbf{u} \quad (10)$$

where $\mathbf{u}_{LB} = [\mathbf{u}_L, \mathbf{u}_B]^T$ and \mathbf{A}_{LB} matrix is composed of $\mathbf{A}_L, \mathbf{A}_B$ in the the same way as in the Kansa method (Eq. (4)).

Matrix $\mathbf{A}_{LB} \mathbf{A}^{-1}$ is a discrete form of differential operators L, B and is called as differentiation matrix in the nomenclature of pseudospectral methods. With the use of this matrix Eq. (1) can be easily discretized:

$$\mathbf{A}_{LB} \mathbf{A}^{-1} \mathbf{u} = \mathbf{b} \quad (11)$$

and solved for unknown function values, which yields:

$$\mathbf{u} = \mathbf{A} \mathbf{A}_{LB}^{-1} \mathbf{b} \quad (12)$$

From the above it can be clearly seen that the solvability of the problem using the RBF-PS is conditioned by the inevitability of the same matrix as in the Kansa approach.

As one can notice, the approach presented is similar to the Kansa method. The main difference between the RBF-PS and Kansa method is that in the latter we introduce the

interpolation function directly into differential equation obtaining the interpolation coefficients. With these coefficients, the interpolation function approximates the solution at any point of the domain. In the RBF-PS we use the same interpolation function to derive a discrete approximation of a differential operator at each node and then this approximation in the form of a differentiation matrix is used to discretize the equation. Finally, in the RBF-PS, the function values at the nodes are obtained as the solution.

Since the RBF-PS operates directly with function values (does not need to evaluate the interpolant) it is more efficient in non-linear problems and in time dependent problems, where a kind of iterations are required to obtain the approximate function values.

3. Adopting “leave-one-out” algorithm for boundary-value-problem

It was found [5, 6, 8] that the shape parameter has a significant influence on accuracy. A larger value of this parameter theoretically should make the solution more accurate but leads to an ill-conditioned system, which may not be accurately solved. Therefore, an important issue in using RBF based methods is the choice of the appropriate value of c .

One of the approaches that can be employed comes from the interpolation problem:

$$\mathbf{A}\boldsymbol{\alpha} = \mathbf{u} \quad (13)$$

where \mathbf{A} , $\boldsymbol{\alpha}$ and \mathbf{u} are the RBF interpolation matrix, vector of interpolation coefficients and vector of nodal function values, respectively. Eq. is a result of the application of the interpolation conditions. In this case values of \mathbf{u} are known.

The optimal value of c depends on the number of nodes and on the pattern of their distribution, on the right-hand-side vector and precision of computation. All these factors are taken into consideration in the approach as it is reported in [13]. The approach is based on cross-validation and is called “leave-one-out”. In this algorithm, an optimal value of c is obtained by minimizing the error of an interpolant based on the data from which one of the nodes was “left out”. The error at the k th node, which was left out can be obtained as:

$$E_k = u_k - u^{[k]}(\mathbf{x}_k) \quad (14)$$

where u_k is the function value at this node and $u^{[k]}(\mathbf{x}_k) = \sum_{\substack{j=1 \\ j \neq k}}^N \alpha_j^{[k]} \varphi(\|\mathbf{x} - \mathbf{x}_j\|)$ is the RBF interpolant to the data $\mathbf{u} = [u_1, \dots, u_{k-1}, u_{k+1}, \dots, u_N]$.

Removing in turn each of the nodes, the vector of errors $\mathbf{E} = [E_1 \ \dots \ E_N]^T$ can be composed. The norm of this vector indicates the quality of the fit, which depends on the shape parameter. By repeating calculations for different values of c , one can choose the optimal one – which minimizes the $\|\mathbf{E}\|$ norm.

Since the implementation of his strategy is rather expensive, Rippa [13] showed that E_k can be computed in a simpler way as:

$$E_k = \frac{\alpha_k}{\mathbf{A}_{kk}^{-1}} \quad (15)$$

where α_k is the k th coefficient in the interpolant u based on a full set of nodes and \mathbf{A}_{kk}^{-1} is the k th element in the diagonal of the inverse of the interpolation matrix.

In the present paper, the above method for estimating the optimal c is adopted to methods of solving differential equations presented in sections 2.1 and 2.2. Here, we follow directly the idea presented by Rippa, understanding the problem described by Eq. (1) as a kind of interpolation problem, but defined for derivatives.

At first, let us consider the method from section 2.1, where the discretized boundary-value-problem is approximated by Eq.(4). We can consider this system of equations as the interpolation conditions such as Eq.(13), but written for derivative of the sought function. In this case the interpolant applied at the interior nodes assumes the form of:

$$u_L(\mathbf{x}) = Lu(\mathbf{x}) = \sum_{i=1}^N \alpha_i L\varphi_i(\|\mathbf{x} - \mathbf{x}_i\|) \quad (16)$$

and interpolant for approximation of boundary values is as follows:

$$u_B(\mathbf{x}) = Bu(\mathbf{x}) = \sum_{i=1}^N \alpha_i B\varphi_i(\|\mathbf{x} - \mathbf{x}_i\|) \quad (17)$$

One can make use of the “leave one out” algorithm to obtain the solution of this interpolation problem in the case, where the k th node is omitted:

$$\boldsymbol{\alpha}^{[k]} = \left(\mathbf{A}_{LB}^{[k]}\right)^{-1} \mathbf{b}^{[k]} \quad (18)$$

With the obtained coefficients, the interpolant for derivative at the k th node is evaluated

$$u_L^{[k]}(\mathbf{x}_k^I) = \sum_{i=1, i \neq k}^N \alpha_i^{[k]} \left[L\varphi_i(\|\mathbf{x} - \mathbf{x}_i\|) \right]_{\mathbf{x}=\mathbf{x}_k^I} \quad \text{or} \quad u_B^{[k]}(\mathbf{x}_k^B) = \sum_{i=1, i \neq k}^N \alpha_i^{[k]} \left[B\varphi_i(\|\mathbf{x} - \mathbf{x}_i\|) \right]_{\mathbf{x}=\mathbf{x}_k^B} \quad (19)$$

yielding the error at the k th node as:

$$E_k = b_k - u_L^{[k]}(\mathbf{x}_k^I) \quad \text{or} \quad E_k = b_k - u_B^{[k]}(\mathbf{x}_k^B) \quad (20)$$

where b_k is the k th element of the right-hand-side vector introduced by Eq.(4).

Making use of Rippa’s acceleration (Eq.(15)), the above error can be computed faster by:

$$E_k = \frac{\alpha_k}{\left(\mathbf{A}_{LB}\right)_{kk}^{-1}} = \frac{\left[\left(\mathbf{A}_{LB}\right)^{-1} \cdot \mathbf{b}\right]_k}{\left(\mathbf{A}_{LB}\right)_{kk}^{-1}} \quad (21)$$

where \mathbf{A}_{LB} is the inverse of derivative interpolation matrix based on full set of nodes, introduced by Eq.(4).

For the method presented in section 2.2, Eq. (11) can be considered as the interpolation problem defined for the derivatives and therefore can be the starting point for derivation of the formula for error in the context of “leave one out” algorithm. Unfortunately, in the RBF-PS approach we are not able to find directly the value of $u_L^{[k]}(\mathbf{x}_k)$. By solving the system in the form of Eq. (11), but defined by omitting the k th node, we obtain $u_i, i = 1, \dots, k-1, k+1, \dots, N$, which can be used by Eq. (10) to approximate the derivatives at all the nodes without the k th node. Therefore, formula (20) cannot be directly obtained – it requires the value of the derivative at the k th node.

To overcome this inconvenience, with the values of $\mathbf{u}^{[k]} = \mathbf{A}^{[k]} (\mathbf{A}_{LB}^{-1})^{[k]} \mathbf{b}^{[k]}$ at all nodes without the k th node, one should make a step back and use Eq. (7) to calculate $\alpha_i^{[k]}$ yielding:

$$\boldsymbol{\alpha}^{[k]} = (\mathbf{A}^{[k]})^{-1} \mathbf{u}^{[k]} = (\mathbf{A}^{[k]})^{-1} \mathbf{A}^{[k]} (\mathbf{A}_{LB}^{[k]})^{-1} \mathbf{b} = (\mathbf{A}_{LB}^{[k]})^{-1} \mathbf{b} \quad (22)$$

where $\mathbf{A}_{LB}^{[k]}$ is a Kansa matrix derived without the k th node. It is obvious that the same coefficients as those used in Eq. (18) are obtained, which allows for evaluating the interpolant for derivative at the k th node and leads to the same formula for the error as in the Kansa approach – (Eq.(21)).

4. Numerical tests

To show the usefulness of the approach proposed in the last section several equations in 2D space have been solved with the Kansa and RBF-PS methods. Due to the limited space, the results of two of them are presented.

Example 1. Poisson equation with Dirichlet boundary conditions:

$$\begin{aligned} \nabla^2 u(x, y) &= \sin(\pi \cdot x) \sin(\pi \cdot y), \quad (x, y) \in \Omega = [0, 1] \times [0, 1] \\ u(x, y) &= 0, \quad (x, y) \in \partial\Omega \end{aligned} \quad (23)$$

for which the analytical solution has the form of:

$$u = -\frac{1}{2\pi^2} \sin(\pi \cdot x) \sin(\pi \cdot y) \quad (24)$$

Example 2. 2D modified Helmholtz equation with non-homogeneous boundary conditions:

$$\begin{aligned} \nabla^2 u(x, y) - u(x, y) &= -(\pi^2 + 1)(y \sin(\pi \cdot x) + x \cos(\pi \cdot y)), \quad (x, y) \in \Omega = [0, 1] \times [0, 1] \\ u(0, y) &= 0, u(1, y) = \cos(\pi \cdot y), u(x, 0) = x, u(x, 1) = \sin(\pi \cdot x) - x \end{aligned} \quad (25)$$

whose exact solution has the form:

$$u(x, y) = y \sin(\pi x) + x \cos(y) \quad (26)$$

As a measure of the quality of results, an error norm in the following form has been introduced $\varepsilon = \sqrt{\sum_{i=1}^N (u_i^n - u_i^e)^2} / \sqrt{\sum_{i=1}^N (u_i^e)^2} \cdot 100\%$, where u^n is numerical solution, u^e – the exact one. The obtained results are shown in Tables 1–4.

Table 1. Results for example 1 solved by Kansa's method

N (regular grid)	c_{opt}	ε_{min}	"leave one out" algorithm	
			c	ε
81	2.2846	5.3802e-04	1.0670	5.6308e-04
121	0.9818	1.5387e-04	0.9518	8.7747e-04
169	0.9167	6.0927e-05	0.9217	1.2719e-04
225	0.8916	3.4936e-05	0.8816	5.8035e-05
N (irreg. grid)				
81	1.8035	1.8135e-04	1.0370	4.6253e-04
121	1.3676	8.3723e-05	0.9367	2.7855e-04
169	0.9868	3.3615e-05	0.9367	3.8024e-05
225	0.8215	1.3580e-05	0.8265	1.6603e-05

Table 2. Results for example 1 solved by the RBF-PS method

N (regular grid)	c_{opt}	ε_{min}	"leave one out" algorithm	
			c	ε
81	1.0720	5.3918e-04	1.0670	5.6319e-04
121	0.9818	1.5665e-04	0.9518	8.8616e-04
169	0.9167	1.0287e-04	0.9217	1.8572e-04
225	0.8866	3.9077e-05	0.8816	5.0806e-05
N (irreg.grid)				
81	1.7935	1.9638e-04	1.0370	4.6253e-04
121	1.2775	8.3239e-05	0.9367	2.7856e-04
169	0.9718	3.2367e-05	0.9367	3.6655e-05
225	0.8716	1.4629e-05	0.8265	2.0200e-05

It is obvious that the presented algorithm for finding a good value of the shape parameter gives the same results for Kansa's method as well as for the RBF-PS when applied on the same grid, since it makes use of the same matrix. Therefore, appropriate columns presenting

a good value of c possess the same values, comparing between two discretization methods, but for clear comparison of the results they are included in both tables. For comparison, the optimal value of c obtained on the base of the exact solution is also included in the tables. By analyzing the results one can conclude that the presented approach gives the values of c that lead to acceptable results.

Table 3. Results for example 2 solved by Kansa's method

N (regular grid)	c_{opt}	ϵ_{min}	"leave one out" algorithm	
			c	ϵ
81	2.4349	4.9988e-04	1.3075	9.000e-03
121	1.8186	2.6106e-04	1.1622	2.5000e-03
169	1.3626	1.4130e-04	1.0921	5.8126e-04
225	1.1973	9.0023e-05	0.9067	4.6734e-04
N (irreg. grid)				
81	1.8587	1.2793e-04	1.5931	6.5335e-04
121	1.5230	1.0177e-04	0.9167	3.8001e-03
169	1.1171	9.9409e-05	1.1722	1.5911e-04
225	1.0019	7.0534e-05	0.9969	4.8329e-04

Table 4. Results for example 2 solved by the RBF-PS method

N (regular grid)	c_{opt}	ϵ_{min}	"leave one out" algorithm	
			c	ϵ
81	2.3547	7.8125e-04	1.3075	9.000e-03
121	1.6733	3.0915e-04	1.1622	2.4174e-03
169	1.5680	2.0440e-04	1.0921	3.7698e-03
225	1.0620	1.5164e-04	0.9067	5.3632e-04
N (irreg.grid)				
81	1.8937	1.8087e-04	1.5931	6.6200e-04
121	1.4878	1.8640e-04	0.9167	3.7853e-03
169	0.9768	1.1707e-04	1.1722	4.7312e-04
225	0.8766	7.9021e-05	0.9969	3.3314e-04

5. Conclusion

In the paper, the problem of accuracy of two meshless collocation methods that employ RBF interpolation is considered. It is well-known that the accuracy of such methods depends on the value of the shape parameter included in RBF. The paper applies a kind of cross validation approach, known from interpolation problems, to find respective value of this parameter.

To this end, the system of algebraic equations following from the application of the Kansa or RBF-PS method is treated as a kind of interpolation problem. The “leave one out” approach takes into consideration several discretization and computational parameters to find the value of c , which is a great value of this approach. The use of this algorithm requires to set a range, which is searched for the optimal value of c and many evaluations of system matrix. These can be considered as some weaknesses of the algorithm that should be improved in future work.

References

- [1] Belytschko T., Krongauz Y., Organ D., Flrming M., Krysl P., *Meshless methods: an overview and recent developments*, Computer Methods in Applied Mechanics and Engineering, vol. 139, 1996, 3-47.
- [2] Liu G.R., *Meshless Methods – Moving beyond the Finite Element Method*, CRC Press, Boca Raton, Florida 2003.
- [3] Kansa E., *Multiquadrics – A scattered data approximation scheme with applications to computational fluid dynamics I: Surface approximations and partial derivative estimates*, Computers and Mathematics with Applications, vol. 19, 1990, 127-145.
- [4] Kansa E., *Multiquadrics – A scattered data approximation scheme with applications to computational fluid dynamics I: Solutions to parabolic, hyperbolic, and elliptic partial differential equations*, Computers and Mathematics with Applications, vol. 19, 1990, 147-161.
- [5] Fasshauer G.E., *Meshfree Approximation Methods with Matlab*, World Scientific Publishing, Singapore, 2007.
- [6] Cheng A.H.D., *Multiquadrics and its shape parameter – a numerical investigation of error estimate, condition number and round-off error by arbitrary precision computation*, Engineering analysis with boundary elements, vol. 36, 2012, 220-239.
- [7] Ferreira A.J.M, *A formulation of the multiquadric radial basis function method for the analysis of laminated composite plates*, Composit Structures, vol. 59, 2003, 385-92.
- [8] Schaback R., *Error estimates and condition numbers for radial basis function interpolation*, Advances in Computational Mathematics, vol. 3, 1995, 251-264.
- [9] Krowiak A., *Radial basis function-based pseudospectral method for static analysis of thin plates*, Engineering Analysis with Boundary Elements, vol. 71, 2016, 50-58.
- [10] Krowiak A., *On choosing a value of shape parameter in Radial Basis Function collocation methods*, Numerical Methods for Partial Differential Equations, submitted for publication.
- [11] Hon Y.C., Schaback R., *On nonsymmetric collocation by radial basis functions*, Appl. Math. Comput., vol. 119, 2001, 177-186.
- [12] Chen W., Fu Z.J., Chen C.S., *Recent Advances in Radial Basis Function Collocation Methods*, Springer, 2014.
- [13] Rippa S., *An algorithm for selecting a good value for the parameter c in radial basis function interpolation*, Adv. in Comput. Math., vol. 11, 1999, 193-210.

Edward Lisowski (lisowski@mech.pk.edu.pl)

Institute of Applied Informatics, Faculty of Mechanical Engineering, Cracow University of Technology

Janusz Rajda

Research and Development Department, Ponar Wadowice S.A.

EVALUATION OF PRESSURE LOSSES REDUCTION POSSIBILITY FOR WEH22 DIRECTIONAL CONTROL VALVE BY INTERNAL GEOMETRY CORRECTION

OCENA MOŻLIWOŚCI OBNIŻENIA STRAT CIŚNIENIA ROZDZIELACZA WEH22 PRZEZ KOREKCJĘ GEOMETRII WEWNĘTRZNEJ

Abstract

The article presents the evaluation of possibility of pressure losses reduction at the flow through a WEH22 hydraulic directional control valve. For this purpose, 3D models of flow paths were built using the Creo Parametric software. Then the models were used in the ANSYS/Fluent software to calculate pressure losses. The results of the analysis have allowed for determination of possibilities of pressure losses reduction without changing overall dimensions of the valve body.

Keywords: hydraulic directional valve, computational fluid dynamics

Streszczenie

W artykule przedstawiono ocenę możliwości obniżenia strat ciśnienia przy przepływie przez rozdzielacz hydrauliczny WEH22. W tym celu zbudowano modele 3D dróg przepływowych, które wygenerowano za pomocą programu CREO Parametric, a następnie te modele wykorzystano w programie ANSYS/Fluent do obliczenia strat ciśnienia. Uzyskane wyniki analiz pozwoliły na określenie możliwości obniżenia strat ciśnienia bez zmian wymiarów gabarytowych korpusu rozdzielacza.

Słowa kluczowe: rozdzielacz hydrauliczny, obliczeniowa mechanika płynów

1. Introduction

Hydraulic drives are used in many machines and devices. Especially electromagnetically controlled elements are suitable for automation, as they can be easily controlled by a computer or digital controllers. Compared to other systems, lower efficiency is a disadvantage of a hydraulic system. However, due to the advantages of a hydraulic drive, it is still being developed and improved. The article aims at minimizing pressure losses for the hydraulic directional control valve WEH22 type without changing its overall dimensions. These directional control valves are widely used in the industry and offered by many companies manufacturing hydraulic elements, e.g. Bosch-Rexroth [1], and Ponar Wadowice in Poland [2]. Their advantage is a simple structure consisting of a cast body containing a spool in various shapes corresponding to different flow path configurations. This valve can be operated at pressure up to 35 MPa and flow rate up to 450 dm³/min. It means that the valve can be applicable to systems with a capacity up to 260 kW. It is produced with a connecting pattern according to the ISO 4401-08 standard [3] so it can be used interchangeably by many manufacturers. The article focuses on a particular solution manufactured by Ponar Wadowice [2]. The solution currently has similar characteristics to Rexroth [1]. Conducting calculations of this type of object is difficult due to the complex geometrical shape of flow paths, which are usually made by means of the casting technology. In order to automatically generate series of objects to investigate them, Creo Parametric software was applied. The flow analysis was carried out using the CFD method in the ANSYS / Fluent software [4]. This approach was also used in other papers, e.g. [5] and [6].

2. Modeling of flow path geometry

Schematic view of the directional control valve WEH22 type is shown in Fig.1. It consists of a body 1, a spool 2 and a pilot valve 3. Body 1 is made in the casting process in which adequate channels are initially performed. Then, the excess of material is machined in the holes where higher accuracy is required. To conduct the analysis, a 3D geometric model of the individual components, as well as a 3D model of liquid in the inner space is required. CAD techniques are used for this purpose. 3D models of the PA (Fig. 2.) and BT (Fig. 3.) flow paths are separable so that their analyses can be carried out independently. The presented model is parametric and can generate many variants of directional control valve design solutions and 3D geometric models of the fluid in the valve at the same time.

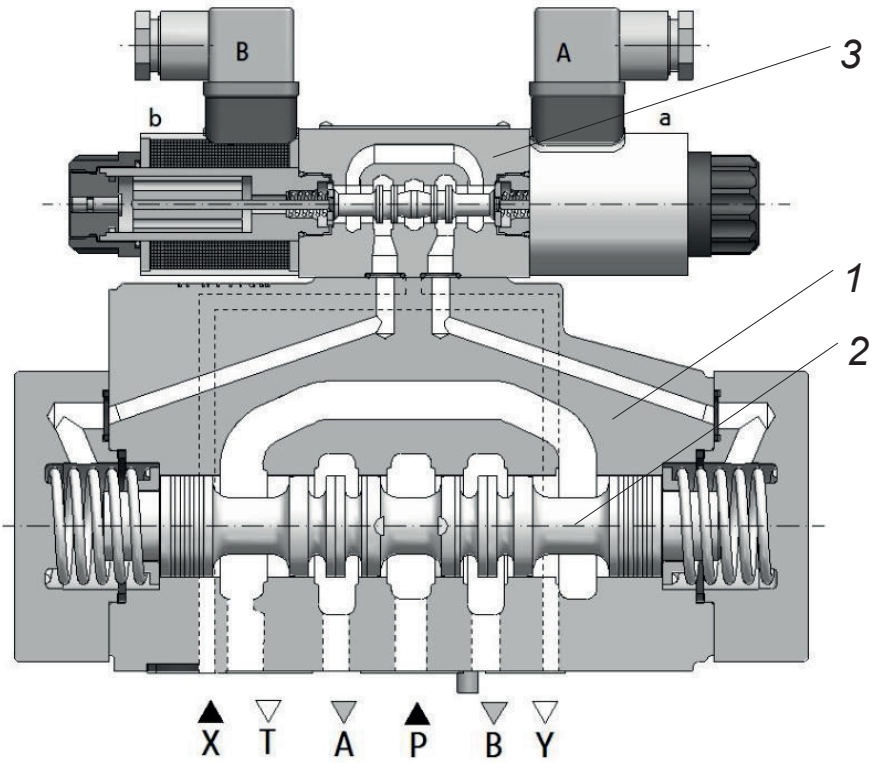


Fig. 1. View of directional control valve WEH22: 1 – body, 2 – spool, 3 – pilot valve

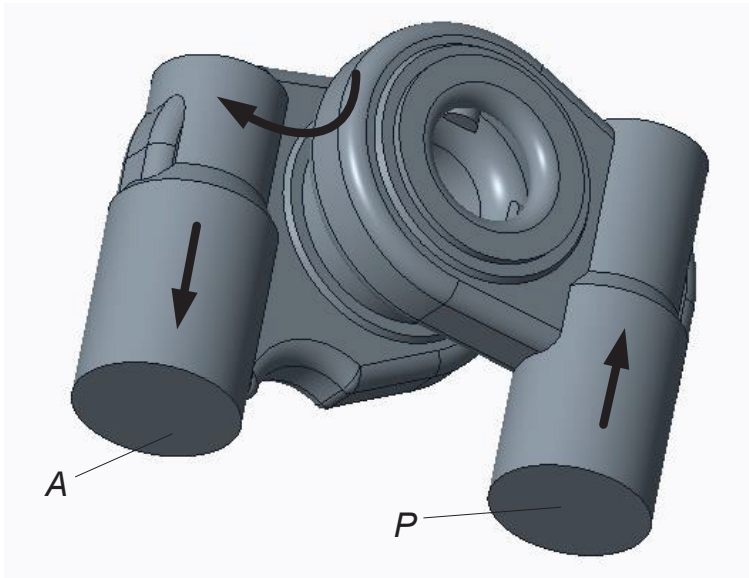


Fig. 2. Automatically generated 3D model of PA flow path

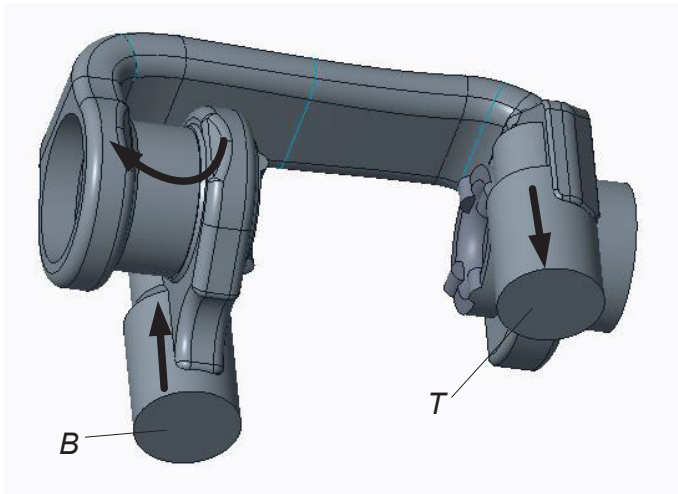


Fig. 3. Automatically generated 3D model of BT flow path

3. CFD analysis

In order to perform the analysis, flow kind must be determined. The ANSYS/Fluent software allows researchers to choose from a variety of models available including: $k-\epsilon$, $k-\omega$, Reynolds etc. In the case of flow through the directional control valve, $k-\epsilon$ model works well enough due to the fact that in the valve there are no conditions for the formation of laminar flow [5, 8]. Thus, the $k-\epsilon$ turbulence model was chosen for the simulation study. The application of this turbulence model in similar cases gave good results also in other authors' works [6, 7]. The kinetic energy of the turbulence and the dissipation factor are computed from the following equations:

$$\frac{\partial}{\partial t}(\rho k) + \frac{\partial}{\partial x_i}(\rho k u_i) = \frac{\partial}{\partial x_j} \left(\left(\alpha + \frac{\mu_t}{\sigma_k} \right) \frac{\partial k}{\partial x_j} \right) + G_k + G_b - \rho \epsilon - Y_M + S_k \quad (1)$$

$$\frac{\partial}{\partial t}(\rho \epsilon) + \frac{\partial}{\partial x_i}(\rho \epsilon u_i) = \frac{\partial}{\partial x_j} \left(\left(\alpha + \frac{\mu_t}{\sigma_k} \right) \frac{\partial \epsilon}{\partial x_j} \right) + C_{1\epsilon} \frac{\epsilon}{k} (G_k + C_{3\epsilon} G_b) - C_{2\epsilon} \rho \frac{\epsilon^2}{k} + S_\epsilon \quad (2)$$

where:

- G_k – represents the increase in the kinetic energy of turbulence caused by the gradient of average velocities,
- G_b – energy generated by the phenomenon of buoyancy,
- Y_M – energy associated with the compressibility of liquids,
- $C_{1\epsilon}, C_{2\epsilon}, C_{3\epsilon}$ – model constants,
- S_k, S_ϵ – Prandtl's numbers, respectively,
- μ_t – turbulent viscosity.

Turbulent viscosity, μ_t , is calculated as follows:

$$\mu_t = \rho C_\mu \frac{k^2}{\varepsilon} \quad (3)$$

Model constants: $C_{1\varepsilon} = 1,44$, $C_{2\varepsilon} = 1,92$, $C_m = 0,09$, $s_k = 1,0$, $s_\varepsilon = 1,3$.

The boundary conditions are set as follows:

1. On the input of flow paths the velocity average magnitude of working liquid is assumed. Considering the flow range of the WEH22 directional valve, five values of flow rate are selected, respectively 100, 200, 300, 400 and 450 dm³/min.
2. On the flow path output the constant pressure value of 0,1 MPa is assumed.
3. Furthermore, it is assumed that the channel walls are smooth, and that the working fluid is hydraulic oil with the following characteristics:
 - ▶ density $\rho_0 = 870$ kg/m³,
 - ▶ dynamic viscosity $\mu = 0,013$ Pa/s.

The series of calculations were programmed in ANSYS/Workbench using the previously created geometry, mesh of one flow path and the assumed boundary conditions.

Mesh of the flow path PA is showed in Fig. 4. It includes 1 085 725 cells and 303 687 nodes. The obtained results of flow simulations for flow rate $Q = 450$ dm³/min. are showed in Fig. 5 and Fig. 6. Fig. 5 shows the distribution of pressure on the walls for flow path PA and Fig. 6. shows the distribution of velocity vectors along the streamlines. The pressure on the walls varies and reaches higher values in the areas of stream direction change, while the velocity reaches the highest values within the spool.

Calculation process was carried out for the BT flow path in a similar way as for the PA flow path. In this case, the mesh model (Fig. 7) contains 2 278 375 cells and 631 977 nodes and also 5 boundary layers. Fig. 8 shows the distribution of pressure on the walls of the BT flow path, while Fig. 9 shows the velocity distribution of velocity vectors along the streamlines. The pressure on the walls of the flow path reaches higher values in the areas of stream direction change, while the velocity reaches the highest values in the gap formed between the spool and the edge of the chamber connecting it with B port.



Fig. 4. Mesh of PA flow path



Fig. 5. Pressure distribution on the channel walls of PA flow path

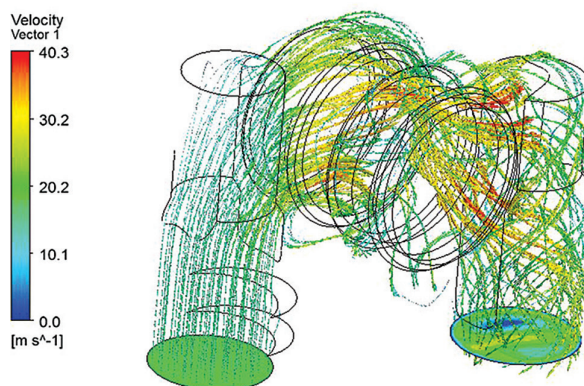


Fig. 6. Fluid velocity vectors along the stream lines for PA flow path

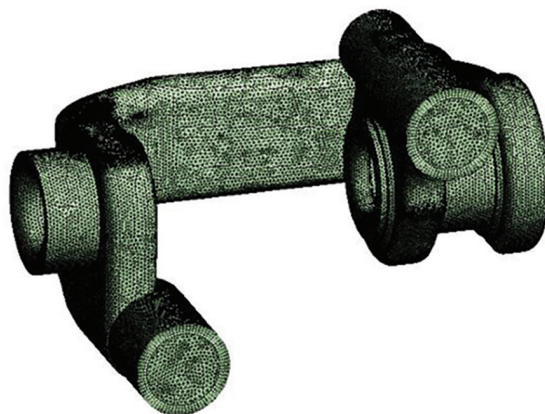


Fig. 7. Mesh of BT flow path

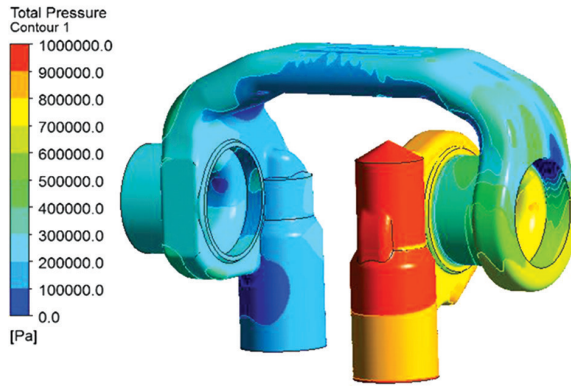


Fig. 8. Pressure distribution on the channel walls of BT flow path

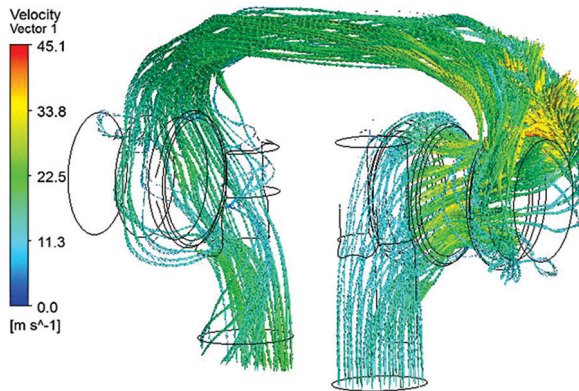


Fig. 9. Fluid velocity vectors along the stream lines for BT flow path

4. Summary

The article proposes the use of parametric modeling capabilities in Creo Parametric software and the possibility of operations on solids using Boole's algebra. As a result, a set of flow paths was generated automatically. Consequently, the paths were examined using ANSYS/Fluent under identical conditions. As a result of the analysis, some possibilities of pressure losses reduction were found. Pressure losses reduction requires an increase of flow path across sections, especially in the surroundings of the control edges. A small effect can also be achieved by the increase of inlet cross sections.

References

- [1] Bosch-Rexroth, Catalogue: *3/2, 4/2 and 4/3 directional valves, internally pilot operated, externally pilot operated RE 24751/08.08*, 2010,
- [2] Ponar Wadowice, Catalogue: *Directional spool valve, WK 460 110, 04.2001*.
- [3] ISO 4401:2005 Hydraulic fluid power – Four-port directional control valves – Mounting surfaces.
- [4] ANSYS/Fluent Inc. 14.0 users guide, 2011.
- [5] Lisowski E., Rajda J., *CFD analysis of pressure loss during flow by hydraulic directional control valve constructed from logic valves*, Energy Conversion and Management 65, 285-291, 2013.
- [6] Xudong Pan, Guanglin Wang, Zesheng Lu, *Flow field simulation and a flow model of servo-valve spool valve orifice*, Energy Conversion and Management 52, 3249–3256, 2011.
- [7] Domagala M., *CFD Analysis of a flow control valve*, Proceedings of 5th FPNI-PhD Symposium, 445-450, Kraków 2008.
- [8] Lisowski E., Czyżycki W., Rajda J., *Multifunctional four-port directional control valve constructed from logic valves*, Energy Conversion and Management 87, 905–913, 2014.

Marcin Migus (mmigus@gmail.com)

Andrzej Kęsy

Zbigniew Kęsy

Faculty of Mechanical Engineering, Kazimierz Pulaski University of Technology and Humanities in Radom

FLOW SIMULATION IN HYDRODYNAMIC TORQUE CONVERTER

SYMULACJA PRZEPLYWU W PRZEKLADNI HYDROKINETYCZNEJ

Abstract

The paper compares the theoretical non-dimensional steady-state characteristics of a hydrodynamic torque converter with the experimental ones. The theoretical characteristics were calculated numerically based on two flow models: a one-dimensional model created by the authors and a three-dimensional model prepared by means of the ANSYS CFX software. The experimental characteristics were obtained on the basis of test rig investigations.

Keywords: hydrodynamic torque converter; numerical calculations; flow models

Streszczenie

W artykule porównano teoretyczne bezwymiarowe charakterystyki przekładni hydrokinetycznej w stanie ustalonym z danymi eksperymentalnymi. Charakterystyki teoretyczne obliczono numerycznie na podstawie modeli przepływu: model jednowymiarowy utworzony przez autorów i trójwymiarowy model przygotowany za pomocą oprogramowania ANSYS CFX. Charakterystyki eksperymentalne zostały uzyskane na podstawie badań na stanowisku badawczym.

Słowa kluczowe: przekładnia hydrokinetyczna, obliczenia numeryczne

1. Introduction

A hydrodynamic torque converter is a component of a driveline system which transfers the engine power to wheels of a vehicle. This torque converter increases the torque produced by the engine, but it can also work as a clutch. Due to the flexible transmission of torque and its high vibration damping capacity, which significantly increases the durability of the driveline system, the hydrodynamic torque converter is widely used in cars, agricultural machines, road-making plants, etc.

The non-dimensional steady-state characteristics of a hydrodynamic torque converter are used to calculate the overall ratio between the engine and the driven wheels and consequently, the motive force required to overcome the traction resistance of vehicles. They consist of curves presenting the torque ratio i_d , the efficiency η and torque coefficient λ versus the velocity ratio i_k .

Currently, design calculations of both geometric parameters of a hydrodynamic torque converter and non-dimensional steady-state characteristics are based on the commonly used one-dimensional model of fluid flow in the working space of the converter [1–3]. The advantage of such a model is its simplicity, but its disadvantage is low calculation accuracy.

Efforts are also made to calculate the non-dimensional steady-state characteristics of a hydrodynamic torque converter by means of a three-dimensional model of fluid flow based on Computational Fluid Dynamics (CFD) methods. The Computational Fluid Dynamics is a new branch of mechanics which uses computer tools to analyze pressure distribution, velocity distribution and heat transfer in the flowing fluid. The results of numerical calculations are verified by laser anemometry measurements of the fluid flow in hydraulic device channels [4]. These attempts, however, are still at the model creating and improving stage [5].

The use of commercial CFD computer programs, developed for the calculation of three-dimensional flows in various channels could improve the accuracy of the non-dimensional steady-state characteristics of a hydrodynamic torque converter.

The paper presents the results of a calculation obtained on the basis of a one-dimensional model of the non-dimensional steady-state characteristics of the PH 305 hydrodynamic torque converter [6]. These calculation results were compared with the ones obtained with the ANSYS CFX software [7] and verified by means of experimental investigations [8].

2. PH 305 Hydrodynamic Torque Converter

The object of this study was a three-element one-phase hydrodynamic torque converter named PH 305 with an active diameter of $D = 0,305$ m. The hydrodynamic torque converter had a pump with alternately long and short blades in order to reduce the flow losses. The basic data of the PH 305 impellers is given in Table 1.

Table 1. Basic data of PH 305

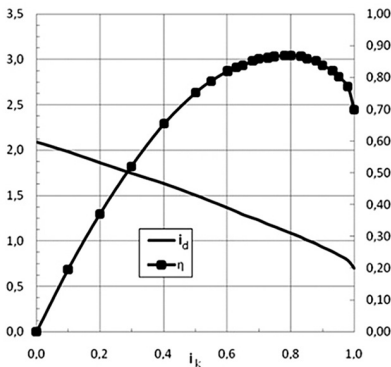
Rotor	Number of blades	Angle of blade β [°]	
		Input	output
Pump	26	90	90
Turbin	26	31.7	155.2
Stator	13	70	24

The HL 46 mineral oil was used as the working fluid in the PH 305 hydrodynamic torque converter.

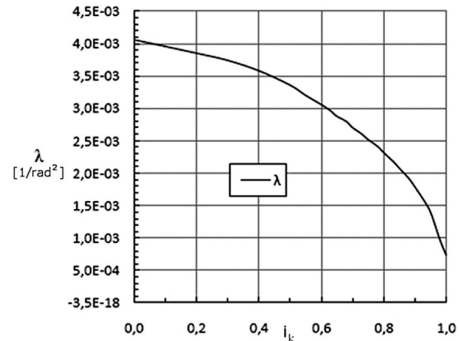
The experimental non-dimensional steady-state characteristics of the hydrodynamic torque converter PH 305 were performed on a specialized test rig. During the test, the input shaft angular velocity ω_1 was kept constant. The output shaft angular velocity ω_2 was changed, so as to obtain the target values of the velocity ratio ($0 \leq i_k < 1$). For each recorded point the values of torques were measured on the input (T_1) and the output (T_2) shafts. During the test, the working fluid temperature was maintained constant. On the basis of the measured values of ω_1 and ω_2 angular velocities and T_1 and T_2 torques, the points coordinates of the non-dimensional steady-state characteristics of the PH 305 hydrodynamic torque converter were calculated by means of the following formulas:

$$i_k = \frac{\omega_2}{\omega_1} \quad \eta = i_k \cdot i_d \quad \lambda = \frac{T_1}{\omega_1^2 D^5} \quad (1)$$

and presented in Fig. 1.



a)



b)

Fig. 1. Test based non-dimensional steady-state characteristics of the PH 305 hydrodynamic torque converter: a – the efficiency η and the torque ratio i_d versus the velocity ratio i_k , b – the torque coefficient λ versus the velocity ratio i_k

3. Calculation models of Hydrodynamic Torque Converter

3.1. One-dimensional model (1D)

The model, which is commonly used in the calculation of the hydrodynamic torque converter, is called “the average stream model”. The model assumes that the flow in the working space of the hydrodynamic torque converter is replaced with a single stream flow on the mean flow path. The parameters of the single stream are treated as the average parameters of all streams. This replacement allows to derive calculation formulas on the basis of a limited number of parameters, without taking into consideration all dimensions of the hydrodynamic torque converter working space. For this purpose, the introduction of further assumptions is as follows [1, 2]:

- ▶ the fluid flow is constant;
- ▶ the inlet and outlet angles of the fluid flowing in the channels are the same as the blades angles;
- ▶ the friction flow losses in the channels depend on the relative velocity of the fluid flow;
- ▶ the impact flow losses linearly depend on the impact angles;
- ▶ the inertia of the fluid flowing in channels is added to the inertia of the pump and the turbine, respectively;
- ▶ the vortex flow occurs in gaps between the pump, the turbine and the stator;
- ▶ there are no volume losses of the fluid;
- ▶ physical properties of the fluid do not depend on the pressure but depend on the temperature;

In order to obtain equations for the calculation of T_1 and T_2 torques on the basis of ω_1 and ω_2 angular velocities, the absolute flow velocity c of the average stream is projected on two planes:

- ▶ the first one passes through the axis of shaft rotation as the meridional speed c_m ,
- ▶ the other one is perpendicular to the axis of shaft rotation as the peripheral velocity c_u .

Three equations are formulated in the following way: two moment-of-momentum equations and the power balance for the hydrodynamic torque converter. The power balance follows from the principle that the net power supplied by the input shaft of the hydrodynamic torque converter is equal to the dissipated power [1]. The dissipated power includes the disc impellers friction, the bearings and the seal friction. The angular velocities of the pump ω_1 and turbine and the volumetric flow rate Q are the independent variables in this equations. The values of T_1 and T_2 torques obtained from the equations solving, together with the values of ω_1 and ω_2 angular velocities are used for the calculations of point coordinates of the non-dimensional steady-state characteristics by means of formula (1). The low accuracy of the average stream model results mainly from simplifying assumptions. On the other hand, the simplicity of the model equations is particularly useful when the calculations are repeated a number of times, for example during optimization. In addition, this model is helpful when the working space geometry of the hydrodynamic torque converter is not fully determined.

3.2. Three –dimensional model (3D)

In order to enhance the calculations accuracy of the non–dimensional steady–state characteristics of the PH 305 hydrodynamic torque converter, a three–dimensional model of the fluid flow was used. This model was based on the Navier–Stokes equations describing three–dimensional fluid flow [9, 10]. The commercial ANSYS CFX program was applied for the numerical calculation of the model. The program allowed to create additional equations for the turbulent flow in the hydrodynamic torque converter working space based on the Navier–Stokes equations. The turbulence should be taken into account when internal forces acting on the fluid molecule are significant in comparison to viscous forces [10]. Before numerical calculations of the non–dimensional steady–state characteristics of the PH 305 hydrodynamic torque converter, the ANSYS CFX option called “ k – ϵ ” was selected. The first parameter k described the turbulent kinetic energy and the second one ϵ described the turbulent dispersion. The Reynolds Number, defined as the ratio of inertia forces to viscous forces within the fluid, which determines turbulent flow was chosen as $4 \cdot 10^3$.

4. Numerical Calculations

4.1. The average stream model calculations

Before the application of the model, the parameters describing the mean path of the PH 305 hydrodynamic torque converter were established by using the estimation methods in order to enhance the accuracy of the calculations. The parameter estimation was made on the basis of the non–dimensional steady–state characteristics of the PH 305 hydrodynamic torque converter obtained from the tests and presented in Fig. 1. Computational programs solving equations of the average stream model were written in the Turbo Pascal language. The results of the calculations according to the model are shown in Fig. 10.

4.2. The CFD methods calculations

The first stage of the CFD method application was to define the working space geometry of the PH 305 hydrodynamic torque converter. It was done by creating the impellers solid models.

Due to the limited power of the computer used for the calculations by means of the ANSYS CFX program, the following simplifications were introduced:

- ▶ the short blades in the pump were replaced by long ones,
- ▶ the meridional cross–section was used as the basis for the solid model creation.

On the basis of the PH 305 specification it was established that the working surface of each impellers blade was described by a set of 398 points (199 internal and 199 external). The CATIA v5 software was used in order to define a data file including the coordinates of

these points. The impellers solid models were created on the basis of the data file by using the ANSYS Turbogrid Module (ANSYS CFX). The solid models are shown in Fig. 2.

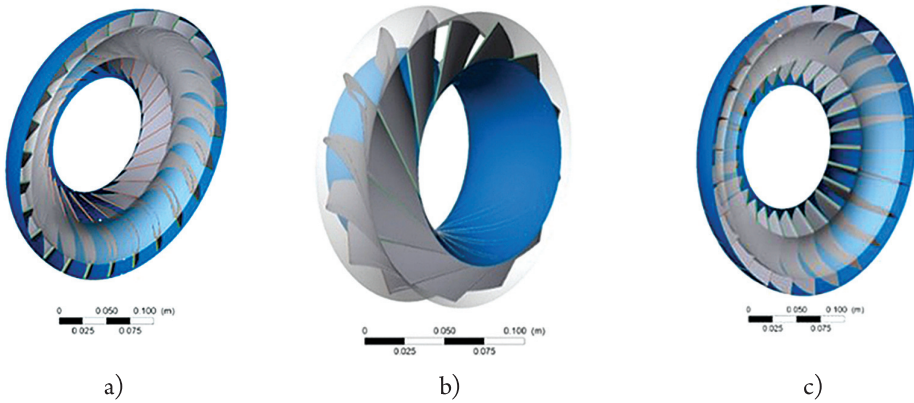


Fig. 2. The PH 305 impellers solid models created by means of the ANSYS Turbogrid Module:
a – pump, b – stator, c – turbine

In order to obtain the continuous fluid flows in the working space of the PH 305 hydrodynamic torque converter, the relationships between the input and the output flow surfaces of the impellers were determined by means of the ANSYS CFX Module, Fig. 3.

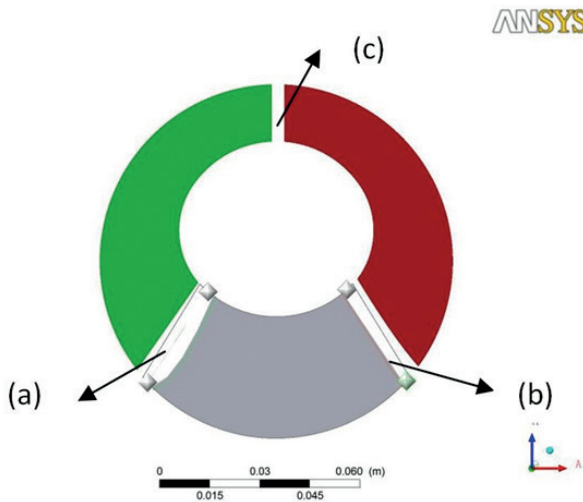


Fig. 3. Relationship between the input and the output flow surfaces of the impellers:
a – stator – pump, b – turbine – stator, c – pump – turbine

The ANSYS CFX Pre Module was used in order to create the PH 305 working space by joining the impeller grid structures. However, due to the low processing power of the computer which was applied for the numerical calculations the model was not useful. The problem was solved by dividing the PH 305 working space solid model into the blade-to-blade segments by means of the “Periodicity” option. The results of the option application are illustrated in Fig. 4.

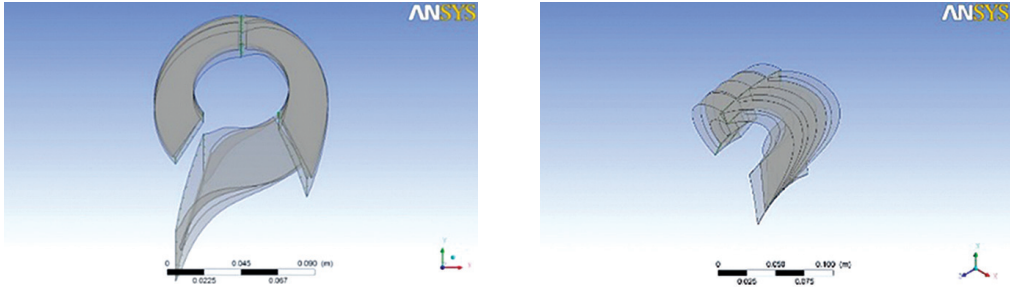


Fig. 4. Application of the “Periodicity” option for the blade-to-blade segment of the PH 305 working space

The boundary conditions and the data for the calculations of the PH 305 hydrodynamic torque converter according to the CFD model were established as shown in Table 2.

Table 2. The data and the boundary conditions for the calculations of the PH 305 hydrodynamic torque converter

Rotor	Fluid flow conditions		Turbulence
Pump	Speed, pressure, rotation axis	40 m/s 0.1 MPa X	none
Turbine	Speed, pressure, rotation axis	40 m/s 0.1 MPa X	$k-\epsilon$ model
Stator	Speed, pressure, rotation axis	40 m/s 0.1 MPa X	none

Due to the computer processing power limitation, the turbulent flow model “ $k-\epsilon$ ” was applied for the calculations of the fluid flow in the turbine. The turbine was selected because of its most complicated shape and a wide range of angular velocity [11].

The calculations were performed by means of the Stationary Model, which was a part of the ANSYS CFX-Pre module for the steady-state working condition of the PH 305 hydrodynamic torque converter. In the model the time was not an independent value. In addition, the “General Connection” option was selected from the menu list of the module in order to determine the working conditions of each impeller. As a reference pressure of the 0,1 MPa value was chosen.

The main aim of the calculations was to obtain the non-dimensional steady-state characteristics of the PH 305 hydrodynamic torque converter on the basis of:

- ▶ one-dimensional average stream model,
- ▶ three-dimensional ANSYS CFX model.

The results of the non-dimensional steady-state characteristics calculations for both models are compared in Fig. 5.

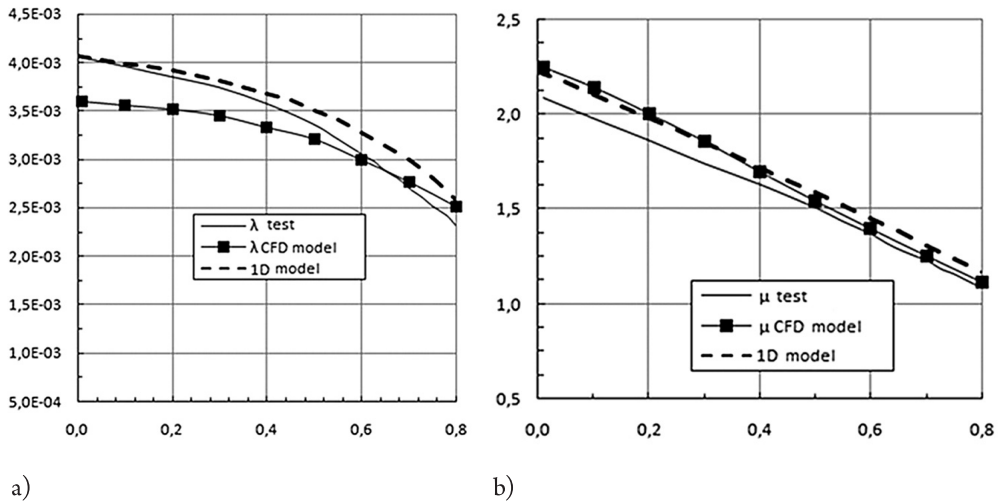


Fig. 5. The non-dimensional steady-state characteristics of the PH 305 hydrodynamic torque converter calculated on the basis of 1D and 3D models: a – torque coefficient λ versus i_k , b – the torque ratio μ versus i_k

It follows from Figure 6 that both 1D and 3D models can be successfully used for calculations of the non-dimensional steady-state characteristics of the PH 305 hydrodynamic torque converter, because the accuracy of both models is similar.

5. Conclusions

The accuracies of one-dimensional mathematical models and three-dimensional mathematical models used in the design process of the hydrodynamic torque converter for calculation of its non-dimensional steady-state characteristics were similar. This conclusion confirms the results obtained by other researchers.

The difficulties associated with the calculation of the hydrodynamic torque converter characteristics resulted from both:

- ▶ the complex fluid flow phenomena occurring in the short, strongly curved, and rotating impellers channels;
- ▶ insufficient processing power of the computer used for the calculations.

References

- [1] Kęsy Z., *Control of hydrodynamic torque converter by means of working fluid*, Wydawnictwo Politechniki Radomskiej, Radom 2003. (in Polish)
- [2] Kęsy A., *Numerical identifications of transport means*, Wydawnictwo Politechniki Radomskiej, Radom 2004. (in Polish)
- [3] Kęsy A., *Numerical modeling of hydrodynamic torque converter rotors*, Wydawnictwo Politechniki Radomskiej, Radom 2008. (in Polish)
- [4] Flack R., *Experimental flow fields in an automotive torque converter – an invited summary and review paper*, Int. J. Vehicle Design, Vol. 38, Nos. 2/3, 2005, 240–258.
- [5] Schweitzer J., Gandham J., *Computational fluid dynamics in torque converters: validation and application*, International Journal of Rotating Machinery, 9, 2003, 411–418.
- [6] A. Kęsy at al., Research project no. 2546/23/P, Technical University of Radom, stage IV, 2011.
- [7] De la Fuente P., Stoff H., Volgmann W., Woźniak M., *Numerical analysis into the effects of the unsteady flow in an automotive hydrodynamic torque converter*, The 2011 International Conference of Mechanical Engineering, London 2011.
- [8] Kęsy A., De La Fuente P., Migus M., *Realization of dynamic loads in test rig investigation of hydrodynamic sub-assemblies*, 24th Scientific Conference “Problems of working machines Development”, Zakopane, 24-27 January 2011. (in Polish)
- [9] Park J. I., Cho K., *Numerical flow analysis of torque converter using interior mixing model*, International Journal JSME, Series B, Vol. 41, No. 4, 1998.
- [10] Wollnik M., Volgmann W., Launder B., Spalding D., *The numerical computation of turbulent flows*, Computer Methods in Applied Mechanics and Engineering, 1974, 269–289.
- [11] Habsieger A., Flack R., *Flow characteristics at the pump–turbine interface of a torque converter at extreme speed ratios*, International Journal of Rotating Machinery, 2003, 419–426.

Andrzej Opaliński (andrzej.opalinski@agh.edu.pl)

Faculty of Metals Engineering and Industrial Computer Science, AGH University of Science and Technology

Mirosław Głowacki (glowacki@metal.agh.edu.pl)

Faculty of Mathematics and Natural Science, The Jan Kochanowski University, Kielce
Faculty of Metals Engineering and Industrial Computer Science, AGH University of Science and Technology

MOBILE REMOTE MONITORING SYSTEM OF WATER RESERVOIRS

MOBILNY SYSTEM ZDALNEGO MONITORINGU ZBIORNIKÓW WODNYCH

Abstract

The article presents the concept, architecture and testing of mobile monitoring system of water reservoirs. Its main elements are a remotely controlled boat with a sonar, which additionally records GPS data. The developed system could be used in several configurations for the achievement of functions such as generating bathymetric maps or the current monitoring of the bottom of a water reservoir. The main functionalities of the system have been tested and presented with the results of the tests and their analysis, conclusions and plan of further development.

Keywords: bathymetric maps, bottom monitoring, mobile systems

Streszczenie

W artykule przedstawiono koncepcję, architekturę oraz testy mobilnego systemu monitoringu zbiorników wodnych. Jego głównymi elementami są zdalnie sterowana łódź oraz echosonda rejestrująca dodatkowo dane GPS. Opracowany system może być wykorzystywany w kilku konfiguracjach, umożliwiając realizację funkcjonalności takich jak generowanie map batymetrycznych lub bieżący monitoring dna zbiornika wodnego. Główne funkcjonalności systemu zostały przetestowane i zaprezentowane wraz rezultatami testów, ich analizą, wnioskami i planem dalszego rozwoju

Słowa kluczowe: mapy batymetryczne, monitoring dna, systemy mobilne

1. Introduction and related works

Oceans and other water reservoirs are one of the least explored areas on the Earth. The need for exploration of aquatic environments applies to both large areas which are seas and oceans, as well as smaller ones, such as lakes, rivers and smaller water reservoirs. Issues related to the exploration of these environments concerning their flora [2], fauna [5], the ecosystem [6] but also the structure and the type of bottom [3, 4], apply to issues of the presented article.

In general, the issue of testing water bottom has been the subject of research for a long time and on a fairly large scale [1, 7]. Exploration of such environment is inherently difficult and expensive and requires sophisticated equipment, advanced data processing algorithms [8, 9] and a huge amount of financial resources [10, 11].

Another phenomenon that is constantly progressing in the world around us is the development of technologies, including electronic solutions, information technology and the new materials with increasingly better mechanical properties. All of this results in the possibility to create better systems and solutions, which perform their tasks faster, more accurately, efficiently and cheaper.

All these reasons have led the authors of this paper to undertake the task of developing a low-budget system, which allows remote monitoring of water reservoirs. The main functionality of the proposed system is mapping of bathymetry of the tank and monitoring its bottom as well as the structure of its surface. The main feature that distinguishes this system from other currently used ones is the cost of its implementation. It does not exceed the amount of several thousand zlotys, which is a value at least one order of magnitude lower than the cost of other systems that are currently used in the field.

2. System architecture

The presented system consists of a number of hardware components and software which collectively provide the main functionality of the system. This section describes the hardware and the two main modes of operation of the whole system.

2.1. Hardware components of the system

Figure 1 shows the major hardware components included in the system. These are (according to the numbering placed on the drawing):

- 1) Remote controlled boat with a transducer sonar built on a solid in the hull, which sends and receives signals in order to obtain information at the bottom of the water reservoir. The boat has dimensions of 64 x 41 x 22 cm and weighs about 5 kg without battery. It is made of ABS plastic and is powered by two motors screw and a gel battery pack with a capacity of 12 000 mAh.
- 2) Software for generating a bathymetric map and interpreting data obtained by an echo sounder. The system uses two different software data-processing components:

- ReefMasterPro (<https://reefmaster.com.au/>) and Insight Genesis (<https://gofreemarine.com/insight-genesis/>).
- 3) Lowrance Elite-4 HDI sonar (depth sounder) allows for collecting data from the sonar transducer, recording the data on the microSD card and visualizing them live on a 4 inch screen. The sounder receives additional data regarding GPS position, which are then used to create bathymetric maps of reservoirs.
 - 4) Wireless communication module with a sonar transducer designed for the needs of the system. The standard depth sounder is connected to the sonar transducer via a cable. In the case of this system, a wireless connection using radio transmission with a frequency of 868MHz was implemented. This allows the observation of data from the transmitter (from the boat) by the operator located on the shore of the water reservoir.
 - 5) Wireless remote controller for the boat operating in the 2.4 GHz band, which allows the system operator to control the boat on the water tank.



Fig. 1. Main hardware components of the system

The system consists of more battery packs, supplying power for the transducer and echo sounder. Those are placed in the middle of the bulkhead of the boat and near the sonar

2.2. Operating modes of the system

Implemented concept of the system allows it to operate in two main modes. They differ in the hardware configuration of the system and functionalities implemented within each mode. Both modes are shown schematically in Fig. 2.

The first mode, as described in part a) of Fig. 2 generates bathymetric maps of water reservoirs. In this mode, the operator of the system is located on the shore with the remote boat controller, and depth sounder is mounted directly on the boat floating on the reservoir. This configuration allows for linking data obtained from the sonar transducer with GPS coordinates received via echo sounder. These data are stored on a microSD card inserted in the depth sounder and then used to generate a bathymetric map of the reservoir. In the mode where the sonar is in the boat, the operator does not have current (live) information about the monitored bottom of the reservoir. It could be obtained only by analyzing logs recorded on the card.

The second operation mode of the system as described in part b) of Fig. 2 is the bottom monitoring mode. In this mode, the depth sounder is on the shore of the reservoir and the operator has the ability to continuously monitor the information returned by the transducer sonar. In this mode, the information about GPS coordinates is not collected by default, as it is related to the location of the operator and not the boat.

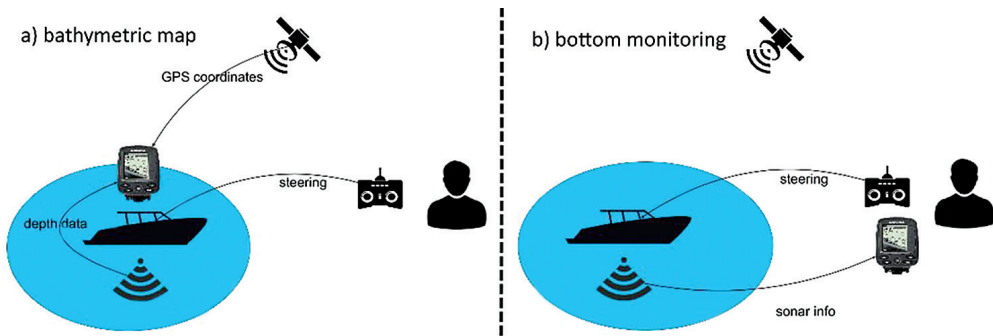


Fig. 2. Two main operating modes of the system

An additional functionality provided by the software used in the system is the ability to identify the bottom types of the reservoir, based on different characteristics of signals received by the signal processor.

3. Application and results

To evaluate the present system, a series of tests on its major features was carried out. The first test was to generate a bathymetric map of a body of water, while the other was to verify the effectiveness of the system in monitoring the bottom of the reservoir, including the detection of bottom type and finding the objects it contains.

3.1. Generating a bathymetric map of water reservoirs

The test consisting in the generation of bathymetric maps of the reservoir was carried out on the reservoir Podgórk Tynieckie on the border of Cracow and Tynec area. The test conducted 4 series of data collection (for a total of about 2 hours of boating), which allowed for generating a map of an area of about 10 hectares. A fragment of bathymetric map of the reservoir, along with the trace route and isobaths indicating its depth is presented in Fig. 3.

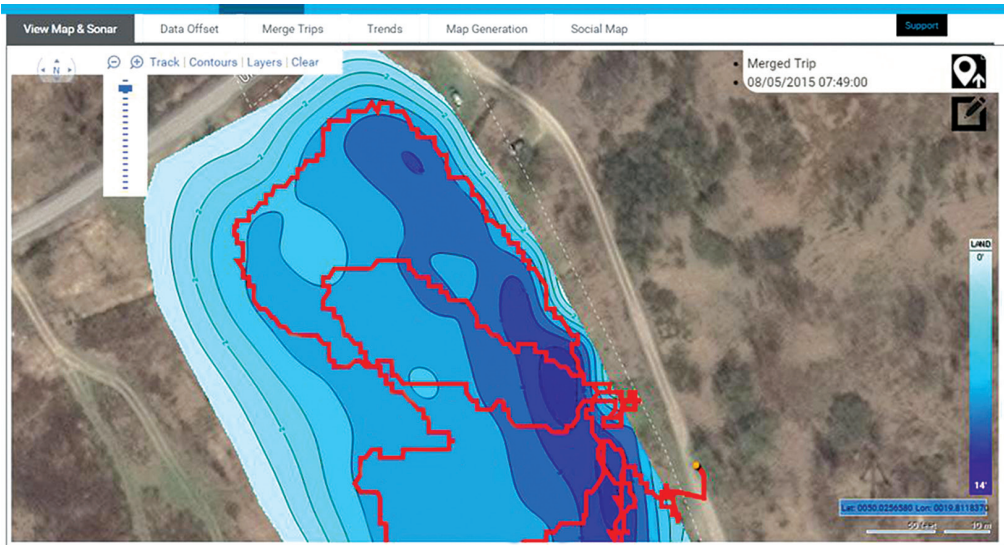


Fig. 3. Bathymetric map of Podgórk Tynieckie reservoir

The map has been developed using free environment Insight Genesis, and is publicly available on the <https://gofreemarine.com/insight-genesis> website.

3.2. Bottom monitoring tests

The second test conducted in order to verify the implementation of the assumptions associated with the system was mapping the bottom and estimating the possibility of using the system to detect objects at the bottom of the reservoir. For this purpose, we performed a series of tests on Zakrzówek reservoir in the city of Cracow. The element that has been selected for testing was sunk at the bottom of the reservoir. It was a wreck of a fishing boat with a length of about 20 m and a height of 5 m, sunk to a depth of about 15 m. A model of the sunk wreck is presented in part a) of Fig. 4.

Elements associated with the process of monitoring the bottom are shown in part b) of Fig. 4. This process was carried out in two phases. In the first phase, the boat monitored the vicinity of the wreck in the configuration with the sonar on the boat (as in the mode

a) wreck model



b) bottom monitoring

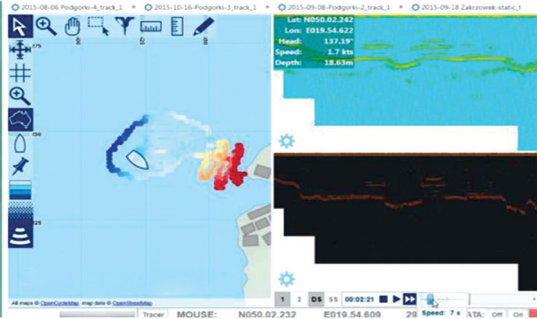


Fig. 4. a) Wreck model (<http://godiving.pl>) and b) software output for bottom monitoring

presented in Fig. 2a), which resulted in logs related to the GPS coordinates shown in Fig. 4b and 5. In the second phase, the sonar was placed near the operator, who was able to monitor the information received from the sonar transducer in a real time. The data obtained in this manner were identical with those on the far right of Fig. 4b. There we can see that during the passage of the boat on the wreck, sharp fluctuations in depth can be seen, which can be interpreted as passage above the level of the deck and wheelhouse later. Immediately, there comes the idea to use these data to carry out a three-dimensional visualization of the object, which in the current version of the system is not available.

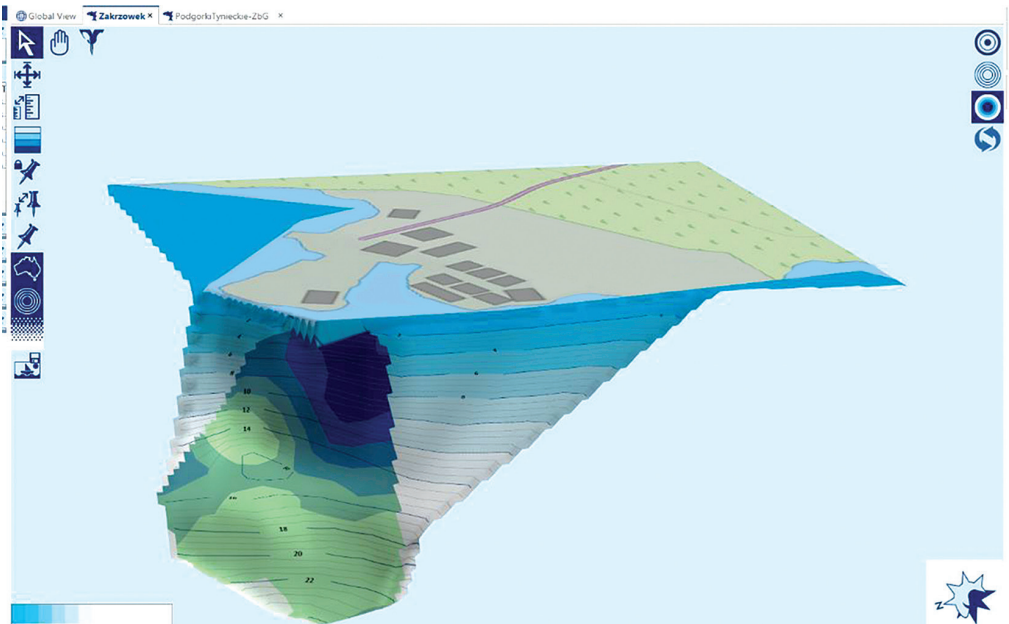


Fig. 5. Bottom types detection

Another stage of this test was to evaluate the ability to generate maps of the bottom of the reservoirs with respect to the types of the substrate, which is illustrated in Fig. 5. We can see the actual difference between the bottom layers, which roughly corresponded to the actual changes occurring on the reservoir. The conclusions of this part of the study are that the full implementation of this functionality requires an additional calibration of the signal level corresponding to various types of substrate and taking them into account in the process of interpreting the results.

The tests carried out have confirmed the practical implementation of goals, involving the development of a system for generating a bathymetric map and monitoring water reservoirs bottom.

4. Conclusions and future works

The developed system presented in this article allows for generating bathymetric maps and monitoring water bottoms. The system implemented in this architecture is much cheaper compared to the currently used professional solutions found in this area. Bathymetric maps obtained by means of the presented system are characterized by relatively high accuracy. The process of bottom monitoring provides accurate data on the depth and basic information about objects at the bottom. It can be developed in the direction of a more accurate visualization of the objects placed at the bottom of the reservoir. In this case it would be necessary to use more advanced devices such as side-scanners and efficient algorithms for processing spatial data. Another direction of development of the presented system is the automation of modules associated with boat control. The mechanism of auto-navigation would greatly facilitate the process of collecting data and generating maps, eliminating the human factor responsible for the manual control of the boat in order to cover the entire area of the reservoir. The presented system appears to be a promising platform for further development and works in a wide range of issues of science and technology related to water reservoirs monitoring and surveys.

The work has been supported by the Polish Ministry of Science and Higher Education – AGH University of Science and Technology Funds No. 11.11.110.300

References

- [1] Hakanson L., *A manual of lake morphometry*, Springer Science & Business Media, 2012.
- [2] Paira, A. R., Drago, E. C., *Origin, evolution, and types of floodplain water bodies*, [in:] *The Middle Paraná River*, Springer Berlin Heidelberg, 2007, 53–81.
- [3] Ng, S. L., Sin, F. S., *A diatom model for inferring sea level change in the coastal waters of Hong Kong*, *Journal of Paleolimnology*, 2003, 30(4), 427–440.

- [4] Sobek, S., Nisell, J., Fölster, J., *Predicting the volume and depth of lakes from map-derived parameters*, *Inland Waters*, 2011, 1(3), 177–184.
- [5] Joyeux, J. C., & Ward, A. B., *Constraints on coastal lagoon fisheries*, *Advances in Marine Biology*, 1998, 34, 73–199.
- [6] Drago, E. C., *The physical dynamics of the river–lake floodplain system*, [in:] *The Middle Paraná River* Springer Berlin Heidelberg, 2007, 83–122.
- [7] Moreno-Amich R., Garcia-Berthou E., *Hydrobiologia*, 1989, 185: 83. DOI: 10.1007/BF00006070.
- [8] Roman C., Singh H., *A Self-Consistent Bathymetric Mapping Algorithm*, *Journal of Field Robotics*, 2007, 24(1-2), 23–50.
- [9] Regulski K., Szeliga D., Kusiak J., *Data Exploration Approach Versus Sensitivity Analysis for Optimization of Metal Forming Processes*, *Key Engineering Materials*, Vol. 611–612, 2014, s. 1390–1395.
- [10] Gao J., *Bathymetric mapping by means of remote sensing: methods, accuracy and limitations*, *Progress in Physical Geography*, 33(1), 2009, 103–116.
- [11] Tripathi N. K., Rao A. M., *Bathymetric mapping in Kakinada Bay, India, using IRS-1D LISS-III data*, *International Journal of Remote Sensing*, 23(6), 2002, 1013–1025.

Paweł Piątek (piatekpawel24@gmail.com)

Graduate of the Institute of Applied Informatics, Faculty of Mechanical Engineering,
Cracow University of Technology

EVALUATION OF PARTICLE SIZE DISTRIBUTION OF AGGREGATES
IN ASPHALT CONCRETE BY MEANS OF IMAGE ANALYSIS SOFTWARE

POMIAR ROZKŁADU WIELKOŚCI KRUSZYW W BETONIE ASFALTOWYM
PRZY ZASTOSOWANIU OPROGRAMOWANIA DO ANALIZY OBRAZU

Abstract

Analysis of (cylindrical) samples of asphalt concrete, in terms of weight and size distribution of different fractions of aggregates and by means of mechanical methods is a complicated and time consuming process. This article presents a proposal of a method for the same kind of analysis, but without the need for machining. The suggested method is based solely on a computer based analysis of photographs of the samples. The mechanism described in this paper is only a preliminary process, illustrating the potential use of an image analysis for this type of study.

Keywords: roads building, asphalt concrete, aggregate distribution, image analysis

Streszczenie

Analiza (walcowych) próbek betonu asfaltowego, pod kątem rozkładu wielkości/wagi różnych frakcji kruszywa, z użyciem metod mechanicznych jest procesem złożonym i długotrwałym. W artykule przedstawiono propozycję metody takiej analizy bez konieczności jakiegokolwiek obróbki mechanicznej. Zaproponowana metoda bazuje wyłącznie na komputerowej analizie zdjęć wykonanych próbek. Przedstawiony w artykule mechanizm jest jedynie procesem wstępnym, przedstawiającym potencjał wykorzystania analizy obrazu do tego typu badań.

Słowa kluczowe: budowa dróg, beton asfaltowy, rozkład kruszywa, analiza obrazu

1. Introduction

The process of measurement of the size distribution of aggregates in asphalt concrete is used in approval procedures for the use of road objects such as roads, expressways and motorways. Such studies help to check whether the Contractor performed construction works in accordance with building regulations, and whether the actual state of the road corresponds with the documentation. Every planned road has its own set of required properties, depending on its location, planned traffic, tonnage limits, etc. However, most of these parameters are included in standards, describing road construction and maintenance, pavement technologies [3], or a type and kind of construction aggregate [2]. Apart from the approval process, the same procedure is used for a periodic examination or in case of events of natural disasters [5]. In this case, surface tests are performed to examine whether the road is suitable for further use or there is a need to perform a maintenance or repair procedure. For example, during major quakes, construction aggregate contained inside asphalt concrete may crack, turn into finer grain and thus lose its original stiffness parameters.

A full examination should be performed in accordance with relevant procedures [4], i.e. cutting out a sample of asphalt concrete from the study area. The sample has the form of a cylinder with a diameter of 100, 150 or 200 mm, with a depth of about 400 mm (although in case of checkups it does not exceed 250 mm in depth). The sample consists of three layers: base, binder and a surface course. The deeper the layer, the more stiff and more coarse aggregate. For a change, the top layer contains more of fine aggregate. There is a justified purpose for each layer. Then, the tests are carried out, as described in the next chapters.

2. Preparation of test samples

For the purpose of the experiment, the samples were prepared according to the author's own procedure, instead of using samples cut out from a road. This was performed to have full knowledge of the sample contents.

The samples are compacted in the Marshall Compactor, and then flooded with asphalt. Aggregate that was used to test this is an assortment (type 1, according to PN-B-11112:1996 norm) of granulated, crushed aggregate, in the following fraction groups: 2/4; 5,6/8; 11,2/14. The X/Y range denotes that a mix of aggregate underwent the procedure a mechanical sieving by means of a sieve with a square mesh. The fraction was able to pass through a sieve which has a Y (and larger) mesh, but was unable to pass through a sieve with an X mesh. Thus, in this fraction there are particles of a diameter greater than X and smaller than Y. The experiment used the grain of all the above groups, in the article and graphs referred to as: „Small” (S), „Medium” (M) and „Large” (L), respectively. 7 samples were prepared, representing all possible combinations of the groups. In the mixed samples, the weight of each fraction group was identical. The contents of each aggregate in the samples formed from two groups was 50% by weight, and those formed from three groups was 33% by weight. As the aggregate used is derived from a single source, thus it has the same density. It can be assumed that if the weight of different fractions of aggregates

are equal, their volume is the same. During the preparation of subsequent samples, the amount of asphalt was varying (and excessively high in relation to the requirements of PN-S-96025:2000 [3]). At this stage of the experiment, asphalt content in each sample is not essential.

The tested samples were prepared as follows:

- 1) Identical sample weight of each fraction was prepared.
- 2) Individual samples were made in such a way that individual fractions or mixtures of the same mass fractions was poured into the prepared containers, so that the entire sample was approx. 1200 grams. Aggregates were then mixed in a container. Asphalt (MODBIT 45/80-55) was heated to 180°C and poured with a significant overmeasure in order to completely fill all voids in the mineral mix. The mix was stirred to paste the asphalt all over the grain.
- 3) The mix was then poured into cylinders. After a slight cooling of the mixture, a Marshall Compactor was used to knead sample and integrate smaller grains in the open spaces. The sample prepared in this way was about 10 cm high.
- 4) The samples were left for 12 hours to fully cool down to ambient temperature (15~20°C).
- 5) Each sample was sliced several times using a stone cutting saw. This way, four subsamples and 6 uniform surfaces, with a visible distribution of aggregate on their both sides, were acquired as material for further studies.

3. The mechanical method of analysis of aggregate distribution

The mechanical method involves a preliminary, mechanical cleaning of a cylindrical sample with a wire brush, to clean it from free, loose parts. The sample is then placed in a laboratory dryer, preheated to 180°C, and after 30 minutes it is hand crushed.

The resulting mixture of asphalt and minerals (not asphalt concrete anymore) is a subject of processing in an automatic asphalt extractor, to get a mixture of powder and dust. The process takes approximately one and a half hour. The asphalt content of the sample is calculated based on a mass difference of the unprocessed sample and the resulting mixture. The combination of ingredients is then sifted to determine the percentage of each fractions, to compare its composition with the recipe.

Each layer of the sample is analysed individually. Therefore, before the main examination, each piece must be sliced in such a way so as to separate the layers (base, binder and a surface course).

4. The method of image analysis of distribution of aggregates

The proposed method of video analysis involves cutting each sample into slices which are then photographed to obtain high quality images. All image files have to be preprocessed. Methods of dealing with compacted group of elements, such as concrete aggregate, of various shapes and sizes in the photographs, are well known and documented [1]. Shortly, each

procedure requires scaling of the photographs to a desired resolution. In the case where we are interested only in two areas of brightness, it is necessary to perform binarization to separate the elements from each other. The resulting image consists of bright, closed shapes, varying in size (intersections of concrete aggregates) on a dark background (asphalt, filling of voids between aggregates). The rest of the analysis and the methods of the conduct are up to the researcher.

To perform the procedure, it is necessary to scan the image both horizontally and vertically, with lines distant from each other by a fixed number of millimeters (or pixels), then compute distribution statistics of length of the „bright” lines (that is, those which pass through the aggregate) for each sample. Based on this principle, a simple database of distribution statistics was created, with the use of test samples made from single and mixed aggregate fractions. It can be assumed that after creating a large database with many uniform and mixed fractions, there will be a way to create a method of calculation, for unknown samples, to find the percentage of a fraction distribution.

The article describes the initial stage of the procedure, which is an analysis of the only samples containing fractions whose size and percentage of the content are known. Mixed samples are included only as a comparative element, because the method to account for their composition is not yet developed.

5. Software

A special software was created to perform preliminary operations of the photographs and to analyze the image. It was decided that for every intermediate stage of the process, a BMP image file will be saved, not to lose any information of every phase of transformations.

First, the software resamples photographs to a desired size. Digital cameras make images of high resolutions. It is assumed that every image will be scaled to 10 pixels per millimeter resolution. At this stage, there is no mechanism to automatically scale the images, users are required to do it on their own. To ease scaling for the user, a photograph should be taken with a ruler in the background. This allows for simplifying the operation by letting the user select a known distance on the image and then type in the real distance.

Then the user selects a rectangular area of the image and cuts it with a cropping tool. In the future, a tool will be added to distinguish between the sample and the background to remove the need for the user to select the sample area.

In the next step, to separate the aggregate from its surroundings, namely the brighter area from the darker area, an image will be converted to a grayscale and then binarized. The grayscale conversion uses generic coefficients for every colour component. Due to the fact that each sample has a slightly different luminosity (it depends on technology of the sample), a fixed threshold for brightness of asphalt and aggregates cannot be used. In addition, the color of the aggregate and the asphalt slightly change even for a single sample. In the course of the experiment, it was determined that classical edge detection algorithms are not suitable for this.

The method of dynamic image analysis was applied in terms of brightness. The image was scanned pixel by pixel, and bright pixel occurrence statistics were calculated. Because

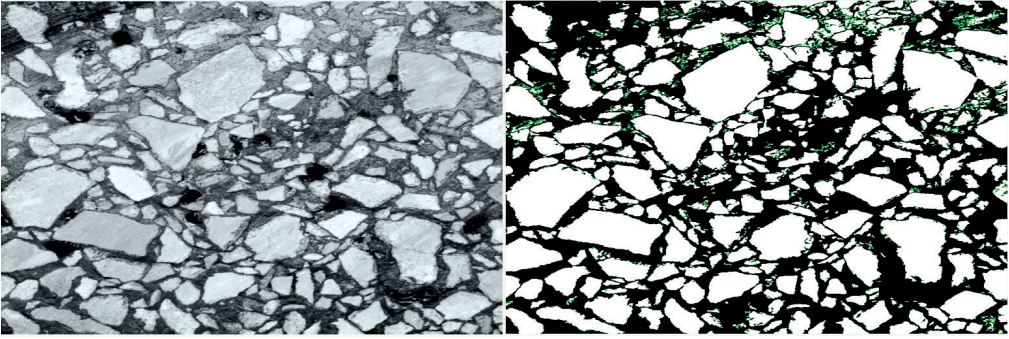


Fig. 1. Example photographs of a sampled mixed fraction and the image after binarization

a significant portion of the image is an aggregate's slice, it was assumed that in the distribution there must be a relatively large „bright” range. However, in the „dark side” there must be a corresponding range for the asphalt. The problem arises in the analysis of brightness that lies between these maxima. It was assumed that in this area, there is a point of minimum for the statistical occurrence of brightness. Therefore, the areas darker than on this point are assumed to be asphalt, and similarly brighter areas belong to aggregate. All pixels which belong to this area were additionally treated with an algorithm, to bring them closer to the brighter or darker range. Additionally, all orphaned pixels, i.e. every lone pixel of an undetermined belonging. Also, all small dark areas contained inside the bright sections were eliminated – it could mean there is a void inside the aggregate, which in practice never occurs. The described algorithm of binarization helped get a fairly accurate reflection of the sample, which can be seen in the picture below.

6. Distribution of the aggregate size for the test samples

The software, as described in chapter 4, was used to perform a scan of binarized samples. The length of a line through the white area (hereinafter „Section”) is an indicator of the area size. All the Sections directly adjacent to the edge of the image were rejected due to the fact

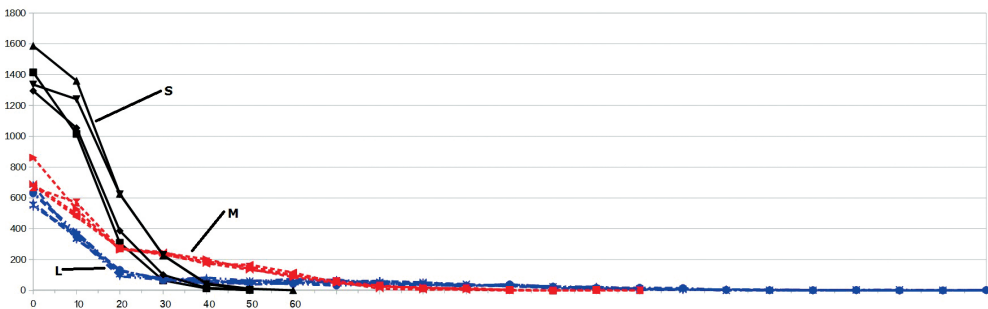


Fig. 2. Distribution of Sections for uniform samples

they may be unreliable. As only a fraction of aggregate might be scanned, it is not known where the Section begins or ends. All the Sections were grouped in ranges named 0, 10, 20 and forth. The size of each Section was mathematically approximated to the nearest range. Since the pictures were scaled to 10 pixels per millimeter, the resulting areas provide a resolution of one millimeter distribution of Sections. Individual distributions were denoted as letters, abbreviations of the sample size: „Small” (S), „Medium” (M) and „Large” (L).

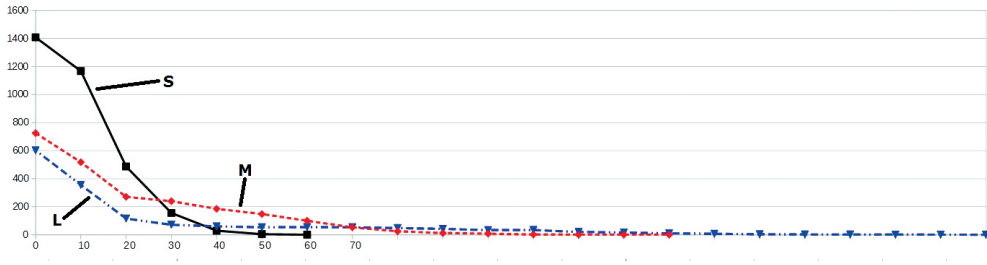


Fig. 3. Distribution of Sections for uniform samples (averaged values for the types of samples)

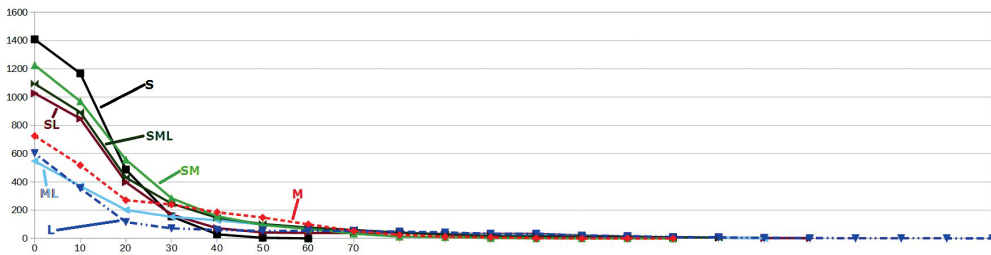


Fig. 4. Distribution of Sections for all samples (averaged values)

When slicing at random a three-dimensional object and then making its two-dimensional representation, small areas tend to occur more often than large areas. This is clearly visible on the example of a significant spread of the Sections distribution of samples 2/4 which contain aggregates of diameters ranging from 2 to 4 mm. In that example, there is an occurrence of Sections larger than 4, which do not exist in a physical sample. However, these are only isolated incidents and are associated with the inaccuracy of the binarization algorithm. The algorithm indentified two adjacent small areas as a single larger area.

It can be spotted on the diagrams that there is a substantial representation of the „0” measurement for each sample. The method gives inaccurate results for image areas of intermediate, unsettled brightness. By averaging the distribution Sections of samples, the differences between them can be distinguished. Due to the scale of the graph it is not visible, but after enlarging the areas of M and L Sections, differences between individual samples can be seen.

Samples ML are very interesting, there is a clear distinction of distribution in the „measures”. It would seem that small Sections should fall somewhere between samples M and L, but it turned out that they fell below the L section. Samples SL also look interesting: in the initial distribution the Sections are similar to S, but for larger Sections the chart „flattens” like for L samples.

7. Conclusion

The first objective of the experiment was to develop a software for the pretreatment of photographs of samples, the binarization, scanning and creation of distribution statistics of Sections. The first phase was a success, although some things will be improved (eg. the binarization algorithm) and additional features will be added (eg. generating full reports of the scans, not only tables).

The second objective was to scan the prepared samples and demonstrate the distribution occurring in the fractions. The graph shows that uniform samples differ considerably. Also, distributions for the samples of mixed fractions are distinct enough to easily classify the mixed samples only with the knowledge of the distribution of homogeneous fractions. However, this would be possible only to distinguish between S, M and L fractions, because the determination of the exact size of fractions is not possible at this stage.

Based on these results, it was found that it would probably be possible to accurately (within a certain error in estimation) determine the percentages of fractions of unknown size and their sizes in the scanned samples. To do this, it is necessary to create a database containing all the possible combinations of distributions for samples of homogeneous and mixed fractions. There are not too many combinations, as fractions are prepared in groups of size ranges, described as size „from-to”. With the database, one could scan a sample, and using a kind of an inference algorithm, perform an „approximation” of the distribution, interpret the deviation points and on this basis determine the actual percentage distribution of aggregate and its size. At this point, it has not yet been found what algorithm should be used. Further studies will be presented to build the database and to create the inference algorithm.

References

- [1] Department of Civil Engineering, Yokohama National University, Japan, *Image Analysis Techniques on Evaluation of Particle Size Distribution of Gravel*, G. H. A. Janaka J. Kumara, Kimitoshi Hayano, Keita Ogiwara.
- [2] Generalna Dyrekcja Dróg Krajowych i Autostrad, *Kruszywa do mieszanek mineralno-asfaltowych i powierzchniowych utrwaleń na drogach krajowych*, WT-1 2014 – Kruszywa – Wymagania Techniczne, Załącznik do zarządzenia Nr 46 Generalnego Dyrektora Dróg Krajowych i Autostrad z dnia 25.09.2014 r.
- [3] Generalna Dyrekcja Dróg Krajowych i Autostrad, *Nawierzchnie asfaltowe na drogach krajowych*, WT-2 2016 – część II – Wykonanie warstw nawierzchni asfaltowych

– Wymagania Techniczne, Załącznik do zarządzenia Nr 7 Generalnego Dyrektora Dróg Krajowych i Autostrad z dnia 09.05.2016 r.

- [4] Jaskuła P., *Instrukcja laboratoryjnego badania szczepności międzywarstwowej warstw asfaltowych wg metody leutnera i wymagania techniczne szczepności*, opracowano w Katedrze Inżynierii Drogowej Politechniki Gdańskiej, opracowano na zlecenie: Generalnej Dyrekcji Dróg Krajowych i Autostrad.
- [5] Generalna Dyrekcja Dróg Publicznych, Instytut Badawczy Dróg i Mostów, *Katalog Wzmocnień i Remontów Nawierzchni Podatnych i Półsztywnych KWRNPP-2012*, opracowanie techniczne, Warszawa, listopad 2012.

Karol Osowski

Zbigniew Kęsy

Andrzej Kęsy (akesy@op.pl)

Institute of Applied Mechanics and Energetics, Faculty of Mechanical Engineering,
Kazimierz Pulaski University of Technology and Humanities in Radom

Artur Olszak (artur.olszak@ins.pulawy.pl)

New Chemical Syntheses Institute, Puławy

APPLICATION OF NUMERICAL CALCULATIONS IN THE DESIGN PROCESS OF HYDRODYNAMIC TORQUE CONVERTER

ZASTOSOWANIE OBLICZEŃ NUMERYCZNYCH W PROCESIE KONSTRUOWANIA PRZEKŁADNI HYDROKINETYCZNEJ

Abstract

The use of numerical calculations to assess the impact of construction parameters on properties of a hydrodynamic torque converter has been presented in the article. The calculations have been based on a verified mathematical model of the transmission system including a hydrodynamic torque converter.

Keywords: numerical methods, mathematical model, hydrodynamic torque converter

Streszczenie

W artykule przedstawiono zastosowanie obliczeń numerycznych do oceny wpływu parametrów konstrukcyjnych na właściwości przekładni hydrokinetycznej. Obliczenia przeprowadzono w oparciu o zweryfikowany model matematyczny układu napędowego z przekładnią hydrokinetyczną.

Słowa kluczowe: metody numeryczne, model matematyczny, przekładnia hydrokinetyczna

1. Introduction

In the design process of technical systems, mathematical models are applied for the construction analysis which allows for defining the impact of construction parameters on the equipment performance. It is very costly and time consuming to analyze a real object. Mathematical models are widely applied for testing technical dynamic systems including mechanical systems. It is caused by the increase of system speed and loads as well as greater demands concerning durability, reliability and quality control. At the current stage of design development, due to the common usage of computers, complex mathematical models are created and their equations can be solved only by means of numerical methods. Solving the equation of a model is connected with writing a computer program, its testing and doing numerical calculations. The way of carrying out these tasks is connected with defining a method for solving a given problem, accuracy of results and selection of a programming language. To establish a method for solving a model equation, a verification of results of numerical calculations should be done depending on checking of the compatibility of the obtained results with the performance of a real system.

The wide application of the hydrodynamic torque converter in the design of machine drive systems and devices resulted in the development of research connected with the improvement of sub-assembly characteristics. According to many theoretical considerations concerning the hydrodynamic torque converter design, the shape of a working space of blade wheels has a great impact on the performance of this sub-assembly [1, 2]. In the process of hydrodynamic torque converter design, the selection of optimal construction parameter values plays a significant role [3–5].

In the article, numerical calculations have been introduced for the assessment of the impact of blade wheel construction parameters on the properties of a hydrodynamic torque converter. The calculations have been carried out on the basis of a mathematical model of a drive system with a hydrodynamic torque converter which has been introduced in the paper [6]. In order to verify the obtained results of calculations, a comparison has been done of steady-state characteristics received on the basis of experimental research. A hydrodynamic PH1 280 1 type torque converter has been the object of the research.

2. Assessment indicators and construction parameters of a hydrodynamic torque converter

The construction of a hydrodynamic torque converter working in a drive system of a selected means of transport should meet kinematic, dynamic, operational and economic requirements, as well as those connected with a motor drive [7]. Steady-state characteristics are the main source of information on the basis of which construction assumptions can be assessed:

$$i_d = M_2 / M_1 \quad (1)$$

where: M_1 , M_2 – torque of the input and output shaft;

$$\eta = i_d i_k \quad (2)$$

with $i_k = \omega_2 / \omega_1$

where: ω_1, ω_2 – angular velocity of the input and output shaft;

$$\lambda_{M,1} = \rho \omega_1^2 D^5 \quad (3)$$

where: ρ – working fluid density,

D – active diameter of hydrodynamic torque converter.

On the basis of steady-state characteristics, the following assessment indicators have been determined:

- ▶ maximum efficiency $\eta_{\max} [-]$,
- ▶ maximum dynamic transmission ratio $i_{d0} [-]$,
- ▶ maximum moment coefficient $\lambda_{M,1\max} [1/\text{rad}^2]$,
- ▶ permeability p , defined by the formula:

$$p = \lambda_{M,1\max} / \lambda'_{M,1} [-] \quad (4)$$

economic range of operation or $d_{\eta p}$, defined by the formula:

$$d_{\eta p} = i_{k,\eta p, \max} / i_{k,\eta p, \min} [-] \quad (5)$$

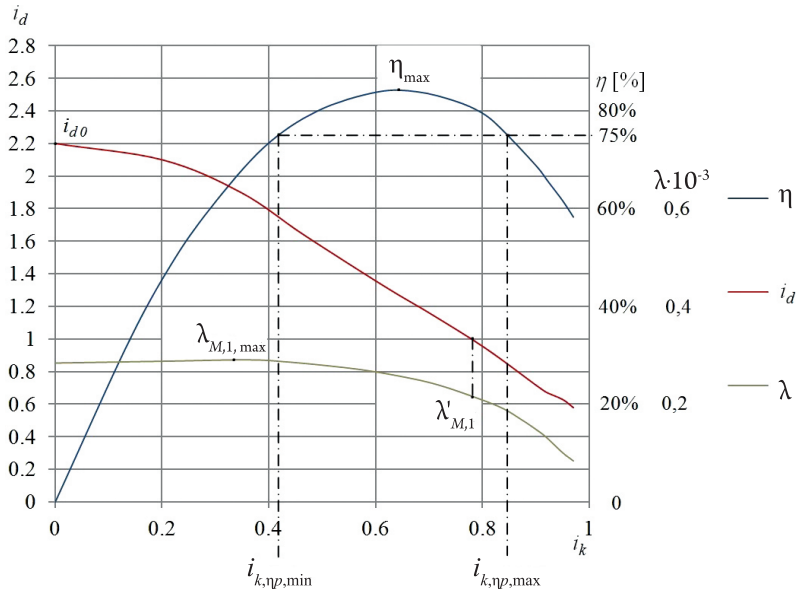


Fig. 1. Indicators: η_{\max} , i_{d0} , $\lambda_{M,1\max}$ and $d_{\eta p}$ determined on the basis of steady state characteristics

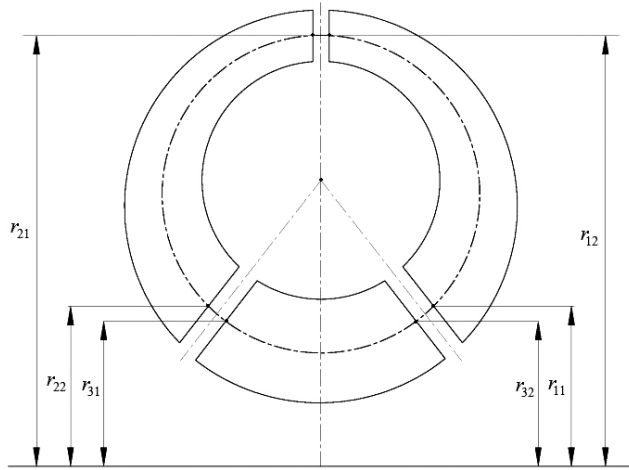


Fig. 2. Blade wheel radiuses of a hydrodynamic torque converter

They enabled the assessment of hydrodynamic torque converter properties. The indicators: η_{\max} , i_{d0} , $\lambda_{M, 1\max}$ and $d_{\eta p}$ have been defined in Fig. 1.

It is usually assumed that hydrodynamic torque converter parameters are radiuses and angles at the input and output of blade wheels defined on the average line of channels [8]. Radiuses of blade wheels, that is, r_{11} , r_{12} , r_{21} , r_{22} , r_{31} , r_{32} for a three-stage hydrodynamic torque converter (pump, turbine, stator) have been defined in Fig. 2. Blade angles β_{11} , β_{12} , β_{21} , β_{22} , β_{31} , β_{32} correspond to the radiuses.

3. Mathematical model used to assess the impact of construction parameters on the assessment indicator of a hydrodynamic torque converter

In order to assess the impact of construction parameters of blade wheels on the assessment indicators of the hydrodynamic torque converter, mathematical model equations of the hydrodynamic transmission system have been used, written in the following form [7]:

$$\begin{aligned}
 M_s &= \rho k_{12/32} Q^2 + \rho r_{12}^2 \omega_1 Q \\
 M_r &= \rho k_{12/22} Q^2 + \rho r_{12}^2 \omega_1 Q - \rho r_{22}^2 \omega_2 Q \\
 a_{1st} \omega_1^2 + a_{2st} \omega_2^2 + a_{3st} Q^2 + a_{4st} \omega_1 Q + a_{5st} \omega_2 Q &= 0
 \end{aligned} \tag{6}$$

where:

- M_s – engine torque reduced on the shaft of the pump blade wheel,
- M_r – torque resistance movement reduced on the shaft of the turbine blade wheel,
- k, a – constant coefficients, depend on radiuses r and angles β blade wheels,
- Q – volumetric flow rate.

A detailed description of the mathematical model of a hydrodynamic torque converter as well as the way of solving equations of the model have been shown in the paper [7].

4. Verification of mathematical model

The mathematical model of a hydrodynamic torque converter used for calculations has been verified by means of comparing steady-state characteristics calculated on the basis of the mathematical model with steady-state characteristics obtained on the basis of experimental research. To improve the accuracy of linear relationship between coefficients of friction losses ϕ_1, ϕ_2, ϕ_3 and angles shock losses α_u :

$$\phi = f(\alpha_u) \tag{7}$$

Coefficients of the function described with formula (7) have been selected as a result of the estimation according to the procedure presented in the paper [7].

The verification has been made for a hydrodynamic PH1 280 1 type torque converter with the active diameter of $D = 280$ mm, used in forklifts. The values of construction parameters of the hydrodynamic torque converter included in the technical specification are shown in Table 1.

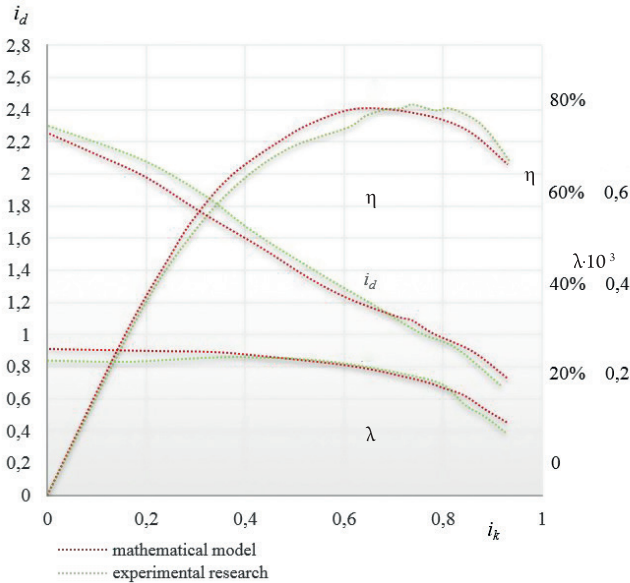


Fig. 3. Steady-state characteristics of type PH1 280 1 hydrodynamic torque converter obtained for the following parameters: $\omega_1 = 200$ rad/s, $T = 96^\circ - 104^\circ\text{C}$

Table 1. Basic construction parameters of a PH1 280 1 hydrodynamic torque converter

Radiuses	r_{11}	r_{12}	r_{21}	r_{22}	r_{31}	r_{32}
Value [mm]	0,085	0,13	0,13	0,085	0,075	0,075
Blade angles	β_{11}	β_{12}	β_{21}	β_{22}	β_{31}	β_{32}
Value [°]	119	111	44	143	105	27

Steady-state characteristics have been made for angular the velocity $\omega_1 = 200$ rad/s and working fluid temperature $T = 96^\circ \div 104^\circ\text{C}$. Steady-state characteristics of a hydrodynamic PH1 280 1 torque converter obtained on the basis of numerical calculations and experimental research have been shown in Fig. 3.

On the basis of the comparison of the steady-state characteristic obtained on the basis of experimental research, one can claim that the standard error of verification for all the curves shown in Fig. 3 does not exceed 8%, which is acceptable during the design process of a hydrodynamic transmission system.

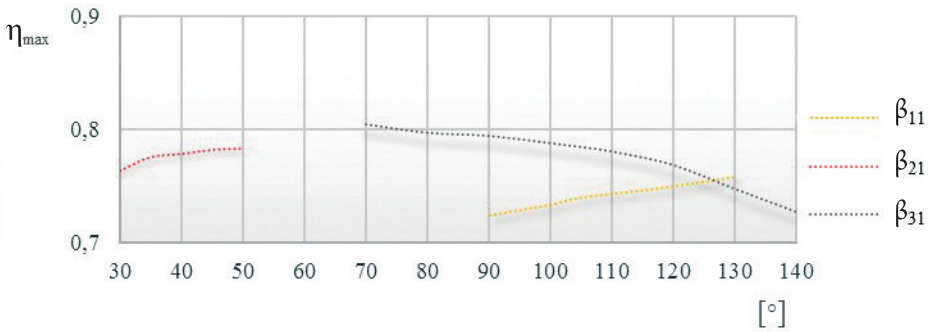


Fig. 4. Impact of $\beta_{11}, \beta_{21}, \beta_{31}$ on η_{\max} for PH1 280 1 type hydrodynamic torque converter

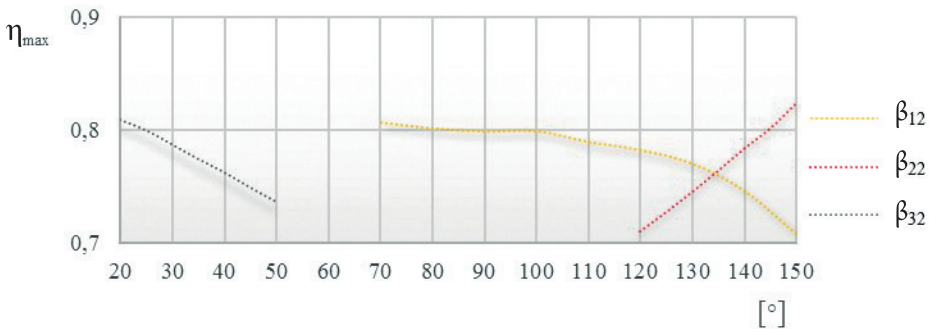


Fig. 5. Impact of $\beta_{12}, \beta_{22}, \beta_{32}$ on η_{\max} for PH1 280 1 type hydrodynamic torque converter

5. Assessment of construction parameters on hydrodynamic torque converter assessment indicators

On the basis of the mathematical model of the transmission system including a hydrodynamic torque converter (6), (7) and computational written programs in Delphi 7 Enterprise, tests of the impact of construction parameters of blade wheels on hydrodynamic torque converter assessment indicators have been made.

For example, in Figs. 4 and 5, the results of calculations concerning the impact of the angles β_{11} , β_{12} , β_{21} , β_{22} , β_{31} , β_{32} on the indicator η_{\max} have been illustrated. The calculations have been made for subsequent values of the selected angle within the accepted range. Ranges of angle values have been determined on the basis of real constructions of hydrodynamic torque converters.

As it is shown in Figures 4 and 5, the increase of angle values β_{11} and β_{22} results in the increase of maximum efficiency η_{\max} , whereas the increase of angle values β_{12} , β_{31} and β_{32} causes a decrease. The increase of β_{21} practically does not change the maximum efficiency value. If it is significant for the transmission system design to obtain the greatest values of maximum efficiency η_{\max} , it is reasonable to select such angle values β_{11} , β_{12} , β_{21} , β_{22} , β_{31} , β_{32} that will fit in strictly determined value ranges. The angle values ranges for which the maximum efficiency has the greatest values have been shown in Table 2.

Table 2. Angles value ranges for which maximum efficiency takes the greatest values

Description	β_{11}	β_{12}	β_{21}	β_{22}	β_{31}	β_{32}
Value ranges [°]	120, 130	70÷80	40÷50	140, 150	70÷80	20, 30

The deviation between the angle value ranges given in Table 2 and the values given in Table 1 for the hydrodynamic PH1 280 1 type torque converter occur since during the design of this hydrodynamic torque converter, the remaining assessment indicators have been considered.

6. Conclusions

On the basis of the considerations presented in the paper that deals with a hydrodynamic PH1 280 1 torque converter, the following conclusions have been formulated:

1. Numerical calculations carried out on the basis of a mathematical model of the transmission system allow for analyzing the assessment of the impact of construction parameters on hydrodynamic torque converter assessment indicators.
2. As it follows from the verifications, mathematical models applied for calculations as well as computational programs used to solve equations of this model allow for modelling steady-state characteristics of a hydrodynamic torque converter with the accuracy which is sufficient for engineering aims.
3. Applications of the numerical calculations can be used during the design of a hydrodynamic torque converter as a supplement of experimental research.

References

- [1] Osowski K., *Systemy ekspertowe wspomagające proces konstruowania i eksploatacji przekładni hydrokinetycznej*, rozprawa doktorska, Uniwersytet Technologiczno-Humanistyczny im. Kazimierza Pułaskiego w Radomiu, Radom 2015.
- [2] Wei W. and Qingdong Y., *Study on Hydrodynamic Torque Converter Parameter Integrated Optimization Design System Based on Tri-Dimensional Flow Field Theory*, SAE International Journal of Fuels and Lubricants, 1(1), 2009, 778–783.
- [3] Kęsy A., Kądziela. A., *Construction Optimization of Hydrodynamic Torque Converter with Application of Genetic Algorithm*, Archives of Civil and Mechanical Engineering, Vol. 11, No. 4, 2001, 905–920.
- [4] Kęsy A., *Numeryczna identyfikacja i optymalizacja napędu hydrokinetycznego środków transportu*, Monografia, Politechnika Radomska, Radom 2004.
- [5] Kęsy Z., Kęsy A., Sarnik P., *Dobór przekładni hydrokinetycznej do silnika napędowego z wykorzystaniem optymalizacji wielokryterialnej*, Zeszyty Naukowe Wydziału Mechanicznego nr 32, Wydawnictwo Uczelniane Politechniki Koszalińskiej, Koszalin 2002.
- [6] Kęsy Z., *Sterowanie przekładni hydrokinetycznej cieczą roboczą*, Monografia, Politechnika Radomska, Radom 2003.
- [7] Kęsy Z., *Hydrokinetyczne układy napędowe*. Monografia. Politechnika Radomska, Radom, 2001.
- [8] Osowski K., Kęsy A., *Systemy ekspertowe wspomagające proces konstruowania i eksploatacji przekładni hydrokinetycznej*, Mechanik 12/2013.

Robert Płatek (robert.platek@pl.abb.com)

Łukasz Malinowski

ABB Corporate Research, Krakow

Piotr Zwoliński

Department of Machine Design and Operation, AGH University of Science and
Technology

NUMERICAL ANALYSIS OF DAMAGE IN SILICA FILLED EPOXY PRODUCTS USING XFEM AND ITS VERIFICATIONS

ANALIZA PROCESU PĘKANIA W PRODUKTACH Z IZOLACJĄ ŻYWICZNĄ PRZY WYKORZYSTANIU METODY XFEM

Abstract

The paper summarizes the study of cracking phenomena in silica filled epoxy material. Numerical analyses of cracking phenomena were performed using Extended Finite Element Method (XFEM) for a full scale element as well as in a microscale, for the Representative Volume Element (RVE). Experimental verification consists of both C2 tests for real products and *in-situ* tensile tests and microstructural observations with the Scanning Electron Microscope (SEM). At the end, a summary with conclusions related to the prepared numerical analyses and experiments is included.

Keywords: XFEM, cracking, epoxy insulation, in-situ tests, C2 test

Streszczenie

W artykule przedstawiono wyniki analiz pęknięcia izolacji żywicznej wypełnionej kwarcem. Analizy numeryczne przeprowadzone były dla obiektu w pełnej skali, jak i dla próbki reprezentatywnej (RVE) w mikroskali. Weryfikacja eksperymentalna zawierała obserwacje produktów po testach C2, testy *in-situ* oraz obserwacje pod mikroskopem zniszczonej struktury. Podsumowanie wraz z wnioskami z badań zawarto na końcu artykułu.

Słowa kluczowe: XFEM, pęknięcie, izolacja żywiczna, testy *in-situ*, test C2

1. Introduction

Nowadays, we can observe a trend of growing requirements for different kinds of products. This especially relates to power products which should be more and more robust. Some of the representative ones are medium and high voltage electrical components, where epoxy resin-based systems with silica filler are widely used as insulation. Such products are required to operate in harsh environments. This may activate the process of formation and propagation of cracks within the resin material, which can be one of the failure modes. The cracking phenomenon affects also manufacturing [1]. Epoxy based parts are very often produced by casting, during which (post)curing cracking may appear if the process is not optimized. Therefore, understanding the cracking phenomena is very desirable, as it could give additional possibilities to modify the composite, allow for a better optimization of production process parameters and would make epoxy based products more robust under harsh conditions.

2. Silica filled epoxy

In the last 30–40 years, epoxy resins have found widespread applications in the manufacturing of medium and high voltage electrical components. However, their low thermal conductivity as well as relatively low toughness (resistance to brittle cracking) may limit their applications. This may be improved somehow by filling polymer matrix with other materials like silica. Silica filled epoxies are commonly used in power products, mainly as insulating materials to encapsulate electrical components, owing to their very good dielectric properties. Application of silica improves thermal conductivity of composite, which is very important in power applications, but it decreases material toughness.

By adding a filler, such as silica, to a polymer matrix, physical, mechanical and thermal properties of composite change. In a simplified way, composite properties can be determined by the rule of mixtures based on volume fractions of components in the composite. However, in that case the filler size, its shape and the strength of filler/matrix interface may have influence on mechanical properties.

3. Fracture mechanics

3.1. Basics

Fracture mechanics is still a new, developing approach to materials strength [2]. Contrary to classic material strength approaches, where it is assumed that material is ideal and does not have any imperfections, in fracture mechanics it is assumed that there are some discontinuities therein. As a consequence, material strength depends on three parameters (applied load, crack size, fracture resistance) instead of two (applied force, material resistance) used in classical

mechanics [3]. Three cracking modes can be distinguished: opening, in-plane shear, out-of-plane shear. It should be noted that usually there is a need to deal with mixed types of cracking modes [4]. Each of the above-mentioned methods corresponds with stress field, which is:

$$\sigma_{ij}^T = \frac{K_T}{\sqrt{2\pi r}} f_{ij}^T(\theta) \quad (1)$$

where

- σ – stress,
- i, j – x, y or z coordinates,
- K – stress intensity factor,
- T – cracking mode (1, 2 or 3),
- r, θ – polar coordinates placed in the crack tip,
- f – functions dependent on θ .

In an isotropic, elastic type of material, f functions take the form of the following equations:

$$\sigma_{xx} = \frac{K_T}{\sqrt{2\pi r}} \cos\left(\frac{\theta}{2}\right) \left[1 - \sin\left(\frac{\theta}{2}\right) \sin\left(\frac{3\theta}{2}\right) \right] \quad (2)$$

$$\sigma_{yy} = \frac{K_T}{\sqrt{2\pi r}} \cos\left(\frac{\theta}{2}\right) \left[1 + \sin\left(\frac{\theta}{2}\right) \sin\left(\frac{3\theta}{2}\right) \right] \quad (3)$$

$$\tau_{xy} = \frac{K_T}{\sqrt{2\pi r}} \cos\left(\frac{\theta}{2}\right) \sin\left(\frac{\theta}{2}\right) \cos\left(\frac{3\theta}{2}\right) \quad (4)$$

and stress distribution around the crack peak can be described as shown in Fig. 1.

One can notice that if $r \rightarrow 0$, then $\sigma \rightarrow \infty$. This means that each crack has a singularity at the peak.

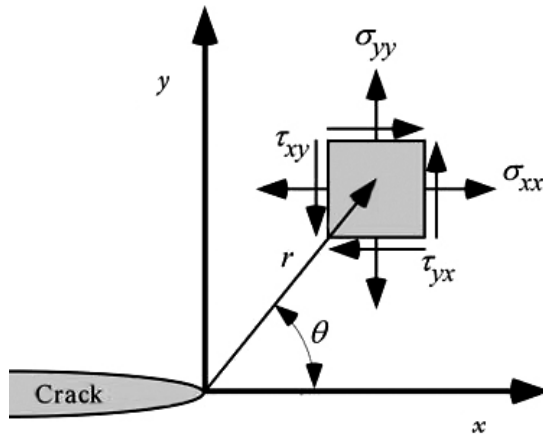


Fig. 1. Stress distribution around the crack peak

There are a lot of approaches for numerical modelling of fracture mechanics. The classic ones are based on time-independent crack behaviour (Linear-Elastic or Elastic-Plastic Fracture Mechanics) and material isotropy. But new computational methods, like time-dependent fracture behaviour or the one based on material microstructure are still being developed by CAE software companies.

3.2. Approaches for numerical analysis of damage process

In the literature, a number of numerical approaches that can be used for analysis of cracking in composites can be found. The most popular methods are the Element-Based Cohesive Behaviour (EBCB), Surface-Based Cohesive Behaviour (SBCB), Virtual Crack-Closure Technique (VCCT) and Extended Finite Element Method (XFEM). Each of these methods has advantages and disadvantages, but two of them may be particularly helpful during the analysis of damage in epoxy resin-based materials. One of them is VCCT, which is one of the newest approaches, based directly on brittle fracture mechanics equations [5]. It is a very powerful technique for modelling brittle fracture and delamination. However, the eXtended-Finite Element Method developed by Belytschko et al. [6] is these days the most promising technique for modelling damage in composite materials. This method is based on the partition of unity instead of crack propagating along the nodes. The traditional Finite Element Method (FEM) coupled with meshing tools does not yet manage to simulate efficiently the propagation of 3D cracks for geometries relevant to engineers in industry [7]. In the XFEM approach, in order to represent a crack on its proper length, nodes whose support contains a crack tip are enriched with discontinuous functions. Such functions are provided by the asymptotic modes of displacement (elastic if calculation is elastic) at the crack tip. Thus, the XFEM is mainly targeted towards problems with strong or weak discontinuities. Application of this technique and the obtained results are presented in the paper.

4. Analysis of damage in dry transformer coil

Dry transformers are very often exposed to harsh operation conditions. In order to evaluate their robustness and minimize the risk of failure, specific standards and tests are defined. An example is C2 test [8], during which a coil or transformer is cooled down to -25 C and heated up by double nominal current. For our study, the coil was cooled down to -50 C in order to evaluate what is its maximal strength.

4.1. 3D simulations

Analysis of dry transformer coil during the C2 test is complex and requires knowledge of temperature distribution in the coil. Therefore, a numerical approach which takes into account all relevant phenomena such as anisotropic and temperature dependent material properties, Joule heat generation, heat transfer by conduction, convection and radiation was

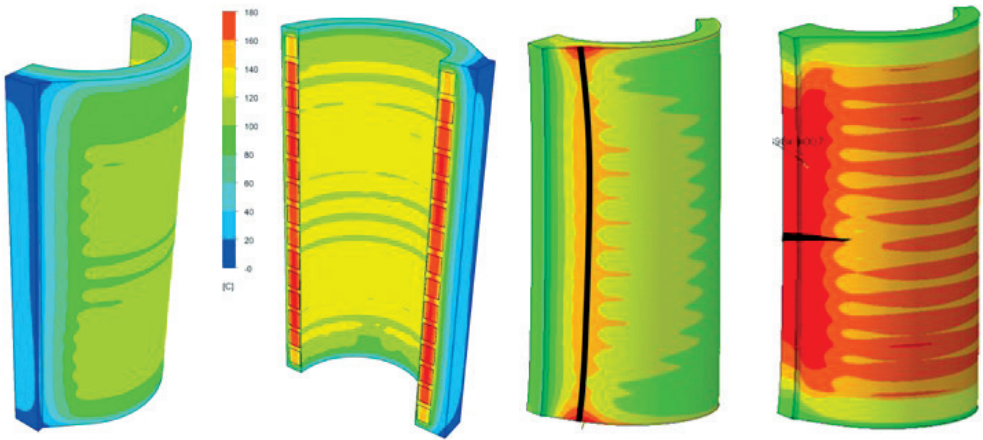


Fig. 2. Calculated temperature distribution (left) and probably crack scheme based on stress distribution (right)

developed and used [9]. Based on the calculated temperature distribution and heat transfer coefficients, it is possible to go to the next step – the cracking analysis. This one has been carried out in commercial software ABAQUS. As a result, the distribution of stress, strain and displacement is obtained. This allows us to estimate the cracking scheme and the risk of its occurrence as depicted in Fig. 2.

4.2. Verification of the simulations

The verification of the results obtained during simulations contains both comparison of temperature distribution (Fig. 3a) as well as crack initiation and propagation after a visual inspection of the coil during and after the C2 test (Fig. 3b).

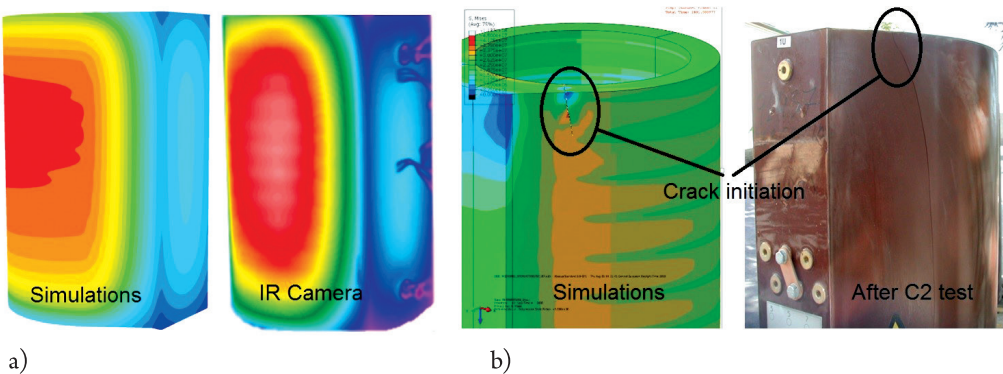


Fig. 3. Comparison of: a) temperature distribution and b) crack initiation and propagation line

5. Microscale analysis of cracking

In the previous chapter, a good agreement between the results from the simulation and the test can be observed. However, if one would like to modify the composite and make epoxy based products more robust, there is a need to investigate microstructural damage.

5.1. Crack simulations of 2D RVE

For numerical analyses of cracking in a microscale, a 2D Representative Volume Element (RVE) was generated on the basis of a real microstructure analysed by a scanning electron microscope (SEM). In such a SEM-image of the real microstructure, the grey scale values of different pixels were evaluated by an in-house developed software tool. In the first analyses, in order to reduce the required computation time, the numerical model has been simplified as presented in Fig. 4. RVE has dimensions of $100 \times 100 \mu\text{m}$.

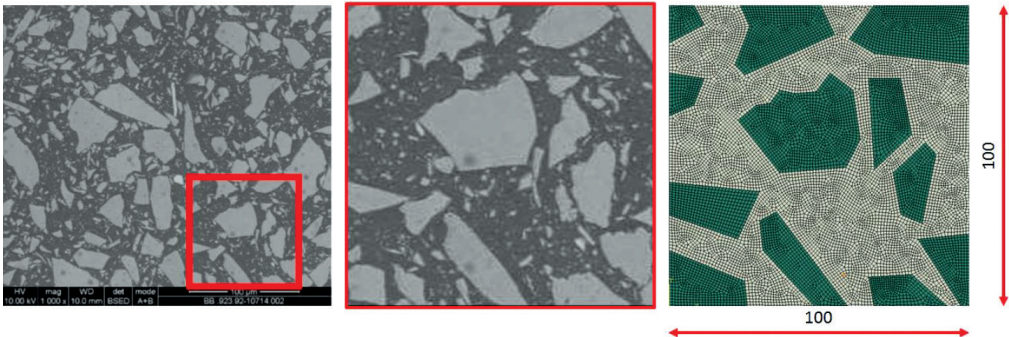


Fig. 4. Exemplary SEM image of the micro-silica filled epoxy composite (left and middle) and 2D FE model (right)

Due to the applied symmetry conditions (in X and Y directions) and displacement condition (0.005mm) applied to one of the edges, the sample was extended during the analysis. Maximal Principal Stress (MaxPS) was chosen for Fracture Initiation Criterion and the value that caused the failure was set to 60 MPa . Adhesion between the matrix and the filler was taken into account during the simulation.

In order to analyze the microstructural cracking of epoxy-based composite, basic mechanical properties have to be determined: Young's modulus and critical strain energy release rate. In case of Young's Modulus, traditional tension test can be used. In case of Critical Strain Energy Release rate, the number of approaches is limited. In this case, special samples were prepared and tested using the Optical Crack Tracing (OCT) technique by Fraunhofer Institute in Germany.

5.2. Results and its verification

As a result, stress-strain curves, stress distribution and crack initiation locations have been obtained. Selected results are shown below. Stress-strain curve is presented in Fig. 5.

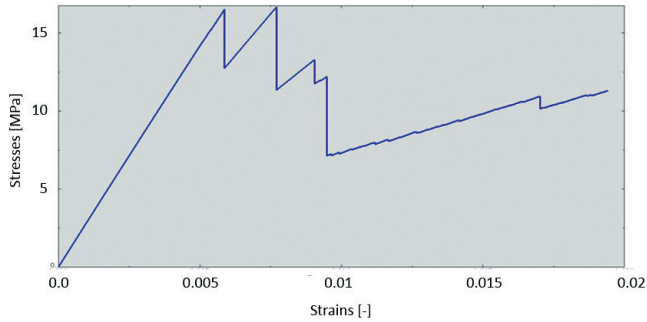


Fig. 5. Stress-strain curve

Peaks visible in Fig. 5. above indicate delamination between the matrix and silica filler, during which a portion of energy was released. Stress distribution for the presented case and crack initiation locations marked with red circles are presented in Fig. 6.

These simulations results would indicate that the initiation of epoxy resin material damage probably takes place at the interface as a result of the loss of interface strength and delamination.

The problem of cracking in polymers and composites is relatively new. Accordingly, the number of standards for the determination of fracture toughness for these materials is limited, although many research institutes have addressed this issue in recent years.

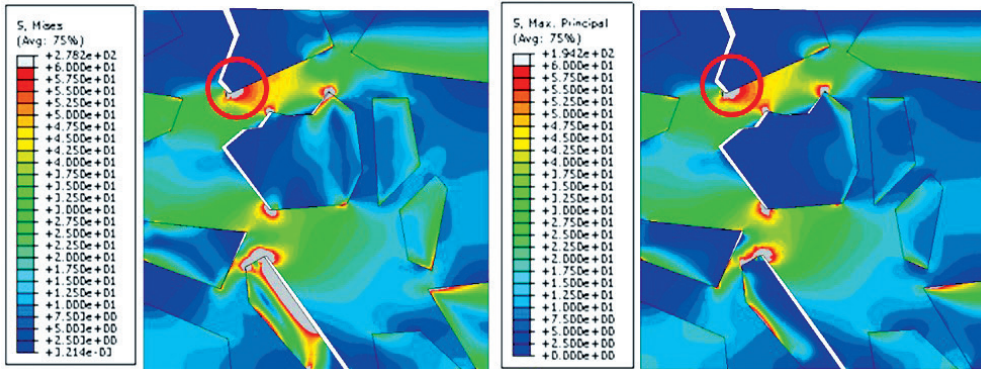


Fig. 6. Stress [MPa] distribution and selected crack initiations (red circles) at the end of analysis

The aim of the experiment was to determine the tensile strength of the composite and to observe the microstructure in order to analyze the process of crack initiation and propagation. At the beginning, by means of a Scanning Electron Microscope (SEM) the microstructure of the composite was obtained. Next, the tensile strength of the samples has been determined by means of a Microtest 5000 tensile machine. Observations performed by means of SEM revealed a complex microstructure of the silica-filled composite (Fig. 7). Observing the process of initiation and propagation of cracks with a scanning electron microscope is very demanding as it is a very rapid process. The resulting images show a breakthrough that in the tested composite crack propagates in the matrix and often runs at the interface between the matrix and the inclusions, which could confirm results from the simulations.

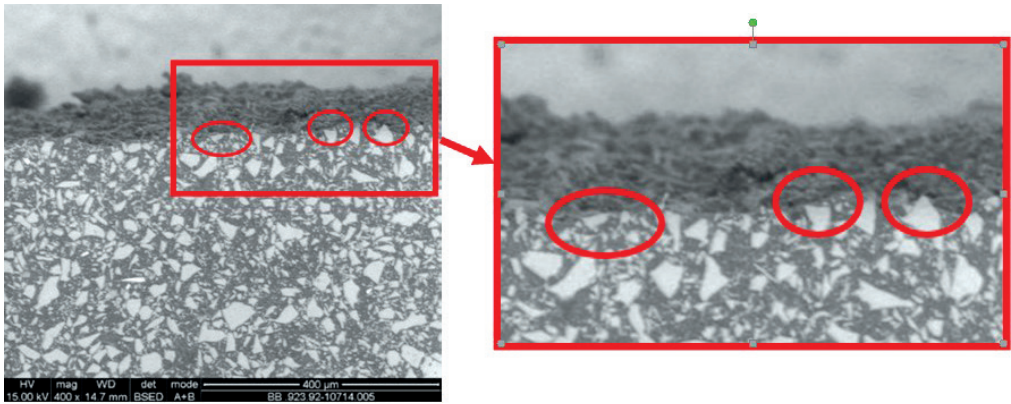


Fig. 7. Fracture surface and microstructure of the composite with marked areas of delamination

6. Summary

Silica filled epoxies are commonly used in power products mainly as insulating materials to encapsulate components on high electrical potential, owing to their very good dielectric properties. Power products are required to operate in harsh environments, for example outdoor applications in regions exposed to intensive sunlight, low temperatures, or excessive thermal extremes. These requirements may activate the process of formation and propagation of the cracks within the resin material. The cracking phenomenon affects not only electrical apparatuses in service conditions, but also causes manufacturing problems.

For the study of cracking phenomena in silica filled epoxy material, the Extended Finite Element Method (XFEM) was selected and mentioned in the first part of the article, together with basics of fracture mechanics. Analyses of cracking phenomena were performed for a full scale element (dry transformer coil) as well as in a microscale (RVE). Experimental verification consists of in-situ tensile tests and microstructural observations with the Scanning Electron Microscope (SEM).

Performed simulations and tests indicate the fact that the initiation of epoxy resin material damage probably takes place at the interface as a result of cracking and loss of a silica/matrix

bond. This results in weakening of the epoxy resin microstructure in this area, which leads to further structural degradation consisting in the propagation of matrix cracks and, as a result, complete damage of the composite structure. The presented research of silica/epoxy composite damage confirmed that analysis of the epoxy resin microstructural damage is not trivial and further study is required for its better understanding.

References

- [1] Nowak T., Kmita G., Sekula R., *Numerical and experimental analysis of thermal-induced residual stresses in epoxy resin based products*, Proc. 8th International Congress on Thermal Stresses, University of Illinois at Urbana-Champaign, USA 2009.
- [2] Anderson T.L, *Fracture Mechanics*, Third Edition, CRC Press 2005.
- [3] Wei R.P., *Fracture Mechanics. Integration of mechanics, materials science, and chemistry*, Cambridge University Press, 2010.
- [4] Ochelski S., *Metody doświadczalne mechaniki kompozytów konstrukcyjnych*, Wydawnictwo Naukowo-Techniczne, Warszawa 2004.
- [5] Krueger R., *Virtual crack closure technique: History, approach, and applications*, Applied Mechanics Reviews, Vol. 57(2), 2014, 109–143.
- [6] Belytschko T. Moës N., Dolbow J., *A finite element method for crack growth without remeshing*, International Journal for Numerical Methods in Engineering 46 (1), 1999 131–150.
- [7] Datta D., *Introduction to eXtended Finite Element (XFEM)*, Erasmus MSc in Computational Mechanics, Ecole Centrale de Nantes 2013.
- [8] IEC 60076-11, Power transformers – Part 11: Dry-type transformers.
- [9] Matysiak Ł., Platek R., Banas M., Sekula R., *eRAMZES – Novel Approach for Simulation of Reactive Molding Process*, 26th European Conference on Modelling and Simulation, Koblenz 2012, 128–135.

Piotr Woś (wos@tu.kielce.pl)

Ryszard Dindorf (dindorf@tu.kielce.pl)

Department of Machine Technology Manufacturing Engineering and Metrology,
Faculty of Mechatronics and Machine Building, Kielce University of Technology

VIRTUAL PROTOTYPING OF ELECTRO-HYDRAULIC PARALLEL MANIPULATOR CONTROL SYSTEMS

WIRTUALNE PROTOTYPOWANIE UKŁADU STEROWANIA ELEKTROHYDRAULICZNEGO MANIPULATORA RÓWNOLEGŁEGO

Abstract

The paper presents the process of virtual prototyping of a parallel manipulator which uses electro-hydraulic servo-mechanisms to drive active elements. A mechatronic solution of tasks of forward and inverse kinematics with the use of a virtual model of the manipulator, as well as a control system for the virtual machine were presented herein. The solution presented in the article makes it possible to study the functions of the control system before its merger with a real manipulator. At the same time, the design process is significantly accelerated.

Keywords: virtual prototyping, electro-hydraulic parallel manipulator, rapid control prototyping

Streszczenie

W artykule zaprezentowano proces wirtualnego prototypowania manipulatora o konstrukcji równoległej, w którym do napędów członów aktywnych wykorzystano serwomechanizmy elektrohydrauliczne. Przedstawiono mechatroniczne rozwiązanie zadań kinematyki z zastosowaniem wirtualnego modelu manipulatora. Zaproponowane w artykule rozwiązanie umożliwia badanie funkcji układu sterowania przed jego połączeniem z rzeczywistym manipulatorem. Jednocześnie proces projektowania zostaje znacząco przyspieszony.

Słowa kluczowe: wirtualne prototypowanie, elektrohydrauliczny manipulator równoległy, szybkie prototypowanie układów sterowania

control algorithm during work in real time and to tune its parameters precisely. When the control performance is satisfactory, the control algorithm on a target hardware platform can be implemented. The project of the manipulator construction in the process of virtual prototyping included the following: formulation of equations describing forward and inverse tasks of the manipulator with a parallel structure and three degrees of freedom, analysis of kinematic structures of a hydraulic parallel manipulator, project of a solid manipulator in 3D CAD software, formulation of dependencies which allow for building a dynamic model of the manipulator, a manipulator prototype with electro-hydraulic axes, development of the manipulator control system, implementation of control algorithm in Matlab/Simulink environment, simulation and verification of the control algorithm, rapid prototyping of the control system and its experimental verification on a real object, verification of the control system operation on a physical manipulator model, experimental studies and an analysis and evaluation of the test results of the parallel manipulator.

2. The design of the parallel manipulator

The prototype of a three-axis electro-hydraulic manipulator with a parallel structure was designed and manufactured in the Division of Mechatronic Devices at the Kielce University of Technology. The entire structure was developed as a test and academic stand, and was dedicated to study the multidimensional algorithms to control the electro-hydraulic servo-mechanisms [2].

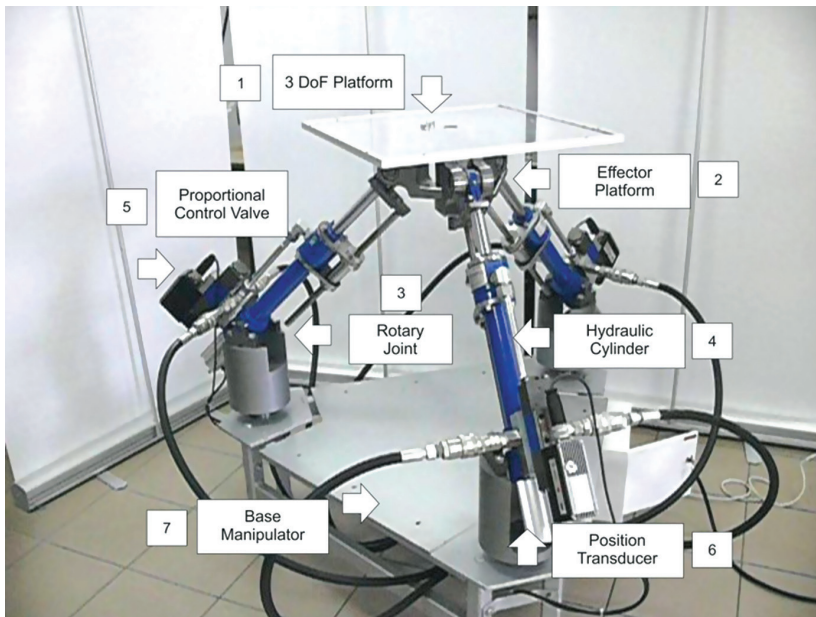


Fig. 2. Manipulator test stand: 1 – hydraulic cylinder 2 – proportional valve, 3 – mobile end-effector platform, 4 – mounting of the manipulator arm, 5 – base manipulator.

The structure of the manipulator presented in this paper is an original solution regarding the application of electro-hydraulic drives for the manipulator with a parallel structure. Figure 2 shows a prototype of the manipulator. The manipulator is placed on a base (7) in the shape of an equilateral triangle. The base apices contain rotating sleeves that make it possible to mount the joint connecting the actuator with the base (3). Active elements of the manipulator include three identical electro-mechanic servo-mechanisms (4). Electro-hydraulic proportional control separators 4/3 (5) were mounted to the actuators. Magnetostrictive sensors were used to determine the position of particular piston rods of the actuators (6).

3. Mechatronic solutions of tasks of the kinematics and dynamics of the model

As far as the design of the mechanical construction of robots is concerned, solutions are sought which will make it possible to use a particular robot in the widest possible range of tasks. In the case of robots with open kinematics, obtaining great flexibility is not a problem, however, as far as the parallel robots are concerned, there is a barrier in the form of design costs and production. This is due to the fact that a parallel robot is comprised of many arms acting directly on the platform. The working space is highly dependent on a range of drive movements and is a common part of all possible positions of each arm. This means that increasing the working space only in one axis is connected with simultaneous increasing of the range of movement of all arms, and thus maintaining adequate stiffness while increasing the dynamics requires the use of better materials or larger cross-sections of structural elements in the places which are most vulnerable to unfavorable tensions. Larger cross-sections mean larger masses which must be moved during work. As a result, any growth of the parameters of a parallel robot associated with space and dynamics increases the cost of the required drives to a much greater extent than it would result from the effects achieved [4].

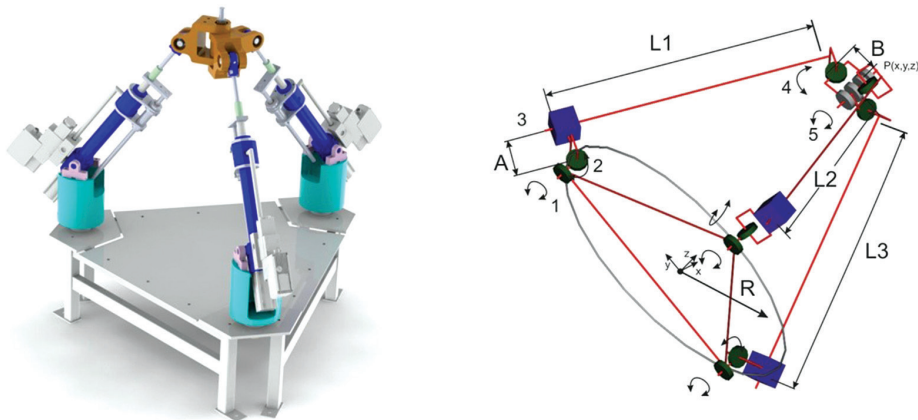


Fig. 3. Kinematic model of the manipulator: 1, 2 4 and 5 – rotating pairs, L1,2 and 3 – sliding pair

The basic issue of the analysis of the kinematic structure is a proper planning of the movement trajectory of the manipulator. The task consists in determining the track transition between the starting and end point of the movement of the effector. It is also necessary to determine displacements, velocity and acceleration for movement connections. While designing a manipulator, solving the tasks of forward and inverse kinematics is an important issue. The task of forward kinematics consists in determining the position of a moveable platform and mapping the system position in the configuration of coordinates against the position of the system in Cartesian space. If one acquaints themselves with the set of values of linear and angular displacements of electro-hydraulic servomechanisms of particular movement connections of the manipulator, the position of its executive element can be determined [6]. The task of inverse kinematics is more difficult to solve and consists in determining the values and configuration of particular positions of the drive elements of the manipulator. Knowledge about the orientation and position of the working end in Cartesian space is required. All possible values of linear and angular displacements which are responsible for achieving the present positions and orientation of the manipulator need to be determined. Solving the task of forward and inverse kinematics is essential in positioning, control and control of the manipulator along a specified curve in Cartesian space [4]. Development of the control system of the manipulator is a complex task which requires i.a.: an analysis of the movement parameters of the effector, development of algorithms to determine non-collision drive movement tracks and determination of the working space of the manipulator in the displacement function of its drives. The whole process requires a lot of trials and modifications. That is why the tasks mentioned before were developed during the process of virtual prototyping with the use of SolidWorks software (development of a solid model) and Matlab/Simulink (implementation and test simulation). This allows for

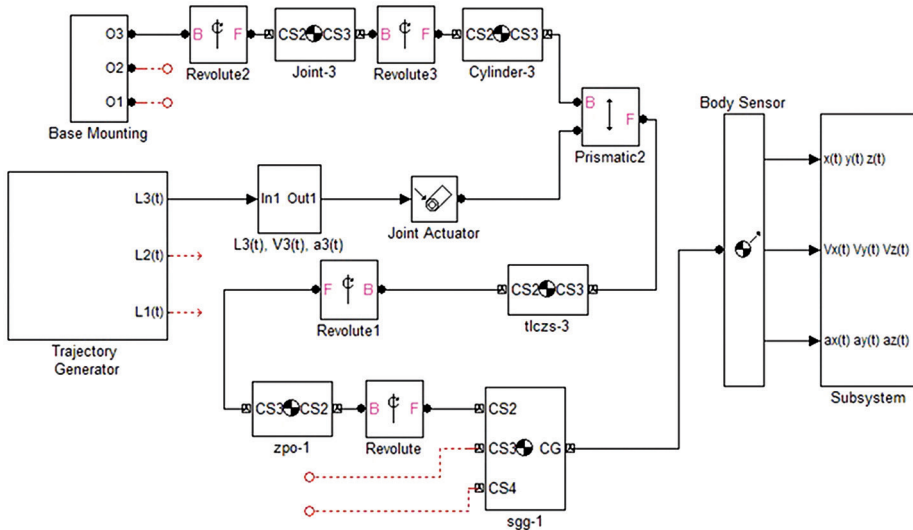


Fig. 4. *SimMechanics* block diagram – inverse kinematics

designing a virtual model and checking its behaviour under fixed initial conditions. Thanks to this solution, the design process was significantly streamlined and accelerated. With the use of *SimMechanics* toolkit, it was possible to import a finished solid model from SolidWorks to Matlab/Simulink, which made it possible to create structures for solutions of forward and inverse kinematics [2]. The block diagram presented in Fig. 4 includes function blocks, i.e.: *Revolute* and *Prismatic*, which provide rotational and translational movements. Moreover, *Joint Actuator* and *Body Sensor* allow respectively: force exertion on a generated binding and measurement of the position of the element to which it is connected. The remaining elements of the diagram include physical elements of the manipulator, such as connectors, joints, cylinders and connecting rods containing information about their mass. This software was used to determine the displacement, velocity and acceleration for the centre point connecting particular arms of the manipulator at fixed displacements of the servo-drives.

This model makes it possible to determine the velocity and acceleration in the remaining moveable elements of the structure. Additionally, the software provides visualization of the movement of the manipulator. Figure 5 shows a virtual model of *SimMechanics* and sample charts of trajectory points of the movement of the manipulator.

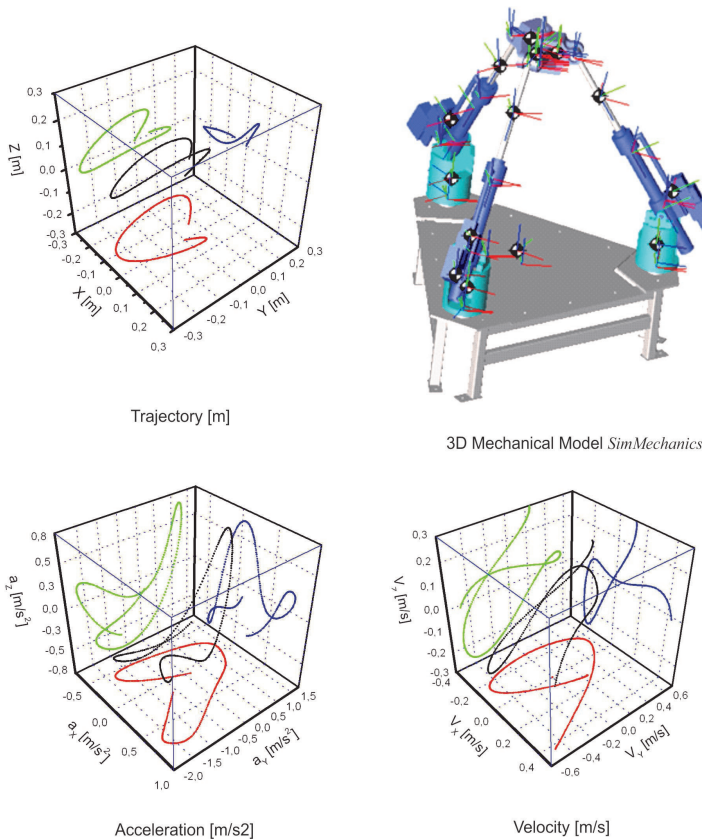


Fig. 5. A virtual model of *SimMechanics* and charts of trajectory points of the movement of the manipulator

4. Rapid prototyping of the control system

Rapid control prototyping (RCP) is treated as real-time simulations and, next to Hardware-in-the-Loop Simulation (HILS) technology, is an important element in the process of design and prototyping of the control systems. Real-time simulation is meant to improve the experimental research due to the application of efficient calculation systems, which, in real-time and on the basis of previously prepared mathematical models, can generate signals corresponding to the simulated device. In Hardware-in-the-Loop technology, on the basis of previously prepared equations, the system simulates the mechanical device in question or a part thereof by generating output signals corresponding to a given object on the basis of the input information received. This method may be used when there is a real driver, but at the same time there is a real danger of damaging the object. In such case, the object is replaced with a simulator, which makes it possible, e.g. to verify the behaviour of the real control system in situations which are difficult to force on a real object due to the associated damage, such as conditions associated with defects or conditions exceeding the permissible parameters. Then, the simulator replaces the real object and thus, the behaviour of the control system might be inspected. A technique which is used more frequently and seems to be more effective is an inverse situation, when the virtual driver simulated on hardware for rapid prototyping co-operates with the real object. Then, while being acquainted with the real object, an individually designed controller can be checked and modified. An important issue which constitutes the basis for rapid prototyping is automation of the code transfer from a virtual desktop (e.g. *Simulink* diagram) to the device conducting rapid prototyping. Subsequently, the equipment designed for rapid prototyping, which is usually based on signal processors, conducts calculations related to the control right and, in that way, generates signals dedicated for a real object [3]. Additionally, such system often provides additional benefits in the form of the possibility to observe the signals associated with control and registration for the sake of later analyses, and it is usually possible to modify the parameters of the control system during the device operation. The parameters of reinforcement coefficients can be changed in real time in the virtual controller for the individual elements thereof, and by observing the behaviour of the system, satisfactory values can be determined (Fig. 6).

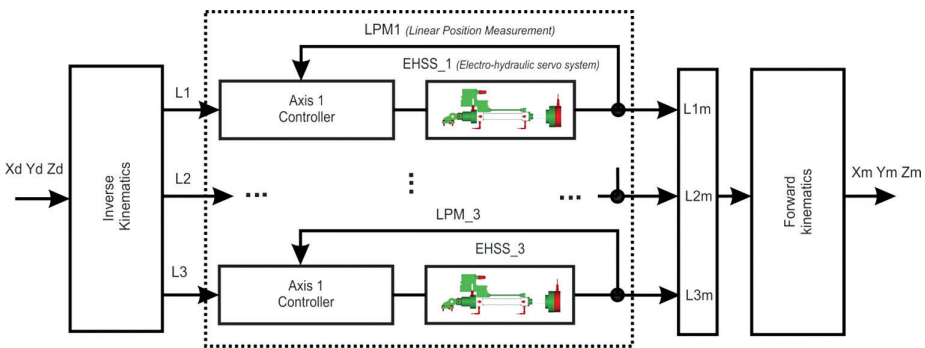


Fig. 6. Block controlled system

Initial axis controller settings were chosen in an experimental way in the process of virtual prototyping. For this purpose, a multi-mass model developed in *SimMechanics* software was incorporated into the model of the control system modelled in Matlab/Simulink environment [3]. Axis controller gain coefficients were chosen in such a way so that the position error of the movement trajectory would be minimized. Only after determining the correct coefficient values for the virtual control system was it possible to proceed with the phase of rapid prototyping. During the designing process, it is possible to match the coefficients of the control algorithm directly in the process of rapid control prototyping, however it is safer and more convenient to conduct the experiment with the use of a virtual object. The control system uses the controller designed on hardware for rapid control prototyping (RCP) and XPC Target computer set equipped with C/A and A/C converter cards of PCI-DAS1602/16 [7].

5. Experimental results

In order to show the accuracy of the control system, an experiment on a real object was conducted. In order to obtain wider information about the control quality, different trajectories of movement were studied. Based on distributed measurement and control system, a test stand for rapid prototyping controller of the electro-hydraulic servo-drive was set up [9]. Fig. 7 presents results of the control process for references signals (X_d , Y_d , Z_d), frequencies 0.16 Hz, 0.32 Hz, 0.48 Hz and 0.8 Hz (Cartesian coordinates).

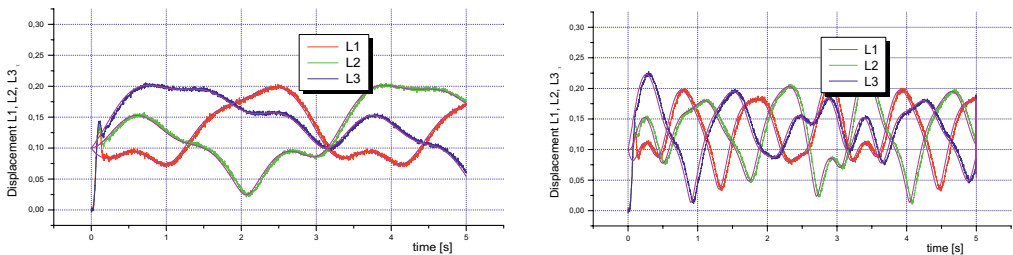


Fig. 7. Displacement of the manipulator arms for control algorithm, according to the sinusoidal reference trajectory in Cartesian coordinates

6. Summary

Research on simulation tests on a developed virtual model makes it possible to verify the software controlling the electro-hydraulic manipulator. Due to the results of the simulations, it is possible to introduce some adjustments in the control algorithm and shorten the time of implementation of the control system in a real device.

References

- [1] Dindorf R., Łaski P., Takosoglu J., Woś P., *Rozproszony system sterowania czasu rzeczywistego do serwonapędów płynowych*, Czasopismo Techniczne, 4–M/2011, 2011.
- [2] Dindorf R., Woś P., *Contour error of the 3-DoF hydraulic translational parallel manipulator*, Advanced Materials Research, Trans Tech Publications Switzerland, Vol. 874, No. 57, 2014, 57–62.
- [3] Dindorf R., Woś P., *Szybkie prototypowanie układu regulacji napędu elektrohydraulicznego*, Napędy i Sterowanie, Nr 10, 2005, 18–22.
- [4] Lung-Wen Tsai, *Robot Analysis, The Mechanics of Serial and Parallel Manipulators*, John Wiley & Sons, Inc, 1999.
- [5] Tlustý J., Ziegert J., Ridgeway S., *Fundamental Comparison of the Use of Serial and Parallel Kinematics for Machine Tools*, Annals of the CIRP, 48/1, 1999, 351–356.
- [6] Tsai L-W., *Robot Analysis, The Mechanics of Serial and Parallel Manipulators*, John Wiley & Sons, New York 1999.
- [7] Woś P., Dindorf R., *Adaptive control of a parallel manipulator driven by electro-hydraulic cylinders*, International Journal of Applied Mechanics and Engineering, Vol. 17, No. 3, 2012.
- [8] Woś P., Dindorf R., Łaski P., Takosoglu J., *Koncepcja sterowania elektrohydraulicznym manipulatorem typu Tricept*, HiP, No. 1, 2011, 9–13.
- [9] Woś P., Dindorf R., *Synchronized trajectory tracking control of 3-DOF hydraulic translational parallel manipulator*, Advances of Intelligent System and Computing, Mechatronics Ideas for Industrial Applications, Springer Verlag, Vol. 317, 2015, 269–277.

Bożena Zwolińska (bzwol@agh.edu.pl)

Faculty of Mechanical Engineering and Robotics, AGH University of Science
and Technology

MODELLING OF PRODUCTION PROCESSES WITH THE USE OF WITNESS SIMULATOR

MODELOWANIE PROCESÓW PRODUKCJI Z WYKORZYSTANIEM SYMULATORA WITNESS

Abstract

Customization of final products forces the so-called "make-to-order" production. In the article, there is a presentation of influence of EPEI changes (Every Part Every Interval indicator) on the efficiency and effectiveness of complex production system. The use of Witness System Simulation Modeling helped to create the model of real object which has been validated in the real work parameters. All of the times of the realized processes have been simulated as random variables with certain density of probability distribution

Keywords: scheduling of the tasks, multi-objective optimization

Streszczenie

Customizacja wyrobów finalnych wymusza produkcję na zasadach make - to - order. W artykule przedstawiono wpływ zmiany wskaźnika EPEI na zmiany wydajności i efektywności złożonego systemu produkcyjnego. Z wykorzystaniem programu Witness System Simulation Modeling opracowano model obiektu rzeczywistego, który następnie został poddany walidacji w zbieżnych z rzeczywistością parametrów pracy. Wszystkie czasy realizowanych procesów zostały w programie Witness zasympulowane jako zmienne losowe o właściwych dla siebie gęstościach rozkładu prawdopodobieństwa.

Słowa kluczowe: harmonogramowanie zadań, optymalizacja wielokryterialna

1. Introduction

Optimization of production processes is one of the most important problems in terms of production. In the production systems, there are multi-criterial and multi-dimensional optimizations. Optimization functions and certain restrictive criteria often vary in some slots (nests) of production stream. In many cases it is a problem of NP – hard [1]. The level of difficulty is caused by the dynamics of changes in statuses of production system, and also by the complexity of particular production system. Dynamics of changes is strictly dependent and connected with changeable environment of the system (like for example: competitors, changes of clients' needs, changes of deliverers, changes of global law regulations). The complexity of production system is affected by the number of active processes, amount of production positions, quality requirements of the process and/or product and also materials which have been used. In changeable conditions, success of the enterprise is caused by its elastics and ability of adapting to a new situation quickly [2, 3]. Frequent changes of statues in the production system impose usage of methods which enable available solutions (which are not always optimal). The use of heuristic algorithms sometimes helps to indicate solutions which are “good enough”.

In the article, there is a presentation of results of the practical use of Witness System Simulation Modelling IT tool from Lanner Group Ltd. The first phase of the model was to identify flow streams and random variables of the times of the process realization in the real object and analyze the similarities between model's parameters. Due to the dependency of many random variables, in the next phase there was multiple validation of the real model executed to reveal representative measurements. There was an interval of trustfulness of 80% set for the results. The achieved results have been named as parameters of the current status and their average values for chosen machines have been presented in Table 1. Based on the analysis of differences of orders there was EPEI set – it was the main parameter of changes for creating extension of efficiency. Table 2 presents average values of parameters of work for chosen machines with EPEI multiplied by two. The results were achieved for the upcoming state of variety of stochastic processes. Analyses of all work's model variants are meeting requirements of stability of processes and “lack of memory”. In case of the analysis of the flows – there is a need to meet the requirement of stream singularity (variant of $\Delta t \rightarrow 0$ has been excluded) in one device.

2. Definition of models and stream flows

To maximize the flexibility of production system in comparison to variables of client's orders – the processes in a considered system should be optimized with the use of the function of minimizing the time which is needed to complete the order. The amount of time which is needed to complete the order is the so called entire lead time of the order (LTO). It is possible to achieve minimal amount of the entire lead time of the order (LTO) through effective scheduling of the tasks [4]. The analyzed example is a convergent structure of serial-parallel production system. In this type of system – optimization of tasks depends on a few different

parameters, such as process, resources (machines and people), materials which empower the system, position of the process in the value stream in comparison to the “narrow throat” and shipment (end of the process) [5, 6]. Moreover, optimization of complex production system depends on the quality of the process, quality of production and also quality of input materials [7]. In such a complex structure, production system has been divided into a group of sub-systems, according to the general theory of complex systems [8, 9]. After that, certain optimization function has been created for all of the extracted sub-systems (to minimize the final time of operations in those extracted sub-systems).

The function of density of realization time probability for consecutive operations has been formulated as a sum of individual times (τ) for the extracted process on certain levels. Optimization in hierarchic production structure is about shaping certain indicators which characterize certain level (sub-system). Complex optimization of the production system should be done based on a weighted mean of particular indicators in a designated sub-system (with an adjustment of certain meaning of particular parameter for the functions of the whole system) [10]. That is why the function of density of realization time probability of consecutive operations is as follows:

$$T_j = \sum_{i=1}^n a_i t_{j,i} \quad \forall \quad j=1,2,\dots,m \wedge i=1,2,\dots,n \quad (1)$$

where T_j is a random variable which describes the whole amount of time for the realization of the processes for j – stream of the value; a_i – weight of the influence of the realization process for the whole time of change, where in every single path of change; n – amount of necessary operations in j – value stream; $t_{j,i}$ – random variable which sets the realization time for the data set necessary to execute all the tasks. Moreover, $t_{j,i} \sim \text{Erlang}(k, \lambda_{j,i})$, where $k=2,3,\dots, l$ for $2 \leq l \leq 20$, k – is a parameter which sets a digit from the same semi-product; $\lambda_{j,i}$ is a parameter of exponential assignment which is caused by the independent time of realization of i production process for single semi-product; $t_{j,i}$ – time of realization of k operations in i process. Random variable $t_{j,i}$ has been assigned based on formula (2):

$$t_{j,i} = \tau_{j,i,1} + \tau_{j,i,2} + \dots + \tau_{j,i,k} \quad (2)$$

where: $\tau_{j,i,1}, \tau_{j,i,2}, \dots, \tau_{j,i,k}$ – random variables which asset the time of realization for a single task, which is caused by the k of orders [11]. Moreover, $\tau_{j,i,k} \sim \text{Exp}(\lambda_{j,i})$. So the density of random variable $t_{j,i}$ is as follows:

$$f_{t_{j,i}}(\tau) = \sum_{k=2}^l \frac{(\lambda_{j,i})^k \cdot (\tau_{j,i,k})^{k-1} \cdot e^{-\lambda_{j,i} \cdot \tau_{j,i,k}}}{(k-1)!} \quad (3)$$

In the article, there was great dynamics of changes of the systems’ statues established. It is caused by differences in client’s orders $t_{j,i} \sim \text{Erlang}(k, \lambda_{j,i})$ for $k=1$, has been skipped, because there will be a different result due to the fact of Erlang’s distribution: $t_{j,i} \sim \text{Exp}(\lambda_{j,i})$ [12, 13]. Then, random variable T_j which defines the whole amount of time for realizing the order will be a sum of independent random variables with different $\lambda_{j,i}$ parameters [16].

The complexity of the scheduling process is affected by the amount of machine resources with the same attributes. The term “machine’s attribute” means its ability to execute certain production task. In the analyzed production system there are two different tasks: 1) dividable and 2) undivided with priority of operation. In both there are different criteria of optimization [3].

Elementary criterion of optimization for dividable alignment is minimal time of ending of the process for the necessary system for the tasks [3].

$$t_{j,i} = \sum_{k=2}^l \tau_{j,i,k} \rightarrow \min \quad \forall \quad 2 \leq l \leq 20 \quad (4)$$

where: $t_{j,i} \sim \text{Erlanga}(k, \lambda_{ji})$ – set random variable of the time of realization of the system necessary to execute k tasks in i – process of j stream, $\tau_{j,i,k} \sim \text{Exp}(\lambda_{ji})$ – random variable of single k – task in i – process of j – stream.

In the case of undivided alignment, the criterion for optimization is aligning the tasks to achieve minimal value of the weighted mean of the flow time [3].

$$\bar{t} = \sum_{i=1}^n b_i \cdot t_{j,i} \rightarrow \min \quad (5)$$

where: \bar{t} – weighted mean of the change’s time of i^* processes with indivisible tasks for j – production stream.

In processes or production sockets of the realization time which is lower than maximal time which is available for value stream – there is a possibility to use aligned algorithms of random limits of the order. In this case, there is a need of meeting the criteria for the stream not to be critical (which do not determine the lead time of order LTO). Moreover, in the case of randomization of the alignment there is a need of the following situation:

$$\tilde{T}_j < T_{\max} \quad (6)$$

where \tilde{T}_j – random variable which defines the time of change of j path of the random alignment of the tasks; T_{\max} – random variable which defines maximal time of change which is a critical path for the data set which is necessary for executing the tasks.

3. Modelling with the use of Witness Simulator

Effective and efficient use of the procedure of scheduling of complex system tasks has to be supported by IT tools. Verification of ideas and proposals of improvements of the complex production system on the real object is risky and often ineffective [14]. That is why a lot of actions are first validated with the use of simulators. Results achieved after the use of IT tools have an impact on decision of implementation of the verified solution. Often simulators help with decision making process in current tasks.

The convergent production system aforementioned in the article was produced in a Witness System Simulation Modeling simulator (from Lanner Group Ltd.). Due to the individual character of the production, the system is not a deterministic model. All the times of the processes are presented with the use of exponential alignment. For each and every time, real data was gathered and then optimal λ_i was assigned. A critical path was analyzed. It determines the time of realization of customer's orders. Picture 1 presents a print screen of the production system which was created in Witness software.

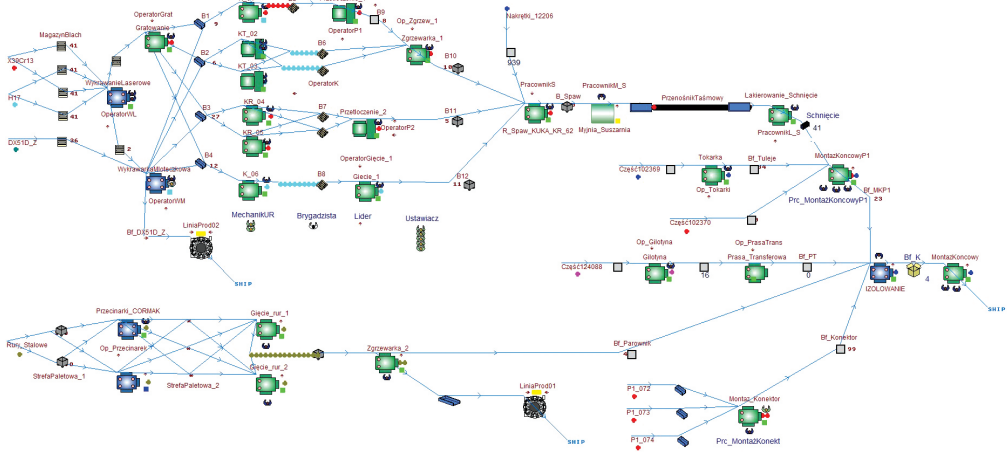


Fig. 1. Layout of the modelled production system

To conduct proper validation of this production system and assign acceptable parameters of work and possible areas of development, there is a need to model the system in IT environment which is the most realistic. Whilst modelling convergent system, it is important to concentrate on proper elaboration of the relation between the objects (machines). Then, parameters of shaping of the intensity of flow stream between the objects were set and also priorities of elementary tasks were presented. The final step was about conducting validation of work of the modelled system. Based on the results, solutions were presented. The final result of the project was to estimate attractiveness of potential implementation of improvements to achieve effectiveness for the future status.

4. Results of the modelled object's simulation

Analysis of the modelled production system was done for the simulation time (t_{sym}) which was equal to two weeks of work in the mode of two changes: $t_{sym} = 9600$ minutes. In this time two tasks of time around 22.500 of workhours for each production socket were executed. After taking into consideration losses after lack of quality, the number of final products were set. The amount of created products for different groups was around 390. Taking into consideration variability of need, the EPEI (Every Path Every Interval) indicator was set (around

1.78 stock). For the aforementioned parameters, a model of validation was conducted. Table 1 presents results of chosen machines of the modelled system before adding adjustments. For the parameters of the actual system, some adjustments were set, which were simulated as upcoming state. Then, a comparison of the results from the current and upcoming states was conducted.

Table 1. Results of the modelled object simulation – current state

Name	$M_{1,1}$	$M_{1,2}$	$M_{2,1}$	$M_{2,3}$	$M_{2,5}$	$M_{2,6}$	M_5	M_6
Idle time %	0	0	35,5	12,9	0,8	3,8	10,1	11,3
Work time %	95,2	24,3	43,6	72,4	84,2	85,6	81,6	86,8
Blocking time %	0	0	0	3,6	9,5	1,5	1,9	0
Wait for worker %	0,2	3,8	0	0	0	0	0	0
Set up %	4,1	70,6	19,4	10,3	4,9	6,8	6,2	1,9
Breakdown %	0,5	1,3	1,5	0,8	0,6	2,3	0	0
Repair–wait for worker %	0	0,3	1,2	0,1	0,3	0,4	0	0
Number operations	11,877	2457	5834	6032	5936	4731	15,793	6769

The assumption of the changes was to shorten the whole time of realization of a single order (LTO) in the enterprise. The target was to be achieved by minimizing the sum of time which do not add the value of NVAT (Non Value Added Time). Those changes extended EPEI – Every Part Every Interval twice to the value of 3.6 stock and effectiveness in aspect of time sorting of the order of the executed tasks in critical stream. All of the semi-products of the critical path which were extracted by the PERT method were assigned with highest priorities. Table 2 presents the results after adding adjustments.

Table 2. Results of the modelled object simulation – upcoming state

Name	$M_{1,1}$	$M_{1,2}$	$M_{2,1}$	$M_{2,3}$	$M_{2,5}$	$M_{2,6}$	M_5	M_6
Idle time %	0	0	27,2	11,3	0,3	3,2	0,2	9,9
Work time %	96,8	37,8	56,1	75,5	88,4	88,7	90,4	88,7
Blocking time %	0	0	0,1	4,2	7,8	0,1	2,7	0
Wait for warker %	0	2,7	0	0	0	0	0	0
Set up %	2,9	57,4	15,7	7,8	3,2	6,3	6,7	1,4
Breakdown %	0,3	2,1	0,9	1,2	0,3	1,7	0	0
Repear–wait for warker %	0	0,5	0,1	0	0	0,1	0	0
Number operations	12,144	3789	7497	6307	6237	4897	16,132	6923

Devices $M_{1,1}$ and $M_{1,2}$ execute processes of cutting 1 – laser and 2 – hammer; $M_{2,1}$, $M_{2,3}$, $M_{2,5}$, $M_{2,6}$ – the group of edge press of the same attributes but different parameters. It realizes the process of curving with dividable sorting; M_5 and M_6 realize processes of varnishing and isolating in which appears coupled, undividable sorting of tasks and flows of random order of semi-product creation.

5. Conclusion

Optimization of complex production systems which carry certain tasks is a difficult process. In this kind of system (with overwhelmed sub-systems and with underload of the other systems), improvement of efficiency and productivity is possible only with the use of IT tools. Without special software it is impossible to achieve acceptable parameters of work. In the production process there are about 600 different kinds of final products. Production process is customized and dedicated to only one client at the same time. Due to a great variety of final products, there is no “stockroom” production. There are about 450 to 650 different subsystems which make one final product. About 15% of these are components delivered by the suppliers. The components are not processed in the production process. These are only edited in certain steps of the production process. The rest of 85% are the elements which are produced whilst analyzing system of stocks.

In the article, there is an attempt of real modelling of convergent production system with the use of Witness Simulation. Assumptions in the modelled system were about maximization of the executed tasks with the minimization of stoppages of machines. The production part was extended to maximize EPEI – Every Part Every Interval indicator. Extension of the indicator led to the extension of the usage of devices and extension of executed tasks. It is important to remember that the simulated solution led to the shortening of LTO time from the enterprise’s position. However, with the extended production part in the MTO structure – “make-to-order” is the average time of waiting for the finalization of the order. If there are a few criteria for the same system, it is impossible to assign the optimal solution which will meet the criteria of a few different functions of the final aim. Heuristic approach enables assigning methods and principles in elaborating parameters of the work.

References

- [1] Gnienenko B.W., Kowalenko I.N., *Wstęp do teorii obsługi masowej*, PWN, Warszawa 1966.
- [2] Nyhuis P., Windhal H.P., *Fundamentals of Production Logistics. Theory, Tools and Applications*, Springer – Verlag, Berlin Heidelberg 2009.
- [3] Rother M., Harris J., *Creating Continuous Flow*, Lean Enterprise Institut Poland, Wrocław 2007.
- [4] Palmer D. R., *Maintenance Planning and Scheduling Handbook*, Mc Graw–Hill Education, New York 2012.
- [5] Wiegand B., Langmaack R., Baumgarten T., *Lean Maintenance System Zero Maintenance Time – Full Added Value Workbook*, Lean Institute, Portsmouth 2005.
- [6] Özgüven C., Özbakir L., Yavuz Y., *Mathematical models for job-shop scheduling problems with routing and process plan flexibility*, Applied Mathematical Modelling, Vol. 34, 2010, 1539–1548.

- [7] Zwolińska B., Michłowicz E., Kubica Ł., *The mathematical model describing the influence of chosen parameters on the quality of final products manufactured from type 1.4307 steel*, METAL 2016, 25th Anniversary International Conference on Metallurgy and Materials, Brno 2016.
- [8] Klir J.G., *Ogólna teoria systemów*, Wydawnictwo WNT, Warszawa 1976.
- [9] Buslenko N.P., Kałasznikow W.W., Kowalenko J.N., *Teoria systemów złożonych*, Wydawnictwo PWN, Warszawa 1979.
- [10] Devore L.J., *Probability and Statistics for Engineering and the Sciences*, Books/Cole, Boston 2012.
- [11] Smaili K., Kadri T., Kadry S., *Hypoexponential Distribution with Different Parameters*, Applied Mathematics, Vol. 4, 2013, 624–631.
- [12] Durrett R., *Probability: Theory and Examples Cambridge Series in Statistical and Probabilistic Mathematics*, Cambridge University Press, New York 2010.
- [13] Akkouchi M., *On the convolution of exponential distributions*, Journal of the Chungcheong Mathematical Society, Vol. 21, No. 4, 2008, 501–510.
- [14] Taylor G.D., *Logistics Engineering Handbook*, CRC Press Taylor & Francis Group, Boca Raton 2008.
- [15] *WITNESS Training Reference manual*, Copyright 2012 Lanner Group Ltd.
- [16] Sum of independent exponentials, <https://people.maths.bris.ac.uk/~mb13434/sumexp.pdf>